

Ludwig-Maximilians-Universität München
Fakultät für Physik

DISSERTATION

Measurement of the Top Quark Mass at DØ Run II
with the Matrix Element Method in the Lepton+Jets
Final State



vorgelegt von

Philipp Schieferdecker

geboren in
München

München, den 5. August 2005

Ludwig-Maximilians-Universität München
Fakultät für Physik

DISSERTATION

Measurement of the Top Quark Mass at DØ Run II
with the Matrix Element Method in the Lepton+Jets
Final State



vorgelegt von

Philipp Schieferdecker

geboren in
München

München, den 5. August 2005

Erstgutachterin: Prof. Dr. D. Schaile
Zweitgutachter: Prof. Dr. W. Dünneberger

Tag der mündlichen Prüfung: 21.10.2005

to my parents

para mi amor, mi vida, mi reina, mi consentida Ana Karina

*“You’ll never walk alone!”
Südtribüne, Westfalenstadion*

Acknowledgments

I owe special thanks to my thesis advisor Prof. Dr. Dorothee Schaile. She gave me a huge leap of faith when she sent me off to Fermilab the first time, and I don't think I ever thanked her for that. She then supported me during my graduate years in any imaginable way while allowing me the greatest possible freedom in choosing my research according to my personal interests. Those interests of mine led to 18 months worth of projects concerning the development of software for the ATLAS experiment, and I enjoyed tremendously to work with Dr. Günter Duckeck and Alexander Brandt during that time. I am thankful to Dr. Thomas Beikircher, who injected me with the enthusiasm for the wonders of physics at an early age. Years later, Prof. Dr. Christoph Paus made a real scientist out of me, and turned my enthusiasm into passion. Dr. Arnulf Quadt took me on the journey towards a top mass measurement at $D\bar{0}$, and guided me and my dear "Co-Forscher" Kevin Kroeninger during those all important first steps. I think we both learned a lot during those endless nights following oversized Mexican meals. My friend Dr. Mike Mulhearn convinced me to change direction on my own terms at just the right time, and Dr. Daniel Whiteson gave me invaluable advice on how to do so. I couldn't have done it without the help of Dr. Frank Fiedler, who supported and guided me until the measurement was finally completed. Dr. Alan Magerkurth's and Petra Haefner's contributions to the analysis presented in this thesis must not be forgotten. I enjoyed the constant support by the $D\bar{0}$ top group conveners: Prof. Dr. Chris Tully, Dr. Aurelio Juste, Prof. Dr. Regina Demina, Dr. Ivor Fleck, and Dr. Erich Varnes. I am very grateful to the members of the $D\bar{0}$ Run II Editorial Board 011: Prof. Dr. Serban Protopopescu, Prof. Dr. Pushpa Bhat, Dr. Gaston Gutierrez, Dr. Abid Patwa, and Dr. Scott Snyder. It is only thanks to their scrutiny and flexibility that this analysis is already published as a preliminary result, which I am quite proud of. I cannot hope to appropriately express my gratitude to my parents, Dr. Friedrich-Karl and Marion Schieferdecker, who always supported me on my way, even though it led me painfully far away from home. Last but not least, I have to thank my beloved wife Ana Karina, the greatest women in the world. She sacrificed a lot in order to bounce around the planet to wherever I needed to be in the last five years. ¡Viva Colombia!

Abstract

The mass of the top quark is a fundamental parameter of the Standard Model. Its precise knowledge yields valuable insights into unresolved phenomena in and beyond the Standard Model. A measurement of the top quark mass with the matrix element method in the lepton+jets final state in DØ Run II is presented. Events are selected requiring an isolated energetic charged lepton (electron or muon), significant missing transverse energy, and exactly four calorimeter jets. For each event, the probabilities to originate from the signal and background processes are calculated based on the measured kinematics, the object resolutions and the respective matrix elements. The jet energy scale is known to be the dominant source of systematic uncertainty. The reference scale for the mass measurement is derived from Monte Carlo events. The matrix element likelihood is defined as a function of both, m_{top} and jet energy scale JES , where the latter represents a scale factor with respect to the reference scale. The top mass is obtained from a two-dimensional correlated fit, and the likelihood yields both the statistical and jet energy scale uncertainty. Using a dataset of 320 pb^{-1} of DØ Run II data, the mass of the top quark is measured to be

$$\begin{aligned} m_{\text{top}}^{\ell+\text{jets}} &= 169.5 \pm 4.4 \text{ (stat. + JES)} {}_{-1.6}^{+1.7} \text{ (syst.) GeV} \\ m_{\text{top}}^{e+\text{jets}} &= 168.8 \pm 6.0 \text{ (stat. + JES)} {}_{-1.9}^{+1.9} \text{ (syst.) GeV} \\ m_{\text{top}}^{\mu+\text{jets}} &= 172.3 \pm 9.6 \text{ (stat. + JES)} {}_{-3.3}^{+3.4} \text{ (syst.) GeV} . \end{aligned}$$

The jet energy scale measurement in the ℓ +jets sample yields $JES = 1.034 \pm 0.034$, suggesting good consistency of the data with the simulation. The measurement forecasts significant improvements to the total top mass uncertainty during Run II before the startup of the LHC, as the data sample will grow by a factor of ten and DØ's tracking capabilities will be employed in jet energy reconstruction and flavor identification.

Zusammenfassung

Die Masse des Top-Quarks ist ein fundamentaler Parameter des Standard-Modells. Ihre genaue Kenntnis liefert wertvolle Aufschlüsse bezüglich unverstandener Phänomene im Standard-Modell und darüber hinaus. Die Messung der Top-Quark-Masse mit der Matrixelement-Methode im Lepton+Jets Zerfallskanal in Run II des DØ Experiments wird präsentiert. Ereignisse werden selektiert, wenn sie ein isoliertes Lepton (Elektron oder Myon), signifikante fehlende transversale Energie und genau vier Kalorimeter-Jets aufweisen. Für jedes Ereignis werden die Wahrscheinlichkeiten berechnet, dass das Ereignis durch den Signal- bzw. Untergrund-Prozess produziert worden ist, basierend auf der gemessenen Kinematik, den Auflösungen der rekonstruierten Objekte und der prozess-spezifischen Matrixelemente. Die Kenntnis der Jet Energie Skala ist die dominierende Quelle systematischer Unsicherheit dieser Messung. Die Referenz-Skala wird in Monte Carlo Ereignissen bestimmt. Die Matrixelement-Likelihood wird definiert als Funktion beider Variablen, m_{top} und JES , wobei letzterer einen Skalierungs-Faktor bezüglich der Referenzskala beschreibt. Die Topmasse wird mittels eines zweidimensionalen korrelierten Fits bestimmt, wobei der Likelihood sowohl den statistischen Fehler als auch den Fehler durch Jet Energie Skala liefert. Die Methode wird auf einen DØ Run II Datensatz angewandt, der einer integrierten Luminosität von 320 pb^{-1} entspricht, und die Messung ergibt

$$\begin{aligned} m_{\text{top}}^{\ell+\text{jets}} &= 169.5 \pm 4.4 \text{ (stat. + JES)} \begin{matrix} +1.7 \\ -1.6 \end{matrix} \text{ (syst.) GeV} \\ m_{\text{top}}^{e+\text{jets}} &= 168.8 \pm 6.0 \text{ (stat. + JES)} \begin{matrix} +1.9 \\ -1.9 \end{matrix} \text{ (syst.) GeV} \\ m_{\text{top}}^{\mu+\text{jets}} &= 172.3 \pm 9.6 \text{ (stat. + JES)} \begin{matrix} +3.4 \\ -3.3 \end{matrix} \text{ (syst.) GeV} . \end{aligned}$$

Die Messung der Jet Energie Skala im ℓ +jets Datensatz ergibt $JES = 1.034 \pm 0.034$, was auf gute Übereinstimmung der Daten mit der Simulation hinweist. Die vorliegende Messung verspricht signifikante Verbesserungen des Gesamtfehlers der Topmasse in Run II noch vor dem Start des LHC, wenn der Datensatz sich verzehnfachen und DØ's Spurvermessung in die Rekonstruktion von Jet Energien und die Identifikation von b Jets einbezogen werden.

Contents

1	Introduction	1
2	The Top Quark	3
2.1	Standard Model	3
2.2	The Top Quark	5
2.2.1	Particle Production in $p\bar{p}$ Collisions	5
2.2.2	Top Quark Production	7
2.2.3	Top Quark Decay	7
2.2.4	The Top Quark and the Higgs Boson	8
3	The Tevatron and the DØ Detector	13
3.1	The Fermilab Accelerator Chain	13
3.2	The DØ Detector	17
3.2.1	DØ Coordinate System	17
3.2.2	The Tracking System	18
3.2.3	The Calorimeter	20
3.2.4	Muon Spectrometer	21
3.2.5	Trigger and DAQ	22
4	Event Reconstruction and Data Selection	27
4.1	Tracks	27
4.2	Primary Vertex	28
4.3	Muons	29
4.4	Electrons	30
4.5	Jets	31
4.5.1	Jet Reconstruction	31
4.5.2	Jet Energy Scale	32
4.5.3	Jet Energy Resolution	33
4.6	Missing Transverse Energy	33
4.7	Event Trigger	39
4.8	Data Sample	41
5	The Matrix Element Method	45
5.1	Method Description	45
5.2	Jet Resolution Handling: Transfer Functions	47

5.2.1	Jet Transfer Function Derivation	47
5.2.2	Jet Transfer Function and the JES parameter	49
5.3	Calculation of the event probability	51
5.3.1	Calculation of the Signal Probability P_{sgn}	51
5.3.2	Normalization of the Signal Probability P_{sgn}	53
5.3.3	Calculation of the Background Probability P_{bkg}	57
5.3.4	Normalization of the Background Probability P_{bkg}	57
5.4	Likelihood Evaluation	61
6	Measurement of the Top Quark Mass	63
6.1	Ensemble Testing Procedure	63
6.2	Validation of the Fit Procedure: Parton-Level Tests	64
6.3	Measurement of the Sample Composition	70
6.3.1	Determination of QCD Contamination: Matrix Method	70
6.3.2	Topological Likelihood Fit	71
6.4	Calibration with Monte Carlo Events	78
6.5	Application to Data	89
6.6	Cross Check: W Boson Mass Fit	94
6.7	Systematic Uncertainties	95
6.7.1	Jet Energy Scale	95
6.7.2	JES p_T dependence	95
6.7.3	b -Jet Energy Scale	95
6.7.4	Signal Modeling	96
6.7.5	Background Modeling	101
6.7.6	Sample Composition	101
6.7.7	QCD contamination	103
6.7.8	MC Calibration	103
6.7.9	Trigger	105
6.7.10	PDF Uncertainty	105
6.7.11	Summary of Systematic Uncertainties	106
7	Conclusion and Outlook	109
A	MC Calibration for $e + jets$ and $\mu + jets$ events	113
B	Solving the Event Kinematics	123
C	The Jacobian Determinant for the P_{sgn} Integration	125
D	Transfer Function Cross-Checks	129
E	Data to Monte Carlo Comparison	145
E.1	Events with exactly 4 jets (signal sample)	145
E.2	Events with exactly 3 jets	158
E.3	Events with exactly 2 jets	169

Chapter 1

Introduction

The top quark was discovered in 1995 by the DØ [1] and CDF [2] collaborations in Run I of the Tevatron $p\bar{p}$ collider. It stands out among other elementary particles with its strikingly high mass and is believed to play a key role to our fundamental understanding of nature beyond the Standard Model. The latter relates the mass of the top quark to the mass of the Higgs boson, the last particle of the Standard Model which is predicted but remains undetected. Consequently, the hunt for the Higgs boson represents a major priority for high energy physics next generation of collider experiments at the LHC, and Tevatron Run II is expected to guide the way with precise information on the top quark mass.

The Standard Model predicts top quarks to be produced dominantly in top-antitop pairs via $q\bar{q}$ annihilation (85 %) and gluon fusion (15 %) in $p\bar{p}$ collisions at $\sqrt{s} = 1.96$ TeV¹. Both top and antitop are predicted to decay almost exclusively to a W boson and a b quark. If one of the W bosons decays hadronically to a pair of light quarks, while the other decays to either an electron or muon and the corresponding neutrino, the event is referred to as a *lepton+jets* event. The signature of this decay in the detector is the presence of four or more jets, an isolated lepton and missing transverse energy \cancel{E}_T from the undetected neutrino. The dominant physics background to this process is the electroweak production of a leptonically decaying W in association with four or more quarks, antiquarks, and gluons. Additional instrumental background arises from multi-jet events, where either a heavy flavor jet decays semi-leptonically but only the muon is reconstructed (μ +jets channel) or a jet is misidentified as an electron (e+jets channel). This instrumental background is referred to as “QCD” background throughout this thesis.

The top mass measurement with the matrix element method at DØ in Run I [3] improved the statistical and systematic uncertainty significantly with respect to previous measurements and generated considerable excitement. It yielded the most precise top mass value to date and fosters the hope for even more stringent constraints in Run II with a much larger data set and an upgraded detector. This thesis describes a measurement of the top quark mass with the matrix element method with a DØ Run II dataset of 320 pb⁻¹ in the lepton+jets (ℓ +jets) channel. Many significant improvements with respect to Run I were introduced to the matrix element method and are described in the following chapters.

For each event in the data sample, the probability for the event to originate from $t\bar{t}$ produc-

¹Natural units are used throughout this thesis, $\hbar = c = 1$.

tion assuming a certain top mass and the probability to arise from the $W(\rightarrow l\nu) + \text{jets}$ process are calculated. Both probabilities are combined into an event probability, and a likelihood is formed and maximized with respect to the assumed top mass. The top mass measurement is systematically limited by the knowledge of the jet energy scale. The Run I matrix element likelihood is extended by an additional parameter, essentially yielding a simultaneous measurement of both the top mass and the jet energy scale. This potential arises mainly from the mass constraint of the hadronically decaying W boson. A correlated fit to the two-dimensional likelihood yields an error on the top mass which includes both the statistical error and the jet energy scale uncertainty by construction. No external knowledge on the uncertainty of the applied jet energy scale is used, and the offset of the jet energy scale with respect to the reference scale is measured, assuming that it does not significantly depend on jet p_T or η . As a consequence, the dominant systematic uncertainty on the top mass will profit from increasing statistics, forecasting excellent potential for the near future.

The increased statistical sensitivity [5] of this method with respect to other methods is largely due to the calculation of the event-per-event signal probability. It allows well-measured events to contribute more information to the likelihood function than poorly measured events. This represents the fundamental difference to methods which are sensitive only to one or more distributions of a whole set of events, where each event is given the same weight. Moreover, the computation of the matrix element represents evaluation of the full kinematics of the event, as opposed to exploiting information from only a few variables.

Chapter 2

The Top Quark

2.1 Standard Model

High energy physics is the quest for the most fundamental building blocks of nature and the rules which govern their interactions. Today, matter appears to consist of no more than twelve elementary particles which reveal no experimental evidence for further underlying structure: Six *quarks* and six *leptons*. In this accounting, particles and their antiparticles are considered as one, and the multitude of particles of different color is not counted separately. All twelve particles carry spin $\frac{1}{2}$ and are referred to as *fermions*. The *u* and *d* quarks are the fundamental constituents of nucleons like protons and neutrons. The electron is the most prominent lepton, as nucleons and electrons form atoms and thus the world as we see and feel it. Quarks and leptons are categorized in three generations, as shown in Table 2.1. Particles in higher generations have higher masses and are mostly unstable; we need to produce them in the laboratory in collisions of stable particles in order to observe and study them.

All experimentally observed phenomena can be described by interactions between those fermions in terms of three forces: *Gravity*, the attractive force between matter and energy; the *Electroweak Force*, a unified description of electricity, magnetism and the weak force; and the *Strong Force*, the force which binds the quarks in the nucleon. The “*Standard Model*” of elementary particle physics successfully describes our current understanding of quarks, leptons and their interactions through the electroweak and strong nuclear forces. It is intimately re-

	Generation			Charge
	I	II	III	
Quarks	<i>u</i>	<i>c</i>	<i>t</i>	$+2/3$
	<i>d</i>	<i>s</i>	<i>b</i>	$-1/3$
Leptons	<i>e</i>	μ	τ	-1
	ν_e	ν_μ	ν_τ	0

Table 2.1: The three generations of spin- $\frac{1}{2}$ -fermions. The letters labeling the quarks are abbreviations for “up” (*u*), “down” (*d*), “charm” (*c*), “strange” (*s*), “top” (*t*) and “bottom” (*b*).

Gauge Boson	Symbol	Charge	Spin	Mass (GeV)	Force
Photon	γ	0	1	0	Electromagnetic
Z^0	Z^0	0	1	91.2	Weak
W^\pm	W^\pm	± 1	1	80.4	Weak
gluon	$g_1 \dots g_8$	0	1	0	Strong
graviton	G	0	2	?	Gravity

Table 2.2: Standard Model gauge bosons: mediators of the fundamental forces between interacting elementary particles.

lated to the development of quantum mechanics and the realization that the laws which govern the universe are fundamentally probabilistic. Consequently, interactions between elementary particles are described by *Quantum Field Theories*: All particles are described as fields; forces are interpreted as the exchange of mediator particles between interacting fermions. These force-carriers are referred to as “*gauge bosons*” and are spin-1 particles¹. Table 2.1 lists all gauge bosons of the Standard Model plus the Graviton, which is postulated to carry the gravitational force but has not been detected. Each Standard Model gauge boson is specific to one of the forces, and its properties determine strength and range of the interaction. The most familiar of these bosons is the photon, which carries the electromagnetic force. It is massless and couples to all charged particles. The weak force is mediated by massive weak gauge bosons W^\pm and Z^0 and is smaller in strength by four orders of magnitude compared to electromagnetism. It has very short range, a consequence of the large boson masses, and governs e.g. the nuclear β decay. Eight massless gluons are held responsible for the strong interaction between quarks.

Symmetries are most valuable assets in physics theories. In classical mechanics, invariance with respect to operations regarding space and time yield the all important laws of energy, momentum and angular momentum conservation. Similarly, the unification of electromagnetic and weak interaction by Glashow, Weinberg and Salam in the 1970’s is based on a symmetry, the gauge group $SU(2)_L \times U(1)$. In order for the W and Z boson to acquire masses of 80.4 and 91.2 GeV, respectively, and the photon to remain massless at the same time, this symmetry must be broken. As a consequence, the theory postulates the existence of yet another particle: the “*Higgs boson*”. It remains the only undetected elementary particle in the Standard Model to date, and its discovery is therefore much anticipated by the high energy physics community. Major experimental efforts are underway to trace it, led by the Large Hadron Collider (LHC) experiments at CERN (Switzerland), which are expected to join the hunt from 2007 on. Feasibility studies based on simulated data reveal that the potential of any search depends largely on the mass of the Higgs boson, which is unknown. Improvements to the precision of the top quark mass - the aim of the work presented in this thesis - will help to narrow the window for the most likely value of the Higgs mass and optimize analysis strategies. The connection between the top quark and Higgs boson masses through loop corrections is discussed in Section 2.2.4.

The success of the Standard Model is perhaps best appreciated by noting its outstanding

¹The graviton is postulated to carry spin 2 and is not a gauge boson.

agreement with nearly all experimental results published in *The Review of Particle Physics* [10], a phone-book-sized compendium which maintains almost the entire scientific output of the field during the last half century. Nonetheless, there are reasons to believe that the Standard Model is incomplete, a low energy effective theory to a more fundamental theory at higher energies. The top quark, standing out among all other quarks with its intriguingly high mass, is suspect to play a key role in the quest to reveal this underlying theory.

2.2 The Top Quark

The top quark was predicted since the discovery of the b quark in 1977 as its electroweak isospin partner. It was discovered in 1995 at the Tevatron, the world's only top factory to date. It has the largest mass of all known elementary particles, approximately the mass of a gold atom. In particular, its mass exceeds the mass of the next heaviest quark, the b quark, by almost a factor of 20. Neither the Standard Model nor any other fundamental theory can explain this remarkable asymmetry. The large mass of the top quark comes with an extremely short lifetime, which does not allow the top quark to form hadronic bound states: its production properties are preserved and can be accessed via the decay products. In particular, the top quark mass is accessible directly by the experiment.

The following sections are concerned with the production and decay of the top quark at the Tevatron, as well as its link to the Higgs boson.

2.2.1 Particle Production in $p\bar{p}$ Collisions

Quantum Field Theory prescribes the calculation of interactions between fundamental particles, such as quarks. The Tevatron, however, collides protons and anti-protons, which consist of three fundamental quarks, a sea of virtual quarks and antiquarks that surround them, and gluons which bind them together. Since the proton cannot be treated perturbatively, only the hard scattering process between partons is considered. The remaining partons are treated as spectators.

Figure 2.1 illustrates this parton model of the hard scattering process: Two partons, one of each colliding (anti-)proton, take part in the interaction, carrying longitudinal momentum fractions x_1, x_2 of the incoming hadrons. These fractions are unknown on an event-by-event basis. The probability density $f_i(x_i, Q^2)$ for a parton with flavor i to participate in the hard scattering interaction with longitudinal momentum fraction x_i and factorization scale Q^2 is referred to as the parton distribution function (PDF). Its derivation from first principles or perturbative calculations has yet to be achieved. Instead, the shapes are extracted from global QCD fits at next-to-leading order from data [11]. Given the PDFs, the total cross section of a process $p_A, p_B \rightarrow p_1, p_2$ can be approximated by summing over all possible parton interactions and weighting each by its probability:

$$\sigma = \sum_{A,B} \int dx_A dx_B f_p(x_A, Q^2) f_{\bar{p}}(x_B, Q^2) \sigma(p_A, p_B \rightarrow p_1, p_2) \quad (2.1)$$

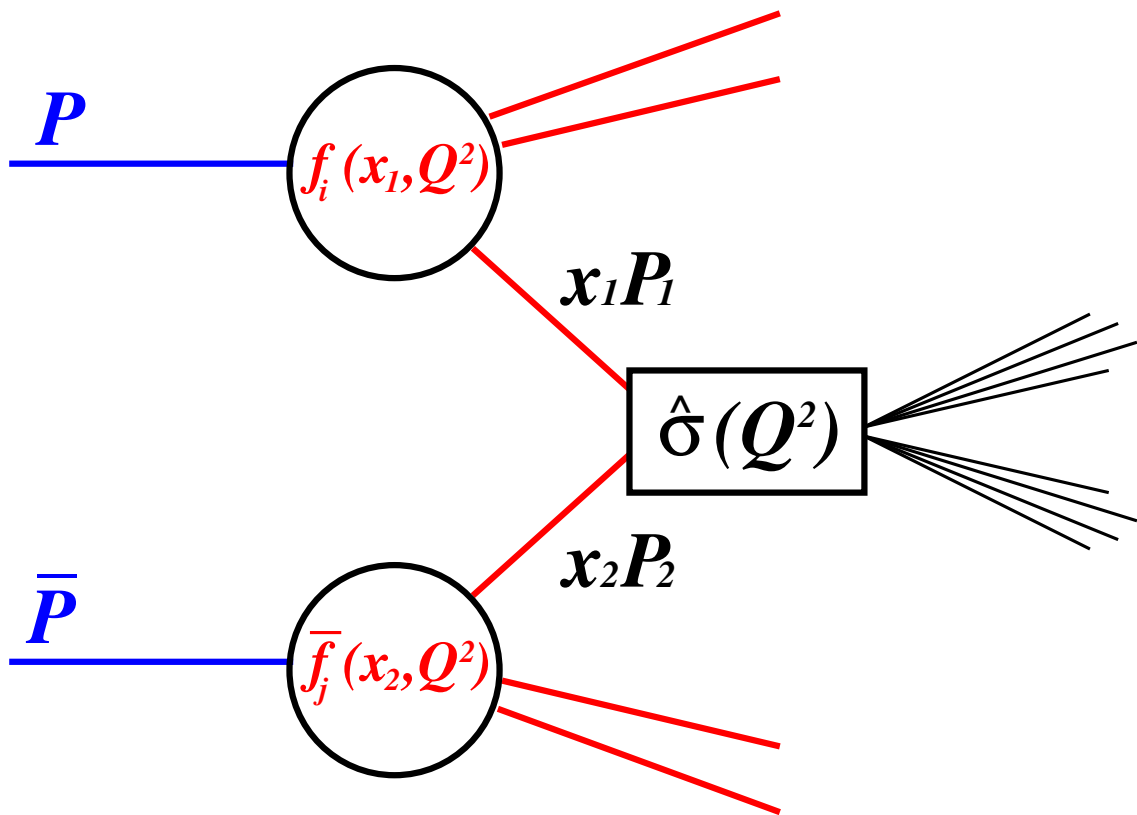


Figure 2.1: Parton model description of a hard scattering process.

2.2.2 Top Quark Production

Top quarks are produced in $p\bar{p}$ collisions both singly and in pairs. The leading order Feynman diagrams for all production processes are shown in Figure 2.2. Single top production via the electroweak interaction suffers from lower cross section and larger experimental background. Hence, only $t\bar{t}$ pair production via the strong interaction is considered for the mass measurement. At the energies of the Tevatron in Run II, top-antitop pairs are primarily produced via quark annihilation, while gluon fusion contributes approximately 15%.

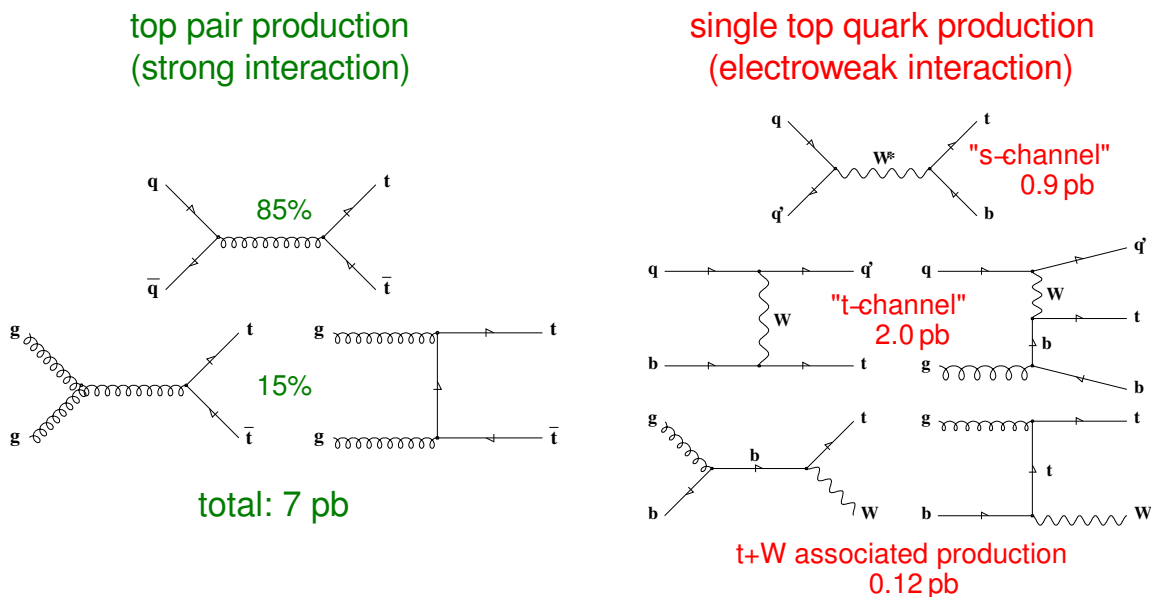


Figure 2.2: Leading order Feynman diagrams, illustrating top quark production mechanisms. The mass analysis considers pair production via the strong interaction only, which is dominated by quark annihilation. The cross sections are rough estimates for the Tevatron Run II center-of-mass energy of 1.96 TeV.

The pair production cross section was recently measured in Run II by the $D\bar{O}$ [12] and CDF [13] collaborations to be:

$$\sigma_{t\bar{t}} = 6.7_{-1.7}^{+2.2} \text{ pb} \quad (D\bar{O}) \quad (2.2)$$

$$\sigma_{t\bar{t}} = 6.6_{-1.9}^{+1.9} \text{ pb} \quad (CDF) \quad (2.3)$$

The measurements are based on 230 pb^{-1} and 194 pb^{-1} respectively and in good agreement with theoretical calculations [14, 15] which predict

$$\sigma_{t\bar{t}} = 6.77 \pm 0.42 \text{ pb}, \quad (2.4)$$

assuming a top quark mass of 175 GeV.

2.2.3 Top Quark Decay

The Standard Model predicts the top quark to almost exclusively decay to a b quark and an on-shell W boson via weak interaction ($BR(t \rightarrow Wb) > 0.998$). Assuming the b quark to be

massless and neglecting higher order terms, the total decay width Γ_t of the top quark can be approximated as

$$\Gamma_{top} = \frac{G_F m_{top}^3}{8\pi\sqrt{2}} \left(1 - \frac{m_W^2}{m_{top}^2}\right) \left(1 + 2\frac{m_W^2}{m_{top}^2}\right) \left[1 - \frac{2\alpha_s}{3\pi} \left(\frac{2\pi^2}{3} - \frac{5}{2}\right)\right], \quad (2.5)$$

where G_F is the Fermi coupling constant. For $m_{top} = 178$ GeV, Equation (2.5) yields $\Gamma_{top} \approx 1.5$ GeV, corresponding to the top quark's lifetime of about 5×10^{-25} s.

Different experimental signatures of the $t\bar{t}$ decay are classified by the patterns of decay of the two W bosons:

- **Dilepton events**, where both W bosons decay into an $e\nu$ or $\mu\nu$ final state, are characterized by two energetic, isolated leptons, two energetic b jets, and two uncaptured neutrinos which appear as missing transverse energy. This analysis channel provides the cleanest signature but suffers from low statistics at current luminosities as the branching ratio is only about 5%.
- For **hadronic events**, where both W bosons decay hadronically, the signature is six jets, two of which are b jets, and no significant missing transverse energy. Though this analysis channel enjoys almost 50% of the decay rate and allows for the full reconstruction of the event kinematics, it is difficult to extract from the overwhelming multijet background.
- **Lepton+Jets events**, where one W boson decays hadronically and the other into an $e\nu$ or $\mu\nu$ final state, are characterized by an energetic, isolated lepton, four energetic jets, and missing transverse energy from the undetected neutrino. This analysis channel accounts for almost 30% of the decay rate while providing a distinct experimental signature through the isolated lepton in a $p\bar{p}$ collision. Depending on the kinematic selection criteria, a $S/(S+B)$ ratio of roughly 1/3 is expected, with W + jets production as the main source of background.
- **τ events**, where at least one W boson decays into a $\tau\nu$ final state, account for about 21% of the decay rate. Depending on its decay, the τ lepton can be identified as a narrow jet, an isolated track, or an electron or muon. Two energetic b jets, missing transverse energy, and the decay products from the second W boson complete the topology. Explicit identification of τ leptons is a major challenge at hadron colliders. However, events in which a τ decays into an electron or muon will appear in the electron/muon+jets signal samples.

Figure 2.3 illustrates all $t\bar{t}$ decay modes and their branching ratios.

2.2.4 The Top Quark and the Higgs Boson

In the Standard Model, the W boson mass is calculated at tree-level as

$$M_W^2 = \frac{1}{2}M_Z^2 \left(1 + \sqrt{1 - \frac{4\pi\alpha}{\sqrt{2}G_F M_Z^2}}\right) = \frac{\pi\alpha}{\sqrt{2}G_F \sin^2 \theta_W}, \quad (2.6)$$

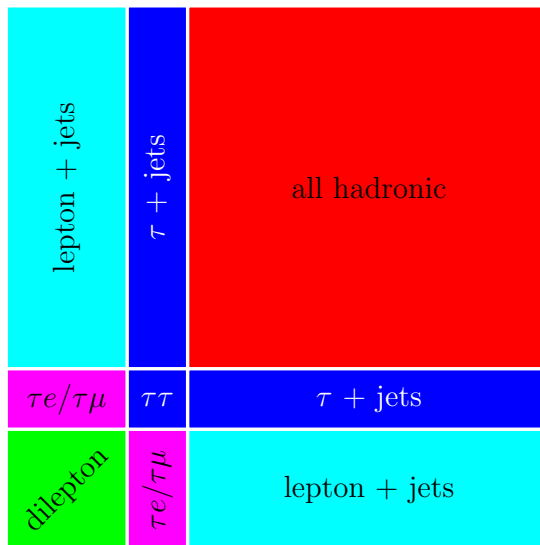


Figure 2.3: $t\bar{t}$ decay modes. The areas are proportional to the branching ratios.

where α is the fine-structure constant, G_F is the Fermi coupling constant, M_Z is the mass of the Z boson, and the Weinberg angle θ_W is defined such that

$$\sin^2 \theta_W \equiv 1 - \frac{M_W^2}{M_Z^2} . \quad (2.7)$$

Additional higher order loop diagrams contribute to the W and Z masses, which contain virtual top quarks and virtual Higgs bosons. The loop diagrams at next-to-leading order are shown in Figures 2.4 and 2.5. If these corrections are considered, the expression in 2.6 transforms to

$$M_W^2 = \frac{\frac{\pi\alpha}{\sqrt{2}G_F}}{\sin^2 \theta_W (1 - \Delta r)} . \quad (2.8)$$

The contribution from virtual top quark loops is given by

$$(\Delta r)_{top} \approx -\frac{3G_F}{8\sqrt{2}\pi^2 \tan^2 \theta_W} \cdot m_{top}^2 , \quad (2.9)$$

whereas the virtual Higgs boson loops account for

$$(\Delta r)_{Higgs} \approx -\frac{11G_F m_Z^2 \cos^2 \theta_W}{24\sqrt{2}\pi^2} \cdot \ln \frac{m_H^2}{m_Z^2} . \quad (2.10)$$

Hence, Equation (2.8) constrains both the mass of the top quark and the mass of the Higgs boson. The dependence on the Higgs mass however is much weaker, since m_{top} enters quadratically, while m_H enters only logarithmically. The result of the electroweak fit [16] of the Higgs boson mass is shown in Figure 2.6. It yields $m_H = 114_{-45}^{+69}$ GeV. Both the W boson and top quark mass enter the fit according to the best measurements [16, 17] of these parameters and the respective uncertainties:

$$m_W = 80.412 \pm 0.042 \text{ GeV} \quad (2.11)$$

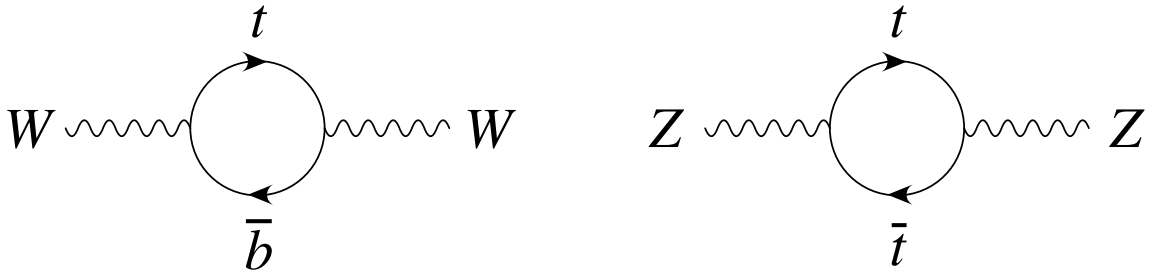


Figure 2.4: Virtual top quark loops which contribute to the W and Z boson masses.

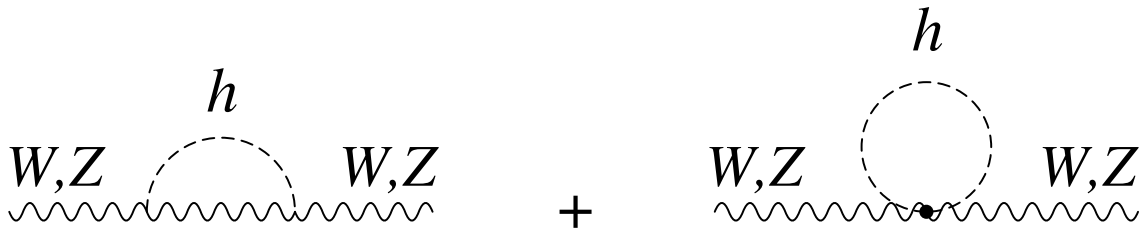


Figure 2.5: Virtual Higgs boson loops which contribute to the W and Z boson masses.

$$m_{\text{top}} = 178.0 \pm 4.3 \text{ GeV} . \quad (2.12)$$

Improvements on the precision of either direct mass measurement translate into better indirect limits on the Higgs boson mass. Narrowing the window on m_H by increasing the precision on m_{top} in direct measurements at the Tevatron is therefore a good service to the LHC experiments: analysis techniques aiming to discover this yet elusive piece of the Standard Model puzzle are optimized for the most likely mass values, as different Higgs boson masses imply different analysis channels and strategies.

Until direct observation of the top quark at the Tevatron in 1995 [1, 2], fits to electroweak data were the only accessible information on the top quark mass. The most recent indirect measurement of m_{top} combining Z -pole data and direct measurements of the W boson mass and total width yield [16]

$$m_{\text{top}} = 179_{-9}^{+12} \text{ GeV} , \quad (2.13)$$

in good agreement with the direct measurements (Equation (2.12)). Figure 2.7 illustrates the rapid evolution of our knowledge of the top quark mass from indirect and direct measurements over the last decades.

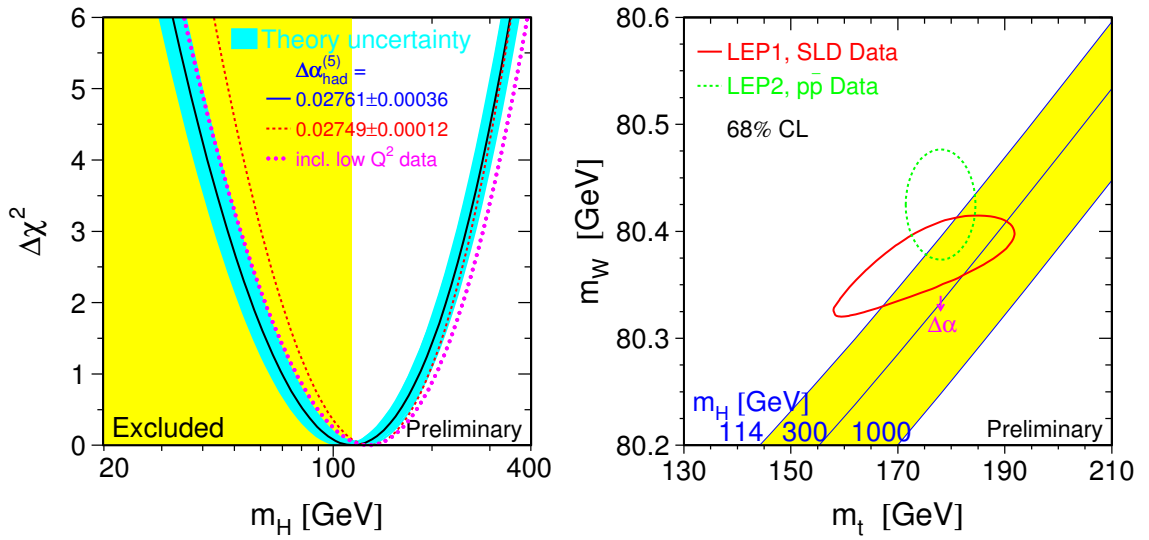


Figure 2.6: Left: “Blueband plot”: indirect measurement of the SM Higgs boson mass via fit to all electroweak data. The highlighted area represents the 95 % confidence exclusion below 114.4 GeV from direct searches [16]. Right: 68 % confidence level contours in the (m_{top}, m_W) -plane, for the indirect (LEP1, SLD data) determination in a global fit to electroweak precision data and direct (LEP2, $p\bar{p}$ data) measurements [16]. The correlation between m_{top} and m_W as expected in the Standard Model for various Higgs boson masses is also shown.

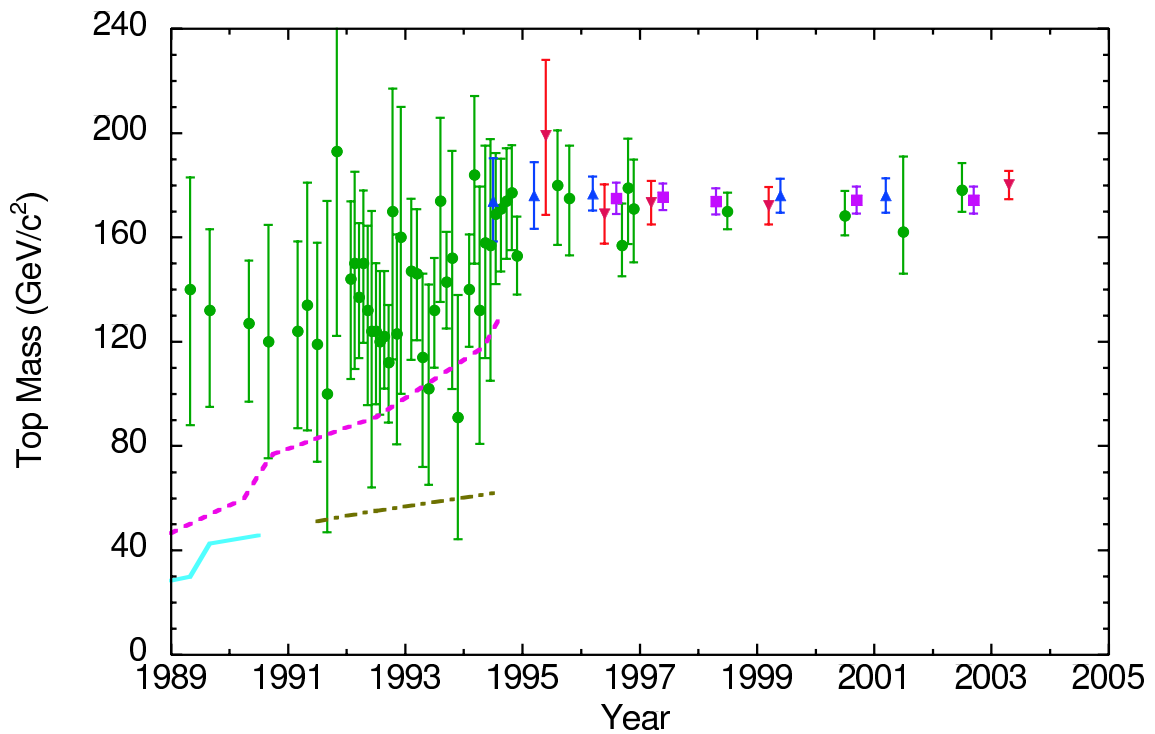


Figure 2.7: Evolution of the indirect prediction and direct measurement of the top quark mass with time [18]. Only indirect measurements (\bullet) from electroweak fits were feasible until the discovery of the top quark in 1995. The latest such results are consistent with direct measurements in $p\bar{p}$ data by DØ (\blacktriangledown) and CDF (\blacktriangle). The world average from both Tevatron experiments is also shown (\blacksquare) as well as the lower bounds from hadron colliders (dashed lines) and e^+e^- colliders (solid line).

Chapter 3

The Tevatron and the DØ Detector

Fermilab's Tevatron currently produces proton-antiproton ($p\bar{p}$) collisions at higher energies than any other experimental facility. It is the world's only top quark factory and will remain on the energy frontier until experiments at the Large Hadron Collider (LHC) begin taking data in about 2007. The Tevatron accelerator hosts two collider experiments: the Collider Detector at Fermilab (CDF) and DØ. This analysis uses data collected by the DØ detector between 2002 and 2004.

During the first data-taking period (Run I) between 1991 and 1995, each experiment collected about 125 pb^{-1} collision data at a center-of-mass energy of 1.8 TeV. The discovery of the top quark and the first measurement of its mass are among the key accomplishments of that era. Between 1997 and 2001, the accelerator complex underwent major upgrades aimed at increasing the luminosity of the accelerator. The center-of-mass energy is raised to $\sqrt{s} = 1.96 \text{ TeV}$. The new period of data-taking (Run II), which began in 2001 and will last until 2009, is planned to accumulate $4 - 8 \text{ fb}^{-1}$ of integrated luminosity, depending on the performance of the accelerator. The upgraded machine accelerates 36 bunches of protons and anti-protons, compared to originally 6 bunches. Consequently, the time between bunch crossings has been decreased from $3.5 \mu\text{s}$ to 396 ns , and the higher rate operation required major detector upgrades to ensure fast enough response time.

3.1 The Fermilab Accelerator Chain

Fermilab uses a series of accelerators to produce the high energy $p\bar{p}$ collisions studied at DØ and CDF [6]. The paths taken by protons and anti-protons from initial acceleration to collision in the Tevatron are shown in Figure 3.1.

The Cockcroft-Walton pre-accelerator provides the first stage of acceleration. Inside this device, hydrogen gas is ionized to create H^- ions which are accelerated to 750 keV of kinetic energy. Next, the H^- ions enter a linear accelerator (Linac), approximately 150 m long, where they are accelerated to 400 MeV [7]. An oscillating electric field in the Linac's RF cavities accelerates the ions and groups them into bunches: the ions moving too fast reach the cavity while the electric field is weak, whereas the ions moving too slow reach the cavity while the electric field is strong.

The 400 MeV H^- ions are then injected into the Booster, a circular synchrotron 74.5 m

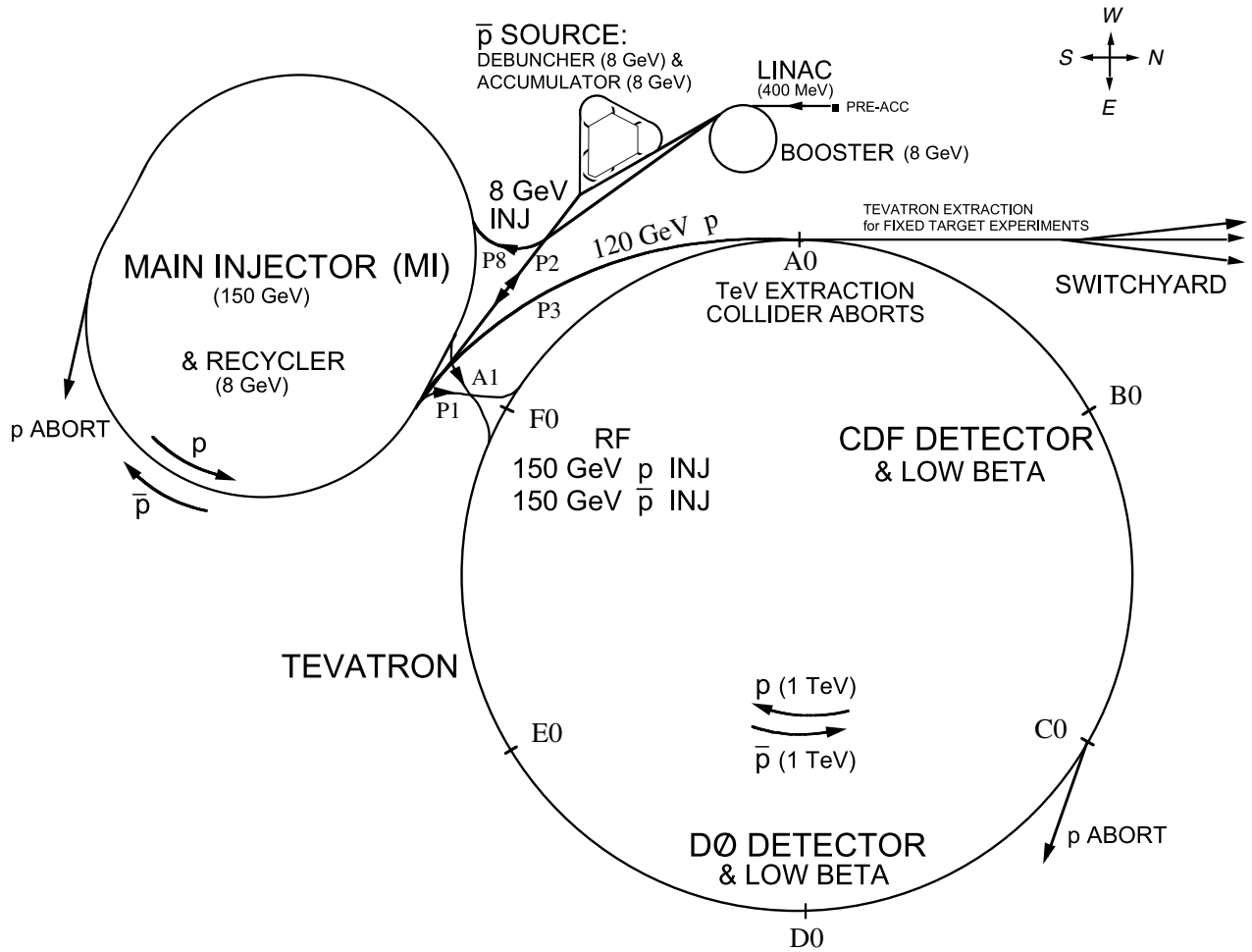


Figure 3.1: The Fermilab accelerator complex.

in diameter [7]. A carbon foil strips the electrons from the H^- ions at injection, leaving bare protons. The intensity of the proton beam is then increased by injecting new protons into the same orbit as the circulating ones. The protons are accelerated from 400 MeV to 8 GeV by another series of RF cavities. Each turn around the Booster, the protons gain 500 keV of kinetic energy, but in the steady state, they lose exactly this much energy through radiation.

To produce anti-protons, protons from the Booster are accelerated to 120 GeV by the Main Injector and directed at a nickel target [6]. It takes 50000 protons on average to produce one anti-proton with a mean energy of 8 GeV in this collision. The anti-protons are focused by a lithium lens and a pulsed magnet separates them from other particle species. The Main Injector replaced the Main Ring accelerator which was situated in the Tevatron tunnel. The injector can carry larger proton currents than its predecessor, which results in a higher rate of anti-proton production.

The RF cavities cannot constrain the anti-protons in the plane transverse to the beam direction. Since the collider requires narrow beams, the transverse excursions of the anti-protons must be kept at a minimum. This process is referred to as “cooling” the beam, as it

reduces the kinetic energy spread of the anti-protons. New batches of anti-protons are initially cooled in the Debuncher synchrotron, collected and further cooled using stochastic cooling [8] in the 8 GeV Accumulator synchrotron. First, pickup sensors sample the average transverse excursions for portions of each bunch. Later, kicker magnets apply correction forces. This has the effect of damping the anti-protons on average, producing a cool narrow beam. Anti-proton availability is most often the limiting factor for attaining high luminosities, as it takes 10-20 hours to build up a “stack” of anti-protons for injection into the Tevatron.

The stochastic cooling is done by the anti-proton Recycler [6], which is also intended to recycle anti-protons when the beam quality has become poor after many collisions. The Recycler cools the anti-protons and integrates them with a new stack.

Once enough particles have been accumulated, stacks of protons and anti-protons are transferred to the Main Injector for acceleration to 150 GeV and injection into the Tevatron. The stacks contain 36 bunches, with a proton bunch containing around 3×10^{11} protons and an anti-proton bunch containing around 3×10^{10} anti-protons.

The Tevatron is the last stage of Fermilab’s accelerator chain [6]. It receives 150 GeV protons and anti-protons from the Main Injector and accelerates them to 980 GeV. The protons and anti-protons circle the Tevatron in opposite directions and collide at the two “collision points”, where the DØ and CDF detectors are located.

The luminosity of collisions is given by:

$$\mathcal{L} = \frac{f N_B N_p N_{\bar{p}}}{2\pi(\sigma_p^2 + \sigma_{\bar{p}}^2)} F \left(\frac{\sigma_l}{\beta^*} \right) \quad (3.1)$$

where f is the revolution frequency, N_B is the number of bunches, $N_{p/\bar{p}}$ are the number of protons/anti-protons per bunch, and $\sigma_{p/\bar{p}}$ are the root mean square (RMS) transverse beam sizes at the interaction point. F is a form factor which corrects for the bunch shape and depends on the ratio of σ_l , the bunch length, to β^* , the beta function, at the interaction point. The beta function is a measure of the beam width.

Figure 3.2 shows the integrated luminosity delivered to and recorded with the DØ detector in Run II until July 2005.

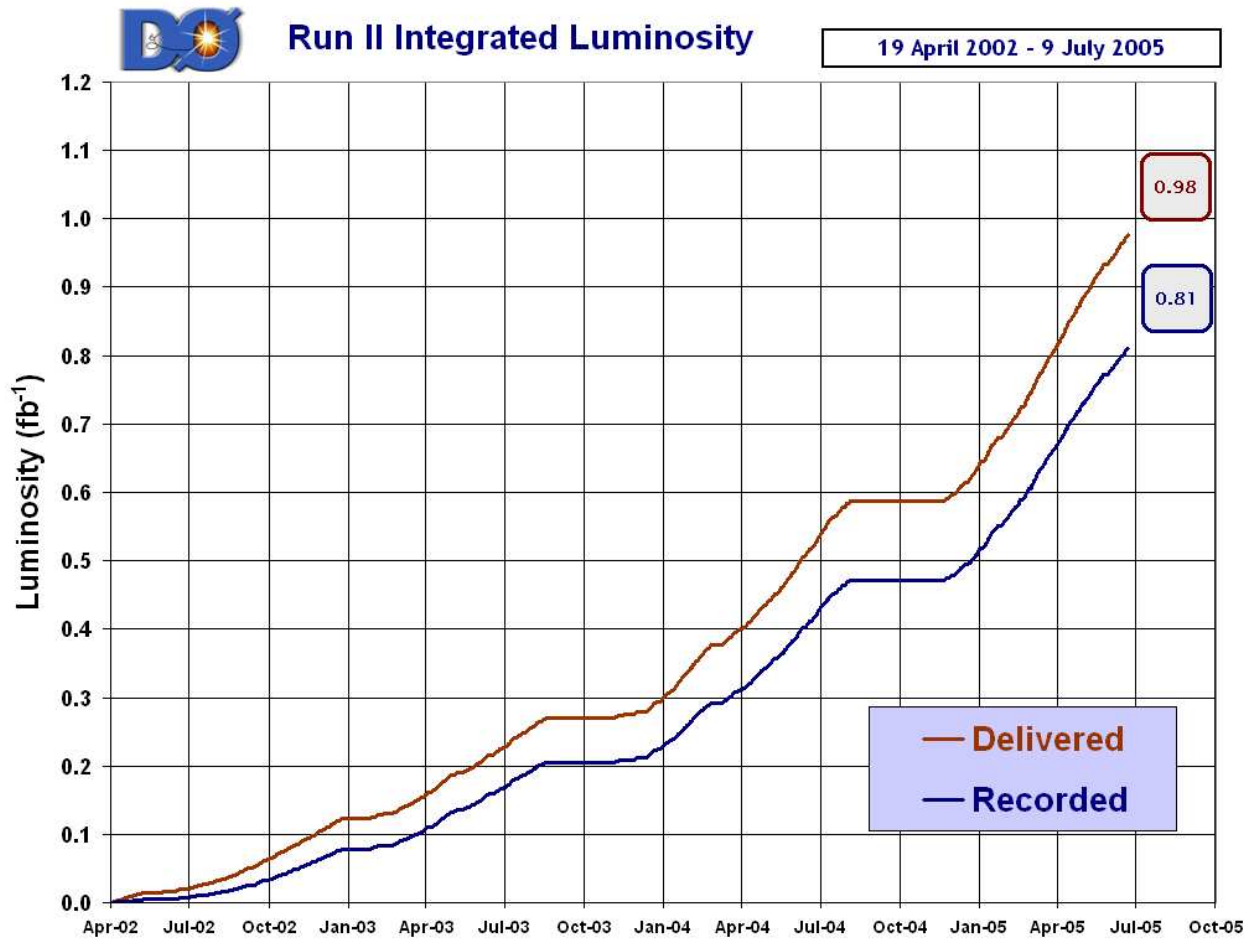


Figure 3.2: Integrated luminosity of $p\bar{p}$ collisions delivered to and recorded with the DØ detector in Run II until July 2005.

3.2 The DØ Detector

The DØ detector is designed to detect particles created in $p\bar{p}$ collisions at the Tevatron and to measure their properties. It is a multipurpose detector, meaning the design is not aimed at one particular physics measurement, but rather at extracting information about the created particles suitable to illuminate a broad spectrum of physics processes.

The outline of the DØ detector [9] is shown in Figure 3.3. The sub-detector systems are arranged around the beam-pipe, where the $p\bar{p}$ collisions occur. The beam-pipe is made of beryllium because this metal combines good mechanical qualities with a low nuclear-interaction cross-section. The detector can be categorized into three layers: high resolution tracking on the inside, electromagnetic and hadronic calorimetry in the middle, and muon identification on the outside.

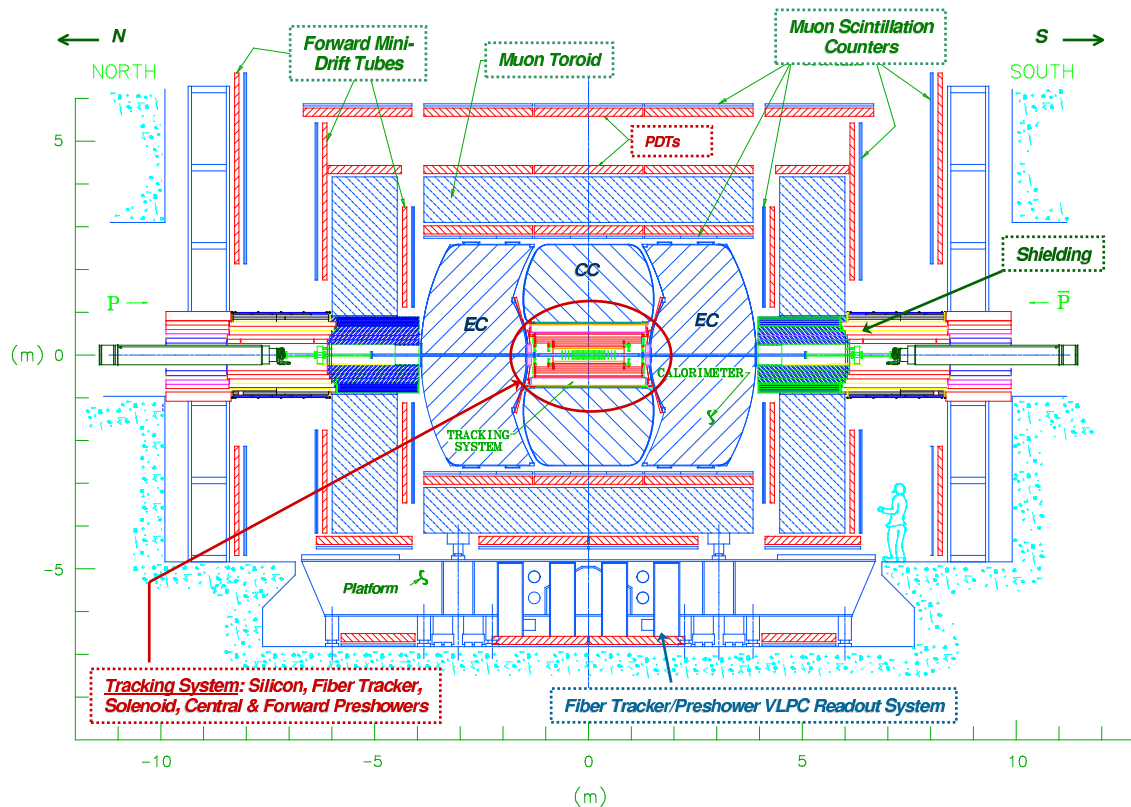


Figure 3.3: Outline of the DØ detector.

3.2.1 DØ Coordinate System

The DØ coordinate system is right-handed with the origin at the center of the detector and the z axis along the nominal direction of the proton beam. The y axis points upwards and the x axis points towards the center of the Tevatron ring. The plane perpendicular to the beam is referred to as the “transverse plane”. As opposed to e^+e^- collisions, in $p\bar{p}$ collisions, not all of the center of mass energy of the $p\bar{p}$ system is absorbed in the collision. The colliding partons

inside the (anti-)proton carry only a fraction of the kinetic energy of the (anti-)proton. As a result, the center of mass system of the parton collisions is boosted along the beam direction (the “longitudinal direction”) by an unknown amount. Quantities defined in the transverse plane are conserved in the collisions. For instance, the sum of all transverse momenta of particles in the collisions is zero: $\sum \vec{p}_T = 0$.

Because of the barrel-like structure of the detector, cylindrical coordinates (r, ϕ) are often used in the transverse plane. An alternate variable to the polar angle θ to describe the angle between the z axis and the momentum of the particle is pseudo-rapidity (η) which is defined as:

$$\eta \equiv -\ln \tan(\theta/2) . \quad (3.2)$$

Consequently, spatial separation between any two physics objects is quantified in terms of

$$\Delta R \equiv \sqrt{\Delta\phi^2 + \Delta\eta^2} , \quad (3.3)$$

which is invariant under Lorentz transformations.

3.2.2 The Tracking System

The first system encountered by a typical particle traversing the DØ detector is the integrated tracking system. The tracking system is barrel-shaped and consists of cylindrical subsystems which are concentric with the beam. It is designed to detect charged particles and measure their momenta and displacements from the point of collision, the primary interaction vertex. The tracking system is encased in a solenoid which provides a nearly uniform 2 T magnetic field parallel to the beam axis. Charged particles penetrating the magnetic field are bent around the field lines, and the curvature allows for a measurement of the transverse momentum. A diagram of the DØ tracking system and its individual components is shown in Figure 3.4.

Silicon Microstrip Tracker (SMT)

The innermost tracking devices are silicon tracking detectors, which make precise position measurements of the path of a charged particle. A silicon tracking detector is a reverse biased p-n junction. When a charged particle passes through the detector material, it causes ionization. In the semiconductor material, electron-hole pairs are produced. Electrons drift towards the anode, and holes drift towards the cathode, where the charge is collected. By segmenting the p or n side of the junction into “strips” and reading out the charge deposition separately on every strip, the position of the charged particle is measured with excellent resolution in one dimension. The SMT is comprised by 300 μm wafers of n-type silicon, which have p-type strips parallel to the beam-axis. Many wafers have n-type strips on the reverse side, placed at 2° or 90° for measurement in two dimensions. The wafers are arranged in six barrels of four hermetic layers, where each layer has two staggered and overlapping sub-layers. These barrel detectors measure primarily the $r - \phi$ coordinate and are supported by disks (“F-disks”) of wafers mounted perpendicular to the beam to measure $r - z$ as well as $r - \phi$. In the far forward and backward regions, units of three F-disks as well as two large-diameter “H-disks” extend the high-precision tracking capabilities up to $|\eta| < 3$. The outline of the silicon tracking system is shown in Figure 3.5.

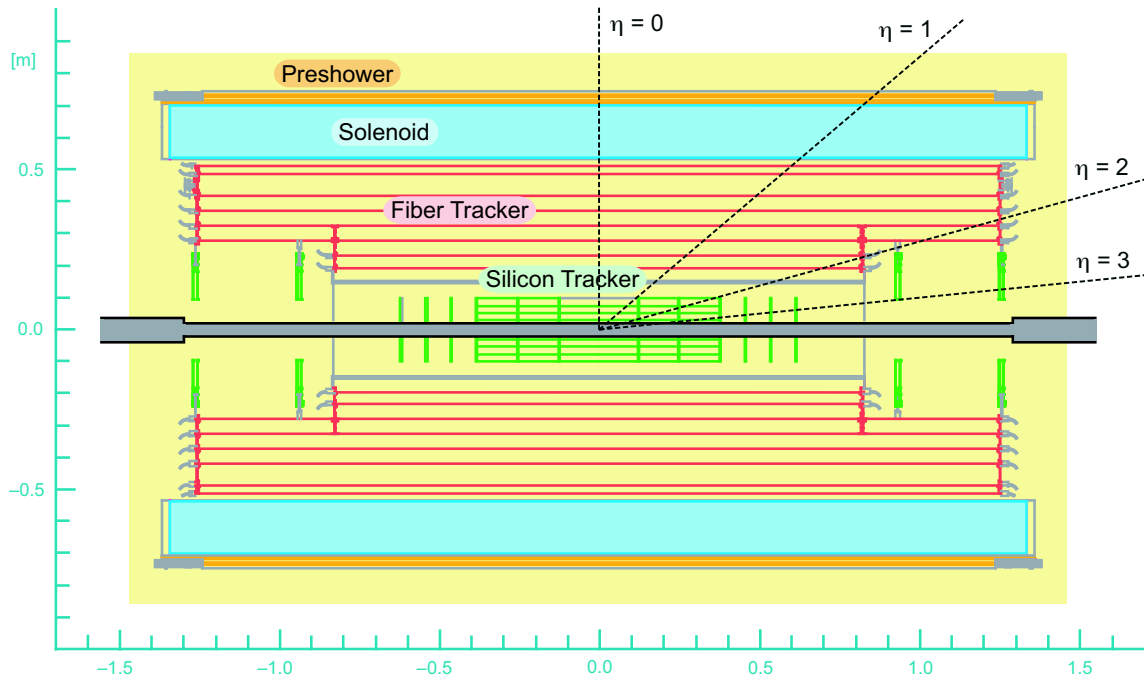


Figure 3.4: The DØ tracking system.

The SMT has about 800000 readout channels and the microstrip detectors provide a hit resolution of approximately $10 \mu\text{m}$. The system is designed to resist a radiation dose of about 1 Mrad, which corresponds to an integrated luminosity of roughly 2 fb^{-1} .

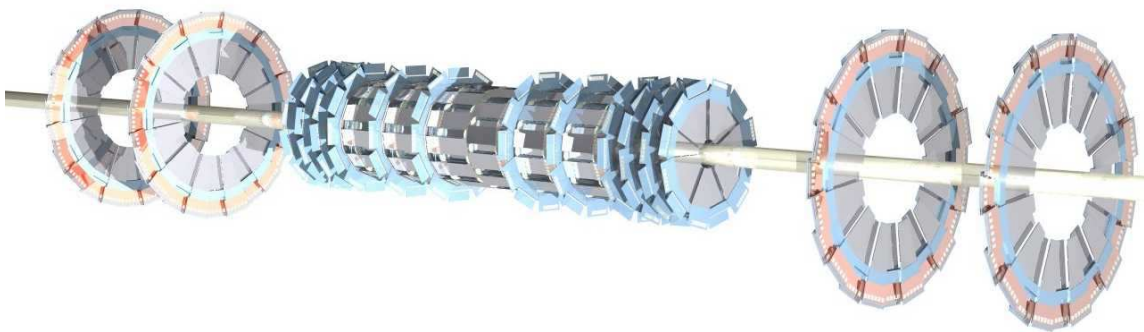


Figure 3.5: The DØ Silicon Microstrip Tracker (SMT).

Central Fiber Tracker (CFT)

The scintillating fiber tracker surrounds the silicon detector with sixteen cylindrical $835 \mu\text{m}$ layers of fibers and occupies the radial space from 20 to 52 cm. The innermost two layers extend 166 cm, the six outer layers 252 cm along the beam axis, providing coverage up to $|\eta| < 1.7$.

The outer layer of each fiber doublet is offset by a half a fiber width for improved resolution in ϕ . Eight of the sixteen layers are parallel to the beam, providing excellent resolution in ϕ . The eight other layers are placed at alternating angles of approximately $\pm 3^\circ$ relative to the beam axis, providing a measurement of the z position with less precision together with the parallel layers.

When a charged particle penetrates one of the fibers, the scintillator emits light at $\lambda \approx 340$ nm through a rapid fluorescence decay. In order to increase the mean free path length of the light in the fiber, a wavelength-shifting dye is used. It absorbs well at $\lambda \approx 340$ nm and emits at $\lambda \approx 530$ nm. At this wavelength, the light can successfully be propagated over 4 m in the scintillator. On one side of each fiber, the light is collected by a wave guide. The fibers are coated on the other side with aluminum to reflect the produced light to the collection end. The wave guides, 7 – 11 m in length, send the light to the extremely sensitive Visible Light Photon Counters (VLPC), which convert it into an electronic pulse. The VLPCs are located below the DØ detector in a liquid Helium cryostat and operate at a temperature of ≈ 9 K.

The CFT detector has about 77000 readout channels and provides a hit resolution of roughly $100 \mu\text{m}$.

Preshower detectors (CPS and FPS)

Two additional tracking detectors are located outside the solenoid magnet: the central and forward preshower detectors (CPS and FPS). The CPS is mounted on the solenoid and covers the range $|\eta| < 1.2$. The FPS sits on the inner surface of the end calorimeter cryostat, covering the range $1.4 < |\eta| < 2.5$. The detectors consist of lead absorbers, followed by several layers of triangular shaped axial and stereo scintillator strips. The absorber converts electromagnetic particles (electrons and photons) into showers, providing discrimination from minimal ionizing particles (MIP) like energetic charged pions. CPS and FPS are tracking detectors which provide a precise position measurement in addition to the central tracking system. They are however used for calorimetry as well and help restore the electromagnetic energy resolution otherwise degraded by the presence of the massive solenoid magnet.

3.2.3 The Calorimeter

The purpose of the calorimeter system is to measure the energy of particles by inducing them to produce electromagnetic and hadronic showers. Inert passive layers of dense material in which the shower begins alternate with active layers, where the surviving fraction of the shower energy is sampled through ionization. The DØ calorimeter itself remains unchanged from Run I, but the readout electronics underwent major redesign to cope with the higher rates and shorter bunch crossing intervals.

The hermetic liquid argon sampling calorimeter is one of the strongest components of the DØ detector, featuring fine granularity and excellent coverage and uniformity. It consists of an electromagnetic and a hadronic section, with several layers of passive and active material each. The active material is liquid argon, and the absorber material is uranium in the electromagnetic and inner hadronic calorimeter, and copper and stainless steel in the outer layers. Figure 3.6 shows the central and the two end-cap calorimeters, each placed in a separate cryostat to keep the Argon in its liquid phase at a temperature of 80 K. The

calorimeter is found to be nearly “compensating”: test beam data with charged pions yield that the energy response for electromagnetic and hadronic particles are roughly the same. The electromagnetic section contains a combined 65.6 mm of uranium, which represents 20 radiation lengths ($X_0^{Ur} \approx 3.2$ mm) to capture the overwhelming fraction of the electromagnetic energy. Because the nuclear interaction length λ_I is much larger than the radiation length X_0 ($\lambda_I^{Ur} \approx 10.5$ cm $\approx 30X_0$), hadrons typically deposit most of their energy in the hadronic section, which contains $\approx 6.4\lambda_I$ of uranium and copper.

The calorimeter is segmented in “cells”, which are arranged such that each covers roughly an area of $\eta \times \phi = 0.1 \times 0.1$. In the far forward region ($|\eta| > 3.2$), the cell size is 0.2×0.2 . In the third layer of the electromagnetic section, where the shower is expected to reach its maximum, the cell size is 0.05×0.05 to provide improved spatial resolution.

The inter-cryostat detector (ICD) covers the pseudo-rapidity range $0.8 < |\eta| < 1.4$, the overlap between the central and end-cap calorimeters. It consists of one layer of 384 scintillating tiles each mounted on both cryostats, and is read out by photo-tubes which are connected with wavelength-shifting fibers.

Due to the addition of the tracking system and the solenoid magnet, particles traverse significantly more material before reaching the calorimeter in Run II than in Run I. In addition, only 70 % of the signal charge can be integrated by the electronics in the narrow time window between bunch crossings (396 ns), leading to larger sensitivity to fluctuations. The Run II electronics are found to show worse noise performance as well. Consequently, the jet energy resolution is slightly degraded with respect to Run I.

3.2.4 Muon Spectrometer

Muons are precious goods in a hadron collider environment. While the majority of proton anti-proton encounters result in collisions of little interest, the presence of a lepton indicates that an event might contain exciting physics. When interacting with matter, muons act as minimally ionizing particles; they only deposit small amounts of ionization energy in the material. They are the only charged particles likely to penetrate both the tracking and calorimeter systems, and produce hits in the muon detection system.

The outline of the DØ muon spectrometer is shown in Figure 3.7. It is divided into the central system covering $|\eta| < 1.0$ and the forward system covering $1.0 < |\eta| < 2.0$. The system consists of proportional drift tubes (PDTs) and scintillating pixels, arranged around a 1973 ton toroidal magnet, which generates a 1.9 T magnetic field perpendicular to the beam axis. The muon system has three layers of drift tubes. The innermost A layer is located between the beam and the magnet, while the B and C layers encase the magnet. Additional special shielding further decreases the likelihood of particles other than muons to reach the outer layers. This setup allows a standalone measurement of the muon momentum with the muon spectrometer. In this analysis however, only those muons are considered which have a signal in the muon system associated with an isolated track in the central tracking system, and the momentum of the track is used.

Drift tubes are rectangular gas filled volumes; the ionization created by a passing charged particle is collected and amplified by a sense wire which runs through the center of the chamber. The drift tubes in the central region are constructed of extruded aluminum coated with steel foil and a gold-plated tungsten sense wire. They are 5.5×10.0 cm in cross section, 240 cm long

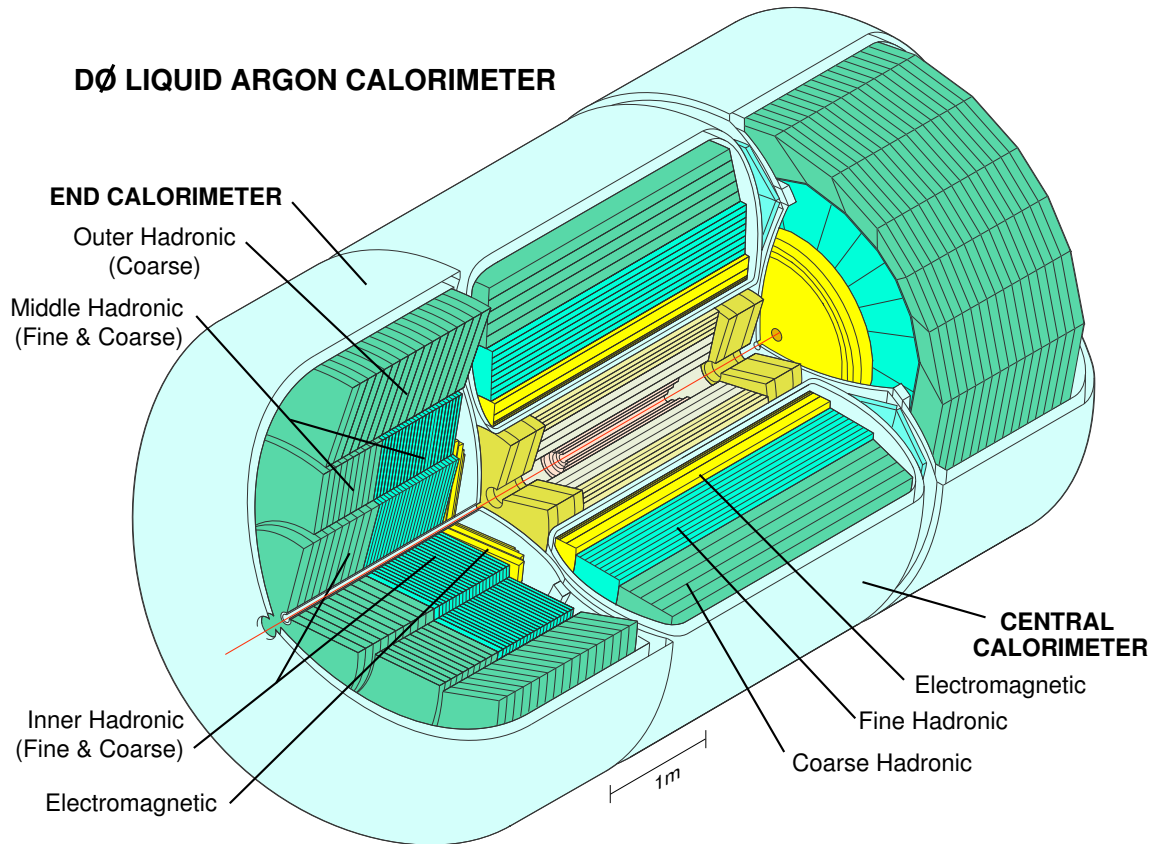


Figure 3.6: The liquid-argon calorimeter of the $D\bar{O}$ detector.

and filled with a gas mixture of 80% argon, 10% CH_4 and 10% CF_4 . The drift tubes in the forward region are significantly narrower at a 1.0×1.0 cm cross-section and varying lengths. A calibration of the drift time of the gas is applied to the measurement of the arrival time of the pulse from the sense wire to calculate the radial distance of the hit from the sense wire. To determine the position of the ionization along the wire in the central region, sense wires for the tubes have been joined at one end. A comparison of arrival times from adjacent wires provides a rough measurement in this dimension.

Sheets of scintillating pixels accompany each layer of drift tubes, with the exception of the B layer. Each pixel covers roughly 4.5° in ϕ and provide an additional position measurement along the direction of the drift tube sense wires. The pixels make a precise measurement of particle arrival times. The coincidence of these signals is used to determine if the signal comes from the center of the detector or is induced from outside by cosmic ray muons. Moreover, the timing measurement from the pixels is fast enough to be used for the trigger decision, whereas the drift time of the PDTs (750 ns) is longer than the bunch crossing interval.

3.2.5 Trigger and DAQ

At the Tevatron, $p\bar{p}$ collisions happen at a rate of 2.5 MHz, and the readout of the full detector produces 250 kB of data. There is no medium available which is capable of recording data

this quickly. It would not be practical to analyze all of this data later on either, as the overwhelming number of collisions are of little interest: Most events are multijet events, while the production of massive particles such as W , Z , t and those which might provide evidence for new physics occur at an extremely low rate. DØ employs a three tiered pipelined trigger system to select the most interesting events for the data acquisition (DAQ) to record. Each second, this trigger decides which 50 of the 2.5 million events to write to tape. Each tier is given more time to examine the event in more detail than lower tiers and restricts the rate of events to be passed to higher tiers. A diagram of the trigger system is shown in Figure 3.8.

Level 1

The first trigger level is allowed $4.2\ \mu\text{s}$ to make a decision and must reduce the rate from 2.5 MHz to 1.4 kHz. The trigger decision is made deadtimeless by a framework built of field programmable gate arrays (FPGAs), which take inputs from the luminosity system, the tracking system, the calorimeter and the muon system. The luminosity system provides indication that a collision occurred within the DØ detector. The tracking system reconstructs tracks of charged particles using fast discriminator data and stores seed track candidates to be used by other trigger units. The calorimeter employs a special data path which performs a very fast summation of electromagnetic and hadronic towers at a resolution of $\eta \times \phi = 0.2 \times 0.2$; the trigger looks for towers which exceed a certain energy threshold. The muon trigger requires coincidence between scintillator signals in the A layer and either the B or C layer.

Level 2

The Level 2 system is comprised of two stages, a preprocessor stage and a global trigger stage. The preprocessors, DEC ALPHA processors running C programs, use information coming from one specific detector to identify objects such as tracks, electrons, jets and muons. The global stage represents the first combination of information coming from different subsystems, such as tracks and leptons. The Level 2 trigger has 100 ns to take a decision at a maximum deadtime of 5% and must reduce the rate to 1 kHz.

Level 3

The Level 3 trigger relies entirely on software algorithms running on a farm of computer nodes which perform an approximate reconstruction of the event. Algorithms for electron, muon and jet reconstruction mimic those employed later for full offline event reconstruction. The Level 3 trigger is given 100 ms to take its decision and must reduce the rate to 50 Hz.

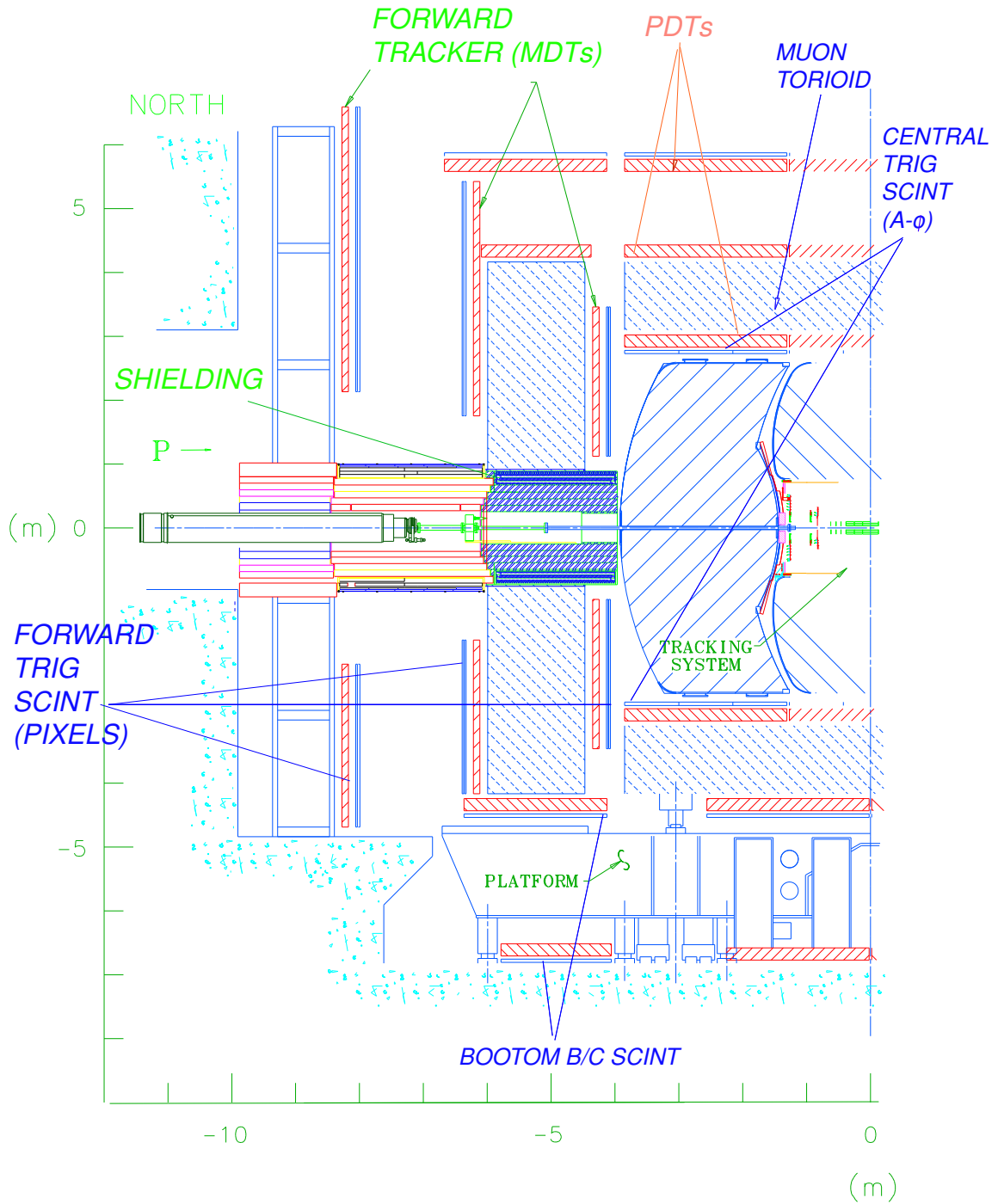


Figure 3.7: Outline of the DØ muon system.

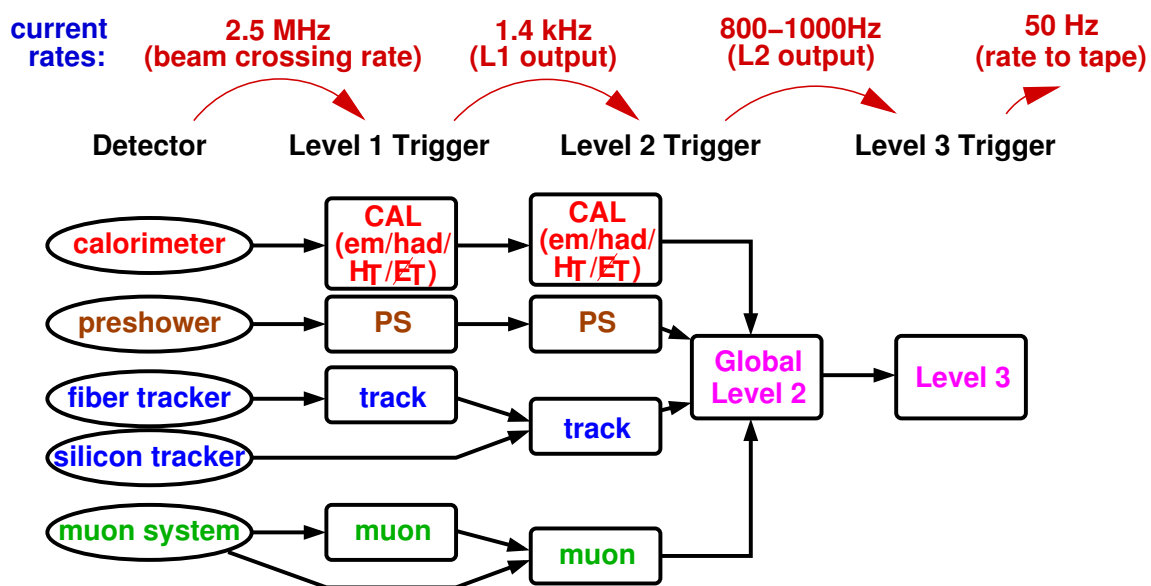


Figure 3.8: Diagram of the DØ trigger system.

Chapter 4

Event Reconstruction and Data Selection

The data as collected consists of nearly one million channels of immediate response from the various detector subsystems. These channels must be carefully processed to reveal evidence for the products of the collision which provide information about the kinematics of the interaction. Hence, the multitude of raw event data is handed to a sophisticated chain of software algorithms. Each algorithm is dedicated to identify the signature of certain physics objects like tracks, leptons, and jets, analyzing data produced by a specific set of subsystems. Algorithms are optimized to identify physics objects with high efficiency and purity, and to provide the best possible measurement of their energies and momenta. The $t\bar{t} \rightarrow \ell\nu q\bar{q}b\bar{b}$ process requires excellent identification and measurement of electrons, muons, hadronic jets and missing transverse energy \cancel{E}_T . As the calorimeter is unable to disentangle transverse and longitudinal momentum, precise knowledge of the point of collision, referred to as the “primary vertex”, is crucial as well. The following sections address the reconstruction of each physics object necessary to resolve the $t\bar{t}$ final state under study and to discriminate it from its backgrounds.

4.1 Tracks

The central tracking system accounts for a large fraction of the event data. Sifting through all of its channels for the signature of a charged particle curving through the magnetic field is the most time consuming task of the reconstruction chain. It is divided into two steps: First, individual channels of a specific tracking layer are grouped into clusters, each of which is likely to originate from a traversing particle (“Hit Clustering”). Then, clusters from different tracking layers which appear to be located along a physical path are combined to a track (“Track Finding”).

Hit Clustering

The energy deposited by a charged particle when traversing a layer of the silicon microstrip detector is typically spread out over more than one readout strip. Adjacent hits are grouped into a cluster if they are above a certain noise threshold. The position of the cluster is calculated as the average position of the individual strips, weighted by the charge deposition.

The spatial resolution achieved by this combination is significantly better than the mere strip width. Similarly, a charged particle illuminates either one or two fibers traversing a layer of the Central Fiber Tracker. Clusters are formed from every pair of adjacent illuminated fibers. If more than two adjacent fibers are illuminated, each pair is considered, and the ambiguity is left to be resolved by the track finding algorithm.

Track Finding

Track finding is subdivided into two steps: pattern recognition and track fitting. Pattern recognition filters the overwhelming number of possible combinations of hit clusters for those which appear to lie along a physical path. Track fitting then explores the candidate cluster collections using sophisticated algorithms [19, 20, 21], testing the consistency of the hits with the path of a particle and extracting physical parameters, such as the particle's momentum.

4.2 Primary Vertex

The point of collision between the proton and the anti-proton is referred to as the “primary vertex”. It is limited in the transverse plane to the size of the beam spot, which is of the order of tens of microns. However, as each proton/anti-proton bunch extends tens of centimeters along the beam axis, the vertex position can vary by this much as well. Precise knowledge of the vertex position is crucial to determine the direction of all calorimeter objects. Furthermore, muon candidates are rejected if they do not originate from the primary interaction in the event. Identification of displaced “secondary vertices” indicating the presence of a b quark requires an accurate estimate of the primary vertex position as well; as such life-time tagging algorithms are not considered in this analysis, they are not discussed further.

The $D\bar{O}$ approach to reconstruct the primary vertex position consists of two steps: reconstruction of candidate vertices [22] and selection of the hard scatter vertex [23] in the event.

Reconstruction of Candidate Vertices

A vertex candidate is a space point along the interaction region from which two or more charged particle tracks appear to originate. Only tracks with $p_T > 0.5$ GeV and at least two hits in the silicon precision tracking detector are considered. In a first pass of the algorithm, all tracks with a significance of their distance of closest approach (*dca*) $S_{(0,0)} < 100$ and within 2 cm along the beam axis are fitted to vertex candidates. The *dca* significance $S_{(x,y)}$ is defined by the *dca*, calculated with respect to (x, y) , divided by its uncertainty. In a second pass of the algorithm, the vertex positions (x', y') found in the first pass are used as seeds and the *dca* significance for each track is recalculated accordingly. Only tracks with *dca* significance $S_{x',y'} < 3$ are used to fit the final list of primary vertex candidates.

Selection of the Hard Scatter Vertex

In general, the vertex reconstruction step yields a number of primary vertex candidates mostly due to superimposed additional $p\bar{p}$ collisions. The fact that tracks from such minimum bias

interactions tend to have smaller transverse momenta is used to identify the hard scatter interaction vertex. The $\log_{10}p_T$ distribution in a minimum bias sample is used to define the probability for each track to originate from a minimum bias vertex. The individual track probabilities of each vertex are then combined to a vertex minimum bias probability. The candidate with the lowest minimum bias probability is selected as the hard scatter vertex in the event.

In this analysis, events are considered only if the primary vertex consists of at least three tracks and is within 60 cm of the center of the detector along the beam axis.

4.3 Muons

Muons are identified in the muon chambers by matching segments on either side of the toroid. The following signature is requested according to standards set by the $D\emptyset$ muon group [24]:

- at least two wire hits in the A layer
- at least one scintillator hit in the A layer
- at least two wire hits in the B or C layers
- at least one scintillator hit in the B or C layers (except for central muons with less than four BC wire hits)

A muon signal established according to these criteria is referred to as a “local muon”. Because of the presence of the toroid magnet, the momentum of the muon can be determined from the muon detector information alone. However, the momentum of the muon is measured with significantly better precision with the tracking detectors, if the local muon can be matched to its corresponding inner track. Consequently, only muons which can be matched to a central track are considered. The local muon track is extrapolated back to the point of closest approach to the beam and its parameters are compared to nearby charged particle tracks. The local momentum measurement in the muon chambers is disregarded entirely in favor of the tracking information. The central track matched to the muon is required to fulfill the following additional quality criteria:

- $\chi_{trk}^2/NDF < 4$ for the track fit
- separation from the primary vertex along the beam axis $\Delta z(\mu, PV) < 1$ cm
- dca significance $dca/\sigma(dca) < 3$, to reject muons from semi-leptonic heavy flavor decays

Momentum resolution degrades significantly for tracks without hits in the high precision silicon tracking detectors. As the above dca significance cut relates the muon to the hard scatter interaction in the event, some of the resolution can be recovered by constraining the muon track to the primary vertex. Track parameters are refit accordingly for muon tracks without SMT hits.

Comparison of the mass peak reconstructed in $Z \rightarrow \mu\mu$ events in data and Monte Carlo reveals a better resolution in Monte Carlo as well as shifted peak position. The muon momentum reconstructed in the simulation is smeared accordingly to reproduce the the scale and resolution found in data. Details of the procedure can be found in [26].

Muons from leptonic W boson decays are expected to be isolated from jets and thus any nearby calorimeter or tracking activity. The main source of misidentified $W \rightarrow \mu\nu$ decays are muons originating from semi-leptonic heavy flavor decays: if the hadronic signature of the b quark is not reconstructed as a calorimeter jet, the muon appears to be isolated. In addition, these muons tend to have lower transverse momentum p_T^μ than in the W decay. Consequently, the following two variables are defined to discriminate between isolated and non-isolated muons:

- **Rat11** $\equiv Halo(0.1, 0.4)/p_T^\mu$, where $Halo(0.1, 0.4)$ is the E_T sum of calorimeter clusters in a hollow cone around the muon direction ranging from $\Delta R = 0.1$ to $\Delta R = 0.4$. Only clusters in the electromagnetic and fine hadronic calorimeter layers are considered, whereas coarse hadronic signals are excluded due to their high noise level. Only muons with $Rat11 < 0.08$ are accepted.
- **Rattrk** $\equiv TrkCone(0.5)/p_T^\mu$, where $TrkCone(0.5)$ is the p_T sum of all tracks within a cone of radius $\Delta R = 0.5$ around the muon direction. The track matched to the muon itself is excluded from the sum. Only muons with $Rattrk < 0.06$ are accepted.

In this analysis, only muons with transverse momentum $p_T > 20$ GeV are considered. They are furthermore required to fulfill $|\eta_{det}| < 2.0$, using nearly the full coverage of the muon system.

4.4 Electrons

Electrons are identified as narrow clusters in the electromagnetic portion of the calorimeter system. Such an EM cluster is defined by one seed tower selected on the basis of its energy content, and the set of towers within a cone of radius $R = \sqrt{\Delta\eta^2 + \Delta\phi^2} = 0.2$ around it. Within this cone, the energy measured in all calorimeter systems is considered, but the cluster is required to have 90% of its total energy in the electromagnetic layers:

$$f_{EM} \equiv E_{EM}/E_{tot} > 0.9 . \quad (4.1)$$

The cluster is only considered as an electron candidate if it is isolated, requiring no significant additional calorimetric activity in a cone of radius $R = 0.4$:

$$f_{iso} = \frac{E_{tot}(R < 0.4) - E_{EM}(R < 0.2)}{E_{EM}(R < 0.2)} < 0.15 \quad (4.2)$$

The longitudinal and lateral development of the shower induced by an electron throughout the layers of the electromagnetic calorimeter is distinct from the properties of showers induced by other particles; each candidate is compared with average distributions from the simulation

and assign a χ^2 as a measure of electron compatibility: The χ^2 fit is based on seven degrees of freedom, and electron candidates must fulfill

$$\chi^2 < 75 \text{ (7 degrees of freedom)}. \quad (4.3)$$

The above criteria are based on calorimeter information only. To further suppress the overwhelming background from jet production, candidates are matched to a track in the central tracking system which points to the reconstructed EM cluster in the calorimeter:

$$|\Delta\phi(EM, track)| < 0.05, \quad |\Delta\eta(EM, track)| < 0.05. \quad (4.4)$$

The major remaining background arises from photons from π^0 decays which happen to overlap with a track from a nearby charged particle. This background is efficiently rejected by an electron likelihood [27], which is referred to as EM-likelihood and based on eight variables. Distribution of each variable are obtained in electron-enriched ($Z \rightarrow \mu\mu$) and fake-enriched (EM+jet back-to-back) data samples, and the likelihood is constructed from these canonical distributions. The likelihood discriminant yields values between 0 and 1, 1 indicating compatibility with the electron hypothesis. Candidates are required to have an EM-likelihood greater than 0.85.

Comparison of the mass peak reconstructed in $Z \rightarrow ee$ events in data and Monte Carlo reveals a better resolution in Monte Carlo as well as shifted peak position. The electron energies reconstructed in the simulation are smeared and scaled accordingly to reproduce the scale and resolution found in data. Details of the procedure can be found in [26].

In this analysis, only electrons reconstructed in the central region of the calorimeter (CC, $|\eta_{det}| < 1.1$), which have transverse momentum $p_T > 20$ GeV are considered. Electrons reconstructed in the ICR and EC calorimeter sections show high misidentification rates and are therefore excluded.

4.5 Jets

4.5.1 Jet Reconstruction

In $p\bar{p}$ collisions at the Tevatron, interactions with quarks and gluons in the final state occur at a very high rate. These particles hadronize immediately after production, creating a multitude of baryons and mesons which subsequently traverse the detector in the approximate direction of the initial parton and hit the calorimeter. The jet algorithm associates adjacent energy depositions in the calorimeter with the initial parton and forms corresponding jets.

At DØ, jets are reconstructed using the improved legacy cone algorithm, which was designed following the recommendation of the Run II QCD workshop [28]. Calorimeter towers are composed from cells (excluding those in the coarse hadronic layer) which share the same pseudorapidity and azimuthal angle. Towers exceeding $E_T > 0.5$ GeV are chosen as seeds, and preliminary jet candidates are identified using a simple cone algorithm with $R = 0.5$. As algorithms operating without seeds show better performance but are computationally too expensive, a compromise is found by considering E_T -weighted centers between pairs of cone jets as candidates as well. A sophisticated split and merge procedure resolves overlapping cones, and all remaining candidates which fulfill $E_T^{reco} > 8$ GeV are considered as reconstructed jets.

Calorimeter cells are subject to Gaussian electronic noise which exceeds the zero suppression threshold: typically, 1000 – 3000 cells are affected in each event. If such cells are assigned to a jet, the jet energy resolution of real jets is degraded, and fake jets can occur. Therefore, $D\mathcal{O}$ employs the T42 algorithm [29, 30, 31] to improve the interpretation of the calorimeter measurement at the cell level: isolated cells are considered noise if they do not appear to be “signal-like”. A cell is considered “signal-like” if its energy is positive and $+4\sigma$ above a threshold, or if it is $+2\sigma$ above the threshold but has a neighboring cell which exceeds the threshold by $+4\sigma$. The T42 algorithm rejects about 30 – 60% of all cells in the event, in good agreement with the noise expectation. Towers are subsequently built only from cells not identified as noise.

Reconstructed cone jets must fulfill the following additional quality requirements:

- $0.05 < f_{EM} < 0.95$, where f_{EM} is the fraction of jet energy deposited in the electromagnetic section of the calorimeter. Isolated electromagnetic particles are rejected.
- $f_{CH} < 0.4$, where f_{CH} is the fraction of jet energy deposited in the coarse hadronic section of the calorimeter. Jets which have been formed mainly from cells in this noisy calorimeter section are removed.
- $f_{hot} < 10$, where f_{hot} is the energy ratio of the highest to next-to-highest calorimeter cell assigned to the jet. A large value of f_{hot} indicates that the jet is clustered around a hot cell (mostly abnormal electronic noise).
- $n_{90} > 1$, where n_{90} is the number of calorimeter towers containing 90% of the jet energy. A small n_{90} indicates that the jet is clustered around a hot cell.
- Confirmation of the jet by the Level1 trigger readout chain. Fake jets surviving all other quality criteria appear mostly at the reconstruction stage, but are not seen in the trigger readout. This electronic noise is due to coherent noise in the precision readout chain and can be efficiently rejected by requiring coincidence between the reconstructed jet and Level1 trigger signals.
- $p_T > 20$ GeV, after jet energy scale correction
- $|\eta| < 2.5$

Electrons and photons which pass the cut on f_{EM} and exceed the reconstruction threshold of $E_T > 8$ GeV appear in the list of reconstructed jets. All such jets which are matched within $\Delta R(jet, EM) < 0.5$ to an electromagnetic object are removed from the list, if $p_T > 15$ GeV.

4.5.2 Jet Energy Scale

The raw energy of a reconstructed jet is given by the sum of energies deposited in the calorimeter cells associated with the jet by the cone algorithm. Several mechanisms cause this energy estimate to deviate from the energy of the initial parton:

- **Energy Offset O :** energy in the clustered cells which is due to noise, underlying event, multiple interactions, energy pile-up and uranium noise lead to a global offset of jet energies. O is determined from energy densities in minimum bias events.

- **Calorimeter Response R :** jets consist of different particles (mostly photons, pions, kaons, (anti-)protons and neutrons), for which the calorimeter response is different. Furthermore, the calorimeter responds slightly non-linearly to particle energies. R is determined with γ +jets events requiring transverse momentum balance. The photon scale is measured independently from $Z \rightarrow ee$ events with high precision.
- **Showering Corrections S :** a fraction of the parton energy is deposited outside of the finite-size jet cone. S is obtained from jet energy density profiles.

Consequently, the corrected particle energy E_{jet}^{corr} before interaction with the calorimeter is obtained from the reconstructed jet energy E_{jet}^{reco} as [32]

$$E_{jet}^{corr} = \frac{E_{jet}^{reco} - O}{R \times S} . \quad (4.5)$$

Note that E_{jet}^{corr} is not the parton energy: the parton may radiate additional quarks or gluons before hadronization, which may or may not end up in the jet cone. The correction of the jet energy down to the parton-level for the mass measurement is achieved in the derivation of the transfer functions, see Section 5.2. The jet energy scales for data and Monte Carlo jets are shown in Figures 4.1 and 4.2 respectively, along with the corresponding uncertainties.

The response measurement is performed for the central and forward calorimeters individually, but statistics do not allow for a finer binning of the scale versus pseudorapidity η . In a second iteration, more subtle features of the jet energy correction are resolved as a function of η [33]: the scale is applied to the jets in a $\gamma + jet$ sample (one hard photon and exactly one calorimeter jet), and the variable

$$\Delta S = \frac{p_{\text{T}}^{jet} - p_{\text{T}}^{\gamma}}{p_{\text{T}}^{\gamma}} \quad (4.6)$$

reveals additional structure of the jet energy scale as a function of pseudorapidity. These “ η -dependent” corrections are shown in Figure 4.3. They are applied to jets in Monte Carlo and data accordingly and propagated to the missing transverse energy, see Section 4.6.

4.5.3 Jet Energy Resolution

The precision of the top mass measurement is intimately related to the resolution of the jet energy measurement. Figures 4.4 and 4.5 show the individual jet resolution measurements for data and Monte Carlo. The width of the jet energy distribution is found to be underestimated in the simulation, and MC jets are smeared accordingly [26].

4.6 Missing Transverse Energy

Neutrinos do not interact with any of the detector systems and can only be identified indirectly by the imbalance of the event in the transverse plane. This imbalance is reconstructed from the vector sum of all calorimeter cells which pass the T42 algorithm, see Section 4.5. Cells in the coarse hadronic system receive special treatment due to their high level of noise: They are only considered if clustered into a reconstructed jet. The momentum vector that

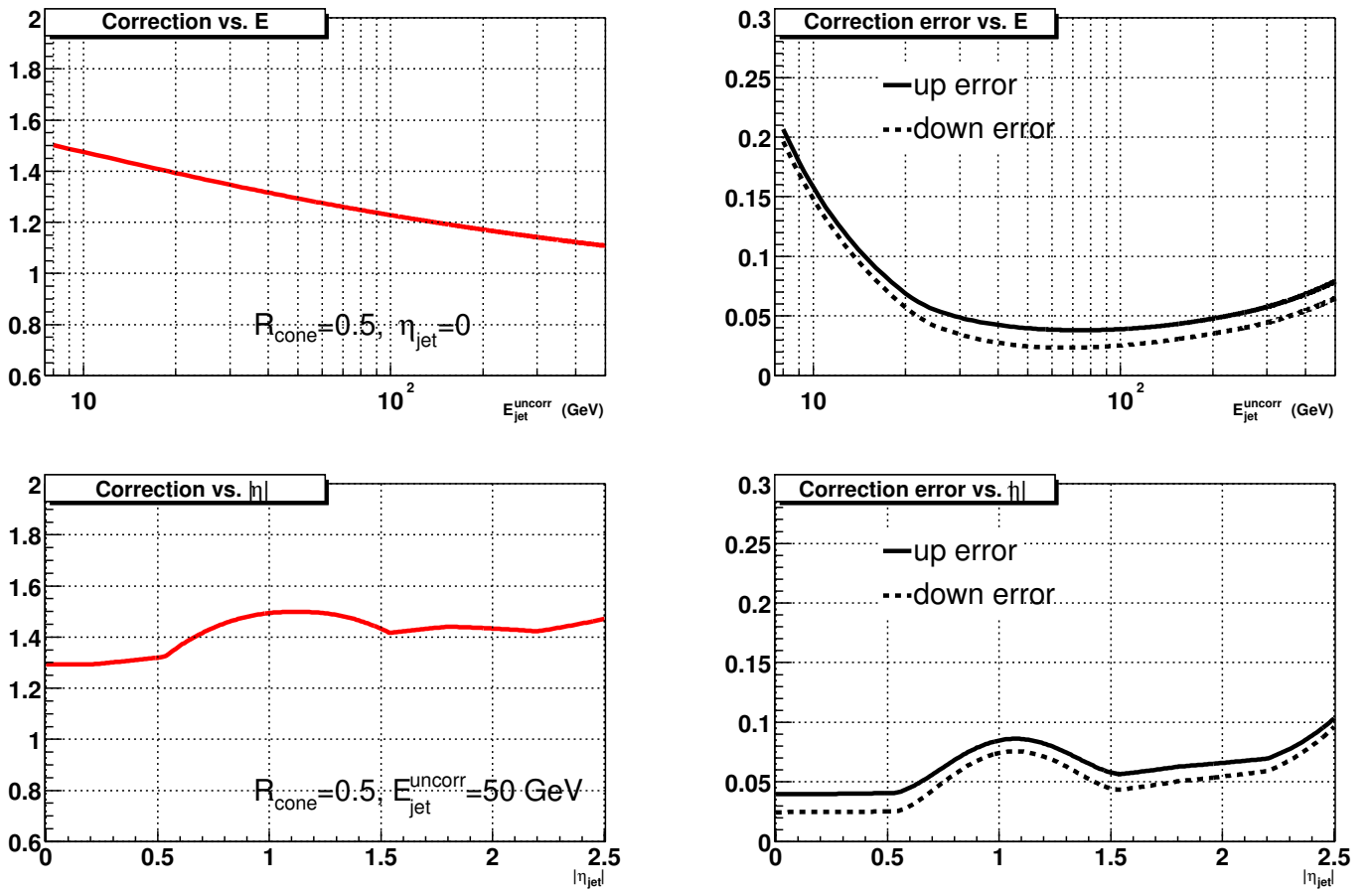


Figure 4.1: Jet energy scale for data jets as a function of jet p_T and jet η , and corresponding uncertainties.

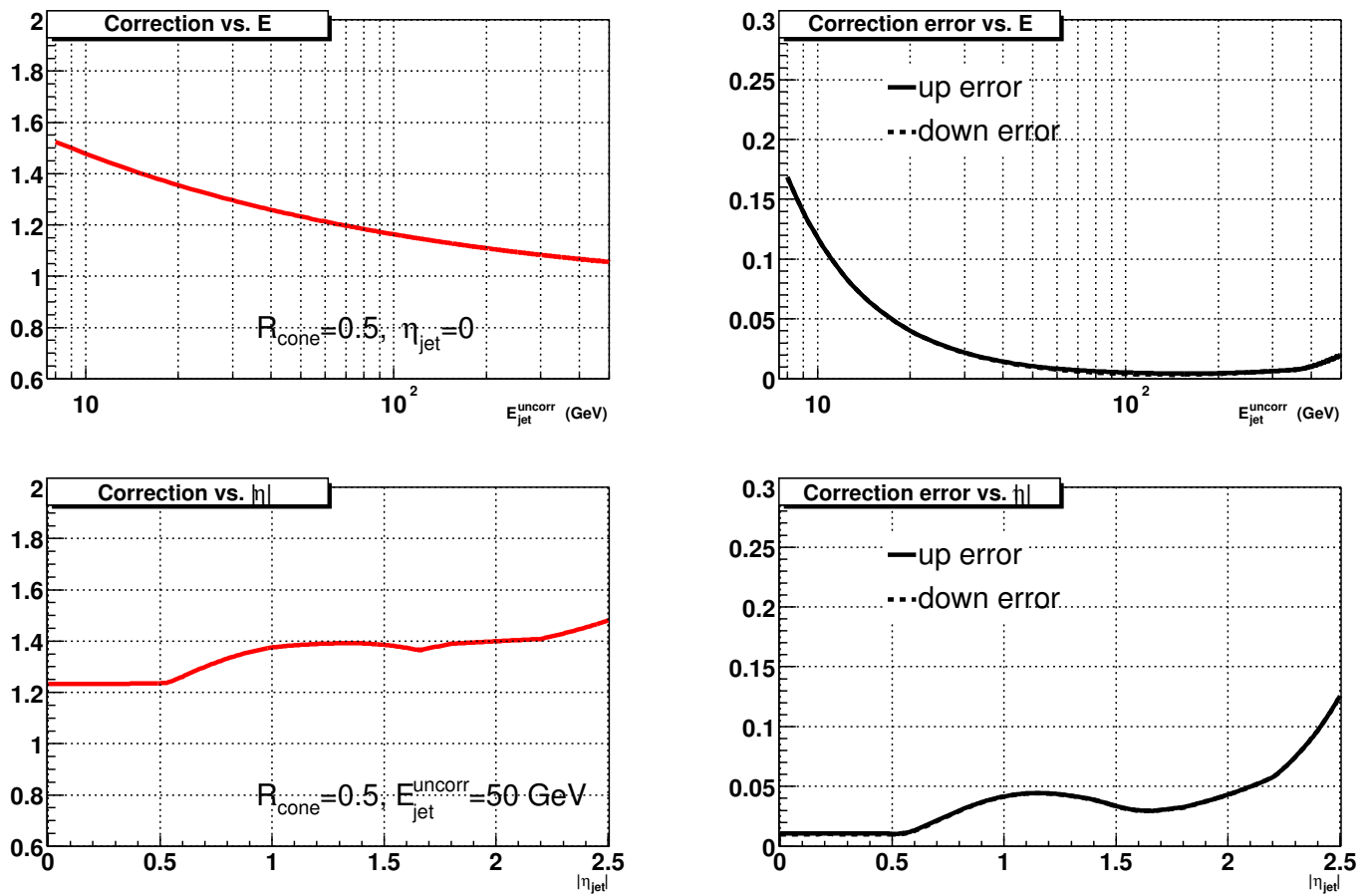


Figure 4.2: Jet energy scale for Monte Carlo jets as a function of jet p_T and jet η , and corresponding uncertainties.

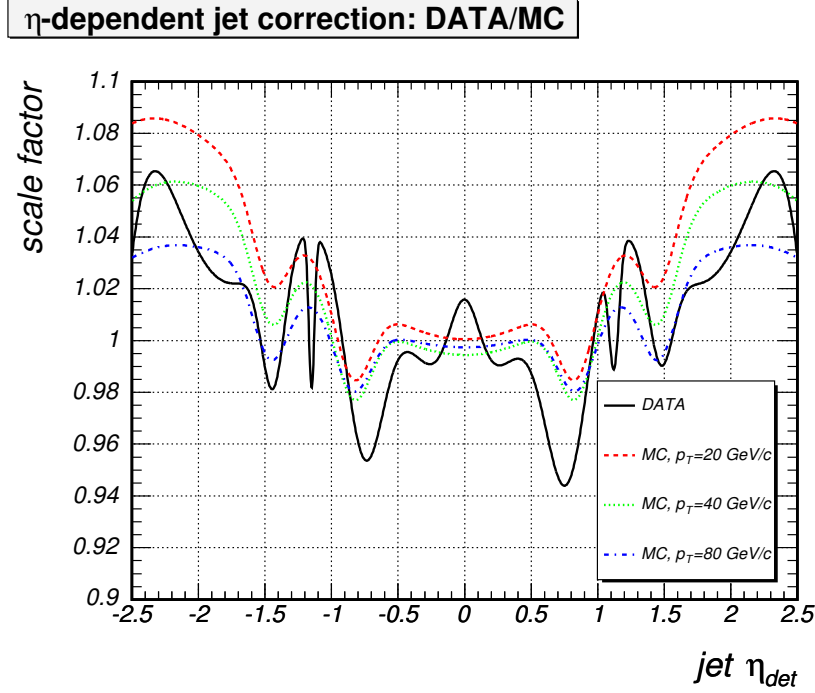


Figure 4.3: η -dependent jet energy corrections after jet energy scale correction for data and Monte Carlo jets. The corrections applied to MC jets depend on jet p_T as well.

balances this vector sum in the transverse plane is denoted the missing energy vector, and its magnitude is the raw missing transverse energy \cancel{E}_T^{raw} . The calorimeter response is different for electromagnetic particles and jets, and the respective corrections are propagated to the \cancel{E}_T vector according to the presence of such objects, resulting in \cancel{E}_T^{CAL} . If a muon is present in the event, it will only deposit a small fraction of its energy in the calorimeter, and the \cancel{E}_T vector is corrected accordingly. The muon energy deposition in the calorimeter is hereby taken from GEANT lookup tables. After all corrections, the magnitude of the missing transverse energy vector represents the quantity \cancel{E}_T referred to throughout the rest of this thesis.

In this analysis, only events with $\cancel{E}_T > 20$ GeV are considered in order to account for the presence of one energetic neutrino in the ℓ +jets final state.

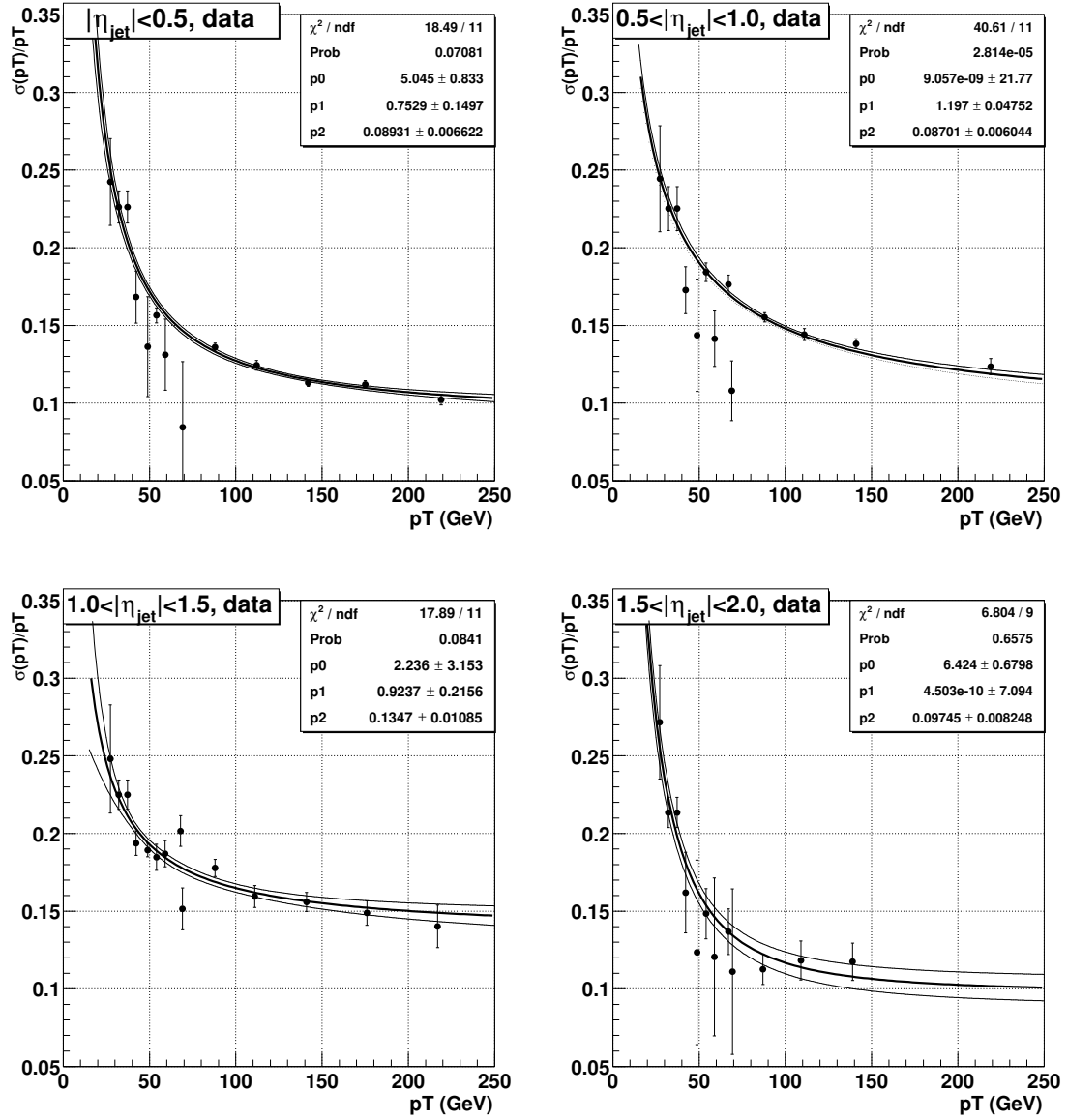


Figure 4.4: Jet energy resolution measurements in DØ Run II data, for different pseudorapidity regions. Points below 50 GeV are obtained from a $\gamma + \text{jet}$ sample. For $p_T > 50$ GeV, dijet events are used. The error bands reflect the statistical uncertainty.

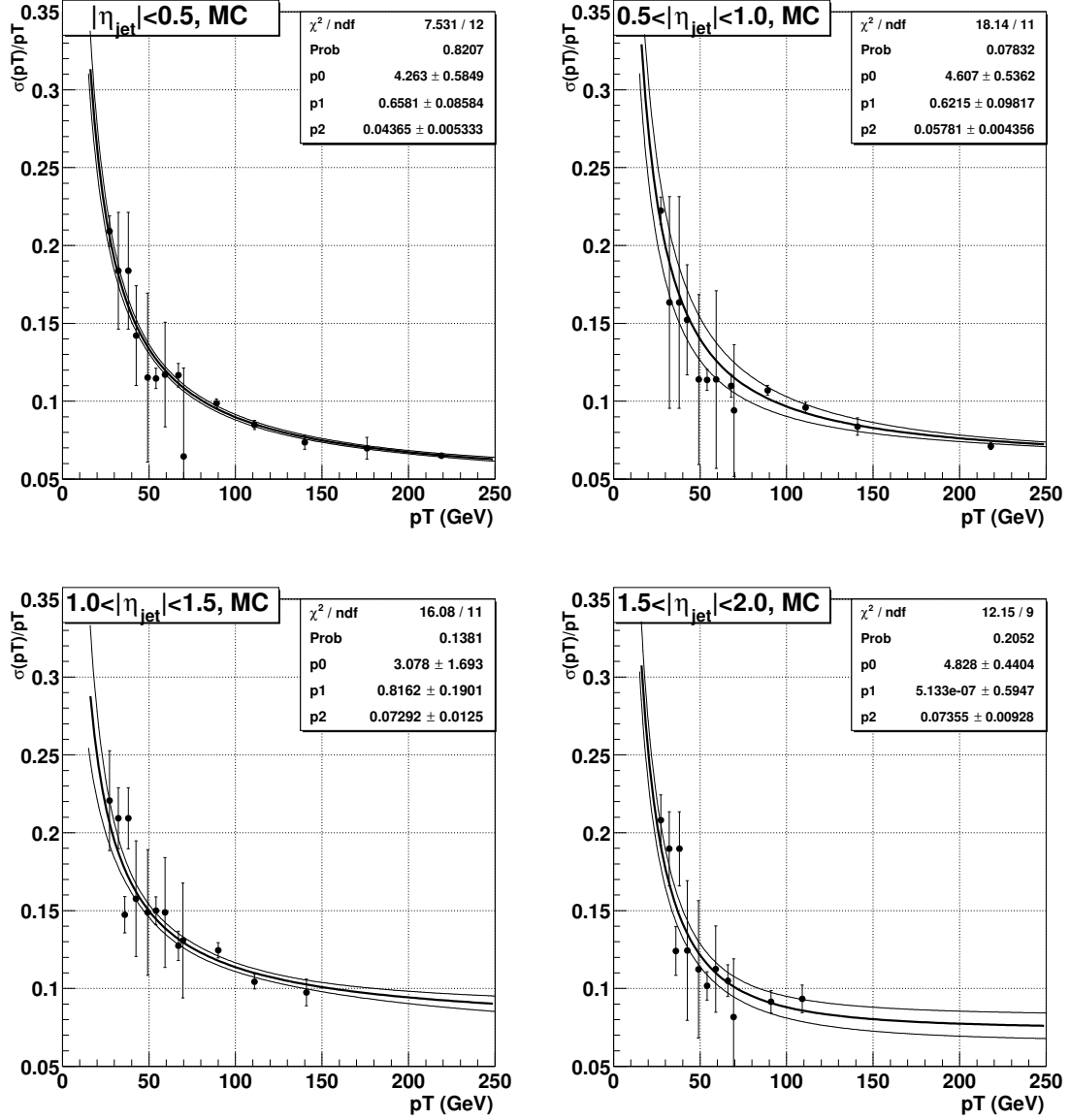


Figure 4.5: Jet energy resolution measurements in Monte Carlo, for different pseudorapidity regions. Points below 50 GeV are obtained from a $\gamma + \text{jet}$ sample. For $p_T > 50$ GeV, dijet events are used. The error bands reflect the statistical uncertainty.

Trigger List	v8-v11	v12
Trigger Name	EM15_2JT15	E1_SHT15_2J20
L1	CEM(1,10)_CJT(2,5)	CEM(1,11)
L2	EM(.85,10)	
L3	ELE_LOOSE_SHT(1,15)_JET(2,15)	ELE_NVL_SHT(1,15)_JET(2,20)

Table 4.1: Summary of e+jets triggers used in trigger lists v8 to v12.

4.7 Event Trigger

DØ employs a sophisticated three-level trigger system to decide for each event if it appears interesting enough to be recorded. The trigger system is described in Section 3.2.5. Several trigger conditions are defined and evaluated, and as the list of triggers evolves with time, a certain set of triggers with well defined conditions is identified by a trigger list version. The data sample under study has been recorded with five different trigger list versions: v8, v9, v10, v11 and v12. The triggers used in this analysis are summarized in Tables 4.1 (e+jets) and 4.2 (μ +jets).

The probability of each Monte Carlo event to pass the trigger requirements is calculated with a dedicated tool developed within the DØ top group [34]. The calculation based on single-object trigger efficiencies is described in [35]. The key concepts are briefly summarized as follows:

The total event probability $P(L1, L2, L3)$ is given by the product of the probabilities for the event to satisfy the trigger conditions at each triggering level,

$$P(L1, L2, L3) = P(L1) \cdot P(L2|L1) \cdot P(L3|L1, L2) , \quad (4.7)$$

where $P(L2|L1)$ and $P(L3|L1, L2)$ represent the conditional probabilities for the event to satisfy a set of criteria, given that it passes the requirements imposed at lower trigger levels. Assuming that the trigger efficiencies for two objects are not correlated, the probability for both objects to pass the trigger is

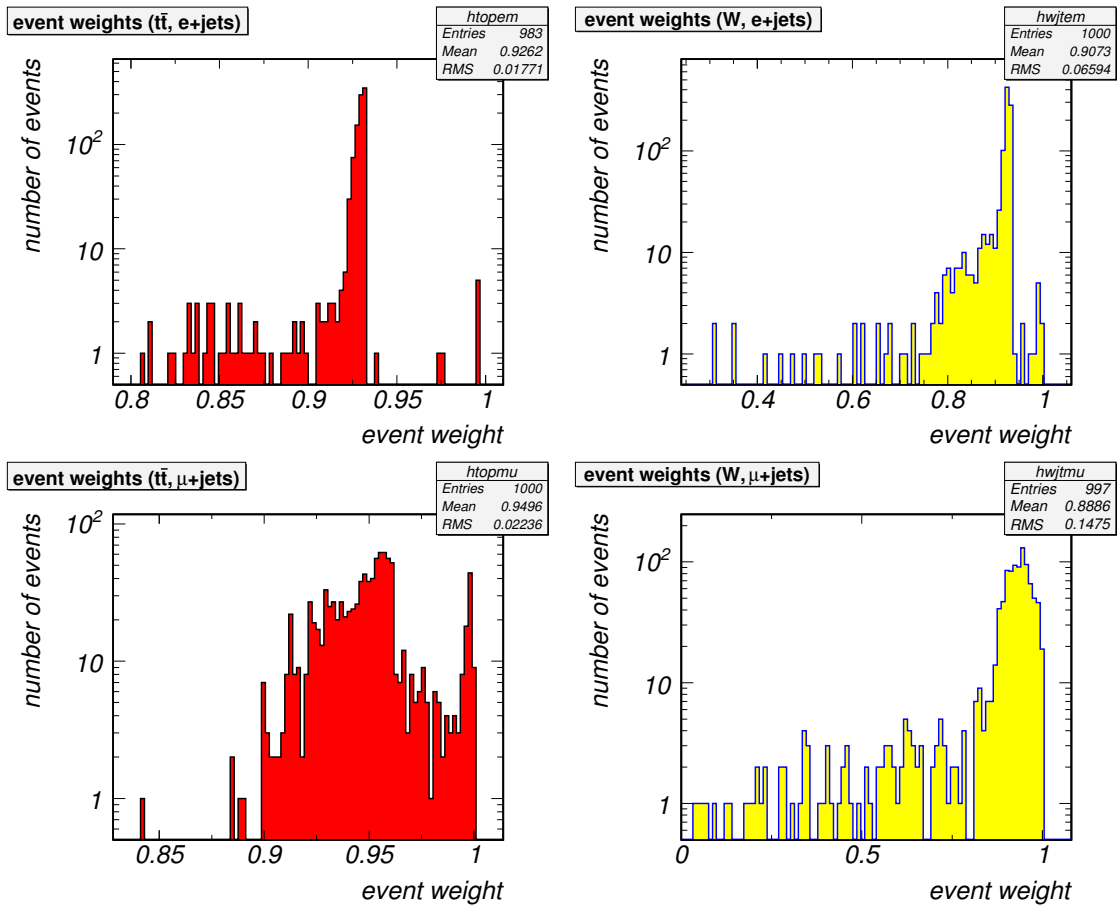
$$P_{obj1\&obj2} = P_{obj1} \cdot P_{obj2} . \quad (4.8)$$

Consequently, the probability for at least one object to satisfy a particular trigger condition, out of N objects present in the events is

$$P = 1 - \prod_{i=1}^N (1 - P_i) , \quad (4.9)$$

with P_i the single object trigger probability of the i^{th} object. The total trigger probability of the event is calculated as the luminosity-weighted average of the trigger probabilities associated to each individual trigger list. The corresponding weight distributions for $t\bar{t}$ ($m_{top} = 175$ GeV) and W + jets Monte Carlo events are shown in Figure 4.6.

Trigger List	v8-v11	v12
Trigger Name	MU_JT20_L2M0	MU_JT25_L2M0
L1	mu1ptxatxx_CJT(1,5)	mu1ptxatxx_CJT(1,3)
L2	MUON(1,med)	MUON(1,med)_JET(1,10)
L3	JET(1,20)	JET(1,25)

Table 4.2: Summary of μ +jets triggers used in trigger lists v8 to v12.Figure 4.6: Event weights for $t\bar{t}$ (left) and $W + \mu$ +jets (right) events for the e+jets (top) and μ +jets (below) channels.

Trigger List	e+jets [pb^{-1}]	μ +jets [pb^{-1}]
v8	19.7	20.1
v9	21.2	21.2
v10	15.2	15.3
v11	55.4	57.3
v12	209.8	209.8
total	321.3	323.7

Table 4.3: Breakdown of integrated luminosities by trigger list version for the e+jets and μ +jets samples, after data quality considerations.

primary vertex selection	
$ z_{PV} $	< 60 cm
N_{tracks} attached to vertex	≥ 3

Table 4.4: Primary vertex selection for the ℓ +jets sample.

4.8 Data Sample

The top mass measurement presented in this thesis is based on data collected with the DØ detector between August 2002 and July 2004 in Run II of the Tevatron. It corresponds to a total integrated luminosity of about 320 pb^{-1} after data quality selection. Table 4.3 gives a breakdown of integrated luminosity by trigger list version for the e+jets and μ +jets samples respectively. The details of the selection applied to obtain the $t\bar{t} \rightarrow \ell + \text{jets}$ candidate sample are described in Sections 4.2-4.6. All selection criteria are summarized in Tables 4.4-4.7.

e+jets events which pass all selection criteria without consideration of the EM-likelihood [27] are called “loose”. If the event passes the EM-likelihood cut, it is also called “tight”. μ +jets events which pass all selection criteria without consideration of the isolation are called “loose”. If the event passes the isolation cut, it is called “tight”. Table 4.8 summarizes the number of loose and tight events in the data sample for different exclusive jet multiplicities. Out of

electron selection	
f_{EM}	> 0.9
f_{iso}	< 0.15
χ^2	< 50
associated track	required
p_T	> 20 GeV
$ \eta $	< 1.1
EM-Likelihood	> 0.85
$\Delta z(e, PV)$	< 1 cm
Second Electron Veto	required

Table 4.5: Electron selection for the e+jets sample.

muon selection	
track match	required
Cosmic veto	required
p_T	> 20 GeV
$ \eta $	< 2.0
Isolation	tight isolation
DCA significance	3
$\Delta z(\mu, PV)$	< 1 cm
Second Muon Veto	required

Table 4.6: Muon selection for the μ +jets sample.

Jet/ \cancel{E}_T selection	
N_{jets}	4
Jet p_T	> 20 GeV
Jet $ \eta $	< 2.5
\cancel{E}_T	> 20 GeV
$\Delta\Phi(\ell, \cancel{E}_T)$ cut	applied

Table 4.7: Jet/ \cancel{E}_T selection for the ℓ +jets sample.

$\approx 1,000,000,000$ total events recorded during the time span, 150 tight events with exactly four jets are considered for the measurement of the top mass.

Events within runs in which the data quality is known to be poor are removed from the data sample. The data quality is considered poor for a run if one or more detector subsystems were not functioning well or were even disabled. The performance of the DØ detector is monitored online by the control room staff: if a problem with one of the detector components, the trigger, or the readout electronics is apparent, experts are consulted to fix the problem as quick as possible. The runs which appear affected are immediately labeled bad, and a central data quality database provides access to this information to analysers. If only a specific subsystem is affected, the run is labeled bad only with respect to this subsystem, and analysers can decide if it concerns their specific study or not. The run based quality criteria imposed on the

	$n_{jet} = 1$	$n_{jet} = 2$	$n_{jet} = 3$	$n_{jet} = 4$
e+jets, loose	14896	4168	781	153
e+jets, tight	10705	2497	398	70
μ +jets, loose	13930	4108	722	139
μ +jets, tight	9266	2459	410	80

Table 4.8: Number of loose and tight events in the e+jets and μ +jets data samples for different exclusive jet multiplicities. For the top mass measurement, 150 tight events with exactly four jets are considered, out of $\approx 1,000,000,000$ recorded events during the relevant time span.

Subsystem	e+jets	μ +jets
MUON	Reasonable	Reasonable
SMT	Not Bad	Not Bad
CFT	Not Bad	Not Bad
CAL	Not Bad	Not Bad

Table 4.9: Run based data quality criteria required for the e+jets and μ +jets sample for the top mass measurement.

e+jets and μ +jets samples for the mass measurement are summarized in Table 4.9.

Some data quality issues are not recognized online. Therefore, the recorded data is monitored offline as well: relevant distributions, mostly concerning kinematics of reconstructed objects like leptons and jets, are compared to canonical distributions which were found to model the expectation well. Deviations are quantified and sensible standards are applied to distinguish good from bad. As such corruptions of the data quality often occur on time scales much smaller than the length of a whole run, the data quality determined offline is classified by luminosity block number (LBN). A LBN typically corresponds to ≈ 1 minute of data taking and several thousand events (while a run can last several hours and contain millions of events). One of the most crucial data quality assessments obtained offline concerns the calorimeter performance: it is required that

- the average \cancel{E}_T is not significantly shifted from 0:

$$\sqrt{\langle \cancel{E}_x \rangle^2 + \langle \cancel{E}_y \rangle^2} < 6 \text{ GeV}$$

- the \cancel{E}_T distribution has a reasonable width (RMS):

$$\sqrt{RMS(\cancel{E}_x)^2 + RMS(\cancel{E}_y)^2} < 20 \text{ GeV}$$

- the average scalar E_T exceeds 60 GeV .

Finally, single events are rejected if the calorimeter energy deposition in the precision readout significantly deviates from the Level 1 readout. A detailed motivation of this strategy can be found in [36].

Chapter 5

The Matrix Element Method

5.1 Method Description

According to Fermi's Golden Rule, the probability of an event decaying into a final state with certain kinematics is proportional to the differential cross section of the event-describing process. The key concept of the Matrix Element Method is to build an event probability accordingly, assuming two processes, one signal and one background process, which the selected event sample is composed of:

$$P_{evt}(x, \alpha_i) = f_{\text{top}} \cdot P_{\text{sgn}}(x; \alpha_i) + (1 - f_{\text{top}}) \cdot P_{\text{bkg}}(x). \quad (5.1)$$

Hereby x denotes the kinematic variables of the events, f_{top} the signal fraction in the sample and α_i the parameter(s) to be measured. The method represents a general approach to extract information about any set of parameters α_i of the signal events.

This analysis is concerned with the measurement of the top quark mass in lepton+jets events: $\alpha_1 = m_{\text{top}}$ and $P_{\text{sgn}} = P_{t\bar{t}}$. $W(\rightarrow l\nu) + \text{jets}$ and QCD events are the main sources of background. The QCD background however is expected to be small and of similar topology as the $W + \text{jets}$ events. $P_{W+\text{jets}}$ is therefore taken as P_{bkg} in the modeling of the event probability (5.1), while the QCD events are not explicitly modeled.

The mass measurement is systematically limited by the uncertainty on the jet energy scale. The signal probability contains information about the jet energy scale, as the mass of the hadronically decaying W boson is constrained (light jets). Consequently, the likelihood can be extended to be a function of $\alpha_2 \equiv JES$. m_{top} and JES are fitted simultaneously, and the likelihood yields an estimate of the top mass error which includes both the statistical and systematic jet energy scale uncertainty. Details of the propagation of the JES parameter to the likelihood are described in Section 5.2.

The differential cross section $d^n\sigma_{hs}$ for any hard-scatter interaction between two partons with four-vector momenta Q_1 and Q_2 decaying into any n -body final state is given by

$$d^n\sigma_{hs} = \frac{(2\pi)^4 |\mathcal{M}|^2}{4\sqrt{(Q_1 \cdot Q_2)^2 - m_1^2 m_2^2}} \cdot d\Phi_n \quad (5.2)$$

where \mathcal{M} is the matrix element describing the process and its kinematics, m_1 , m_2 are the

particle masses associated to Q_1 and Q_2 , and the n -body phase space $d\Phi_n$ is

$$d\Phi_n(Q_1 + Q_2; p_1, \dots, p_n) = \delta^4(Q_1 + Q_2 - \sum_{i=1}^n p_i) \prod_{i=1}^n \frac{d^3 p_i}{(2\pi)^3 2E_i}. \quad (5.3)$$

To obtain the differential cross section in $p\bar{p}$ collisions, (5.2) is convoluted with the parton density functions (PDF) in order to take all possible kinematics and flavor compositions of Q_1 and Q_2 into account:

$$d^n \sigma = \sum_{\text{flavors}} \int_{q_1} \int_{q_2} d^n \sigma_{hs} dq_1 dq_2 f(q_1) f(q_2). \quad (5.4)$$

Here q_1 and q_2 denote the momentum fractions of the colliding partons relative to the proton (anti-proton) momentum. The probabilities P_{sgn} and P_{bkg} in (5.1) are then proportional to $d^n \sigma_{t\bar{t}}$ and $d^n \sigma_{W+\text{jets}}$, where appropriate matrix elements $\mathcal{M}_{t\bar{t}}$ and $\mathcal{M}_{W+\text{jets}}$ are substituted respectively.

In the experimental setup of the DØ detector, the kinematic variables of the final state particles are reconstructed with finite resolution. The resolution functions $W(x, y, JES)$ are referred to as *transfer functions* and describe the probability density of a parton state y to be reconstructed as x . Given the total cross section

$$\sigma(m_{\text{top}}) = \int d^n \sigma(x; m_{\text{top}}), \quad (5.5)$$

the final probability P_{sgn} is computed as

$$P_{\text{sgn}}(x; m_{\text{top}}, JES) = \frac{1}{\sigma(m_{\text{top}})} \cdot \int d^n \sigma_{hs}(y; m_{\text{top}}) dq_1 dq_2 f(q_1) f(q_2) \cdot W(x, y, JES). \quad (5.6)$$

Hence the probability is derived by integrating over all possible parton states, and each configuration is weighted according to its probability to produce the observed measurement. The background probability P_{bkg} is calculated accordingly.

In order to extract the top quark mass from a set of n events with measurements x_1, \dots, x_n , a likelihood function is built from the event probabilities,

$$L(x_1, \dots, x_n; m_{\text{top}}, JES) = \prod_{i=1}^n P_{\text{evt}}(x_i; m_{\text{top}}, JES) \quad (5.7)$$

and evaluated for different values of m_{top} and JES . The top quark mass is determined by minimizing

$$-\ln L(x_1, \dots, x_n; m_{\text{top}}, JES) = -\sum_{i=1}^n \ln(P_{\text{evt}}(x_i; m_{\text{top}}, JES)) \quad (5.8)$$

with respect to m_{top} and JES simultaneously, taking the correlation between both parameters into account.

5.2 Jet Resolution Handling: Transfer Functions

The energy resolution of leptons and jets in the event is parametrized with transfer functions $W(E_{rec}, E_{true})$: they yield the probability for a measurement E_{rec} in the detector, if the true object energy is E_{true} . The energy resolution of electrons in the DØ detector is found good enough to be neglected in the likelihood calculation. The description and derivation of the transfer function for muons can be found in [37]. All object directions are considered well-measured and do not require transfer functions.

For calorimeter jets, the transfer function $W(E_{jet}, E_{parton}; JES = 1) \equiv W(E_j, E_p)$ is parametrized as

$$L(\delta E) = \frac{1}{\sqrt{2\pi}(p_2 + p_3 p_5)} \left[\exp\left(-\frac{(\delta E - p_1)^2}{2p_2^2}\right) + p_3 \exp\left(-\frac{(\delta E - p_4)^2}{2p_5^2}\right) \right], \quad (5.9)$$

with $\delta E \equiv E_j - E_p$. The behavior of the jet energy transfer function for $JES \neq 1$ is discussed in Section 5.2.2. The p_i are themselves functions of the parton energy, and are parameterized as linear functions of the parton energy, so that

$$p_i = a_i + E_p \cdot b_i, \quad (5.10)$$

where all energies are in GeV.

A different set of parameters is derived for four η regions: $|\eta| < 0.5$, $0.5 < |\eta| < 1.0$, $1.0 < |\eta| < 1.5$, and $1.5 < |\eta| < 2.5$, and for three different quark varieties: light quarks (u , d , s , c), b quarks with a soft muon tag, and all other b quarks. 120 parameters describe the transfer function for all jets.

5.2.1 Jet Transfer Function Derivation

The transfer function parameters for calorimeter jets are determined from $t\bar{t}$ Monte Carlo, at top masses of 150, 160, 165, 170, 175, 180, 185, 190, and 200 GeV. On top of the standard jet energy corrections, η -dependent corrections are applied as well, see Section 4.5.2. To be used in the calculation of the transfer function parameters, events are required to have one top quark decay to a b quark and two light quarks and the other top quark decay to a b quark and an electron or muon and corresponding neutrino. The four decay partons are required to have a unique one-to-one correspondence with exactly four jets in the event, where correspondence means that the parton and jet are within $\Delta R < 0.5$ ($\Delta R \equiv \sqrt{\Delta\phi^2 + \Delta\eta^2}$). We also apply quality cuts on the lepton and on missing transverse energy \cancel{E}_T .

The parton and jet energies are fed to an unbinned likelihood fit that minimizes the χ^2 of the fit to Eq. (5.9) with respect to a_i and b_i . The parameter a_3 was fixed to 0 for two reasons. First, since the transfer function is a probability distribution function, allowing negative p_3 could allow the transfer function to give negative likelihoods. Second, fixing this parameter helps constrain the fit since the two Gaussians are no longer interchangeable. Since extreme outliers in the δE distribution will drastically skew the fit, all jet-parton pairs with $|\delta E| > 100$ GeV are excluded from the fit.

The final parameters from the fits are given in Tables 5.1-5.3. Additional cross-checks of the transfer functions can be found in Appendix D.

parameter	$ \eta $		region	
	< 0.5	$0.5 - 1.0$	$1.0 - 1.5$	> 1.5
a_1	-0.30	0.73	4.00	10.1
b_1	-0.028	-0.052	-0.108	-0.116
a_2	3.47	2.05	2.65	5.54
b_2	0.097	0.144	0.151	0.122
a_3	0.	0.	0.	0.
b_3	3.73×10^{-4}	3.98×10^{-4}	7.74×10^{-4}	0.00106
a_4	18.1	22.3	17.1	37.7
b_4	-0.170	-0.157	0.0309	-0.154
a_5	17.1	19.8	20.0	29.1
b_5	0.0970	0.0804	0.0561	-0.0445

Table 5.1: Light quark transfer function parameters.

parameter	$ \eta $		region	
	< 0.5	$0.5 - 1.0$	$1.0 - 1.5$	> 1.5
a_1	-5.08	-2.38	0.68	33.0
b_1	0.0024	-0.065	-0.124	-0.337
a_2	3.80	2.40	0.91	13.2
b_2	0.087	0.155	0.181	0.132
a_3	0.	0.	0.	0.
b_3	0.00212	3.49×10^{-4}	7.46×10^{-4}	0.0406
a_4	2.23	26.2	11.7	-1.90
b_4	-0.181	-0.407	-0.0075	-0.0509
a_5	11.2	20.1	18.0	3.42
b_5	0.112	0.122	0.075	0.134

Table 5.2: b quark transfer function parameters.

parameter	$ \eta $		region	
	< 0.5	$0.5 - 1.0$	$1.0 - 1.5$	> 1.5
a_1	11.0	4.97	12.9	13.6
b_1	-0.133	0.0053	-0.165	-0.132
a_2	2.99	3.85	4.02	5.42
b_2	0.118	0.040	0.125	0.118
a_3	0.	0.	0.	0.
b_3	3.02×10^{-4}	0.0114	4.30×10^{-4}	2.42×10^{-4}
a_4	45.3	13.3	45.1	71.8
b_4	-0.454	-0.191	-0.215	-0.124
a_5	15.8	5.6	13.9	16.4
b_5	0.225	0.135	0.142	0.034

Table 5.3: Muon-tagged b quark transfer function parameters.

5.2.2 Jet Transfer Function and the JES parameter

The JES parameter fitted simultaneously with m_{top} is defined such that it yields 1.0 if the reference scale is found to describe the data best. Reference scale hereby refers to the standard $D\bar{O}$ jet energy scale plus η -dependent corrections for Monte Carlo events, the scenario for which the parameters for the jet transfer function are derived. The JES parameter describes an additional scale factor between the reference jet energy scale and the jet energies in the data sample being fitted. if the fit yields $JES = 1.1(0.9)$, it means that the fit prefers a jet energy scale 10 % higher (lower) than the reference scale derived in Monte Carlo, and all jets would have to be scaled by $1/1.1(1/0.9)$ for the sample to correspond to $JES = 1$.

The JES parameter is introduced to the likelihood as an additional parameter of the jet transfer function:

$$W(E_j, E_p; JES) \equiv \frac{W\left(\frac{E_j}{JES} - E_p\right)}{JES}. \quad (5.11)$$

Figures 5.1, 5.2 and 5.3 illustrate that (5.11) correctly describes the desired effect, using transfer function parameters derived for $JES = 1.0$ only.

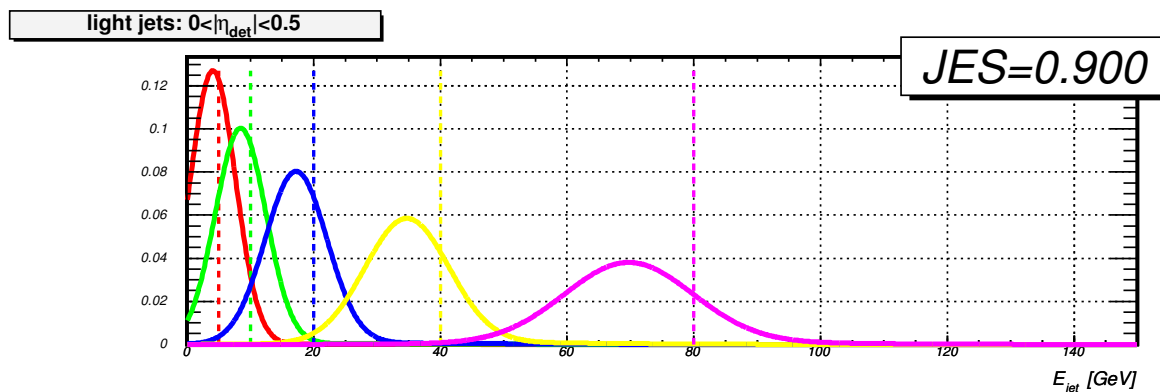


Figure 5.1: Jet transfer function for light jets, $0.0 < |\eta| < 0.5$, for various parton energies E_p (dashed lines). The JES parameter is arbitrarily chosen to be 0.9: for a given parton energy E_p , the probability for a jet to be reconstructed with $0.9 \cdot E_j^{JES=1}$ is equal to $W(E_j^{JES=1}, E_p; 1)$, see Figure 5.2.

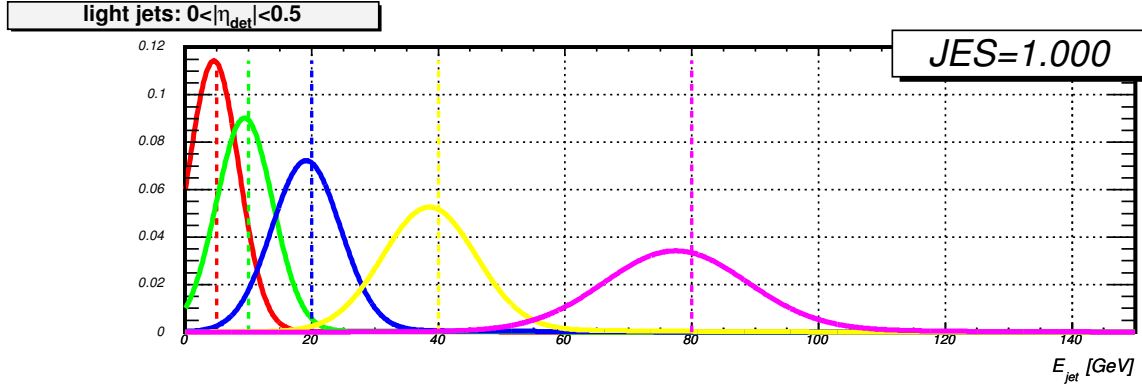


Figure 5.2: Jet transfer function for light jets, $0.0 < |\eta| < 0.5$, for various parton energies E_p (dashed lines). The parametrization corresponds to the reference jet energy scale, $JES = 1.0$.

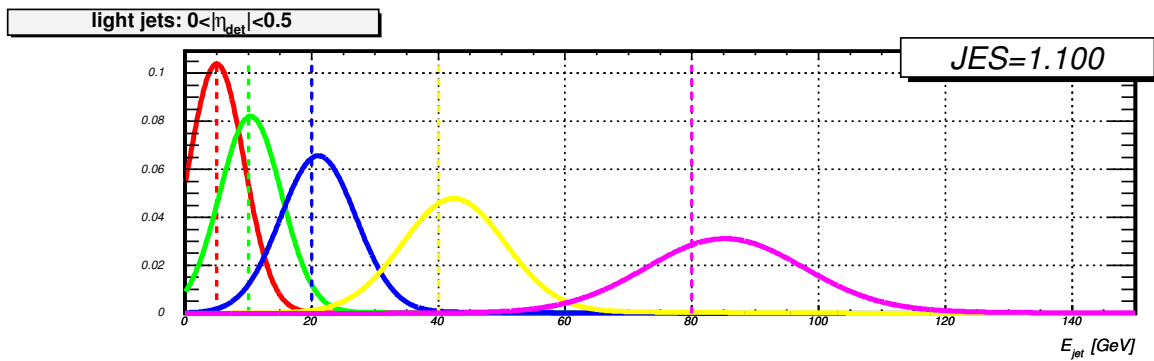


Figure 5.3: Jet transfer function for light jets, $0.0 < |\eta| < 0.5$, for various parton energies E_p (dashed lines). The JES parameter is arbitrarily chosen to be 1.1: for a given parton energy E_p , the probability for a jet to be reconstructed with $1.1 \cdot E_j^{JES=1}$ is equal to $W(E_j^{JES=1}, E_p; 1)$, see Figure 5.2.

5.3 Calculation of the event probability

5.3.1 Calculation of the Signal Probability P_{sgn}

This section describes the computation of the signal probability P_{sgn} defined in Equations (5.1) and (5.6) in Section 5.1. Note that P_{sgn} is also a function of the jet energy scale parameter JES . This parameter enters the probability calculation via the jet transfer function, as described in Section 5.2.2, and is not considered here.

The leading order matrix element for the process $q\bar{q} \rightarrow t\bar{t}$ is taken to compute P_{sgn} . When neglecting spin correlations, the matrix element is given by [41]

$$|\mathcal{M}|^2 = \frac{g_s^4}{9} F \bar{F} (2 - \beta^2 s_{qt}^2), \quad (5.12)$$

where g_s is the strong coupling constant, β is the velocity of the top quarks in the $t\bar{t}$ rest frame, and s_{qt} denotes the sine of the angle between the incoming parton and the outgoing top quark in the $t\bar{t}$ rest frame. The factors F and \bar{F} describe the kinematics of the top and anti-top quark decay. If the top quark decay products include the leptonically decaying W , while the antitop decay includes the hadronically decaying W , one has

$$F = \frac{g_w^4}{4} \left(\frac{m_{b\ell\nu}^2 - m_{\ell\nu}^2}{(m_{b\ell\nu}^2 - m_t^2)^2 + (m_t \Gamma_t)^2} \right) \left(\frac{m_{b\ell\nu}^2 (1 - \hat{c}_{b\ell}^2) + m_{\ell\nu}^2 (1 + \hat{c}_{b\ell}^2)^2}{(m_{\ell\nu}^2 - m_W^2)^2 + (m_W \Gamma_W)^2} \right), \quad (5.13)$$

$$\bar{F} = \frac{g_w^4}{4} \left(\frac{m_{b\bar{d}\bar{u}}^2 - m_{\bar{d}\bar{u}}^2}{(m_{b\bar{d}\bar{u}}^2 - m_t^2)^2 + (m_t \Gamma_t)^2} \right) \left(\frac{m_{b\bar{d}\bar{u}}^2 (1 - \hat{c}_{b\bar{d}}^2) + m_{\bar{d}\bar{u}}^2 (1 + \hat{c}_{b\bar{d}}^2)^2}{(m_{\bar{d}\bar{u}}^2 - m_W^2)^2 + (m_W \Gamma_W)^2} \right) \quad (5.14)$$

(for the other case, replace $b \leftrightarrow \bar{b}$, $\ell \leftrightarrow d$, and $\nu \leftrightarrow \bar{u}$). Here, g_w denotes the weak coupling constant ($G_F/\sqrt{2} = g_w^2/8M_W^2$), m_t and m_W are the mass of the top quark (which is to be measured) and the W boson, and Γ_t and Γ_W are their widths. Invariant top and W masses in a particular event are denoted by m_{xyz} and m_{yz} , respectively, where x , y , and z are the decay products. The cosine of the angle between particles x and y in the W rest frame is denoted by \hat{c}_{xy} . Here and in the following, the symbols d and \bar{u} stand for all possible decay products in a hadronic W decay.

The correct association of reconstructed jets with the final state quarks in Equations (5.13) and (5.14) is not known. Therefore, the signal probability is computed as the mean of the P_{sgn} values for all 24 possible jet-parton assignments. The mean value of the two combinations with the 4-momenta of the quarks from the hadronic W -decay interchanged is computed explicitly by using the symmetrized formula

$$\bar{F} = \frac{g_w^4}{4} \left(\frac{m_{b\bar{d}\bar{u}}^2 - m_{\bar{d}\bar{u}}^2}{(m_{b\bar{d}\bar{u}}^2 - m_t^2)^2 + (m_t \Gamma_t)^2} \right) \left(\frac{m_{b\bar{d}\bar{u}}^2 (1 - \hat{c}_{b\bar{d}}^2) + m_{\bar{d}\bar{u}}^2 (1 + \hat{c}_{b\bar{d}}^2)^2}{(m_{\bar{d}\bar{u}}^2 - m_W^2)^2 + (m_W \Gamma_W)^2} \right) \quad (5.15)$$

instead of (5.14).

The signal probability P_{sgn} depends on the final state particle 4-momenta, some of which are not directly measured in the detector. Therefore, the computation involves an integral

over all possible final states, i.e. an integral over all possible momenta of the colliding partons and over 6-body phase space to cover all possible final states, cf. Equation (5.6). Several assumptions are made to reduce the number of dimensions of the integration:

- The transverse momentum of the colliding partons is assumed to be zero. of 4-momentum then implies zero transverse momentum of the $t\bar{t}$ system and relates the momenta of the colliding partons to the longitudinal momentum and energy of the $t\bar{t}$ system.
- The directions of the quarks and the charged lepton in the final state are assumed to be exactly measured. This is justified since the angular resolutions of the detector lead to a much smaller broadening of the reconstructed m_{top} distribution than the energy resolution.
- The energy of electrons from W decay is assumed to be perfectly measured as well since the electron energy resolution is much better than the jet energy resolution. The corresponding statement is not necessarily true for high momentum muons, and an integration over the muon momentum is performed.

After these considerations, an integration over the quark momenta, the lepton momentum (μ +jets only), and the longitudinal component of the neutrino remains to be calculated. This calculation is performed numerically with the Monte Carlo program VEGAS [38, 39]. The interface to the VEGAS integration algorithm is provided by the GNU Scientific Library (GSL) [40]. The adaptive VEGAS algorithm relies on importance sampling and works most efficiently if the one-dimensional projections of the integrand onto the individual integration variables have well-localized peaks. The integrand contains peaks from the transfer functions, and from four Breit-Wigner peaks corresponding to the two top quark and two W boson decays in the $t\bar{t}$ matrix element. These Breit-Wigner peaks are more localized than the peaks from the jet transfer functions, suggesting the corresponding masses are better integration variables leading to faster convergence. The computation of the parton kinematics however must be performed in each integration step from the integration variables, which is greatly simplified by choosing $p_{b\nu}^z$ as an integration variable instead of the mass of the leptonically decaying W . Therefore only three of the masses are used as integration variables. In summary, the following integration variables are chosen for the computation of P_{sgn} :

- the magnitude $|\vec{p}_a|$ of the momentum of one of the quarks from the hadronic W decay, with $0 \leq |\vec{p}_a| \leq 500$ GeV,
- the squared mass $m_{d\bar{u}}^2$ of the hadronically decaying W , $0 \leq m_{d\bar{u}}^2 \leq (400 \text{ GeV})^2$,
- the squared mass $m_{b\bar{d}\bar{u}}^2$ of the top quark with the hadronic W decay, $0 \leq m_{b\bar{d}\bar{u}}^2 \leq (500 \text{ GeV})^2$,
- the squared mass $m_{b\ell\nu}^2$ of the top quark with the leptonic W decay, $0 \leq m_{b\ell\nu}^2 \leq (500 \text{ GeV})^2$,
- the z component $p_{b\nu}^z$ of the sum of the momenta of the b quark and neutrino from the top quark with the leptonic W decay, $-500 \text{ GeV} \leq p_{b\nu}^z \leq +500 \text{ GeV}$, and

- the muon charge divided by the muon transverse momentum p_μ^T (in the μ +jets channel only), $-1/(100 \text{ MeV}) \leq q_\mu/p_\mu^T \leq +1/(100 \text{ MeV})$.

Thus, for each point in the $(|\vec{p}_d|, m_{d\bar{u}}^2, m_{b\bar{d}u}^2, m_{b\ell\nu}^2, p_{b\nu}^z [, q_\mu/p_\mu^T])$ integration space the following computation is performed for each of the 12 possible jet-parton assignments (where the symmetrized form of the matrix element according to Equation (5.15) is used):

1. The 4-momenta of the $t\bar{t}$ decay products are calculated from the values of the integration variables, the measured jet and lepton angles, and the electron energy (in the e+jets case) as derived in Appendix B. The particular choice of integration variables is also motivated by the fact that this problem can be solved analytically.
2. The matrix element is evaluated according to Equations (5.12), (5.13), and (5.15).
3. The parton distribution functions are evaluated. For consistency with the leading-order matrix element, we use the CTEQ5L parton distribution functions, summing over all possible quark flavours.
4. The probabilities to observe the measured jet energies and muon transverse momentum given the energies and momentum computed in the first step are evaluated (transfer functions).
5. The Jacobian determinant for the transformation from momenta in Cartesian coordinates to the $(|\vec{p}_d|, m_{d\bar{u}}^2, m_{b\bar{d}u}^2, m_{b\ell\nu}^2, p_{b\nu}^z [, q_\mu/p_\mu^T])$ integration space is included. This determinant is derived in Appendix C.

The achieved precision of the P_{sgn} calculation varies from typically 2% to a maximum of 10%, where one jet permutation requires about 1 – 5 seconds of processing time on a Pentium IV CPU, depending on whether the lepton p_T integration is performed.

5.3.2 Normalization of the Signal Probability P_{sgn}

To normalize the probabilities calculated in Section 5.3.1, the total cross-section (5.5) is computed as a function of m_{top} and JES for the matrix element given in (5.12). The 16 dimensional phase-space integral is computed using VEGAS [38, 39]. The algorithm's performance is maximized by choosing top and W masses with their well-localized Breit-Wigner peaks as integration variables. However, the total cross section σ does not correctly normalize the probability; the kinematic selection has to be taken into account to calculate σ_{obs} , the cross-section actually observed in the detector:

$$\sigma_{\text{obs}}(m_{\text{top}}, JES) = \int d^n \sigma(x; m_{\text{top}}) f_{\text{acc}}(x; JES) . \quad (5.16)$$

The acceptance function $f_{\text{acc}}(x; JES)$ describes the efficiency of a phase-space state x to pass the trigger and offline event selection criteria. The kinematic selection on the other hand applies to jets, not partons, and the transfer functions provide the mapping between them.

Thus, σ_{obs} can be calculated by adding the jet energies as additional integration variables and interpreting $f_{acc;JES}$ as a function of jet energies:

$$\sigma_{obs}(m_{top}, JES) = \int d^n \sigma(x; m_{top}) d^4 E_{jq} f_{acc}(E_j; JES) \cdot W(E_j, E_p; JES) \quad (5.17)$$

E_j and E_p represent the four four-momenta for jet and parton states respectively, and $W(E_j, E_p; JES)$ denotes the jet transfer function. The kinematic selection requires significant missing transverse energy \cancel{E}_T , which during phasespace integration is approximated as

$$\begin{aligned} \cancel{E}_x^{ps} &= -\left(\sum_{i=1}^4 p_{x,jet}^i + p_{x,lep}\right) \\ \cancel{E}_y^{ps} &= -\left(\sum_{i=1}^4 p_{y,jet}^i + p_{y,lep}\right) \\ \cancel{E}_T^{ps} &= \sqrt{\cancel{E}_x^{ps2} + \cancel{E}_y^{ps2}}. \end{aligned} \quad (5.18)$$

No integration over the muon q/p_T is needed, because the p_T^μ resolution is very good in the domain of the respective selection cut. The acceptance function f_{acc} yields

- 0, if any jet fails the kinematic jet cuts
- 0, if the (parton-level) lepton fails the kinematic lepton cuts
- 0, if \cancel{E}_T^{ps} fails the \cancel{E}_T cut
- 0, if $\Delta R(j, j') < 0.5$
- 0, if $\Delta R(j, \ell) < 0.5$ for any jet
- w , if the jet state passes all selection criteria.

The trigger weight w represents the probability of an event to pass the $D\emptyset$ trigger system. Its calculation is described in Section 4.7.

For a given value of the jet energy scale parameter JES , the normalization is calculated as a function of m_{top} , as shown in Figure 5.4 for e+jets and μ +jets events. the normalization changes significantly with the choice of the JES parameter, as the mapping between jet energies and parton phasespace depends on it. Hence, a two-dimensional parametrization is derived as follows: For each JES value, the normalization as a function of m_{top} is fitted with a 3^{rd} -order polynomial. A linear fit to each of the four parameters as a function of the JES parameter (see Figure 5.5) yields the two-dimensional parametrization functions for e+jets and μ +jets events, shown in Figure 5.6. The difference between e+jets and μ +jets arises from the different η_ℓ requirements ($|\eta_e| < 1.1$, and $|\eta_\mu| < 2.0$). The same procedure is applied to obtain the normalization for parton-level events, see Section 6.2.

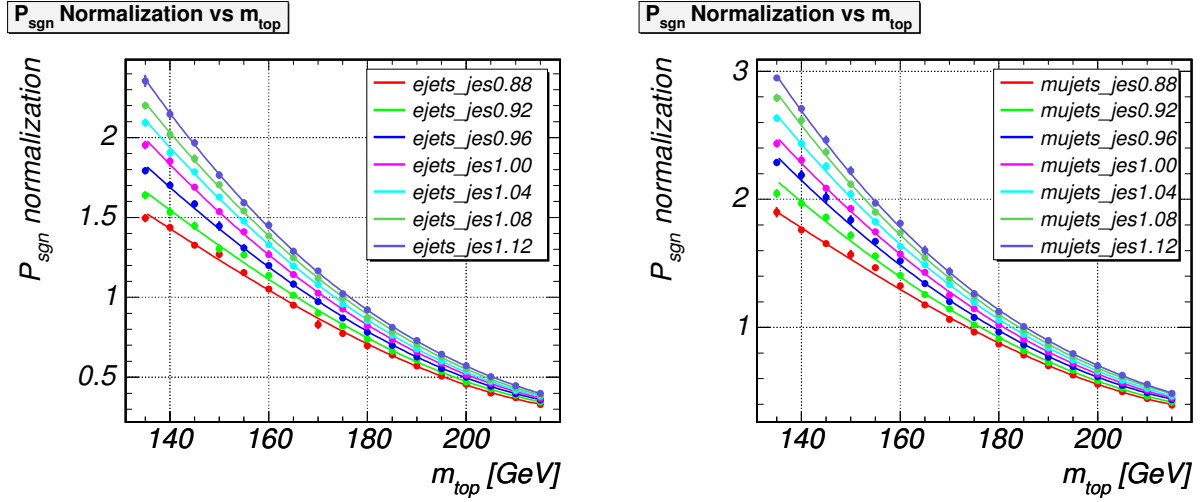


Figure 5.4: P_{sgn} normalization as a function of m_{top} for e+jets (left) and μ +jets (right) events, for various values of the JES parameter.

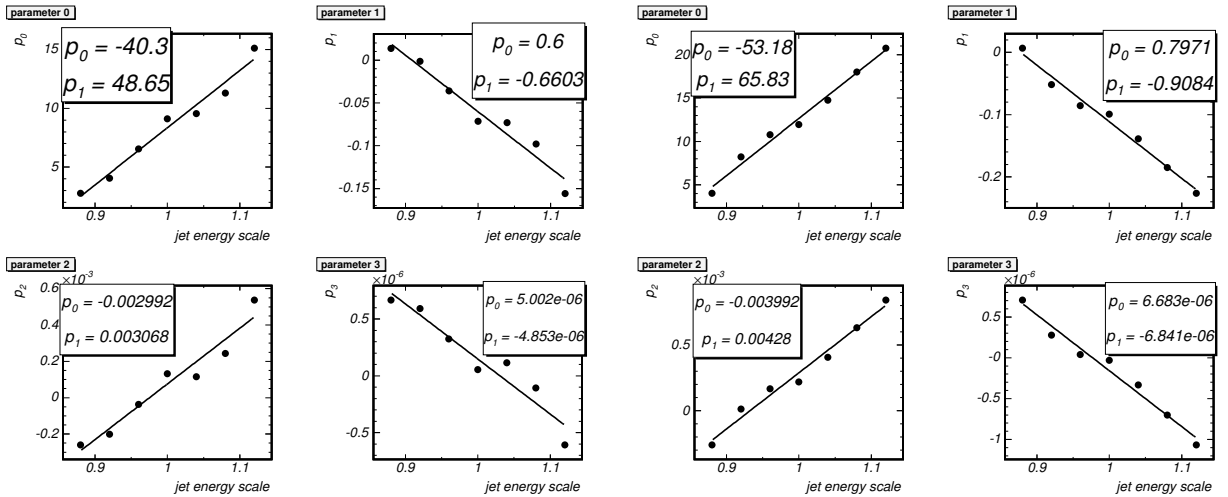


Figure 5.5: Linear fit as a function of JES to each parameter of the P_{sgn} normalizations in Figure 5.4, for e+jets (left) and μ +jets (right) events.

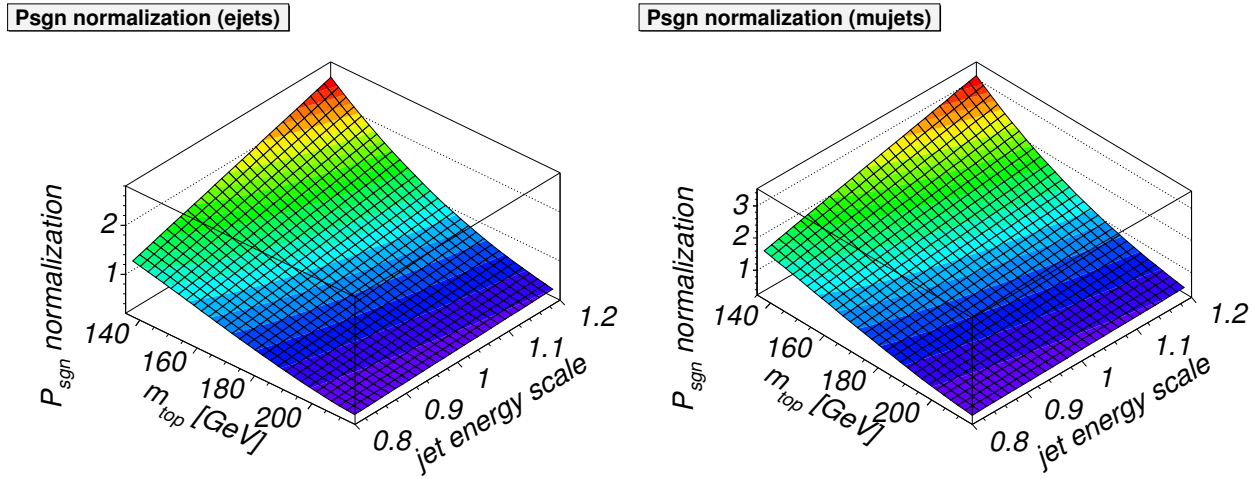


Figure 5.6: Parametrized two-dimensional P_{sgn} normalization functions for e+jets (left) and μ +jets (right) events.

5.3.3 Calculation of the Background Probability P_{bkg}

Generally, the background probability $P_{\text{bkg}} = P_{W+\text{jets}}$ can be calculated in a similar way as the signal probability P_{sgn} by replacing the $t\bar{t}$ matrix element $\mathcal{M}_{t\bar{t}}$ by a $W + \text{jets}$ matrix element $\mathcal{M}_{W+\text{jets}}$. Two important differences aggravate the computation however:

- Even in leading order, hundreds of Feynman graphs are needed to describe electroweak $W + \text{jets}$ production, leading to a significant increase in computing time per evaluation of the matrix element \mathcal{M} .
- Only the mass of the leptonic W is available as an integration variable with a well localized Breit-Wigner peak, which decreases the performance of the integration algorithm VEGAS.

The leading order $W + \text{jets}$ matrix element is calculated with the VECBOS [42] program. Attempts to use VEGAS for the integration of the VECBOS matrix element in 5 dimensions (see Section 5.3.1) yield processing times of several hours per event to achieve a precision of 20%.

Therefore, the background probability P_{bkg} is calculated as in the Run I measurement [4]. $\mathcal{M}_{\text{Vecbos}}$ is evaluated at N phase space points which are randomly chosen according to the transfer functions. P_{bkg} is estimated to be the mean of all evaluations. The stability of the result is tested by comparing the results after i and $i - 1$ iterations and up to 1000 evaluations are performed if indicated necessary. The minimum number of evaluations N_{min} is chosen to be 100, which is found to yield about 10% uncertainty.

The background probability P_{bkg} depends on the jet energies and thus on the value of the JES parameter. Tests however convinced us to calculate P_{bkg} only for $JES = 1$ and assign the result to P_{evt} for all JES values for two reasons:

- The calculation of P_{bkg} for several JES values leads to likelihood discontinuities, which degrade the quality of the mass fit. The precision of the P_{bkg} calculation is not good enough to resolve the subtle effect caused by varying the jet energy scale by a few percent on the event level.
- Looking at the combined background likelihood for 1000 events as a function of JES , the behavior turns out to be the same for signal and background events: higher JES values correspond to lower parton energies and thus higher P_{bkg} .

Sections 6.2 and 6.4 reveal that the mass fitting procedure shows great performance despite this simplification.

5.3.4 Normalization of the Background Probability P_{bkg}

To extract the top mass, the negative log likelihood defined in (5.8) is minimized with respect to m_{top} , JES and f_{top} . If the background probability P_{bkg} is normalized correctly, the fit yields an unbiased estimate of the signal fraction. Hence, the P_{bkg} normalization can be calibrated with Monte Carlo samples, requiring the signal fraction fit to yield the true signal fraction on average.

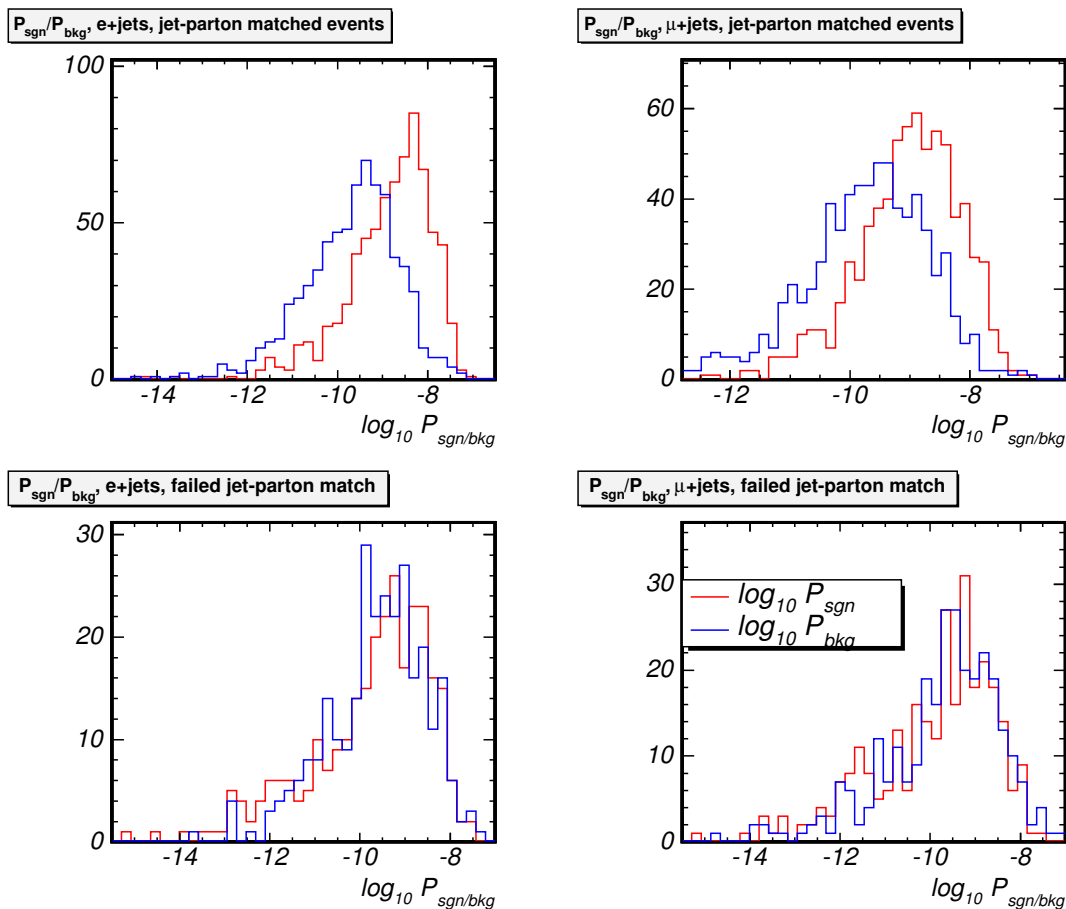


Figure 5.7: P_{sgn} and P_{bkg} for events which pass (above) and fail (below) the requirement of jets matched to partons. Left: e+jets events. Right: μ +jets events.

The P_{sgn} calculation uses a leading-order matrix element, see Section 5.3.1. 20 – 30 % of the signal events in the sample are expected to fail the *jet-parton match* requirement: at least one of the four reconstructed jets cannot be matched to a parton from the $t\bar{t}$ decay within $\delta R < 0.5$. These events yield poor mass information and degrade the error estimate of the likelihood fit. Their signal probability however is typically lower, enabling us to treat them as background events which do not contribute significant mass information to the likelihood. Figures 5.7 and 5.8 illustrate the key difference between both event classes: Jet-parton matched events tend to have a higher signal than background probability, which is how the mass fit identifies them as signal-like. There is no such separation between P_{sgn} and P_{bkg} for events failing the jet-parton match for at least one jet, both are on average equal. Therefore, only jet-parton matched events are used to calibrate the P_{bkg} normalization. Application to inclusive samples will consequently yield the fraction of jet-parton matched (leading-order) $t\bar{t}$ events as the result of the f_{top} fit on average, and only those will contribute m_{top} information to the likelihood.

The P_{bkg} normalization is determined by the following iterative procedure:

- For each channel and each top mass, all corresponding jet-parton matched $t\bar{t}$ and $W +$

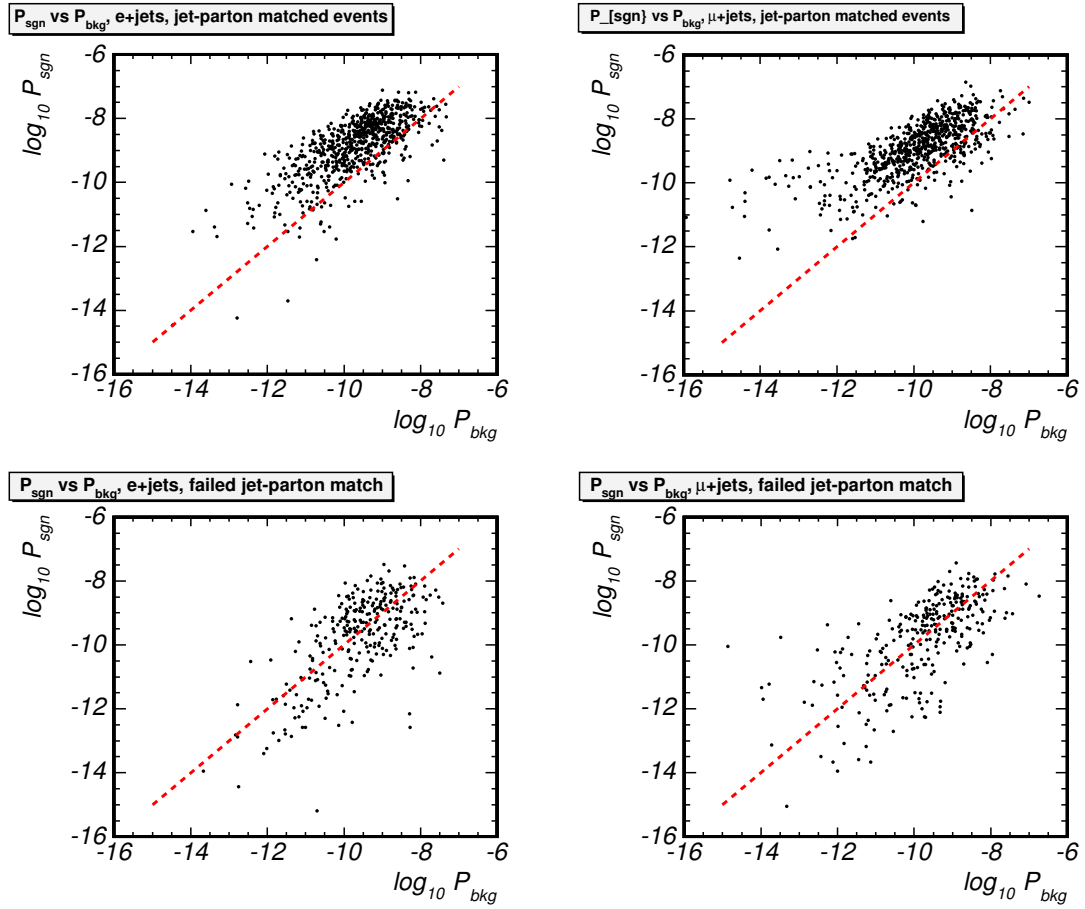


Figure 5.8: P_{sgn} vs P_{bkg} for events which pass (above) and fail (below) the requirement of jets matched to partons. Left: e+jets events. Right: μ +jets events. The dashed line indicates $P_{\text{sgn}} = P_{\text{bkg}}$.

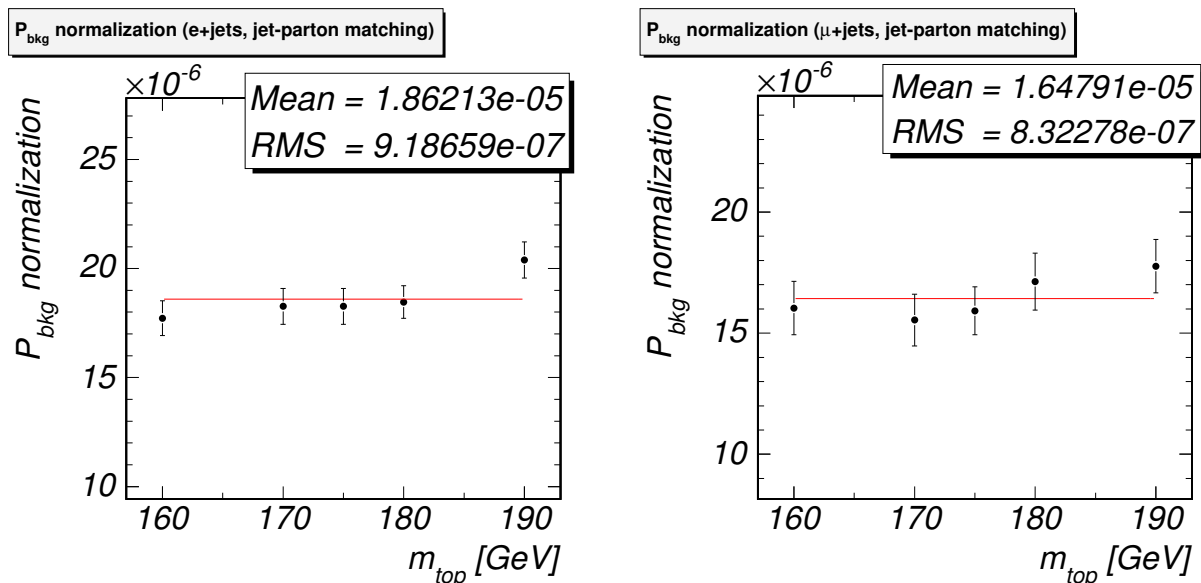


Figure 5.9: P_{bkg} normalization for e+jets and μ +jets events.

jets Monte Carlo events are used to compose one large ensemble. Events are removed from the sample until the true signal fraction represents the expectation in data (see Section 6.3).

- The likelihood fit procedure is applied to the sample and the normalization of P_{bkg} is adjusted after each fit, until the estimate $f_{\text{top}}^{\text{fit}}$ yields the true signal fraction $f_{\text{top}}^{\text{true}}$:

$$\left| f_{\text{top}}^{\text{fit}} - f_{\text{top}}^{\text{true}} \right| < 0.005 \quad .$$
- The normalization of P_{bkg} cannot depend on the top quark mass of the $t\bar{t}$ sample. Therefore, the above steps are applied to each available $t\bar{t}$ Monte Carlo sample. The mean of all results is taken as the P_{bkg} normalization.

Figure 5.9 shows the results for e+jets and μ +jets events. The same procedure is applied to parton-level events and used in Section 6.2.

5.4 Likelihood Evaluation

To obtain a measurement of the top mass m_{top} , the jet energy scale JES , and the $t\bar{t}$ fraction f_{top} from any candidate sample of events in data or Monte Carlo, the signal and background probabilities for each event are computed. Only one P_{bkg} is computed per event, while P_{sgn} is calculated for various values of m_{top} in steps of 2.5 GeV and various values of JES in steps of 0.02. In Monte Carlo samples, the parameter ranges are adjusted according to the true top quark mass and true jet energy scale. Both P_{sgn} and P_{bkg} are normalized according to the flavor of the isolated lepton in the event as described in Sections 5.3.2 and 5.3.4. For given values of JES and m_{top} , each event probability $P_{\text{evt}} = f_{\text{top}}P_{\text{sgn}} + (1 - f_{\text{top}})P_{\text{bkg}}$ depends on the signal fraction f_{top} , and consequently, the value of $-\ln L$ for the whole event sample as given in Equation (5.8) is a function of f_{top} . For each (JES, m_{top}) parameter pair, the value of $-\ln L$ is therefore calculated for 250 equidistant f_{top} parameter values between 0 and 1, and the minimum $-\ln L$ value is considered as the result for this parameter pair. The overall result quoted for the fitted signal fraction f_{top} is the value obtained at the (JES, m_{top}) point in the grid with the minimum $-\ln L$ value for the event sample. The error on f_{top} is computed by varying f_{top} at fixed JES and m_{top} until $\Delta(-\ln L) = +\frac{1}{2}$. This error does not account for the correlation with JES and m_{top} .

The resulting two-dimensional grid of $-\ln L$ values is subsequently fitted with the following functional form:

$$f(JES, m_{\text{top}}) = a_0 + a_1 \cdot JES + a_2 \cdot m_{\text{top}} + a_3 \cdot JES \cdot m_{\text{top}} + a_4 \cdot JES^2 + a_5 \cdot m_{\text{top}}^2 . \quad (5.19)$$

The measurements of m_{top} and JES and the corresponding uncertainties are obtained by projecting the fit result to the respective parameter axis while preserving the correlation with the other parameter: the one-dimensional likelihood projection as a function of m_{top} is computed by evaluation of $f(JES, m_{\text{top}})$ under the constraint that

$$\frac{\partial f}{\partial JES} = 0 ; \quad (5.20)$$

analogously, the one-dimensional likelihood projection as a function of JES is computed by evaluation of $f(JES, m_{\text{top}})$ under the constraint that

$$\frac{\partial f}{\partial m_{\text{top}}} = 0 . \quad (5.21)$$

The minimum of each of these resulting 2^{nd} -order polynomials is interpreted as the measurement of the respective parameter, the respective statistical error is retrieved by considering the parameter value that yields $\Delta(-\ln L) = +\frac{1}{2}$ relative to the minimum. Hence, the errors account for the correlation between both parameters of the likelihood, and the error obtained for m_{top} is quoted as (stat.+JES). Figure 5.10 illustrates the procedure. The projections of the two-dimensional likelihood fit to both parameters are shown in the upper right (m_{top}) and lower left (JES) plots. The $-\ln L$ values which are shown as points in these plots correspond to the best likelihood value for the respective parameter value. Note that the other parameter is restricted to be in the grid of computed parameters. The dots are therefore not to be interpreted as the fitted points, but merely included to guide the eye.

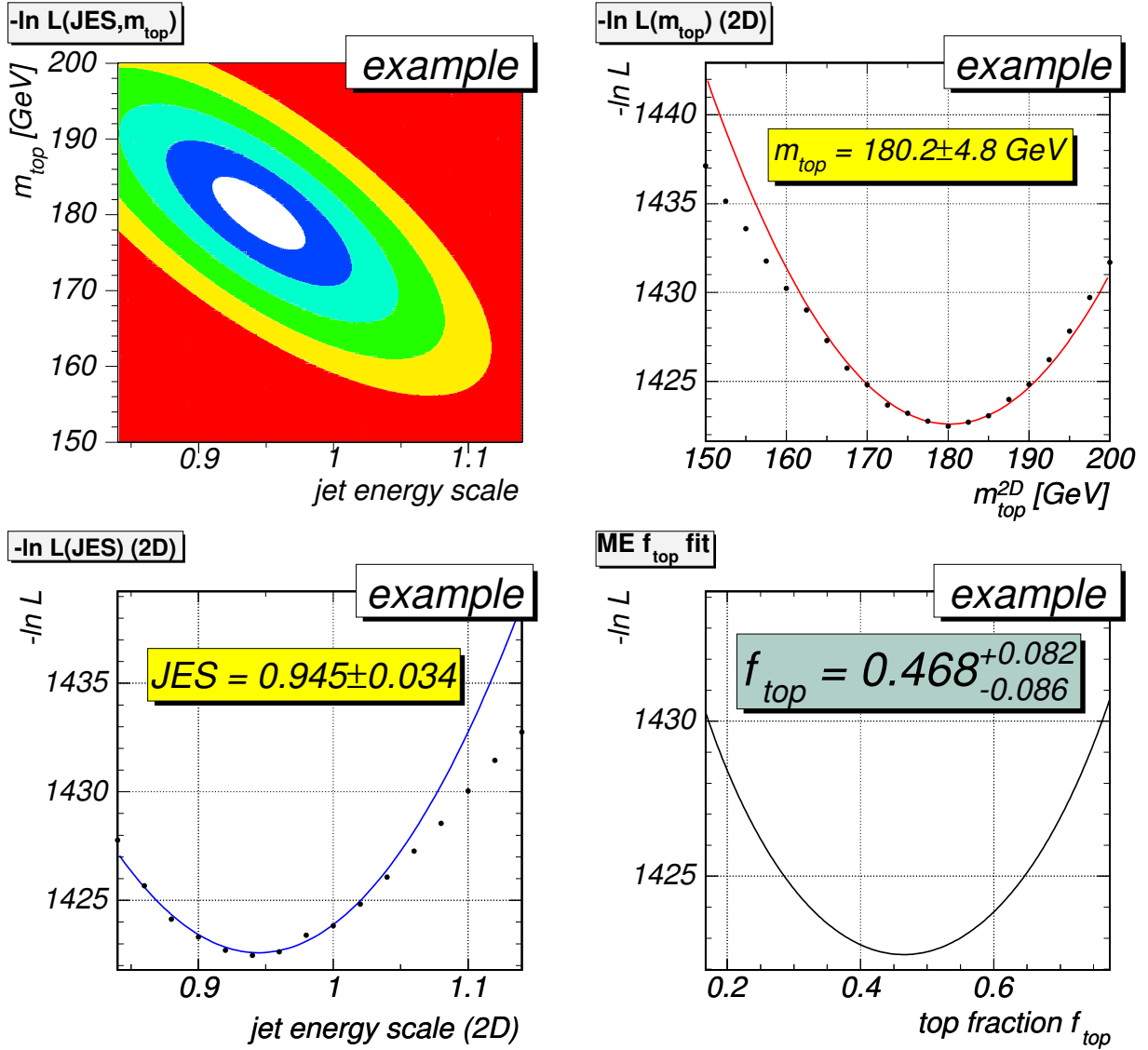


Figure 5.10: Example of the determination of m_{top} , JES , and f_{top} from an event sample with the matrix element likelihood. The sample contains 70 $e+\text{jets}$ Monte Carlo events, where 31 of them are $t\bar{t}$ events ($m_{\text{top}} = 175 \text{ GeV}$). A $-\ln L$ grid is computed for various values of the m_{top} and JES parameters, where at each grid point the result is minimized with respect to the $t\bar{t}$ fraction f_{top} . The two-dimensional fit to the grid is shown in the upper left plot. The colored regions correspond to the $n\sigma$ contours, $n = 1, \dots, 5$. The projections of this fit to the m_{top} and JES parameters are shown in the upper right and lower left plots and are used to calculate the central measured values of both parameters, along with the corresponding uncertainties. The points shown in these plots represent the minimum $-\ln L$ value for the respective parameter value. The fit of the $t\bar{t}$ signal fraction is obtained at the point in the $(\text{JES}, m_{\text{top}})$ grid with the minimum $-\ln L$ value, and the respective likelihood function at this grid point is shown as a function of f_{top} in the lower right plot.

Chapter 6

Measurement of the Top Quark Mass

Before the matrix element method is applied to the selected data sample, the fit procedure is validated by undergoing a number of tests. Ideally, the likelihood fit yields bias-free m_{top} and JES estimates and trustworthy statistical errors. Any deviations from this behavior need to be understood and quantified to calibrate the final result extracted from data events. The tests are carried out by applying the mass fit to a large number of pseudo experiments (ensembles) built from Monte Carlo event pools. A statistical evaluation of the results yields bias and pull, as well as an estimate of the expected statistical uncertainty.

6.1 Ensemble Testing Procedure

The calculation of event probabilities for a large number of Monte Carlo events is very CPU intensive. The computation of the signal probability for one m_{top}/JES parameter pair and 1000 events takes 5 – 15 hours on one Pentium IV 2.5 GHz CPU, which needs 15 – 30 hours to calculate the background probability for 40 events. The numbers of available signal and background Monte Carlo events which pass the event selection are limited as well. Therefore, ensembles are built such that events are not removed from the pool of available events once they are drawn. Each event must be allowed to appear in multiple ensembles, and even multiple times in the same ensemble [43, 44]. No further information on the bias is achieved by increasing the number of ensembles according to this procedure. However, the precision on the estimated error, and therefore the knowledge of the pull width increases significantly [43, 44].

In the studies presented in the following sections, ensemble tests typically consist of 1000 ensembles, drawn from signal and background event pools of 2000 – 4000 events each. Each ensemble is composed according to the measured composition of the DØ Run II ℓ +jets data sample (150 total events, 55 $t\bar{t}$ events in the ℓ +jets channel, see Section 6.3). The number of ensembles is sufficiently higher than the maximum number of independent ensembles (ensembles drawn such that each event can only appear once in all ensembles). Therefore, no biases are expected from some events being used significantly more often than others.

In the case of fully reconstructed Monte Carlo events (Section 6.4), each event is weighted according to its probability to pass the DØ trigger system. This probability is calculated as described in Section 4.7 and taken into account in the ensemble composition.

6.2 Validation of the Fit Procedure: Parton-Level Tests

The studies presented in this section are based on *parton-level events*:

- They are generated with leading-order event generators, no initial or final state radiation is applied. MADGRAPH [45] is used to generate $t\bar{t}$ signal events, $W + \text{jets}$ events are generated with ALPGEN [46].
- They are not processed with any detector simulation. The jet and lepton energies are smeared according to the transfer functions obtained from Monte Carlo with detector simulation (see Section 5.2); the direction of the parton remains unchanged.

The kinematics of these parton-level events correspond well to the leading order matrix element used in the likelihood fit. The resolutions represent the real $D\emptyset$ detector well and, in contrast to the full simulation, are described precisely by the transfer function. Each “jet” (smeared parton) corresponds to a tree-level parton from the $t\bar{t}$ decay, whereas in fully reconstructed events, some jets arise from other physics or detector effects such as radiation or calorimeter noise.

Using only signal events without applying any kinematic selection and fixing JES to 1.0 serves as a first cross-check, which addresses the impact of the muon transfer function as well. 1000 events for top masses of 150, 160, 170, 175, 180, 190, and 200 GeV are used. 25 events are drawn in each ensemble, and P_{bkg} is not considered in the fit. A dedicated P_{sgn} normalization without any kinematic cuts is applied. Three different scenarios are considered:

- *Only partons are smeared, the muon momentum integration is not carried out.* Mass and pull calibrations are shown in Figure 6.1. The pull is in good agreement with 1.0. The small mass bias is attributed to the fact that no kinematic cuts are assumed, whereas the parton event generator applies a modest selection.
- *Partons and lepton are smeared, the muon momentum integration is not carried out.* Mass and pull calibrations are shown in Figure 6.2. The pull of 1.16 deviates significantly from 1.0, corresponding to a 16% underestimated statistical error. The mass bias is increased.
- *Partons and lepton are smeared, the muon momentum integration is carried out.* The lepton resolution is taken into account in an additional integration over inverse lepton p_T [37]. The calibration curves are shown in Figure 6.3. The pull is in good agreement with 1.0 again. The bias is reduced to the observation in events without lepton smearing.

We conclude: the likelihood fit significantly underestimates the statistical m_{top} error if any sizable object resolutions are neglected.

To evaluate the full capabilities of the two-dimensional likelihood fitting procedure, ensembles are composed with 75 events, 40% of them $t\bar{t}$ signal events. 1000 events for top masses of 160, 170, 175, 180, and 190 GeV each are used, and 1000 $W + \text{jets}$ events. In addition, samples with $m_{\text{top}} = 175$ GeV with all jet energies scaled by 0.95 and 1.05 are prepared in order to validate the JES fit result. Only the partons are smeared according to the jet transfer functions, and the integration over inverse lepton p_T is not carried out. All events are required to pass the following kinematic selection criteria:

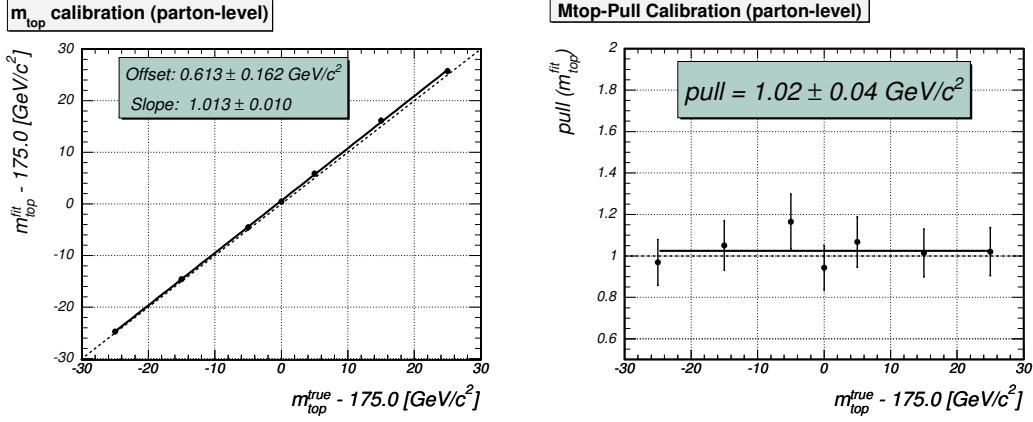


Figure 6.1: m_{top} and m_{top} -pull calibration curves for parton-level events without kinematic selection and $JES = 1$. Only partons are smeared according to transfer functions, and the additional integration over inverse lepton p_T is not carried out.

- jet $p_T > 20$ GeV, jet $|\eta| < 2.5$
- lepton $p_T > 20$ GeV, lepton $|\eta| < 2$
- $\cancel{E}_T > 20$ GeV (where \cancel{E}_T is calculated as in Equations 5.18)
- $\Delta R(j, j') > 0.5$
- $\Delta R(\ell, j) > 0.5$

The signal normalization is obtained according to this selection, see Section 5.3.2. m_{top} and JES are obtained for each ensemble as described in Section 5.4.

Figure 6.4 shows the m_{top} and JES as well as the corresponding pull distributions for a generated value of $m_{\text{top}} = 175$ GeV. Figure 6.5 shows the performance of the f_{top} fit, which correctly yields the true signal fraction on average. The results for different top masses are summarized in Figure 6.6. The results for both m_{top} and JES fits are unbiased and the pulls are in good agreement with 1.0. Figure 6.7 shows the same convincing performance of the fit procedure for various jet energy scales.

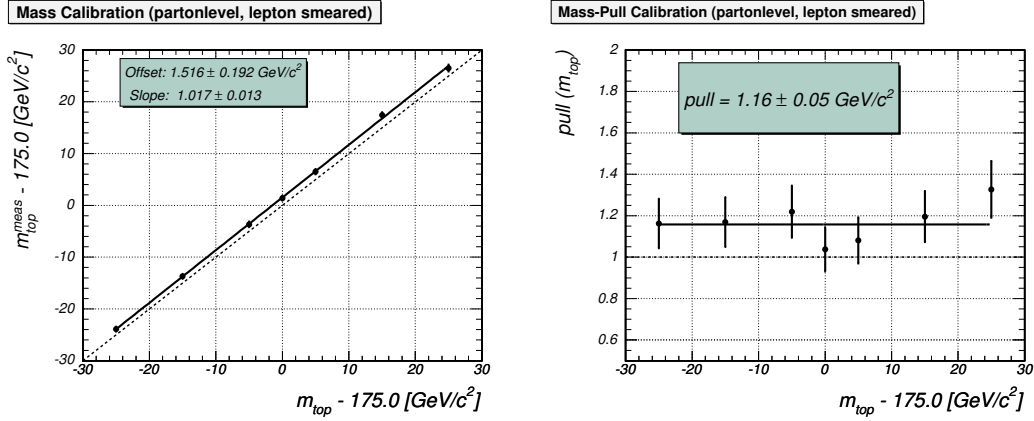


Figure 6.2: m_{top} and m_{top} -pull calibration curves for parton-level events without kinematic selection and $JES = 1$. Partons and lepton are smeared according to transfer functions, and the additional integration over inverse lepton p_T is not carried out.

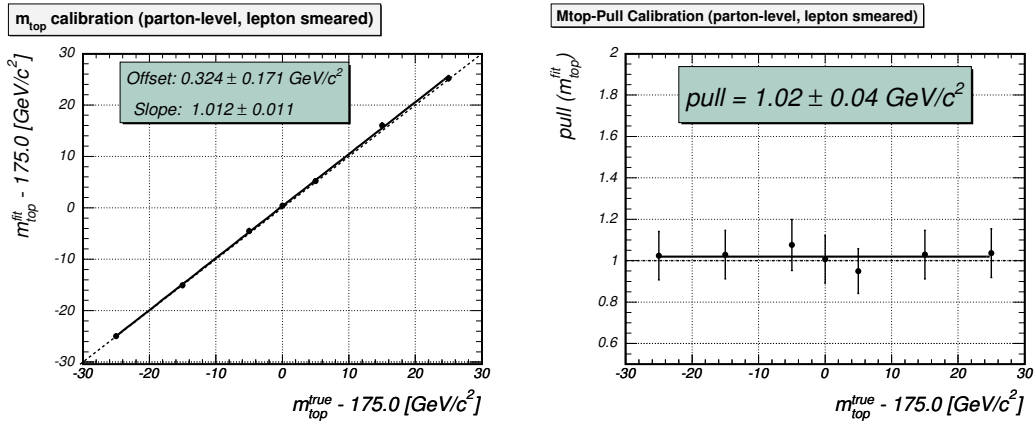
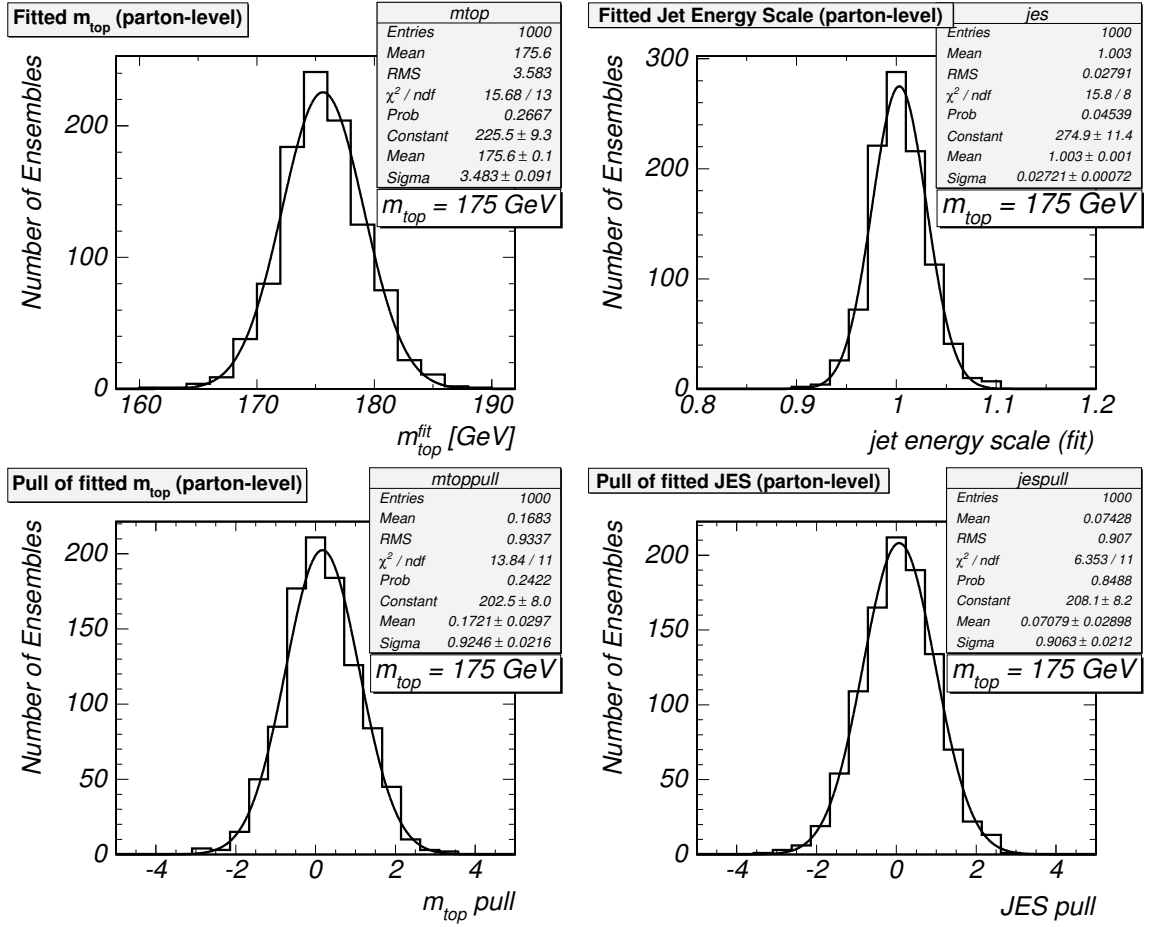
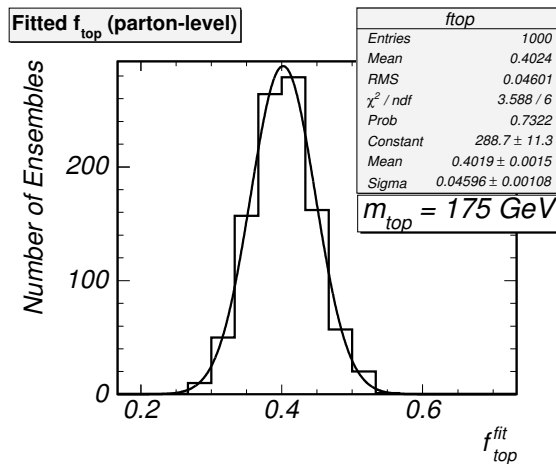


Figure 6.3: m_{top} and m_{top} -pull calibration curves for parton-level events without kinematic selection and $JES = 1$. Partons and lepton are smeared according to transfer functions, and the additional integration over inverse lepton p_T is carried out.

Figure 6.4: Parton-level ensemble test results for $m_{\text{top}} = 175 \text{ GeV}$.Figure 6.5: Distribution of fitted f_{top} in parton-level ensemble tests.

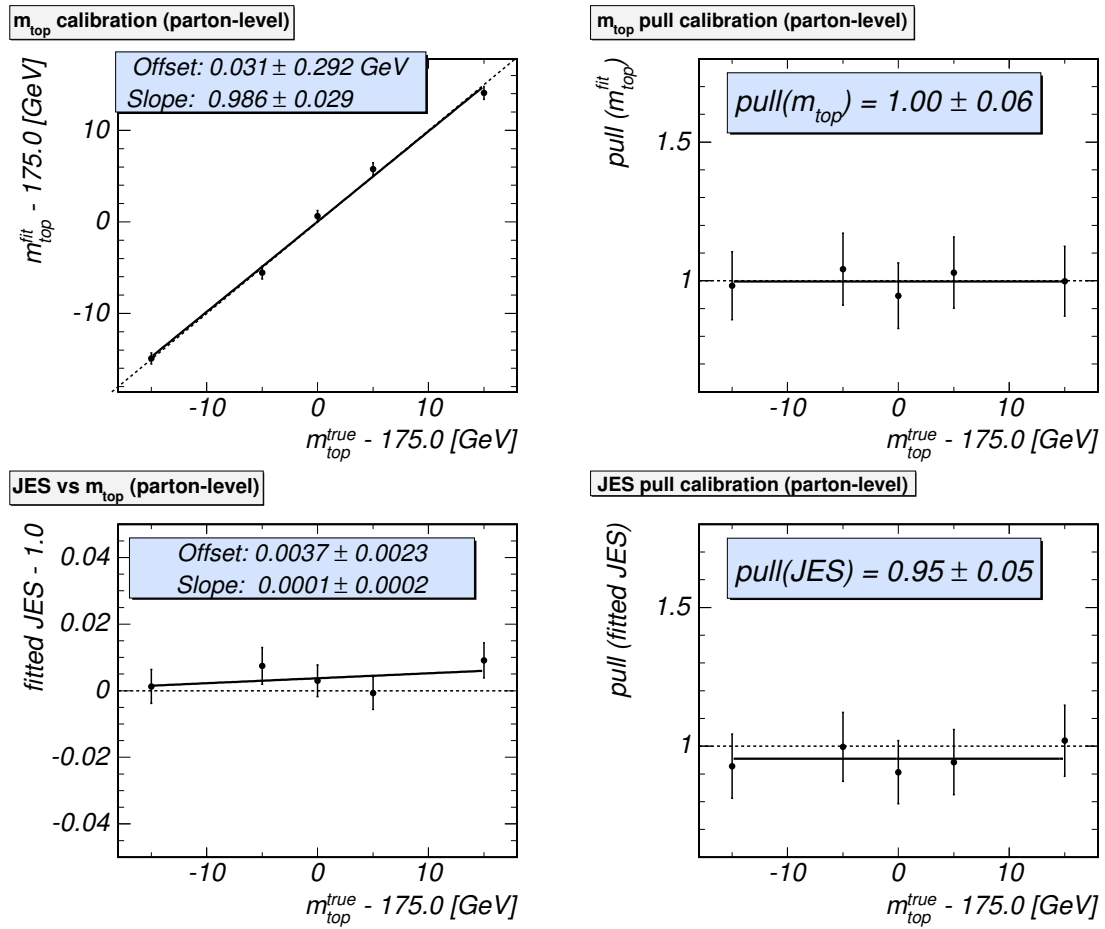


Figure 6.6: Parton-level ensemble test results for various top masses.

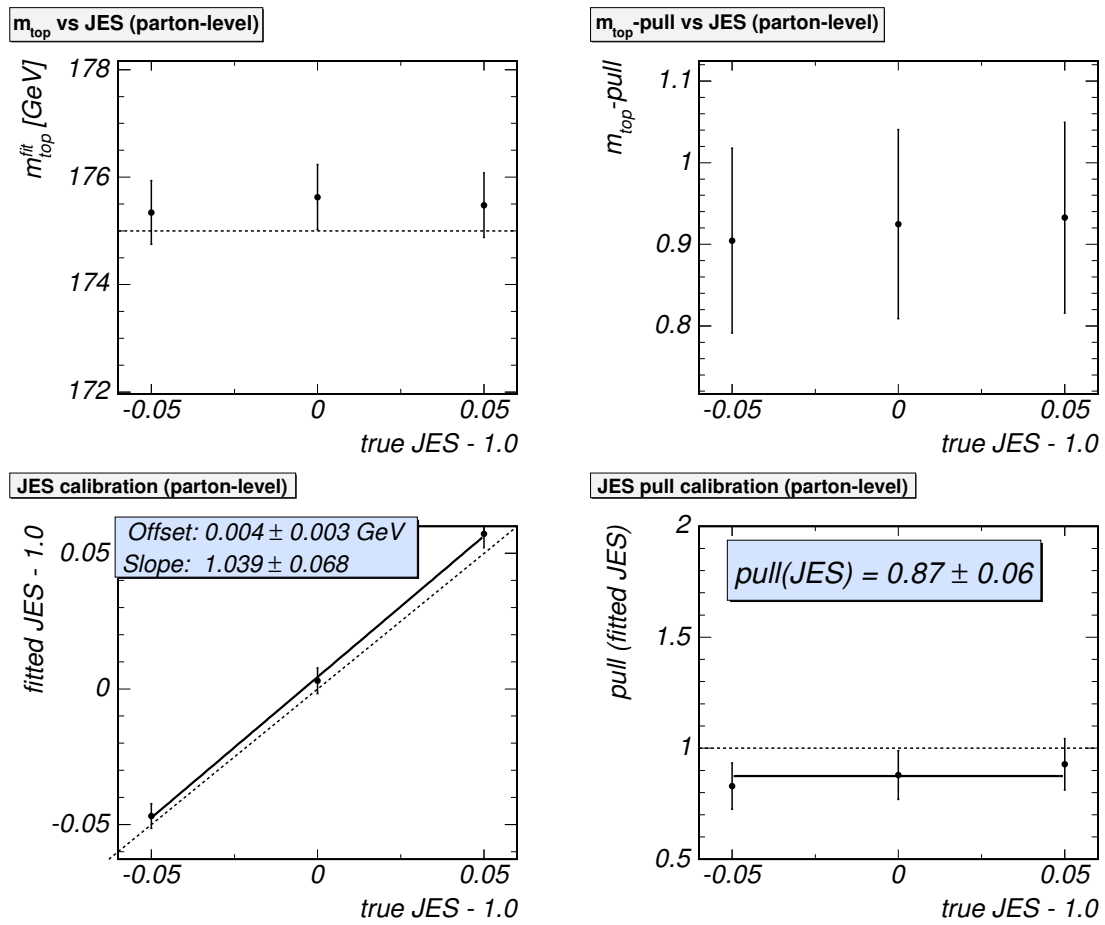


Figure 6.7: Parton-level ensemble test results for three different jet energy scales.

6.3 Measurement of the Sample Composition

Before the final calibration curves are derived from Monte Carlo events which have been run through a full simulation of the DØ detector, the composition of the data sample is determined. The motivation for this measurement is twofold:

1. To compose the ensembles for the calibration procedure to the best of our knowledge.
2. To derive an additional offset correction which arises from the dependence of the fitted mass on the signal fraction. The uncertainty of the signal fraction measurement yields the systematic uncertainty on that calibration.
3. To obtain the normalization of the background probability P_{bkg} such that it is optimal for the expected signal fraction, see Section 5.3.4.

Note though that no assumption on the top fraction f_{top} in the data sample is made, since for each assumed value of the top mass both m_{top} and f_{top} in (5.1) are fitted simultaneously.

The signal fraction in both the e+jets and μ +jets data samples is measured with a topological likelihood method developed at DØ to measure the cross-section in $t\bar{t}$ lepton+jets events. A description of the method can be found in [47] and [48]. This section provides a brief overview of the topological variables used, a description of how the likelihood is constructed and the measurement of the composition of the data sample.

6.3.1 Determination of QCD Contamination: Matrix Method

Apart from W +jets the selected data sample is expected to contain instrumental background from multijet events (“QCD”). The QCD fraction is expected to be small and only the W +jets process is modeled in the event probability (5.1). To study the effect of the presence of QCD events on the mass measurement, the fraction in the data sample is estimated. The procedure is called *Matrix Method* [49] (not to be confused with the Matrix Element Method!) and relies on the definition of a loose and a tight sample, as explained in Section 4.8. The tight sample is the selected data set (N_t events) and is a subset of the loose sample (N_l events), which contains events which pass all selection criteria but one: the EM-likelihood cut for e+jets events, and the isolation cut for μ +jets events. The numbers of loose and tight events in the data sample are given in Table 4.8. If ϵ_{sig} denotes the efficiency for a real lepton and ϵ_{QCD} for non-isolated muons/fake electrons to pass the isolation cut, N_l and N_t are given by

$$\begin{aligned} N_l &= N_l^{W+t\bar{t}} + N_l^{\text{QCD}} \\ N_t &= \epsilon_{\text{sig}} N_l^{W+t\bar{t}} + \epsilon_{\text{QCD}} N_l^{\text{QCD}}. \end{aligned} \quad (6.1)$$

For the e+jets channel, ϵ_{sig} and ϵ_{QCD} are measured [47] to be

$$\epsilon_{\text{sig}}^{e+\text{jets}} = 0.817 \pm 0.011 \quad (6.2)$$

$$\epsilon_{\text{QCD}}^{e+\text{jets}} = 0.160 \pm 0.040. \quad (6.3)$$

For the μ +jets channel, ϵ_{sig} and ϵ_{QCD} are measured [48] to be

$$\epsilon_{\text{sig}}^{\mu+\text{jets}} = 0.810_{-0.017}^{+0.021} \quad (6.4)$$

$$\epsilon_{\text{QCD}}^{\mu+\text{jets}} = 0.085_{-0.030}^{+0.034}. \quad (6.5)$$

Given ϵ_{sig} and ϵ_{QCD} , the number of QCD events N_t^{QCD} can be calculated from (6.1). In the following section, the number of $t\bar{t}$, $W + \text{jets}$ and QCD events is fitted simultaneously, and a Poissonian constraint is applied to N_t^{QCD} during the fit.

6.3.2 Topological Likelihood Fit

The method described in this section has been developed and applied to measure the $t\bar{t}$ cross-section at DØ [47, 48]. Since the cross-section event selection accepts events with four or more jets, whereas this analysis is restricted to events with exactly four jets, the likelihood discriminant and the sample composition are rederived.

A total of six event shape variables, each of which shows decent discrimination power between $t\bar{t}$ and $W + \text{jets}$ events, are used to form a topological likelihood. These variables are [47, 48]:

- Centrality \mathcal{C} : H_T/H , the scalar sum of transverse energies divided by the scalar sum of energies of the four leading jets
- Aplanarity \mathcal{A} : The normalized momentum tensor \mathcal{M} is defined as

$$\mathcal{M}_{jk} = \frac{\sum_i p_j^i p_k^i}{\sum_i |\vec{p}^i|^2}, \quad (6.6)$$

where \vec{p}^i is the momentum vector of a reconstructed object, j and k are Cartesian coordinates. By standard diagonalization of \mathcal{M}_{jk} one may find three eigenvalues $\lambda_1 \geq \lambda_2 \geq \lambda_3$, with $\lambda_1 + \lambda_2 + \lambda_3 = 1$. The aplanarity is defined as $\mathcal{A} = \frac{3}{2}\lambda_3$, and represents a measure of the flatness of the event.

- $\Delta\phi(\ell, \cancel{E}_T)$: the azimuthal opening angle between the lepton and the missing transverse energy.
- Sphericity \mathcal{S} : defined as

$$\mathcal{S} = \frac{3}{2}(\lambda_2 + \lambda_3), \quad (6.7)$$

where λ_2 and λ_3 are eigenvalues of the normalized momentum tensor \mathcal{M} (Equation (6.6)).

- H_T : the scalar sum of the p_T of the four leading jets.
- $K'_{T,\text{min}}$: defined as

$$K'_{T,\text{min}} = \Delta R^{\text{min}} E_T^{\text{min}} / E_T^W, \quad (6.8)$$

where ΔR^{min} corresponds to the minimum separation in η - ϕ between any pair of jets, E_T^{min} is the minimum E_T of those two jets, and $E_T^W = E_T^\ell + \cancel{E}_T$.

The discrimination power of these variables is typically based on one or both of the following two assumptions:

- The top quark mass is large (≈ 178 GeV), and the decay products are very energetic in comparison to additional jets produced in association with a W boson, which originate from QCD bremsstrahlung.

- $t\bar{t}$ pairs are mainly produced at rest just above the kinematic threshold in $p\bar{p}$ collisions at $\sqrt{s} = 1.96$ TeV, resulting in isotropic and central distribution of the decay products. Additional jet production in association with a W boson on the other hand peaks in the forward direction, as it originates from QCD bremsstrahlung.

The QCD background is expected to be small and of similar topology as the $W + \text{jets}$ background and is therefore not treated separately. The probability density functions for signal (S_i) and background (B_i) of these variables (x_i) are determined by histogramming the respective quantities for $t\bar{t}$ and $W + \text{jets}$ Monte Carlo samples and normalizing each to unity. The likelihood function is then approximated, assuming no correlations between the input variables, and parametrized as a function of the probability ratios $\frac{\mathcal{P}_{\text{signal}}}{\mathcal{P}_{\text{backgr.}}} = \frac{\mathcal{P}_{t\bar{t}}}{\mathcal{P}_{W+\text{jets}}}$:

$$\mathcal{L} = \frac{S(x_1, \dots, x_6)}{S(x_1, \dots, x_6) + B(x_1, \dots, x_6)} \approx \frac{\prod_i S_i}{\prod_i S_i + \prod_i B_i} = \frac{\exp(\sum_i (\ln \frac{S_i}{B_i}))}{\exp(\sum_i (\ln \frac{S_i}{B_i})) + 1}. \quad (6.9)$$

For the likelihood to be less sensitive to statistical fluctuations of any of the inputs, the distributions are transformed and the logarithms of the ratios $(\ln \frac{S_i}{B_i})$ are parameterized with functional fits. The transformed variables are

- $\ln(\mathcal{C})$
- $\exp(-11 \cdot \mathcal{A})$
- $\Delta\phi(\ell, \cancel{E}_T)$
- $\ln(\mathcal{S})$
- $\ln(H_T)$
- $\ln(K'_{T,\text{min}})$

The fits to the ratios are shown in Figures 6.8-6.13.

The likelihood discriminant (6.9) is calculated for the $t\bar{t}$, $W + \text{jets}$ and QCD sample for events which pass the selection of this analysis. The distributions of the likelihood discriminant are shown in Figure 6.14.

The composition of the $e+\text{jets}$ and $\mu+\text{jets}$ data samples is determined in a linear fit of the templates in Figure 6.14 to the data distribution of the discriminant. The relative fractions of $W + \text{jets}$ and QCD background however are already determined by the Matrix Method in Section 6.3.1 and are therefore constrained during the fit. The result of the fit is shown in Figure 6.15. It yields the following compositions of the $e+\text{jets}$ and $\mu+\text{jets}$ samples:

$$\begin{aligned} n_{t\bar{t}}^{e+\text{jets}} &= 31.4^{+8.6}_{-8.3} & f_{t\bar{t}}^{e+\text{jets}} &= 44.9^{+12.3}_{-11.9} \% \\ n_{W+\text{jets}}^{e+\text{jets}} &= 25.7^{+9.0}_{-8.4} & f_{W+\text{jets}}^{e+\text{jets}} &= 36.7^{+12.8}_{-11.9} \% \\ n_{QCD}^{e+\text{jets}} &= 13.2^{+1.9}_{-1.7} & f_{QCD}^{e+\text{jets}} &= 18.4^{+2.7}_{-2.5} \% \\ n_{t\bar{t}}^{\mu+\text{jets}} &= 23.3^{+8.2}_{-7.7} & f_{t\bar{t}}^{\mu+\text{jets}} &= 29.1^{+10.3}_{-9.6} \% \\ n_{W+\text{jets}}^{\mu+\text{jets}} &= 53.0^{+9.2}_{-8.7} & f_{W+\text{jets}}^{\mu+\text{jets}} &= 66.4^{+11.4}_{-10.9} \% \\ n_{QCD}^{\mu+\text{jets}} &= 3.6^{+0.8}_{-0.6} & f_{QCD}^{\mu+\text{jets}} &= 4.5^{+0.9}_{-0.8} \% \end{aligned} \quad (6.10)$$

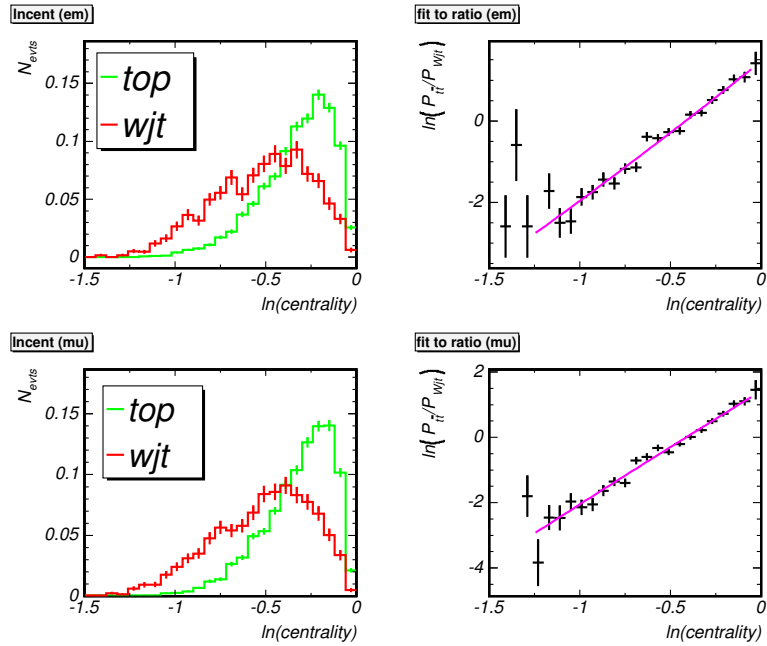


Figure 6.8: Centrality $\ln(\mathcal{C})$ for $t\bar{t}$ (“S”, green histogram) and $W + \text{jets}$ (“B”, red histogram) events, and the fit (magenta line) to the ratio $\ln \frac{S}{B}$ (black points with error bars) for e+jets and μ +jets.

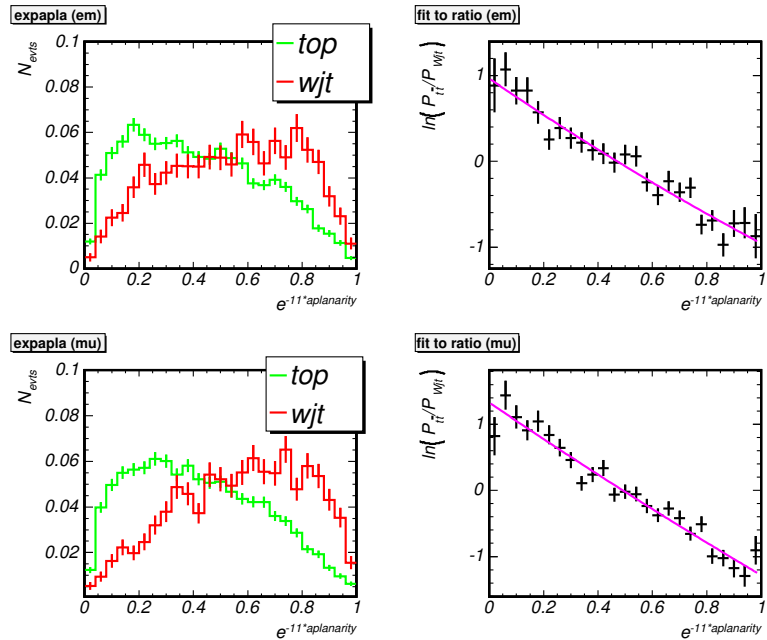


Figure 6.9: Aplanarity $\exp(-11 \cdot \mathcal{A})$ for $t\bar{t}$ (“S”, green histogram) and $W + \text{jets}$ (“B”, red histogram) events, and the fit (magenta line) to the ratio $\ln \frac{S}{B}$ (black points with error bars) for e+jets and μ +jets.

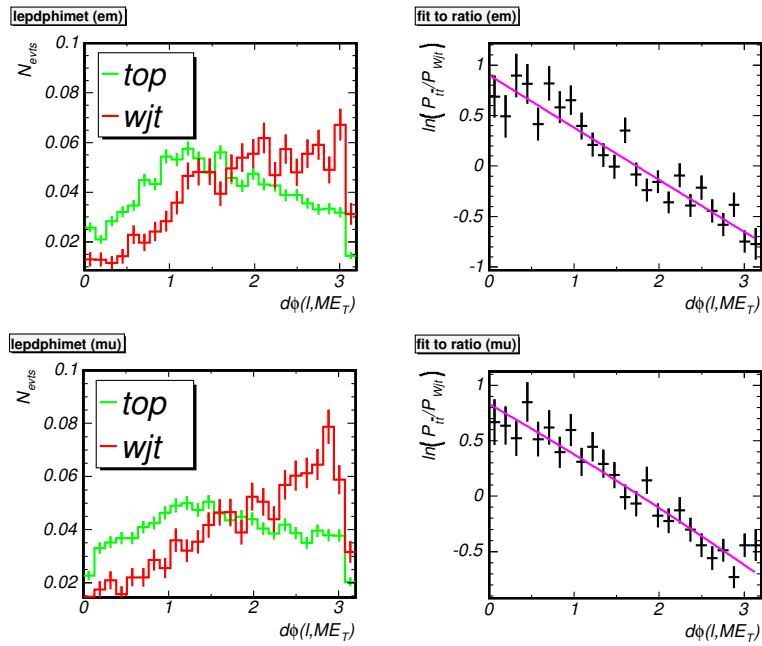


Figure 6.10: $\Delta\phi(\mu, \cancel{E}_T)$ for $t\bar{t}$ (“S”, green histogram) and $W + \text{jets}$ (“B”, red histogram) events, and the fit (magenta line) to the ratio $\ln\frac{S}{B}$ (black points with error bars) for e+jets and μ +jets.

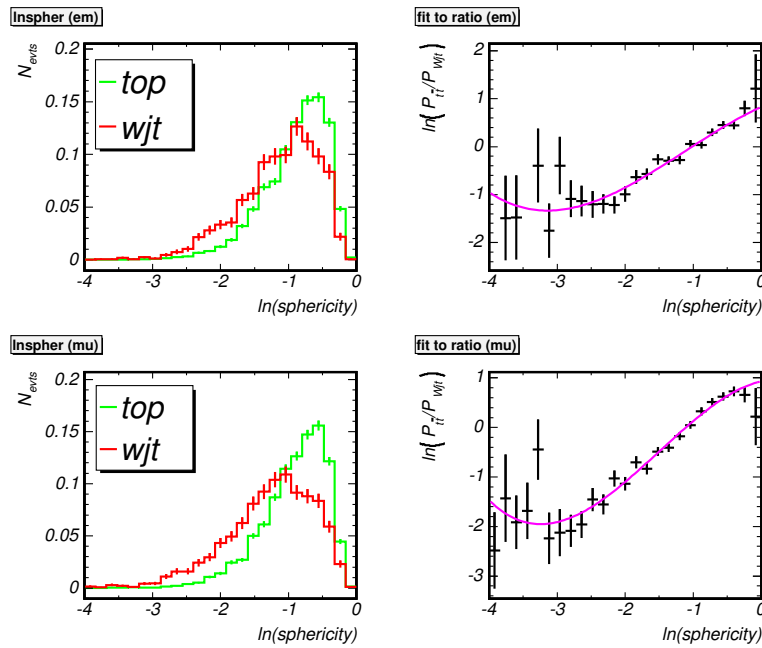


Figure 6.11: Sphericity $\ln(\mathcal{S})$ for $t\bar{t}$ (“S”, green histogram) and $W + \text{jets}$ (“B”, red histogram) events, and the fit (magenta line) to the ratio $\ln\frac{S}{B}$ (black points with error bars) for e+jets and μ +jets.

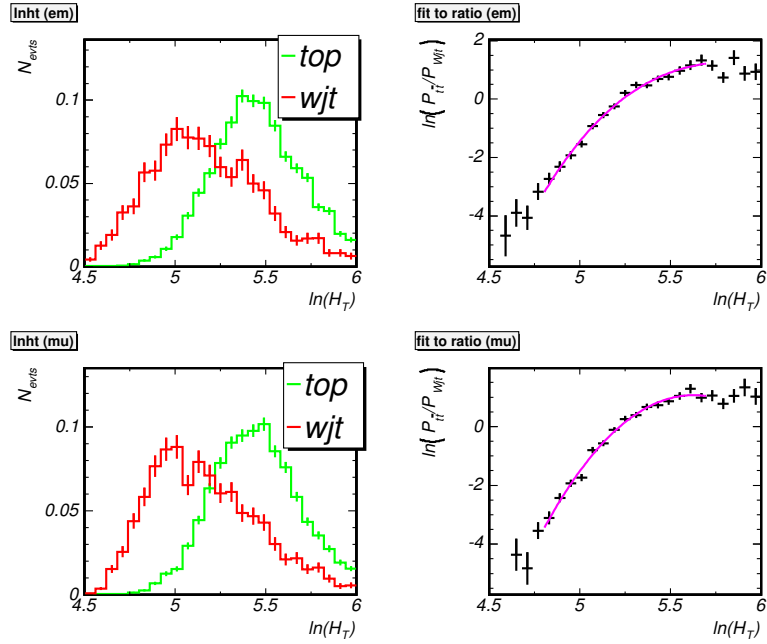


Figure 6.12: $\ln(H_T)$ for $t\bar{t}$ (“S”, green histogram) and W + jets (“B”, red histogram) events, and the fit (magenta line) to the ratio $\ln\frac{S}{B}$ (black points with error bars) for e+jets and μ +jets.

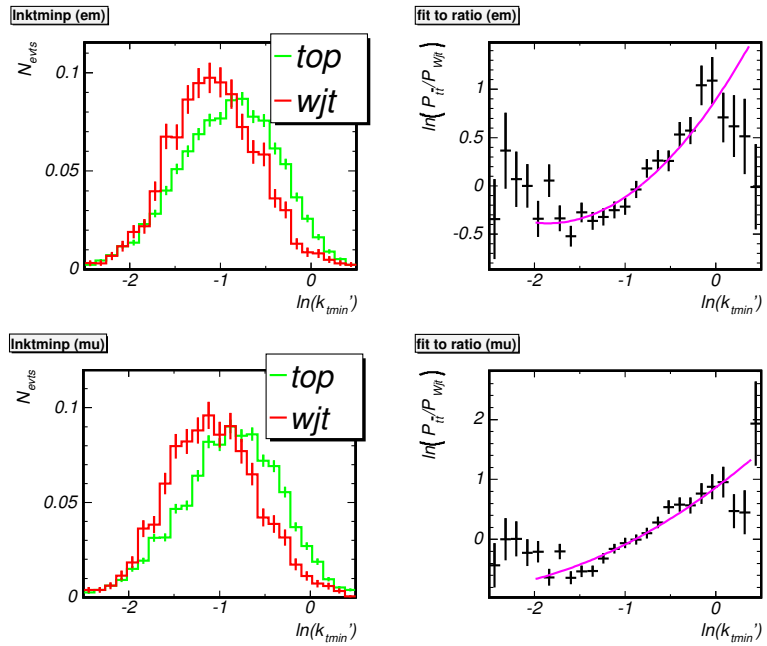
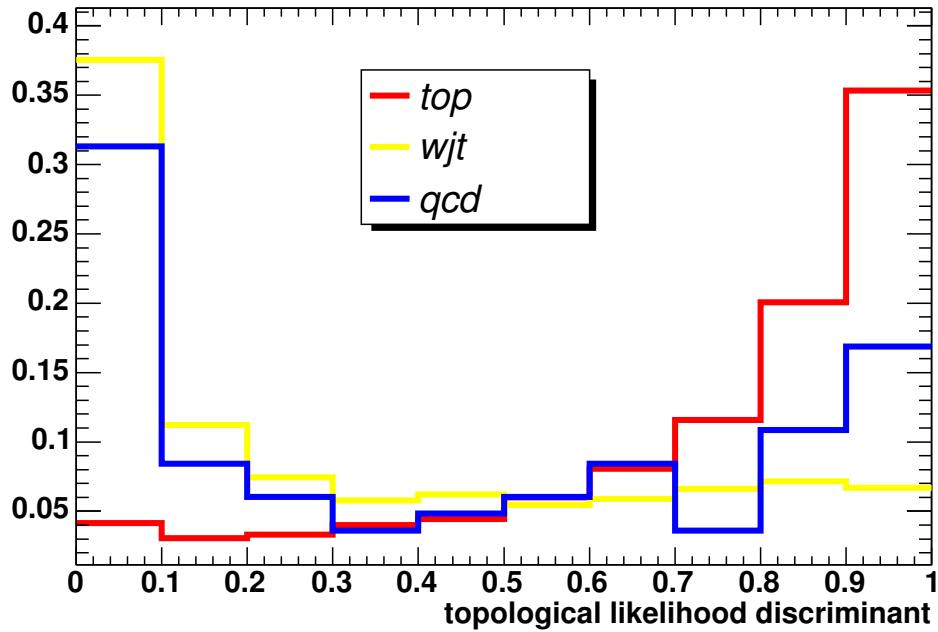


Figure 6.13: $\ln(K'_{T,\min})$ for $t\bar{t}$ (“S”, green histogram) and W + jets (“B”, red histogram) events, and the fit (magenta line) to the ratio $\ln\frac{S}{B}$ (black points with error bars) for e+jets and μ +jets.

Topo. Likelihood Templates (ejets)



Topo. Likelihood Templates (mujets)

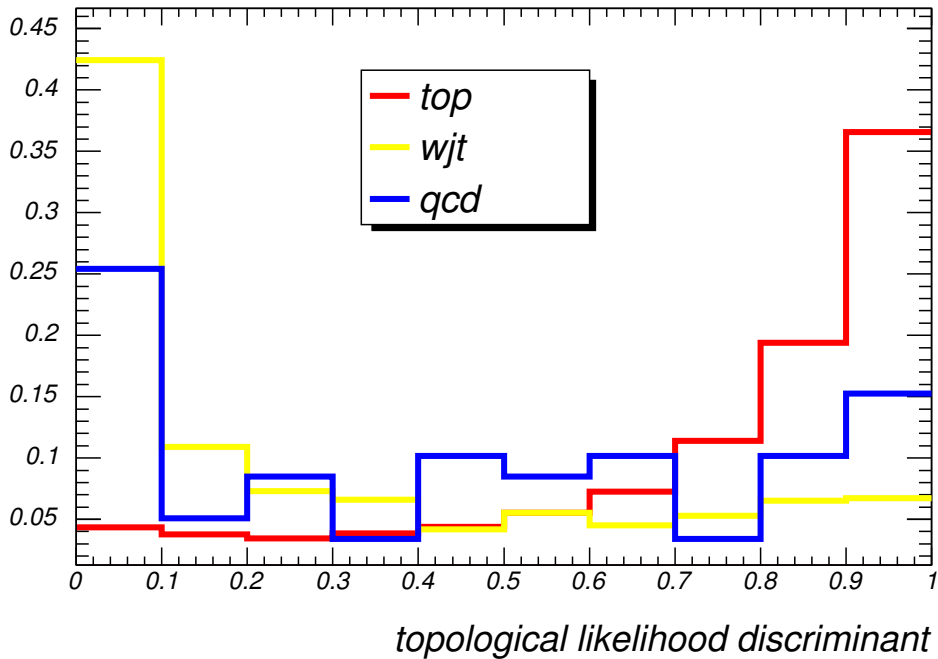


Figure 6.14: Normalized distributions of the topological likelihood discriminants for $t\bar{t}$, W +jets and QCD events for e+jets and μ +jets.

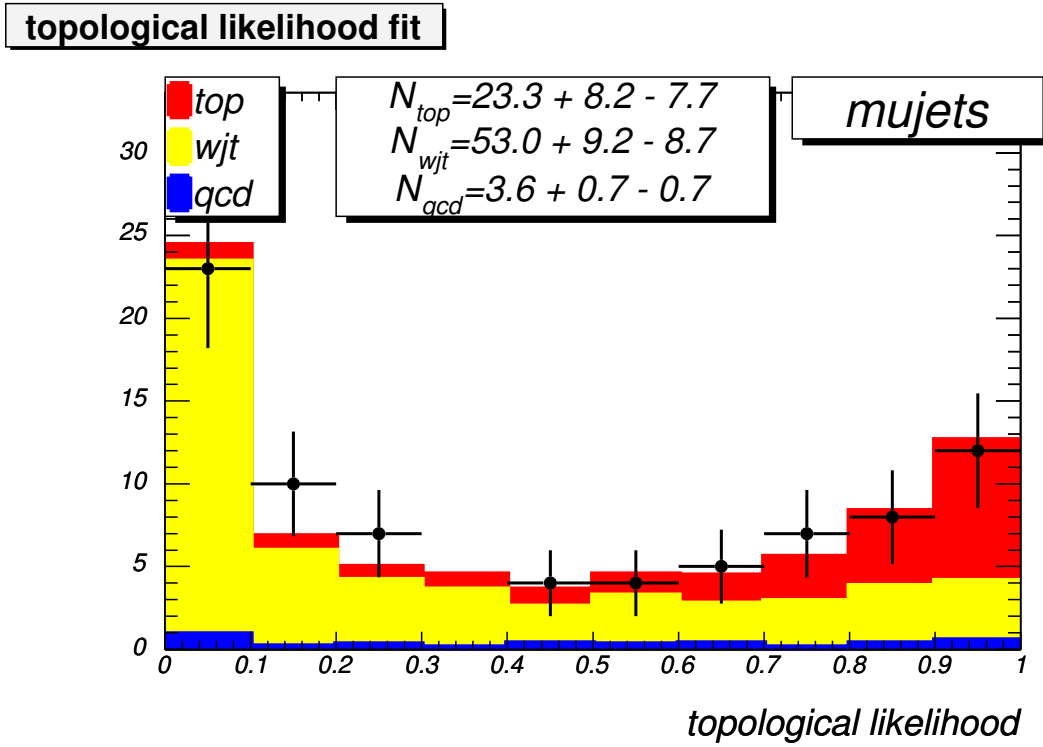
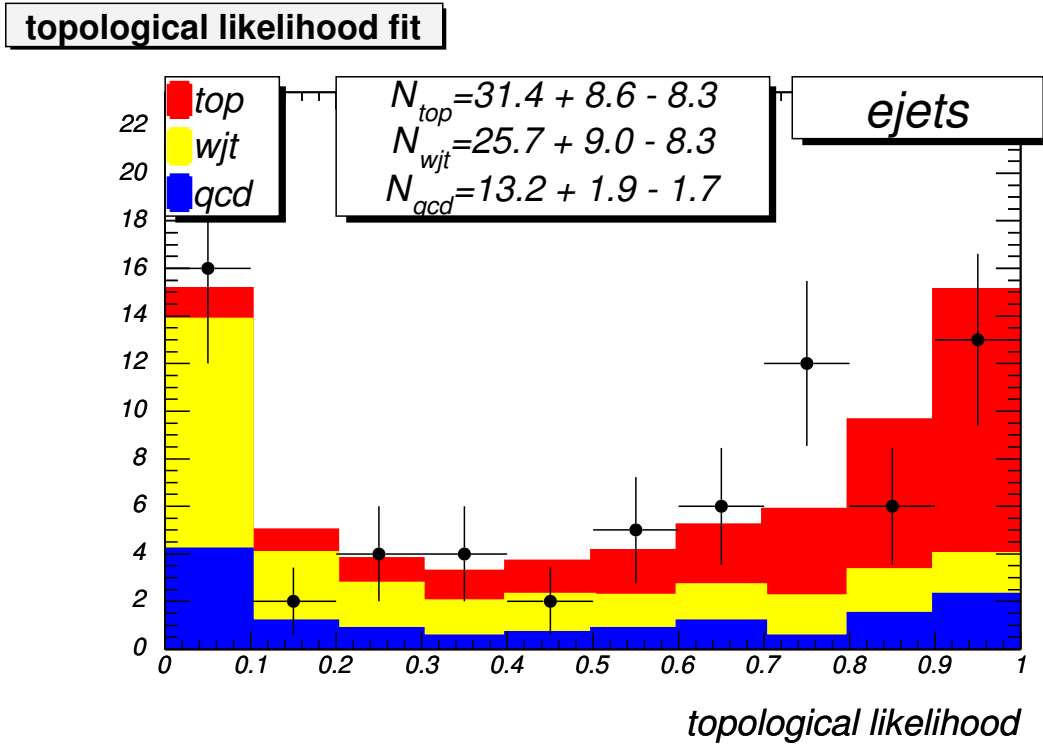


Figure 6.15: Result of the topological likelihood fit for e+jets and μ +jets.

channel	N_{evts}	f_{top}	N_{top}
ℓ +jets	150	0.364	54.7
e+jets	70	0.449	31.4
μ +jets	80	0.291	23.3

Table 6.1: Ensemble composition for e+jets, μ +jets and ℓ +jets calibration. No QCD events are drawn into the ensembles. The presence of QCD events is treated as a systematic uncertainty.

6.4 Calibration with Monte Carlo Events

Monte Carlo events which have been run through the full simulation of the DØ detector are found to describe the collected data well (see Appendix E). They are therefore used to derive the final calibration of the fitting procedure. $t\bar{t}$ samples with top quark masses of 160, 170, 175, 180 and 190 GeV and a W + jets sample are used. In addition, samples with $m_{top} = 175$ GeV, where all jets are scaled by 0.92, 0.96, 1.04 and 1.08 are prepared in order to calibrate the JES fit. For each sample and each lepton channel (e+jets and μ +jets), P_{sgn} and P_{bkg} are calculated for 1000 events which pass the kinematic selection (see Section 4.8). Ensembles are drawn from these event pools as described in Section 6.1. The ensemble composition is as measured in Section 6.3. Each event probability is normalized according to the flavor of the isolated lepton (see Sections 5.3.2 and 5.3.4). The QCD contribution is not added during the calibration but treated as a systematic uncertainty (Section 6.7). Table 6.1 summarizes the event numbers and fractions considered in the calibration ensembles.

A $t\bar{t}$ Monte Carlo event is considered *jet-parton matched*, if all four jets in the event can be unambiguously matched to the four partons from the $t\bar{t}$ decay. The matching requirement for a jet to a parton is $\Delta R < 0.5$. W + jets events are not included in the procedure: in a “jet-parton matched” sample with signal and background events, only the signal events are required to be matched.

In the following, ℓ +jets refers to the combination of the e+jets and μ +jets channel. To derive combined calibrations, a pair of e+jets and μ +jets ensembles is merged to a combined ℓ +jets ensemble. As the measurements of the top quark mass in the e+jets and μ +jets channels are merely cross-checks for the measurement in the combined ℓ +jets channel, only the calibration plots for the latter are included in this section. The calibration plots corresponding to the e+jets and μ +jets channels can be found in Appendix A.

In addition to considering all events which pass the selection criteria and assuming the expected sample compositions, three simpler scenarios are studied:

- *1st scenario*: Consider only $t\bar{t}$ signal events which are jet-parton matched. The results for ℓ +jets are shown in Figure 6.16. 20 events are drawn in each ensemble, and P_{bkg} is not taken into account.
- *2nd scenario*: Consider only $t\bar{t}$ signal events, no jet-parton matching required. The results for ℓ +jets are shown in Figures 6.17. 20 events are drawn in each ensemble, and P_{bkg} is not taken into account.

- *3rd scenario*: Consider ensembles with both $W + \text{jets}$ background and $t\bar{t}$ signal events, require the latter to be jet-parton matched. The results for $\ell + \text{jets}$ are shown in Figures 6.18 and 6.19. The ensembles are composed according to the expectation summarized in Table 6.1, and P_{bkg} is taken into account. The scaled samples are fitted as well to evaluate different jet energy scales.

Finally, all restrictions are lifted and the final calibrations are derived using all events passing the kinematic selection (*4th scenario*). The results for $\ell + \text{jets}$ are shown in Figures 6.20 and 6.21. The resulting m_{top} and JES fit distributions for a generated value of $m_{\text{top}} = 175$ GeV are shown in Figures 6.22 and 6.23, along with the respective pull distributions.

The calibration results for all four scenarios are summarized in Table 6.2. A significant bias of the fitted JES parameter is observed in all scenarios and attributed to the jet transfer function: as large Monte Carlo statistics are required to derive the parameters, the selection cuts were relaxed relative to the selection of the candidate sample. Studies which confirm that the transfer function derivation is the source of the JES bias can be found in Appendix D. Because of the correlation of both parameters, this JES bias causes the fitted top mass to be biased as well.

The only scenario which yields significantly different results is the second one: if only signal events are considered but the background probability is not included in the construction of the event probability P_{evt} , top events which are affected by radiation (failed jet-parton match) are not accounted for. The mass information in these events is poor and biased, but nevertheless these events are treated like good jet-parton matched events, leading to an overall bias and a significant deviation of the pull from 1. In the fourth scenario however, which does contain such events as well, no significant degradation with respect to the third scenario are observed, even though the latter does not contain these events: Thanks to the background probability normalization procedure described in Section 5.3.4, such radiation-affected events are treated as background and their mass information contributes little to the sample likelihood. Consequently, the fitted signal fraction f_{top} (Figure 6.24, $m_{\text{top}} = 175$ GeV) is about 10 – 20% lower than the true $t\bar{t}$ fraction.

We conclude that neither the addition of $W + \text{jets}$ background events nor the presence of $t\bar{t}$ signal events which are not described by the leading-order matrix element significantly degrade the performance of the mass fitting procedure. The final result obtained from the DØ Run II $\ell + \text{jets}$ data sample in Section 6.5 is corrected for the bias and pull-deviation from 1 according to the values in the last column of Table 6.2.

	1 st scenario sgn only, jpm	2 nd scenario sgn only	3 rd scenario sgn+bkg, jpm	4 th scenario sgn+bkg
$m_{\text{top}}\text{-offset}$	1.762 ± 0.277	0.861 ± 0.308	1.535 ± 0.329	1.442 ± 0.345
$m_{\text{top}}\text{-slope}$	1.004 ± 0.027	1.036 ± 0.030	1.021 ± 0.032	1.027 ± 0.034
$m_{\text{top}}\text{-pull}$	1.00 ± 0.05	1.15 ± 0.05	0.99 ± 0.06	1.05 ± 0.06
$JES\text{-offset}$	-	-	-0.023 ± 0.002	-0.025 ± 0.002
$JES\text{-slope}$	-	-	0.922 ± 0.040	0.936 ± 0.040
$JES\text{-pull}$	-	-	1.04 ± 0.07	1.05 ± 0.06

Table 6.2: Summary of the Monte Carlo calibration results for ℓ +jets events. “sgn only” indicates that only signal events are used to construct ensembles, and the background probability P_{bkg} is not considered. “jpm” means “jet-parton matched”, see the explanation in the text. “sgn+bkg” describes ensembles where the number of total events and the number of signal events are chosen according to the expectation in the DØ ℓ +jets data sample, and both P_{sgn} and P_{bkg} are considered in the construction of the likelihood.

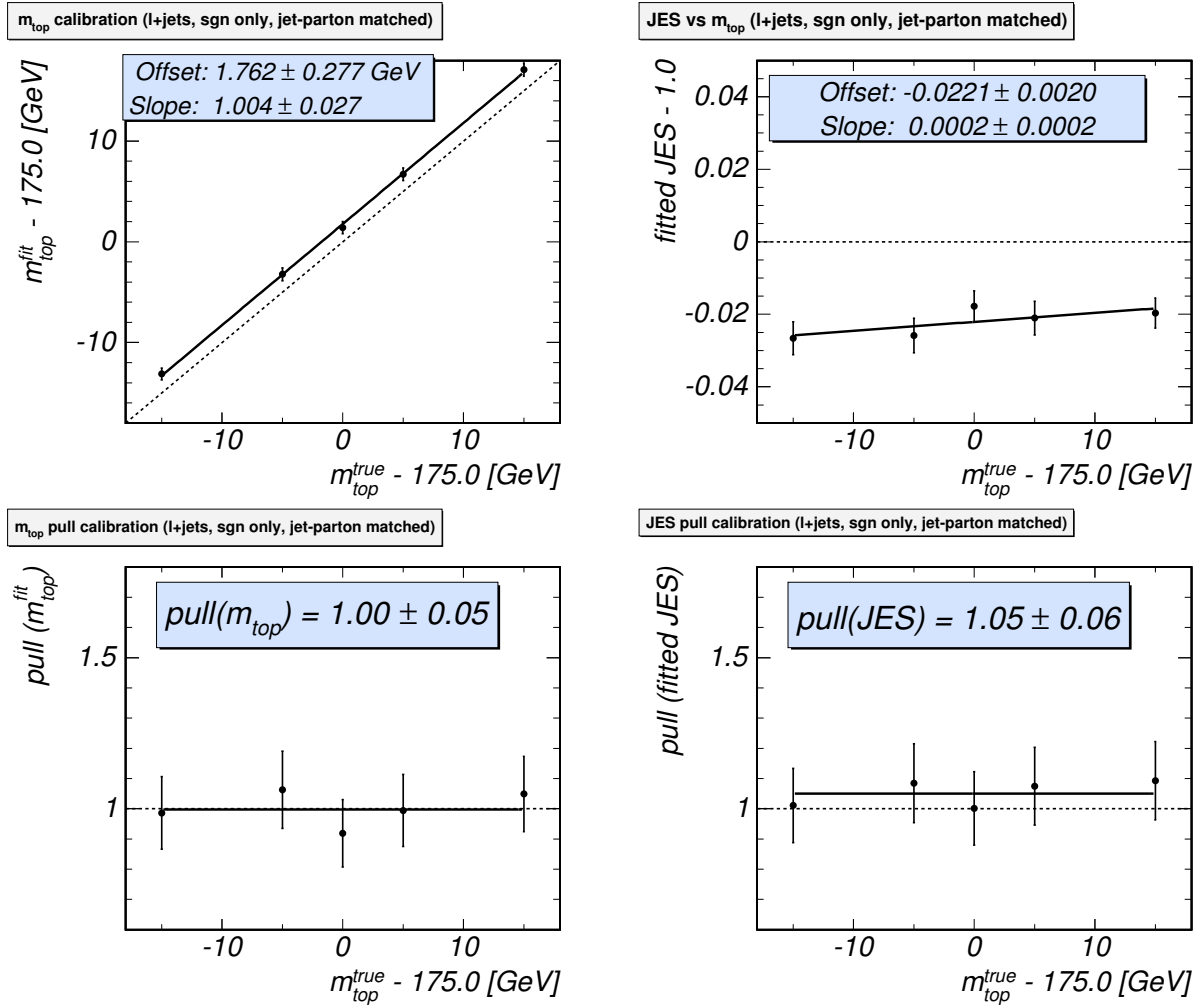


Figure 6.16: Fitted m_{top} , JES , and corresponding pull calibrations for jet-parton matched ℓ +jets signal events (1st scenario) as a function of the true top quark mass.

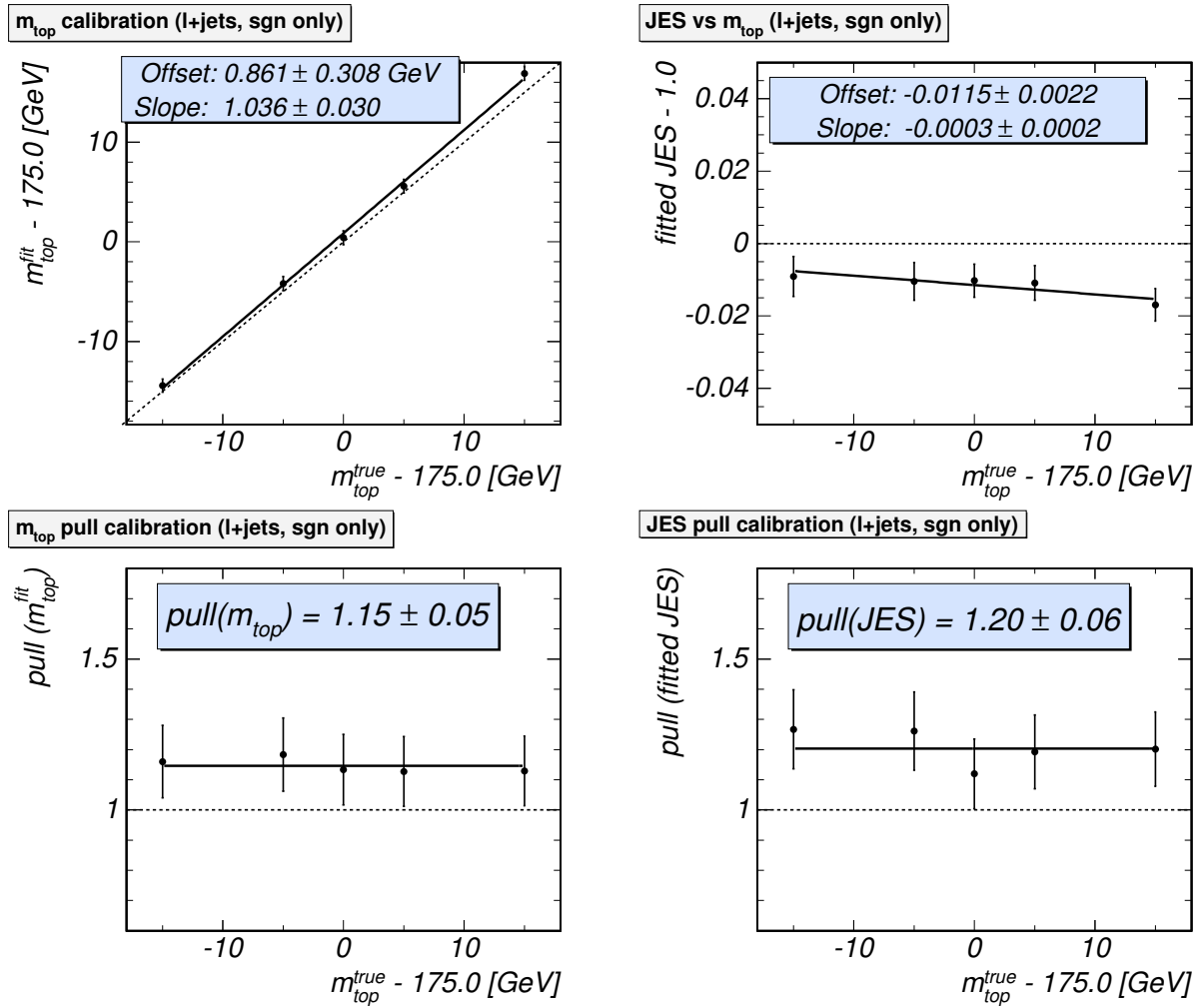


Figure 6.17: Fitted m_{top} , JES , and corresponding pull calibrations for ℓ +jets signal events (2^{nd} scenario) as a function of the true top quark mass.

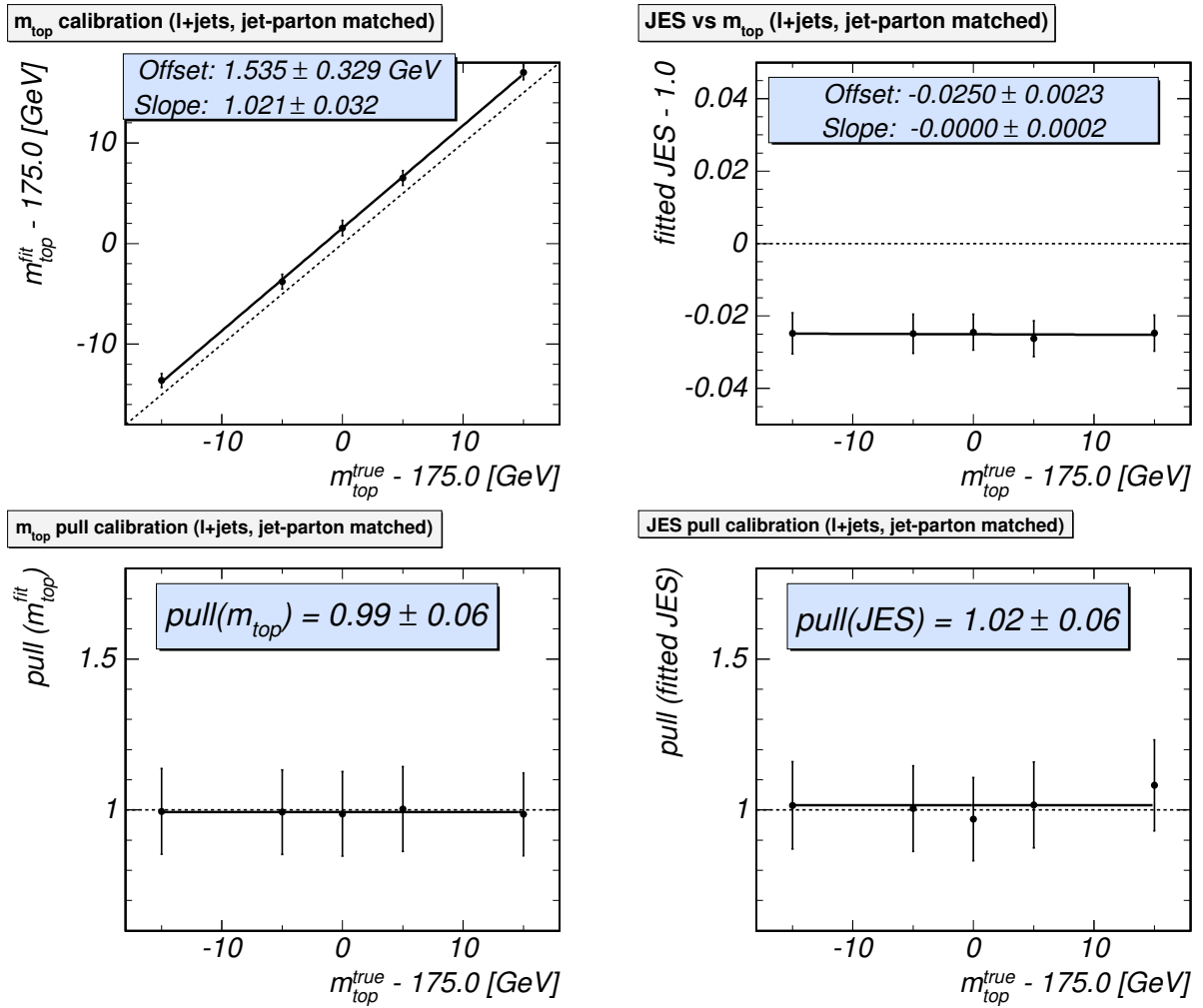


Figure 6.18: Fitted m_{top} , JES , and corresponding pull calibrations for jet-parton matched ℓ +jets events (3^{rd} scenario) as a function of the true top quark mass.

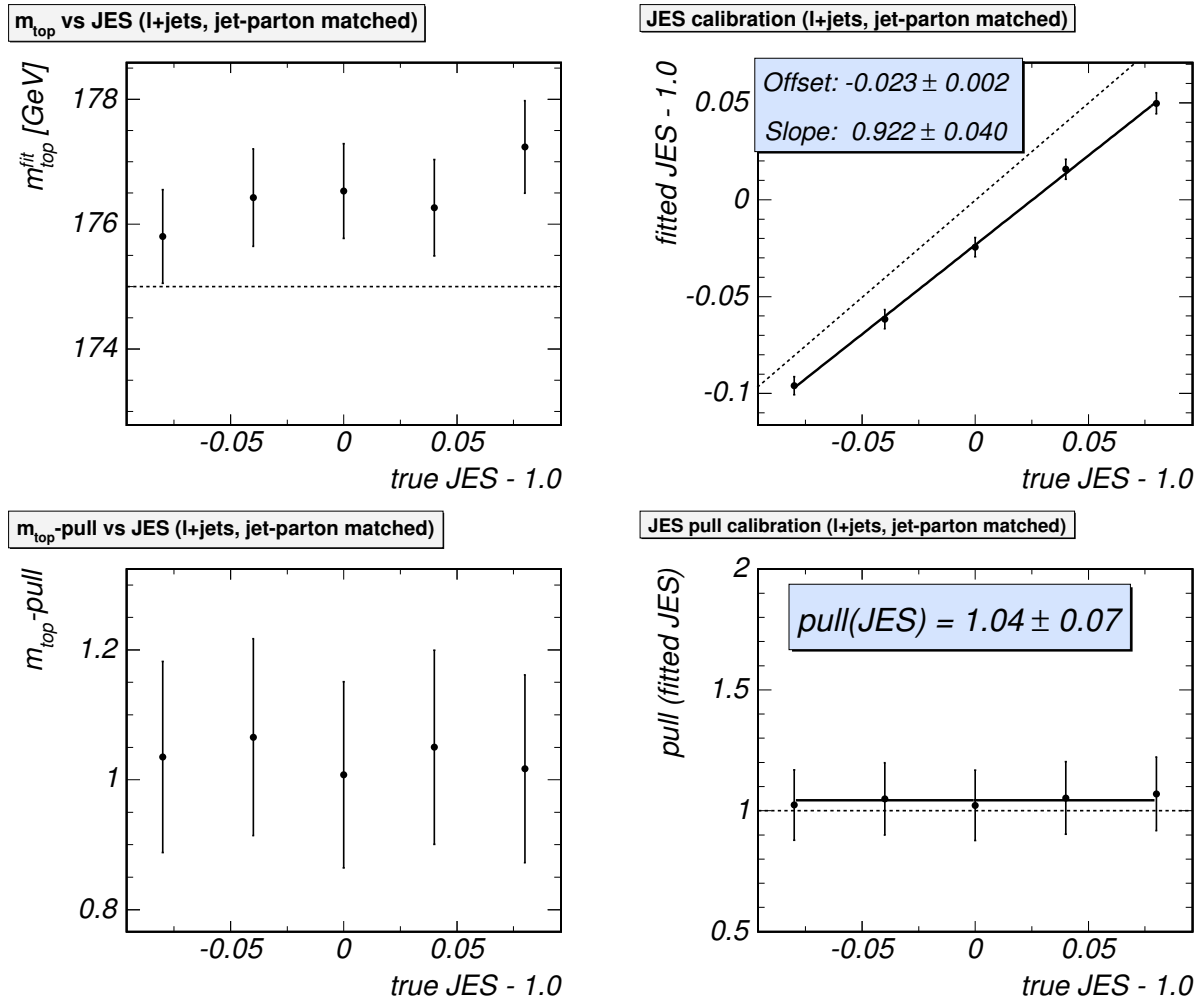


Figure 6.19: Fitted m_{top} , JES , and corresponding pull calibrations for jet-parton matched ℓ +jets events (3^{rd} scenario) as a function of the true jet energy scale.

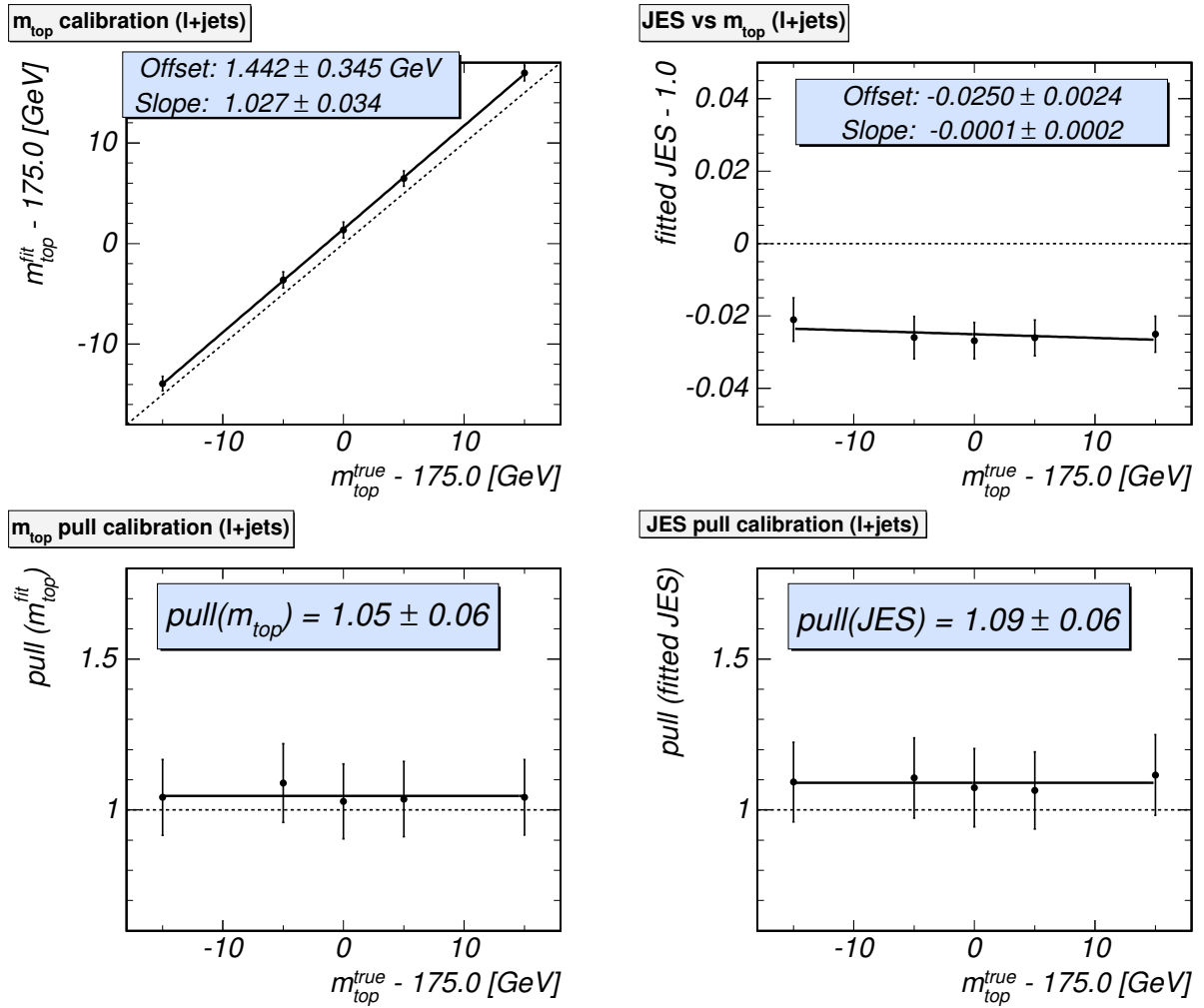


Figure 6.20: Final calibration: fitted m_{top} , JES , and corresponding pull calibrations for ℓ +jets events (4^{th} scenario) as a function of the true top quark mass.

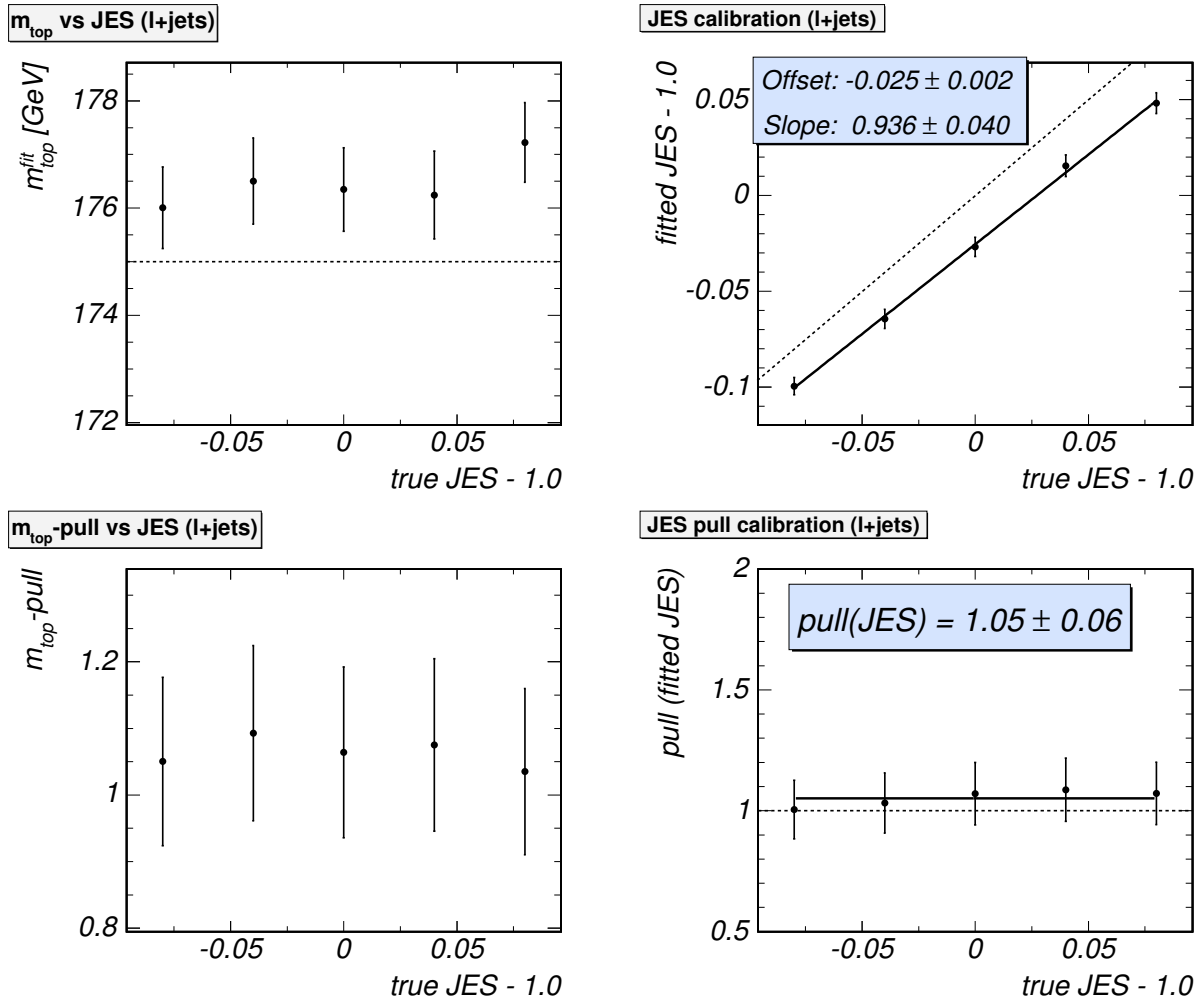


Figure 6.21: Final calibration: fitted m_{top} , JES , and corresponding pull calibrations for ℓ +jets events (4^{th} scenario) as a function of the true jet energy scale.

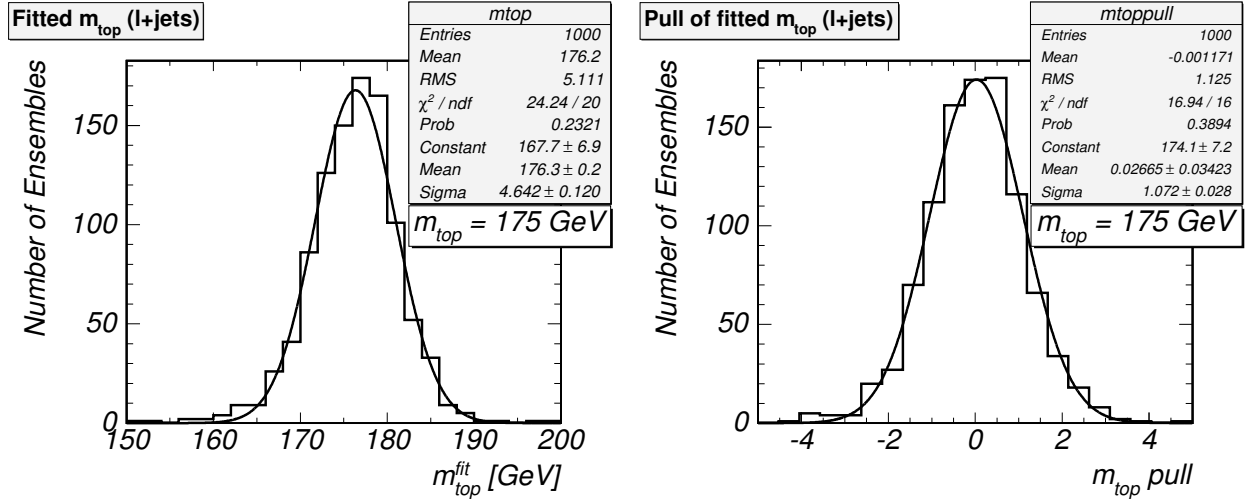


Figure 6.22: Fitted m_{top} (left) and m_{top} -pull (right) distributions for a generated value of $m_{\text{top}} = 175 \text{ GeV}$ for ℓ +jets events.

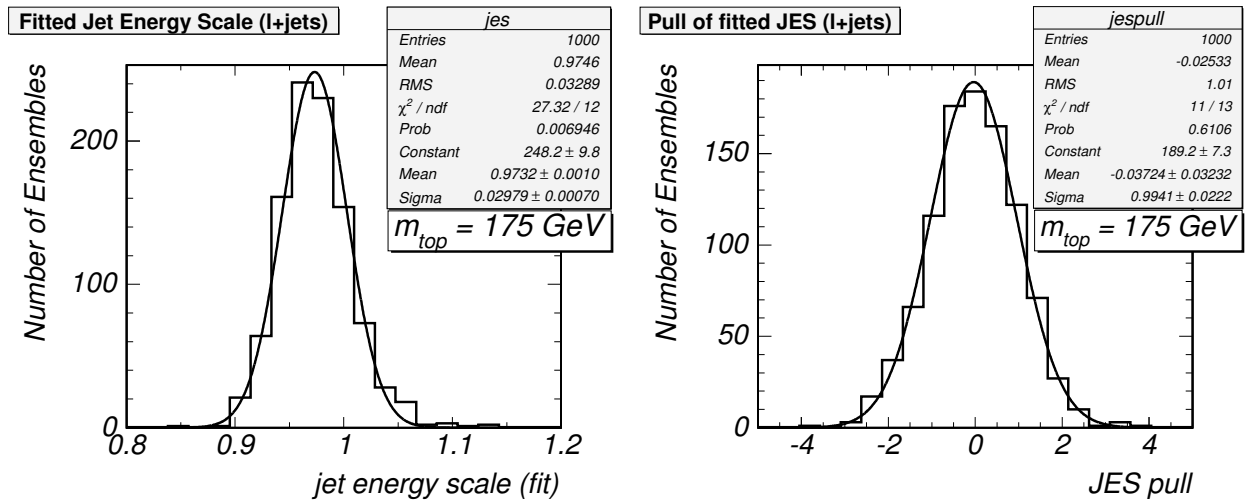


Figure 6.23: Fitted JES (left) and JES -pull (right) distributions for a generated value of $m_{\text{top}} = 175 \text{ GeV}$ for ℓ +jets events.

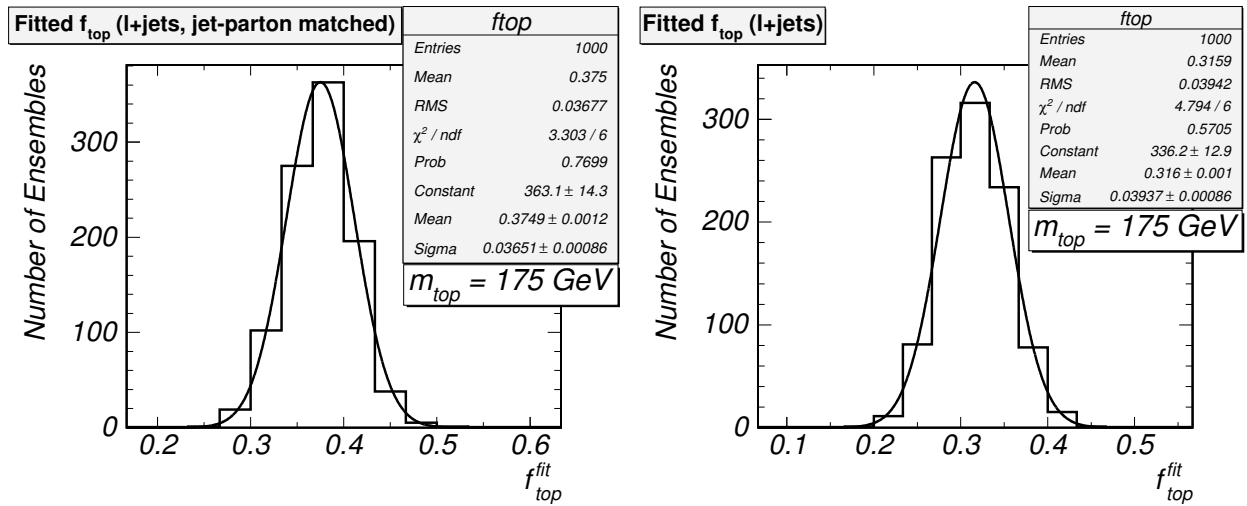


Figure 6.24: Fitted signal fraction f_{top} for a generated value of $m_{\text{top}} = 175 \text{ GeV}$ for ℓ +jets events. The left plot corresponds to the 3rd scenario, while the right plot is derived for the 4th scenario. In the 4th scenario, the fit of the $t\bar{t}$ fraction yields an average 0.316, which is lower than the true signal fraction of 0.364: radiation-affected $t\bar{t}$ events are treated as background. In the 3rd scenario, the true $t\bar{t}$ fraction is well reproduced by the fit (average: 0.375).

channel	m_{top} [GeV]	$m_{\text{top}}^{\text{clb}}$ [GeV]	JES	JES^{clb}
ℓ +jets	170.8 ± 4.3	169.5 ± 4.4	1.007 ± 0.030	1.034 ± 0.034
e+jets	170.9 ± 5.2	168.8 ± 6.0	1.025 ± 0.040	1.060 ± 0.047
μ +jets	172.4 ± 10.5	172.3 ± 9.6	0.976 ± 0.069	0.997 ± 0.086

Table 6.3: Fitted m_{top} and JES for the ℓ +jets, e+jets and μ +jets samples, before and after calibration.

channel	$f_{\text{top}}^{\text{exp}}$ (topo)	$f_{\text{top}}^{\text{exp}}$ (MC)	$f_{\text{top}}^{\text{fit}}$
ℓ +jets	$36.4^{+11.3}_{-10.7} \%$	0.319 ± 0.04	$0.316^{+0.049}_{-0.055}$
e+jets	$44.9^{+12.3}_{-11.9} \%$	0.395 ± 0.06	$0.340^{+0.074}_{-0.075}$
μ +jets	$29.1^{+10.3}_{-9.6} \%$	0.263 ± 0.05	$0.276^{+0.069}_{-0.071}$

Table 6.4: Signal fraction f_{top} for ℓ +jets, e+jets and μ +jets samples: expectation from topological likelihood fit (second column), expectation from MC ensemble testing (third column, see Figure 6.28), and fit result (fourth column).

6.5 Application to Data

The matrix element method is applied to the 320 pb^{-1} ℓ +jets dataset collected at DØ Run II. The calibrations for m_{top} derived in Section 6.4 are taken into account (see Figures 6.20-6.21). Table 6.3 summarizes uncalibrated and calibrated results. Although pull deviations from 1.0 are not significant in most cases, the statistical uncertainty yielded by the likelihood fit is scaled accordingly. The calibrated fit results are shown in Figures 6.25 and 6.26. The top mass is measured to be

$$\begin{aligned}
 m_{\text{top}}^{\ell+\text{jets}} &= 169.5 \pm 4.4 \text{ (stat. + JES) GeV} \\
 m_{\text{top}}^{e+\text{jets}} &= 168.8 \pm 6.0 \text{ (stat. + JES) GeV} \\
 m_{\text{top}}^{\mu+\text{jets}} &= 172.3 \pm 9.6 \text{ (stat. + JES) GeV}
 \end{aligned}
 \tag{6.11}$$

$$\tag{6.12}$$

The distribution of uncalibrated statistical uncertainties in ensemble tests ($m_{\text{top}} = 170.0 \text{ GeV}$) are shown in Figure 6.27. The arrows indicate the uncalibrated statistical uncertainty found in the data sample. Figure 6.28 shows the fitted signal fraction f_{top} . The fit result maximizes the likelihood at the (JES, m_{top}) values closest to the (JES, m_{top}) fit result. Correlations with JES and m_{top} are not taken into account in the evaluation of the f_{top} uncertainty. As explained in Section 5.3.4, the f_{top} fit is calibrated such that it does not yield the true $t\bar{t}$ fraction, but the fraction of signal events not affected by radiation. Table 6.4 summarizes the expected true signal fractions from the topological likelihood fit, and the expected and measured f_{top} fit result from the matrix element method.

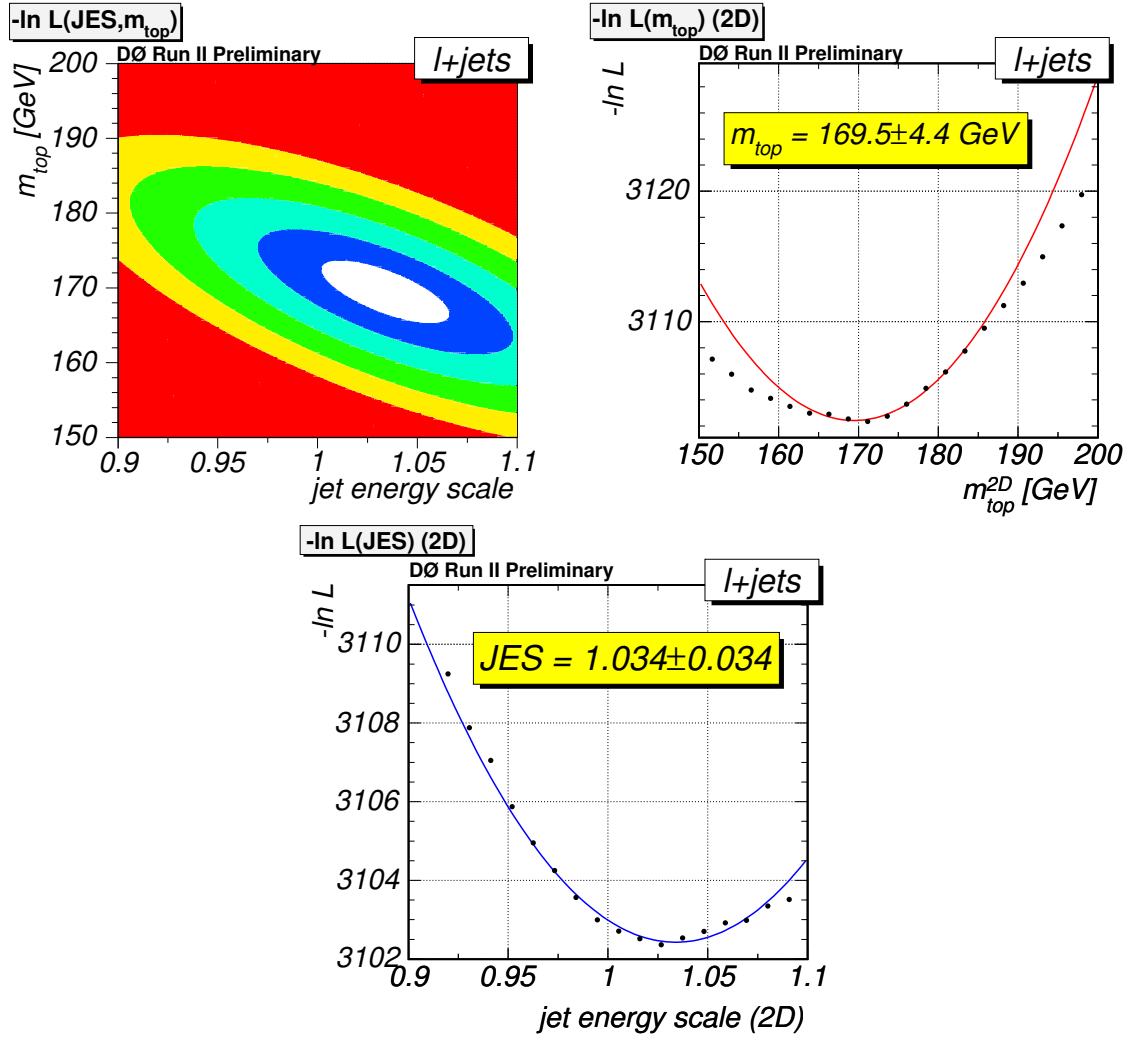


Figure 6.25: Application of the matrix element method to the $320 \text{ pb}^{-1} \ell+\text{jets}$ dataset. m_{top} and JES axes correspond to the calibration derived in Section 6.4. Top left: the two-dimensional $m_{\text{top}}-JES$ fit, with $n\sigma$ contours. Top right: Projection to m_{top} parameter, taking correlations into account. The corresponding $-\ln L$ points are shown as well. Below: Projection to JES parameter, taking correlations into account. The corresponding $-\ln L$ points are shown as well.

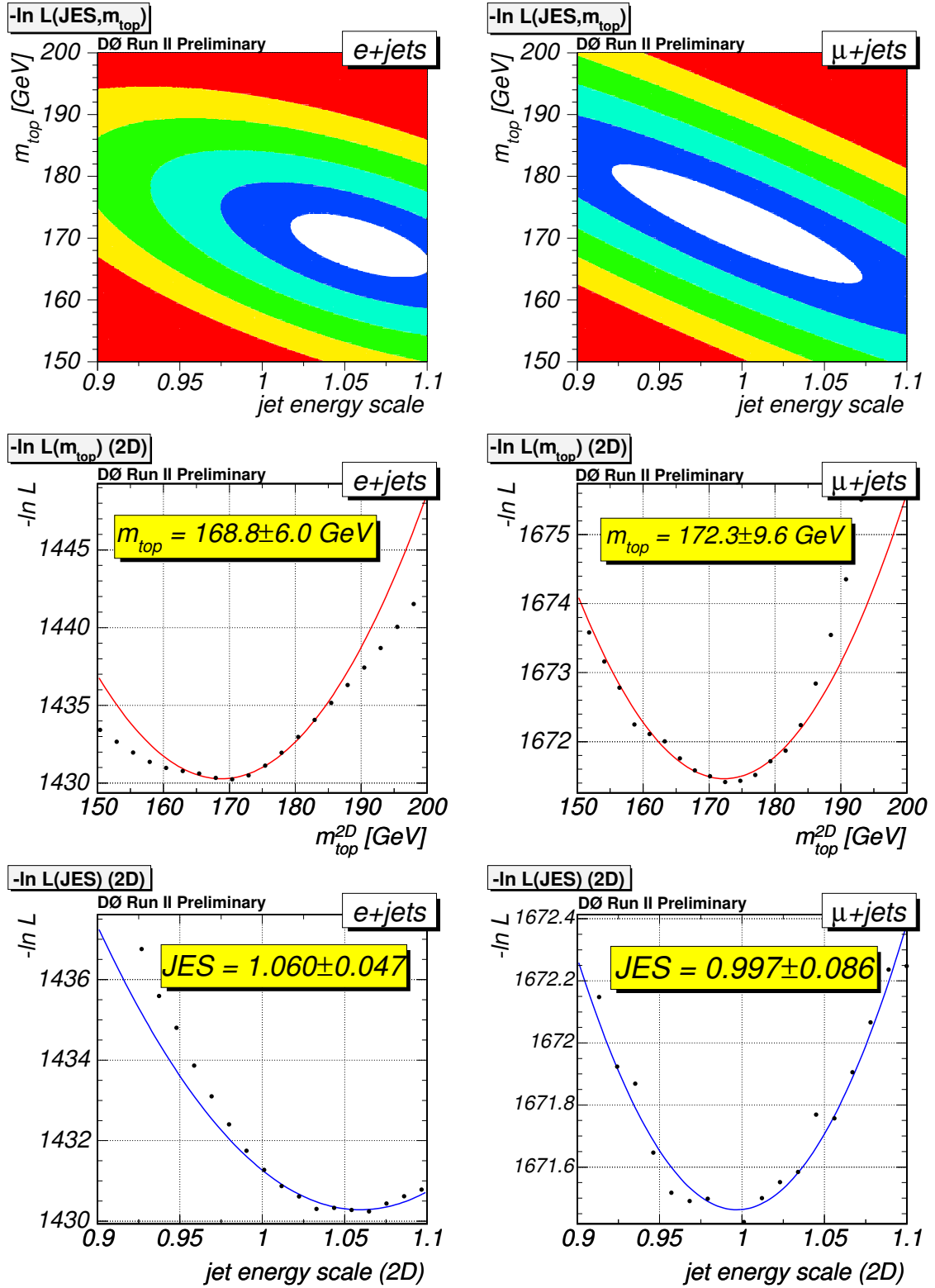


Figure 6.26: Application of the matrix element method to the 320 pb⁻¹ e+jets (left column) and μ +jets (right column) datasets. m_{top} and JES axes correspond to the calibration derived in Section 6.4. Top: two-dimensional m_{top} - JES fit, with σ contours. Middle: Projection to m_{top} parameter, taking correlations into account. The corresponding $-\ln L$ points are shown as well. Below: Projection to JES parameter, taking correlations into account. The corresponding $-\ln L$ points are shown as well.

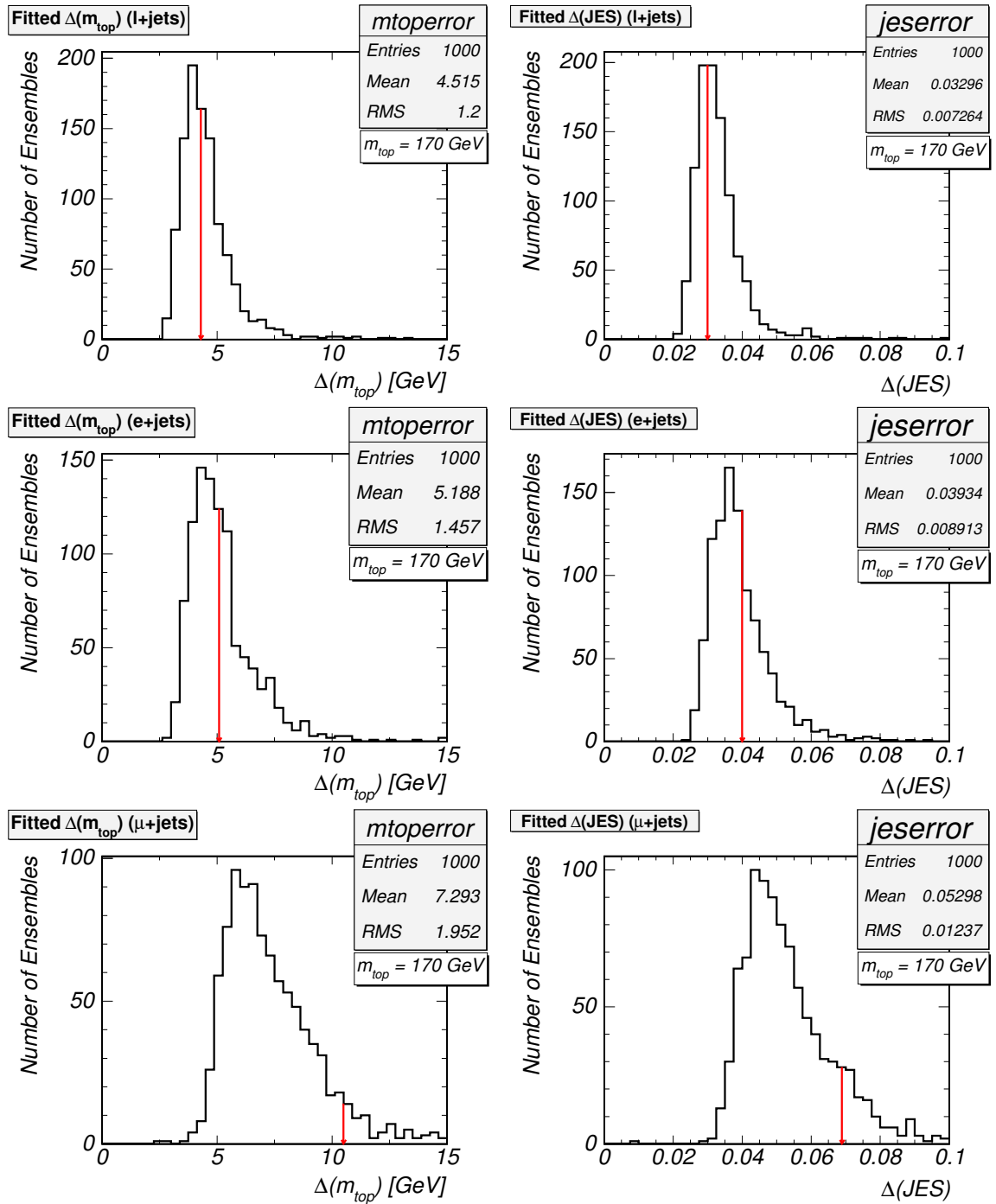


Figure 6.27: Uncalibrated error distributions for the m_{top} (left column) and JES (right column) estimators in Monte Carlo for ℓ +jets, e +jets, and μ +jets events. The arrow indicates the uncalibrated statistical uncertainties observed in data.

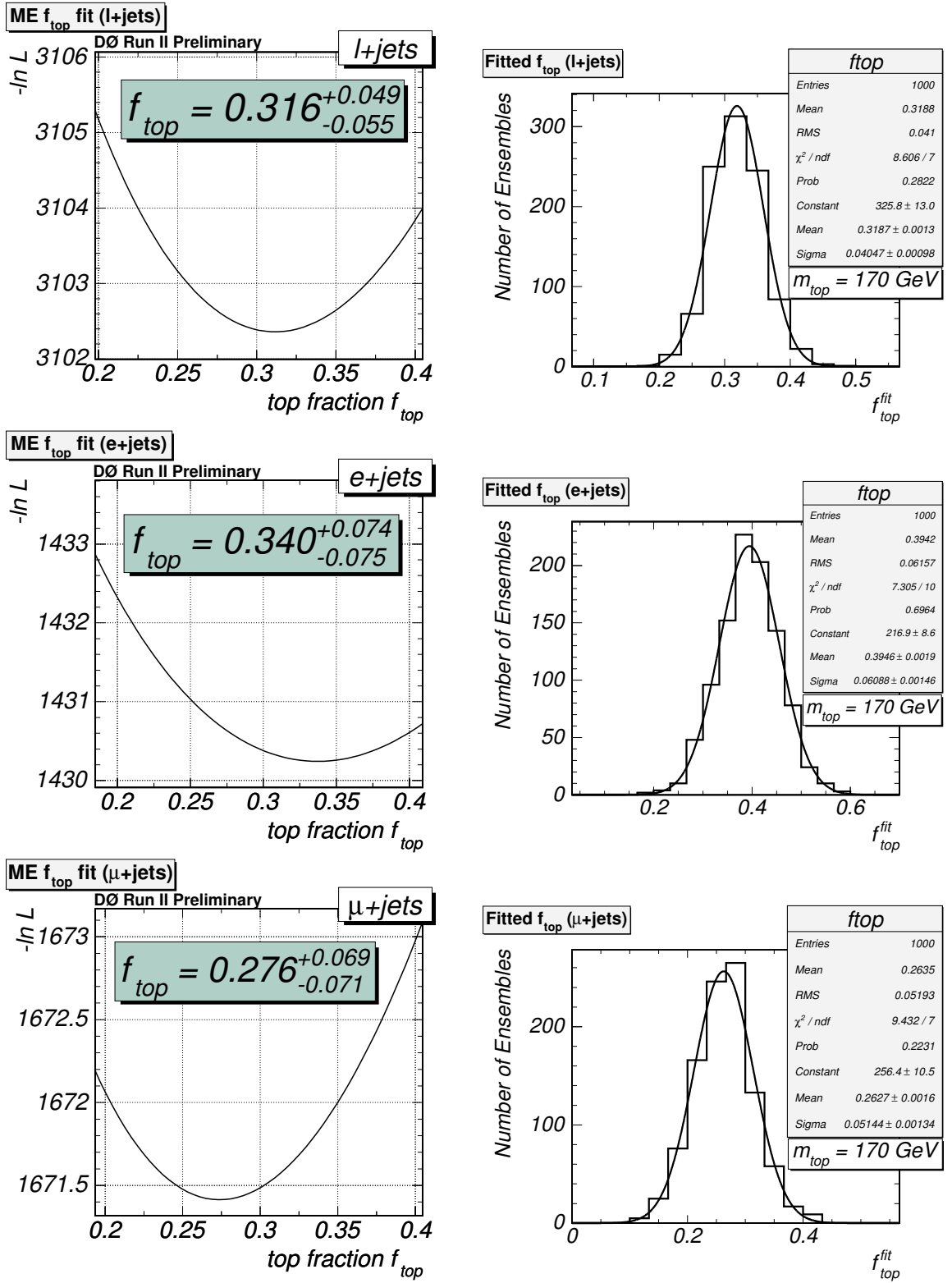


Figure 6.28: Likelihood curves for the fitted signal fraction f_{top} (left column) and MC f_{top} ensemble distributions (right column) for the $l+jets$, $e+jets$ and $\mu+jets$ channels.

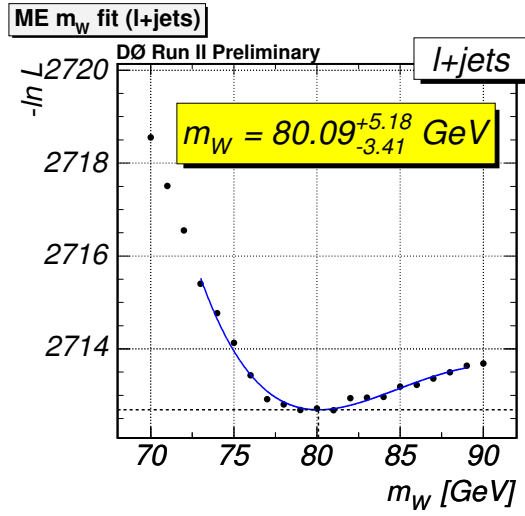


Figure 6.29: Fit to the $-\ln(\text{likelihood})$ as a function of m_W for the sample of 132 events with jet energies scaled by $1/1.034$.

6.6 Cross Check: W Boson Mass Fit

As a cross-check, the jets in the data events are scaled by a factor of $1/1.034$ according to the JES fit result in Figure 6.25. The missing transverse energy is adjusted in each event. 132 data events pass the event selection after scaling and are used to determine the $-\ln(\text{likelihood})$ as a function of the W boson and top masses. Hereby, the variation of the jet energy scale parameter in the transfer functions is replaced by a variation of the hadronic W boson mass in the leading order $t\bar{t}$ matrix element. The best $-\ln(\text{likelihood})$ value as a function of the W boson mass is shown in Figure 6.29. The fitted W boson mass of $m_W = 80.1^{+5.2}_{-3.4}$ GeV is in good agreement with the expectation of the value $m_W = 80.4$ GeV assumed in the matrix element.

6.7 Systematic Uncertainties

6.7.1 Jet Energy Scale

The systematic uncertainty on the top mass measurement due to our knowledge of the jet energy scale is already covered by the two-dimensional likelihood fit. To estimate the contribution from the jet energy scale alone, the JES parameter is fixed to 1. The one-dimensional fit without JES correlations yields a top mass error of 3.0 GeV, 4.5 GeV, and 4.3 GeV for the ℓ +jets, e+jets and μ +jets samples respectively. The jet energy scale contribution to the error on m_{top} in the two-dimensional fit is therefore approximately

$$(\Delta m_{\text{top}})_{JES}^{\ell+\text{jets}} = \pm 3.2 \text{ GeV} \quad (6.13)$$

$$(\Delta m_{\text{top}})_{JES}^{e+\text{jets}} = \pm 4.0 \text{ GeV} \quad (6.14)$$

$$(\Delta m_{\text{top}})_{JES}^{\mu+\text{jets}} = \pm 8.6 \text{ GeV} . \quad (6.15)$$

6.7.2 JES p_{T} dependence

The relative difference between the jet energy scales in data and Monte Carlo is fitted with a global scale factor, and the corresponding uncertainty is included in the quoted (stat. + JES) error. Any discrepancy between data and simulation other than a global scale difference may lead to an additional uncertainty on the top quark mass. A reasonable p_{T} dependence of the discrepancy between data and Monte Carlo is assumed, and the uncertainty is estimated to be

$$(\Delta m_{\text{top}})_{JES,p_{\text{T}}}^{\ell+\text{jets}} = \pm 0.70 \text{ GeV} \quad (6.16)$$

$$(\Delta m_{\text{top}})_{JES,p_{\text{T}}}^{e+\text{jets}} = \pm 0.70 \text{ GeV} \quad (6.17)$$

$$(\Delta m_{\text{top}})_{JES,p_{\text{T}}}^{\mu+\text{jets}} = \pm 0.70 \text{ GeV} . \quad (6.18)$$

6.7.3 b -Jet Energy Scale

Differences in the b and light quark jet energy scales between data and Monte Carlo may affect the result, as the JES parameter applies to all jet flavors. The jet energy scale for DØ Run II is derived using an inclusive γ +jets sample. In the mass measurement, the flavor of the jet is taken into account by individual treatment of light and heavy flavor jets in the transfer function derivation (Section 5.2): reconstructed jet energies are compared to parton energies, and the bias due to the inclusive jet energy scale is thus corrected.

To verify that the Monte Carlo simulation models the differences between both types of jets well, the response for b and light quark jets is compared in data. Figure 6.31 shows a comparison of the b -to-light jet energy response derived for Run II data and Monte Carlo events [50]. Within the statistical significance of both samples, no deviation between both scales is observed. We consider two physics effects to derive the systematic due to b -Jet Energy Scale: the choice of the fragmentation model and h/e calorimeter response (h= hadronic response, e=electromagnetic response).

b Fragmentation Model

In the standard Monte Carlo samples, the Bowler fragmentation scheme [51] with $r_t = 1.0$ is applied in the event generators. Two $t\bar{t}$ Monte Carlo samples with different b-fragmentation models are studied to evaluate the systematic effect due to our choice of the model:

- Peterson fragmentation [52], $\epsilon = 0.00191$ (“P-sample”)
- Bowler fragmentation, $r_t = 0.69$ (“B069-sample”)

Figure 6.30 shows the calibrated m_{top} ensemble distribution for the standard sample (left column), the P-sample (middle column), and the B069-sample (right column) for ℓ +jets (top), e+jets (middle) and μ +jets (bottom) respectively. The deviations from the standard sample are added in quadrature yielding the systematic uncertainty due to the choice of b -fragmentation model:

$$(\Delta m_{\text{top}})_{bfrag}^{\ell+jets} = \pm 0.71 \text{ GeV} \quad (6.19)$$

$$(\Delta m_{\text{top}})_{bfrag}^{e+jets} = \pm 0.86 \text{ GeV} \quad (6.20)$$

$$(\Delta m_{\text{top}})_{bfrag}^{\mu+jets} = \pm 0.92 \text{ GeV}. \quad (6.21)$$

h/e Calorimeter Response

The DØ calorimeter is not fully compensating, hadronic and electromagnetic particles have different calorimeter response. b and light jets on the other hand have different charged hadron multiplicities, and different charged hadron energy spectra. A reasonable representation of the h/e response is assumed and the average response for b and light jets is computed, considering the respective charged hadron multiplicities and energy spectra. The h/e response is varied by 15%, resulting in a b -to-light jet response variation of $+1.5 - 1.3\%$ for $20 < p_T^{jet} < 95$ [53]. This variation is taken to compute the systematic uncertainty on m_{top} . Figure 6.32 shows the bias on m_{top} (left) and JES (right) due to different b-to-light response deviations in data and Monte Carlo. The calibrations are derived by scaling the b-jets in a jet-parton matched Monte Carlo sample ($m_{\text{top}} = 175 \text{ GeV}$) by 0.94, 0.97, 1.03 and 1.06 and performing ensemble tests. The linear fits relates the above deviation to the corresponding systematic uncertainty on m_{top} :

$$(\Delta m_{\text{top}})_{bresp}^{\ell+jets} = +0.87 - 0.75 \text{ GeV} \quad (6.22)$$

$$(\Delta m_{\text{top}})_{bresp}^{e+jets} = +0.73 - 0.63 \text{ GeV} \quad (6.23)$$

$$(\Delta m_{\text{top}})_{bresp}^{\mu+jets} = +1.11 - 0.96 \text{ GeV}. \quad (6.24)$$

6.7.4 Signal Modeling

The $t\bar{t}$ signal Monte Carlo samples are generated with the ALPGEN event generator and subsequently processed with PYTHIA to simulate radiation effects. However, $t\bar{t}$ pairs are predicted to be produced at the Tevatron in association with another parton 1 out of 4 times

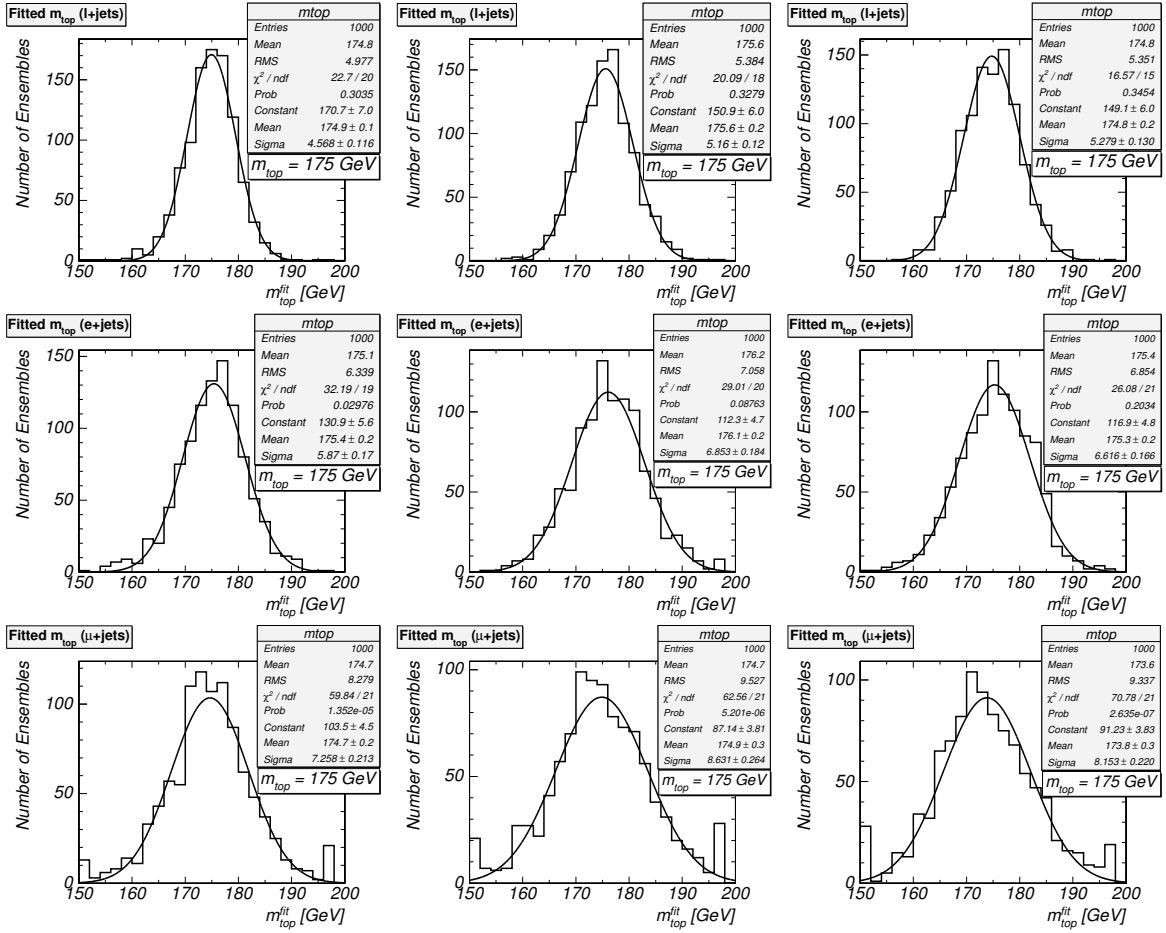


Figure 6.30: Calibrated m_{top} distributions for the standard (left), P-sample (middle), and B069-sample (right) ensembles, for ℓ +jets (top), e+jets (middle) and μ +jets (right) respectively.

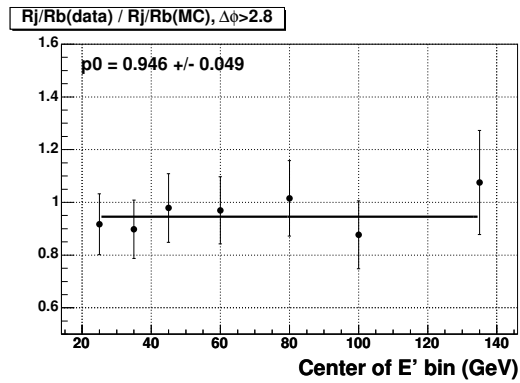


Figure 6.31: b-to-light jet response comparison between data and Monte Carlo, using photon+jet data and various b lifetime tagging algorithms [50].

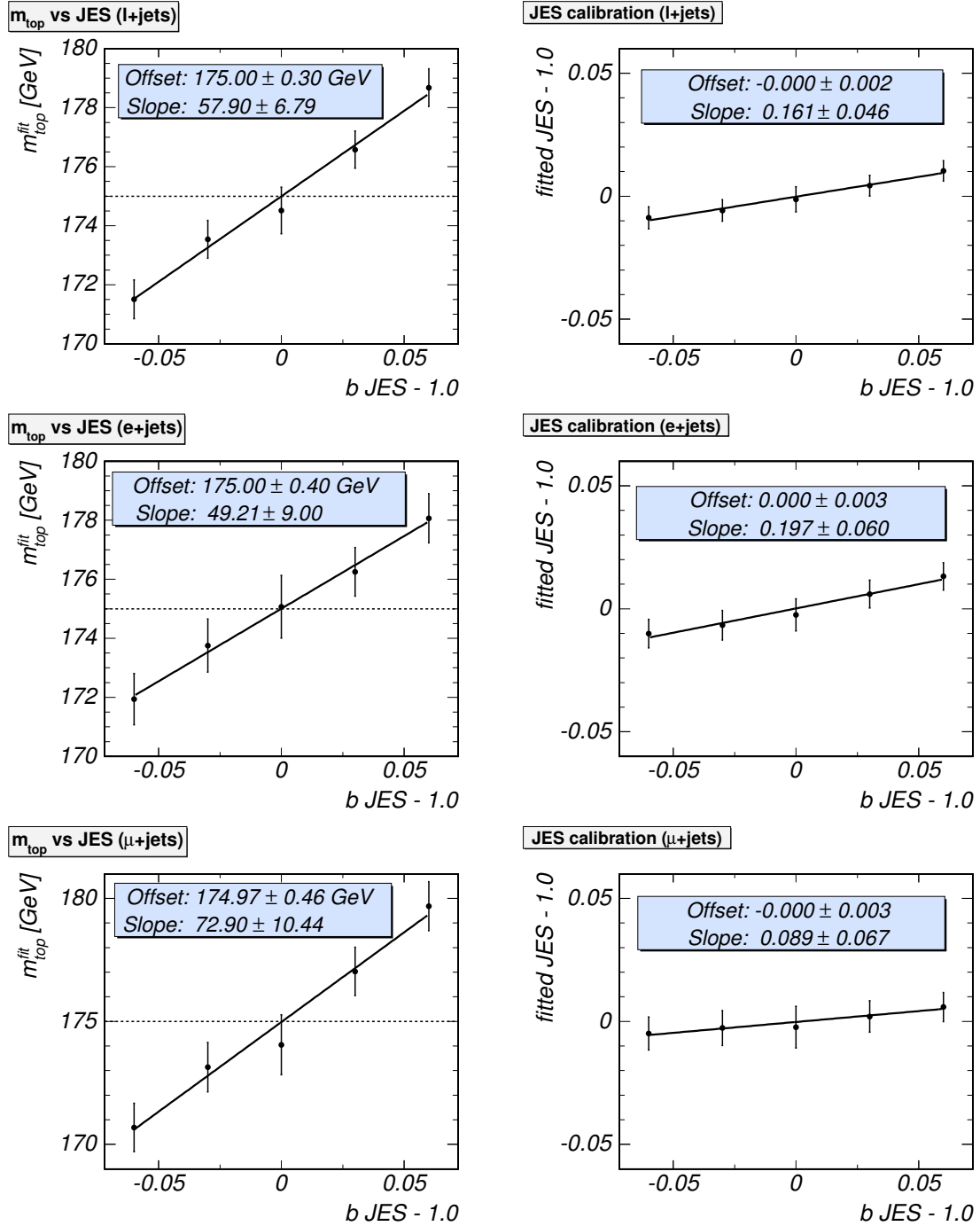


Figure 6.32: Fitted top mass (left column) and fitted jet energy scale (right column) for various b-jet energy scales. The light quark jet energy scale is set to 1.0.

with a cross section of 2.5 pb, compared to 6.0 pb for $t\bar{t}$ only. In spite of requiring exactly four jets, these events can be selected in our sample if one of the jets is not reconstructed. The additional jet can be misinterpreted as a product of the $t\bar{t}$ decay. The $t\bar{t}$ system is then produced with significant transverse momentum, in contrast to the assumption made in the calculation of P_{sgn} . A dedicated $t\bar{t}j$ Monte Carlo sample is processed and the signal and background probabilities calculated to study the effect of the presence of such events. Figure 6.33 shows the difference Δm_{top} between ensembles generated with $t\bar{t}j$ fraction $f_{t\bar{t}j} > 0$ and the default simulation, separately for ℓ +jets, e+jets, and μ +jets events. The total $t\bar{t}$ fraction in the sample is fixed to the expectation in data, and the relative fraction of $t\bar{t}j$ events is varied from 0%-100%. The efficiencies for both $t\bar{t}$ and $t\bar{t}j$ events to pass all event selection criteria (including the trigger) are obtained from Monte Carlo to be

$$\begin{aligned}
\epsilon_{t\bar{t}}^{e+\text{jets}} &= 9.93 \pm 0.12 \% \\
\epsilon_{t\bar{t}}^{\mu+\text{jets}} &= 10.25 \pm 0.13 \% \\
\epsilon_{t\bar{t}j}^{e+\text{jets}} &= 10.22 \pm 0.24 \% \\
\epsilon_{t\bar{t}j}^{\mu+\text{jets}} &= 9.71 \pm 0.24 \% .
\end{aligned} \tag{6.25}$$

The fraction of $t\bar{t}j$ events predicted by this LO estimation is therefore

$$\begin{aligned}
f_{t\bar{t}j}^{\ell+\text{jets}} &= 29.1 \% \\
f_{t\bar{t}j}^{e+\text{jets}} &= 30.3 \% \\
f_{t\bar{t}j}^{\mu+\text{jets}} &= 27.9 \% .
\end{aligned} \tag{6.26}$$

The deviation Δm_{top} between ensembles generated with $f_{t\bar{t}j} \leq 1$ and $f_{t\bar{t}j} = 0$ is consistent with 0 for ℓ +jets, e+jets, and μ +jets events. Therefore, the error on $\Delta m_{\text{top}}(f_{t\bar{t}j} = 1)$ is multiplied by the estimated fraction of $t\bar{t}j$ events to obtain the systematic uncertainty. Another possible scenario to be considered are events without any radiation. Comparison of the calibrations in Figures 6.20-6.21 with jet-parton matched events (Figures 6.18-6.19) approximates this effect, but no significant deviation is observed. The resulting uncertainties are

$$(\Delta m_{\text{top}})_{\text{sgn.mod.}}^{\ell+\text{jets}} = \pm 0.34 \text{ GeV} \tag{6.27}$$

$$(\Delta m_{\text{top}})_{\text{sgn.mod.}}^{e+\text{jets}} = \pm 0.33 \text{ GeV} \tag{6.28}$$

$$(\Delta m_{\text{top}})_{\text{sgn.mod.}}^{\mu+\text{jets}} = \pm 0.42 \text{ GeV} . \tag{6.29}$$

The leading order matrix element used in the calculation of the signal probability contains $q\bar{q} \rightarrow t\bar{t}$ production only, and the effect of $g\bar{g} \rightarrow t\bar{t}$ events in the sample is evaluated. At $\sqrt{s} = 1.96 \text{ TeV}$, 15 – 20 % of all $t\bar{t}$ pairs are expected to originate from gluon-gluon fusion. MADGRAPH parton-level, $g\bar{g} \rightarrow t\bar{t}$ -only samples with top masses of 150, 160, 170, 175, 180, 190 and 200 GeV are generated and ensembles are composed and fit. The jet energy scale is fixed to 1.0. An alternative mass calibration is derived and compared to one obtained for $q\bar{q} \rightarrow t\bar{t}$ (Figure 6.34). The offset of the calibration does not significantly change, and no systematic uncertainty is assigned to this effect. This behavior is not unexpected as the mass-dependence of $\mathcal{M}_{t\bar{t}}$ comes mostly from its decay, not the production terms. However, a more accurate description of the production part of the matrix element might yield better discrimination from background and will be pursued in the future.

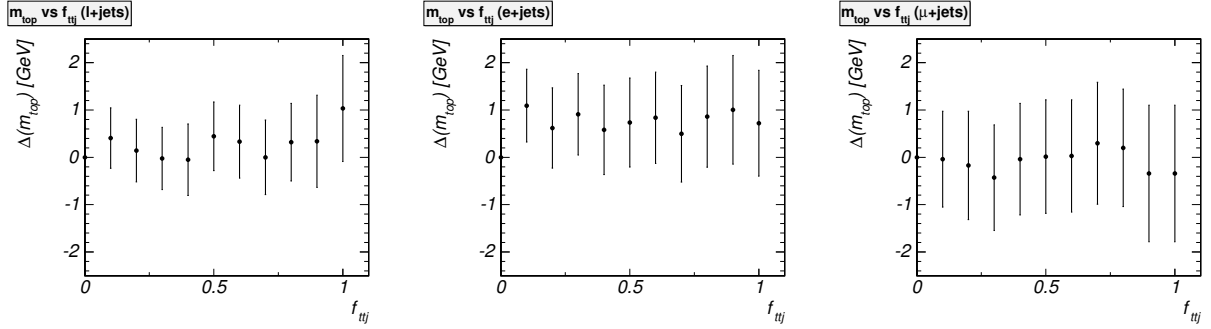


Figure 6.33: Difference between the fitted top mass in ensembles with fraction $f_{t\bar{t}j} > 0$ of $t\bar{t}$ +jet events and the default at $f_{t\bar{t}j} = 0$, as a function of $f_{t\bar{t}j}$. The error bars for values $0.1 \leq f_{t\bar{t}j} \leq 0.9$ do not reflect the statistical correlation between the respective ensembles. The systematic uncertainty is based on the error on Δm_{top} at $f_{t\bar{t}j} = 1$, times the expected $t\bar{t}$ +jets fraction in the data.

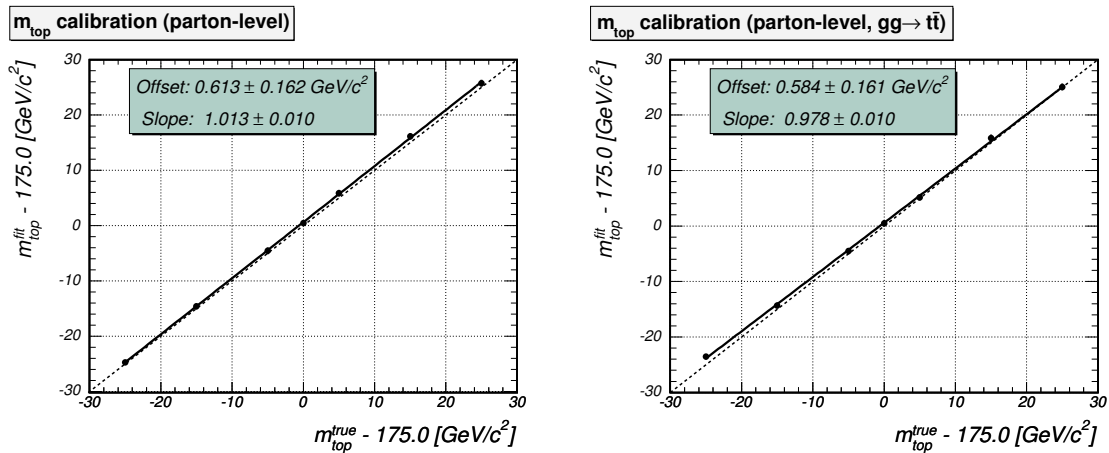


Figure 6.34: m_{top} calibrations for $gg \rightarrow t\bar{t}$ and $q\bar{q} \rightarrow t\bar{t}$ parton-level events. No statistically significant bias is observed.

6.7.5 Background Modeling

In order to study the sensitivity of the measurement to the choice of background model, the standard $W + \text{jets}$ Monte Carlo sample is replaced by an alternative sample with different factorization scale. Both samples are produced with the ALPGEN event generator and subsequently run through PYTHIA, which accounts for the showering of the final-state partons. The factorization scale in the default sample is

$$Q^2 = m_W^2 + \sum_j p_{T,j}^2 \quad (6.30)$$

whereas it is

$$Q^2 = \langle p_{T,j} \rangle^2 \quad (6.31)$$

for the alternative sample. Statistics for the alternative sample is limited, only 180 (208) events pass all selection criteria for the $e+\text{jets}$ ($\mu+\text{jets}$) channel. Therefore, the uncertainty is estimated by comparison of two large ensembles of ≈ 500 $\ell+\text{jets}$ events, such that the 388 alternative $W + \text{jets}$ events are sufficient considering the expected fraction of background events. The different expected signal fraction, not the lepton flavor is expected to be the dominant effect when varying the background model, and is taken into account for each channel. The fit of the sample with the default $W + \text{jets}$ events is calibrated and yields 175 GeV. The same calibration is applied to the alternative sample, and the difference of the two fits (Figure 6.35) yields the systematic error as

$$(\Delta m_{\text{top}})_{bkg.mod.}^{\ell+\text{jets}} = \pm 0.32 \text{ GeV} \quad (6.32)$$

$$(\Delta m_{\text{top}})_{bkg.mod.}^{e+\text{jets}} = \pm 0.66 \text{ GeV} \quad (6.33)$$

$$(\Delta m_{\text{top}})_{bkg.mod.}^{\mu+\text{jets}} = \pm 2.82 \text{ GeV} . \quad (6.34)$$

The observed shift is one-sided and symmetrized when quoting the systematic uncertainty.

6.7.6 Sample Composition

The normalization of the background probability and the mass calibration are performed for the signal fractions determined by the topological likelihood fit in Section 6.3.2. For the normalization of P_{bkg} , the f_{top} fit is required to yield the true signal fraction for jet-parton matched events on average, if the true $t\bar{t}$ fraction is given by the expectation for the topological likelihood fit. The f_{top} calibration curves for jet-parton matched events are shown in the left column of Figure 6.36 for $\ell+\text{jets}$, $e+\text{jets}$ and $\mu+\text{jets}$ events. The slope is in decent agreement with 1.0, indicating that the fit yields the correct signal fraction for any true $t\bar{t}$ fraction in the sample. The f_{top} calibration curves in the middle column of Figure 6.36 however reveal that the fit is slightly biased if all events are considered: it will systematically overestimate the signal fraction, if the true $t\bar{t}$ content is lower than expected, and vice versa. Underestimation of f_{top} by the fit is less critical: Some top events are treated as background, and the statistical power of the top mass fit decreases slightly. Overestimation of the signal fraction on the other hand leads to background events being treated as signal. As background events tend to yield low top mass estimates, the top mass fit will be biased accordingly. The dependence of the

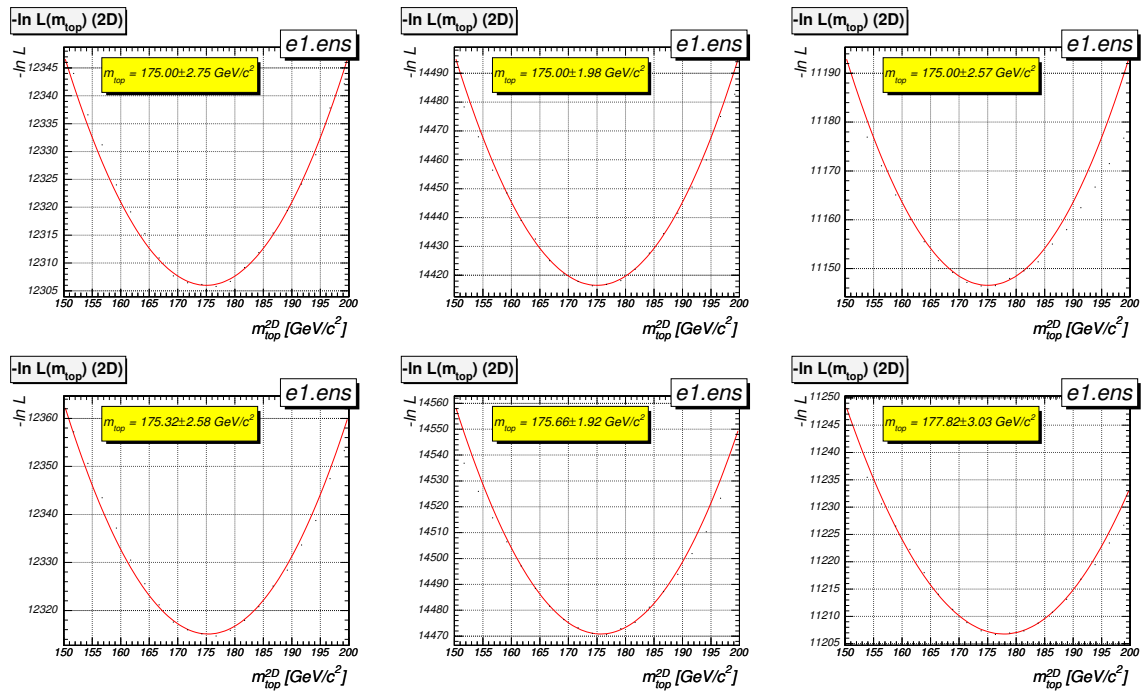


Figure 6.35: Mass fit to Monte Carlo samples with default and alternative $W + \text{jets}$ events. Each sample has ≈ 500 $e + \text{jets}$ and $\mu + \text{jets}$ events. The top fraction is set to the expectation in each channel. The same set of $t\bar{t}$ events but different types of $W + \text{jets}$ events are used in each comparison.

fitted top mass on the true signal fraction is shown in the right column of Figure 6.36, and the systematic uncertainty is based on the statistical uncertainty on the signal fraction estimate of the topological likelihood fit as shown in the figure:

$$(\Delta m_{\text{top}})_{\text{composition}}^{\ell+\text{jets}} = +0.50 - 0.17 \text{ GeV} \quad (6.35)$$

$$(\Delta m_{\text{top}})_{\text{composition}}^{e+\text{jets}} = +0.10 - 0.10 \text{ GeV} \quad (6.36)$$

$$(\Delta m_{\text{top}})_{\text{composition}}^{\mu+\text{jets}} = +0.48 - 0.38 \text{ GeV} . \quad (6.37)$$

6.7.7 QCD contamination

In addition to $W + \text{jets}$ events, the background contains a small fraction of multijet (QCD) events, which are not explicitly modeled in the likelihood. The measurement of the number of QCD events in the data sample is described in Section 6.3. Theoretical uncertainties on this kind of jet production are large and no suitable Monte Carlo model exists. Instead, a dedicated sample is extracted from data: reversal of the lepton isolation requirement yields a sample which is enriched in events where the lepton either is faked or within a jet which is not reconstructed, while passing all other selection criteria.

There are however both $t\bar{t}$ and $W + \text{jets}$ events in this sample. Furthermore, only 89 and 59 events are selected for the $e + \text{jets}$ and $\mu + \text{jets}$ samples respectively, not sufficient to construct statistically unbiased ensembles as described in Section 6.1. Nevertheless, the calibration is re-derived with the measured fraction of QCD events added to each ensemble, replacing the same number of simulated $W + \text{jets}$ events. The alternative calibrations are shown in Figure 6.37 and the systematic uncertainty is derived through application to the data sample and comparison with the nominal value:

$$(\Delta m_{\text{top}})_{QCD}^{\ell+\text{jets}} = \pm 0.67 \text{ GeV} \quad (6.38)$$

$$(\Delta m_{\text{top}})_{QCD}^{e+\text{jets}} = \pm 1.09 \text{ GeV} \quad (6.39)$$

$$(\Delta m_{\text{top}})_{QCD}^{\mu+\text{jets}} = \pm 0.29 \text{ GeV} . \quad (6.40)$$

6.7.8 MC Calibration

The calibration curves shown in Figure 6.20 and Figure A.5 come with a statistical uncertainty on the linear fit parameters. Each parameter is varied independently, and the m_{top} fit result is calibrated with each variation. The deviations from the result obtained with the default calibration are added in quadrature to obtain the systematic uncertainty:

$$(\Delta m_{\text{top}})_{\text{calib}}^{\ell+\text{jets}} = \pm 0.50 \text{ GeV} \quad (6.41)$$

$$(\Delta m_{\text{top}})_{\text{calib}}^{e+\text{jets}} = \pm 0.38 \text{ GeV} \quad (6.42)$$

$$(\Delta m_{\text{top}})_{\text{calib}}^{\mu+\text{jets}} = \pm 0.55 \text{ GeV} . \quad (6.43)$$

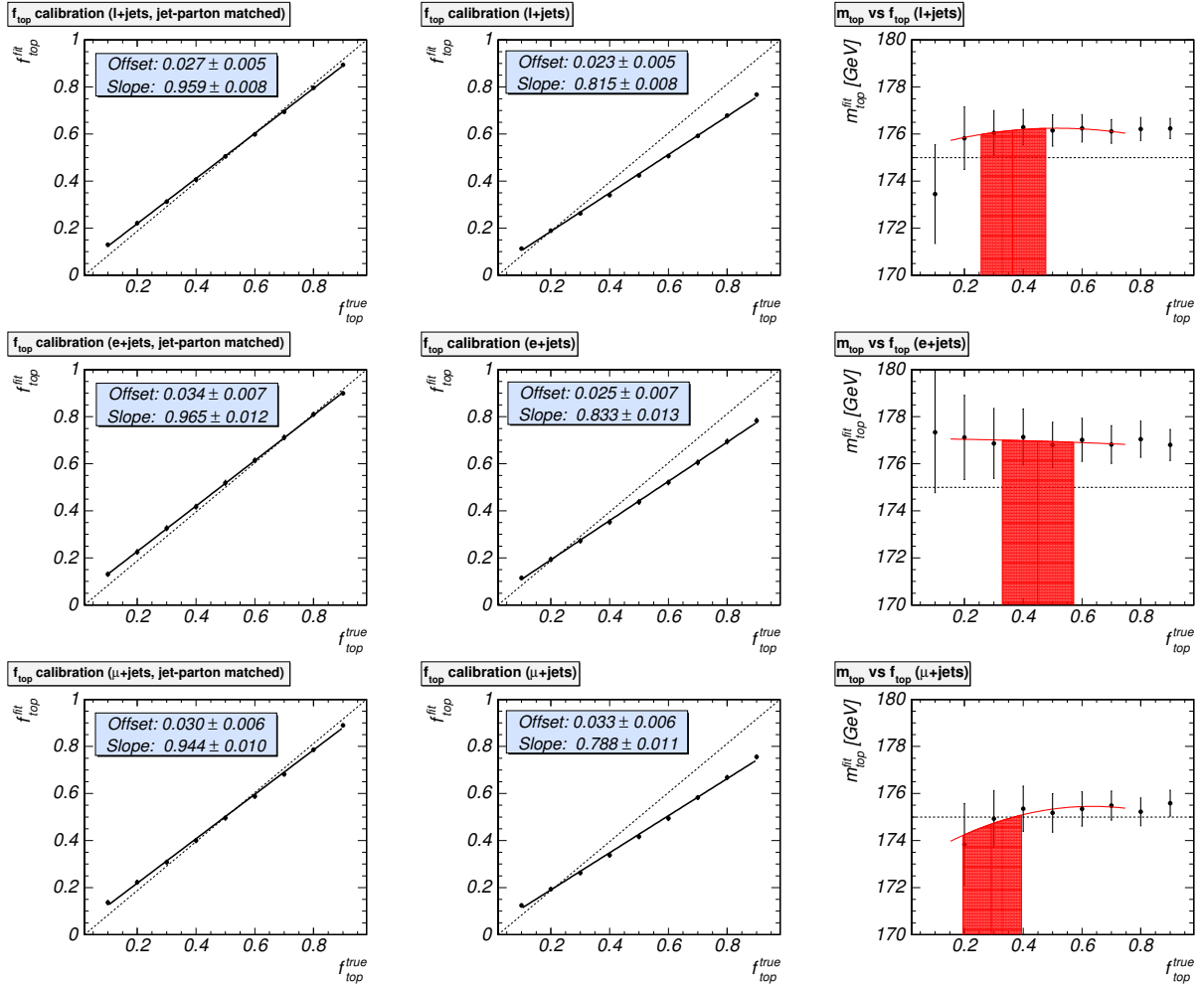


Figure 6.36: Mass bias as a function of the true signal fraction f_{top} . Based on the statistical uncertainty of the topological likelihood fit of the signal fraction. Left: f_{top} calibration for jet-parton matched events. Middle: f_{top} calibration for all selected events. Right: top mass bias as a function of the true signal fraction f_{top} . The error bands are based on the estimates derived with the topological likelihood fit.

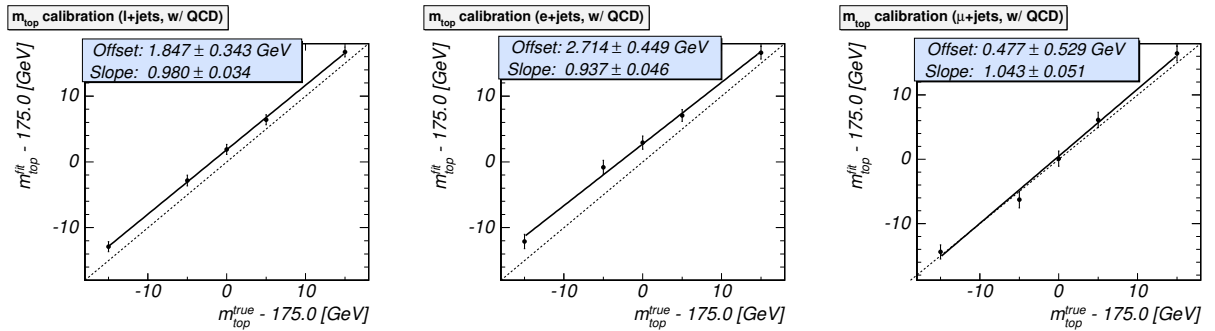


Figure 6.37: Calibration curves derived including admixture of QCD background.

Variation	ℓ +jets [GeV]	e+jets [GeV]	μ +jets [GeV]
EM Level1	± 0.02	± 0.03	± 0.00
EM Level2	± 0.00	± 0.00	± 0.00
EM Level3	± 0.00	± 0.01	± 0.00
MU Level1	± 0.03	± 0.00	± 0.07
MU Level2	± 0.07	± 0.00	± 0.04
MU Level3	± 0.00	± 0.00	± 0.00
JT Level1	± 0.00	± 0.00	± 0.00
JT Level2	± 0.00	± 0.00	± 0.00
JT Level3	± 0.03	± 0.01	± 0.21
TOTAL	± 0.08	± 0.03	± 0.22

Table 6.5: Systematic error on the top mass measurement due to trigger selection efficiencies.

6.7.9 Trigger

The efficiency for events to pass the $D\bar{O}$ trigger system is taken into account by calculating a weight for each event which reflects its probability to be accepted. This calculation is based on single-object turn-on curves for leptons and jets derived from data and described in Section 4.7. The tool takes different trigger versions into account and weights each contribution according to the corresponding integrated luminosity. Systematic variations of the single-object turn-on parametrizations are provided and the weight is recalculated for $\pm 1\sigma$ variations of each of them. The same ensembles are fitted for the nominal values and each variation, where the weights are adjusted accordingly. The $D\bar{O}$ trigger system consists of three levels, and a turn on is measured for each level as a function of transverse momentum and pseudorapidity. This yields 9 variations: electron (EM), muon (MU) and jets (JT) for Level1, Level2, and Level3. The results are summarized in Table 6.5, and combination of the single contributions yields

$$(\Delta m_{\text{top}})_{\text{trigger}}^{\ell+\text{jets}} = \pm 0.08 \text{ GeV} \quad (6.44)$$

$$(\Delta m_{\text{top}})_{\text{trigger}}^{e+\text{jets}} = \pm 0.03 \text{ GeV} \quad (6.45)$$

$$(\Delta m_{\text{top}})_{\text{trigger}}^{\mu+\text{jets}} = \pm 0.22 \text{ GeV} . \quad (6.46)$$

6.7.10 PDF Uncertainty

Leading-order matrix elements are used to calculate both P_{sgn} and P_{bkg} . Consequently, both calculations evaluate a leading order parton distribution function (PDF): CTEQ5L [54]. To study the systematic uncertainty on m_{top} due to this choice, the next-to-leading-order PDF set CTEQ6M [11] is used as it provides several variations accounting for its uncertainty. Parton-level events which are smeared according to the transfer function parameters found in Monte Carlo are used: A $t\bar{t}$ signal sample produced with MADGRAPH ($m_{\text{top}} = 175 \text{ GeV}$), and a $W + \text{jets}$ sample generated with ALPGEN. To avoid generation of large event samples with a different PDF, the default samples generated with CTEQ5L are used, and each event is

channel	n_{top}	n_{wjt}	f_{top}
ℓ +jets	572	1000	0.364
e+jets	815	1000	0.449
μ +jets	410	1000	0.291

Table 6.6: Ensemble composition for the evaluation of PDF uncertainty for ℓ +jets, e+jets and μ +jets respectively.

assigned a weight according to its q_1 and q_2 to represent CTEQ6M generation. q_1 and q_2 hereby denote the momentum fractions of the colliding partons relative to the proton (anti-proton) momentum. These weights are used as reference weights, and the reference top mass is obtained from one large ensemble per channel. The composition of each ensemble is given in Table 6.6. The integration technique remains unchanged, i.e. based on LO matrix elements and CTEQ5L PDF. The weights are then recomputed for each variation provided with the CTEQ6M PDF set and the same reference ensembles are refit using the alternative weights. The 20 variations described in [11] are considered, the results are summarized in Table 6.7. The total systematic uncertainty due to the choice of PDF is obtained by summing the individual contributions in quadrature:

$$(\Delta m_{top})_{PDF}^{\ell+jets} = \pm 0.07 \text{ GeV} \quad (6.47)$$

$$(\Delta m_{top})_{PDF}^{e+jets} = \pm 0.04 \text{ GeV} \quad (6.48)$$

$$(\Delta m_{top})_{PDF}^{\mu+jets} = \pm 0.08 \text{ GeV}. \quad (6.49)$$

6.7.11 Summary of Systematic Uncertainties

Table 6.8 summarizes all systematic uncertainties on the top mass measurement with the matrix element method. The total systematic uncertainty on the top mass measurement is obtained by adding all contributions in quadrature:

$$(\Delta m_{top})_{syst}^{\ell+jets} = +1.7 - 1.6 \text{ GeV} \quad (6.50)$$

$$(\Delta m_{top})_{syst}^{e+jets} = +1.9 - 1.9 \text{ GeV} \quad (6.51)$$

$$(\Delta m_{top})_{syst}^{\mu+jets} = +3.4 - 3.3 \text{ GeV}. \quad (6.52)$$

Variation	ℓ +jets [GeV]	e+jets [GeV]	μ +jets [GeV]
1	± 0.01	± 0.01	± 0.01
2	± 0.00	± 0.00	± 0.00
3	± 0.01	± 0.00	± 0.01
4	± 0.00	± 0.00	± 0.00
5	± 0.02	± 0.00	± 0.00
6	± 0.03	± 0.01	± 0.02
7	± 0.04	± 0.01	± 0.03
8	± 0.03	± 0.02	± 0.03
9	± 0.01	± 0.01	± 0.03
10	± 0.01	± 0.00	± 0.01
11	± 0.01	± 0.01	± 0.02
12	± 0.01	± 0.01	± 0.02
13	± 0.01	± 0.01	± 0.01
14	± 0.00	± 0.00	± 0.00
15	± 0.01	± 0.00	± 0.01
16	± 0.01	± 0.01	± 0.02
17	± 0.01	± 0.01	± 0.02
18	± 0.01	± 0.00	± 0.00
19	± 0.01	± 0.01	± 0.02
20	± 0.01	± 0.00	± 0.01
TOTAL	± 0.07	± 0.04	± 0.08

Table 6.7: Systematic error on the top mass measurement due to PDF uncertainties. Each line corresponds to one of the 20 uncertainties described in [11].

Uncertainty	ℓ +jets [GeV]	e+jets [GeV]	μ +jets [GeV]
JES p_T dependence	± 0.70	± 0.70	± 0.70
b fragmentation	± 0.71	± 0.86	± 0.92
b response (h/e)	$+0.87 - 0.75$	$+0.73 - 0.63$	$+1.11 - 0.96$
signal modeling	± 0.34	± 0.33	± 0.42
background modeling	± 0.32	± 0.66	± 2.82
signal fraction	$+0.50 - 0.17$	$+0.10 - 0.10$	$+0.48 - 0.38$
QCD contamination	± 0.67	± 1.09	± 0.29
MC calibration	± 0.38	± 0.55	± 0.50
trigger	± 0.08	± 0.03	± 0.22
PDF uncertainty	± 0.07	± 0.04	± 0.08
TOTAL	$+1.7 - 1.6$	$+1.9 - 1.9$	$+3.4 - 3.3$

Table 6.8: Summary of systematic uncertainties.

Chapter 7

Conclusion and Outlook

This thesis describes the first measurement of the top quark mass in ℓ +jets $t\bar{t}$ events with the matrix element method in DØ Run II data. The method underwent significant improvements with respect to the Run I measurement: the jet energy scale is now fitted simultaneously with the top quark mass in a two-dimensional correlated likelihood fit; the signal probability is calculated with a new algorithm based on a new and improved set of integration variables, yielding better precision while maintaining bearable processing times; the normalization of the signal probability is handled through full phase-space integration, translating kinematic selections regarding jets precisely to parton phase-space via the transfer functions; the muon momentum resolution is handled via an additional integration in data and Monte Carlo.

Events are selected requiring an isolated energetic charged lepton (electron or muon), significant missing transverse energy, and exactly four jets. For each selected event, a probability P_{sgn} is computed as a function of the assumed top mass m_{top} and the jet energy scale JES that this event is compatible with $t\bar{t}$ production. The algorithm for the computation of P_{sgn} has been newly developed. It takes into account the leading order matrix element for the process $q\bar{q} \rightarrow t\bar{t}$, the parton distribution functions for all quark flavours in the proton, as well as the resolutions for the jet energy and muon transverse momentum measurements in the detector. The trigger efficiency and detector acceptance are taken into account in the proper normalization of the quantity P_{sgn} .

Similarly, a background probability P_{bkg} is computed for each selected event. The P_{bkg} computation relies on the algorithm that was used in the Run I measurement. It uses the VECBOS program to calculate the probability for the $W(\rightarrow l\nu) + \text{jets}$ process.

The method has been tested extensively on parton-level Monte Carlo. The measured mass has been found to agree well with the input mass, and the uncertainty obtained is reproduced in the ensemble tests. It has then been calibrated using ensemble tests with Monte Carlo events that have passed the same DØ event reconstruction as the data.

The matrix element method has then been applied on a dataset of 320 pb^{-1} of DØ Run II data and yields

$$\begin{aligned} m_{\text{top}}^{\ell+\text{jets}} &= 169.5 \pm 4.4 (\text{stat.} + \text{JES})_{-1.6}^{+1.7} (\text{syst.}) \text{ GeV} \\ m_{\text{top}}^{e+\text{jets}} &= 168.8 \pm 6.0 (\text{stat.} + \text{JES})_{-1.9}^{+1.9} (\text{syst.}) \text{ GeV} \\ m_{\text{top}}^{\mu+\text{jets}} &= 172.3 \pm 9.6 (\text{stat.} + \text{JES})_{-3.3}^{+3.4} (\text{syst.}) \text{ GeV} . \end{aligned}$$

The jet energy scale measurement in the ℓ +jets sample yields $JES = 1.034 \pm 0.34$, suggesting good consistency of the data with the simulation.

The above result contributes to a new preliminary derivation of the top mass world average, where preliminary results from both DØ and CDF in Run II are combined with Run I results [55]. The new preliminary world average is

$$m_{\text{top}} = 172.7 \pm 1.7 \text{ (stat.)} \pm 2.4 \text{ (syst.) GeV} , \quad (7.1)$$

and the individual measurements are summarized in Figure 7.1. Adding the statistical and systematic uncertainties in quadrature yields the total uncertainty as ± 2.9 GeV. Figure 7.2 illustrates the impact of the new preliminary top mass combination on the most likely value of the Higgs boson mass with respect to the previous world average of the top mass [56].

Significant improvements of the DØ top mass measurement can be expected over the next years, as the final Run II data sample is projected to exceed the current sample by more than a factor of ten in size. Thanks to the consideration of the jet energy scale in the likelihood fit, both the statistical and dominant systematic uncertainty will benefit from a larger dataset. Big potential lies in the combination of information from the calorimeter and the newly installed tracking system: Tracks which are significantly displaced from the primary interaction vertex indicate that a jet originates from a b quark, and the number of physical jet permutations considered in the P_{sgn} calculation can be reduced; and the most important ingredient to a precise mass measurement, the jet energy resolution, can be significantly improved by considering the momentum measurements of tracks pointing to the respective calorimeter cluster. The current measurement establishes a strong base for the upcoming exciting era of precision measurements at the Tevatron, which will likely see the total uncertainty of the m_{top} world average drop below 2 GeV before startup of the LHC.

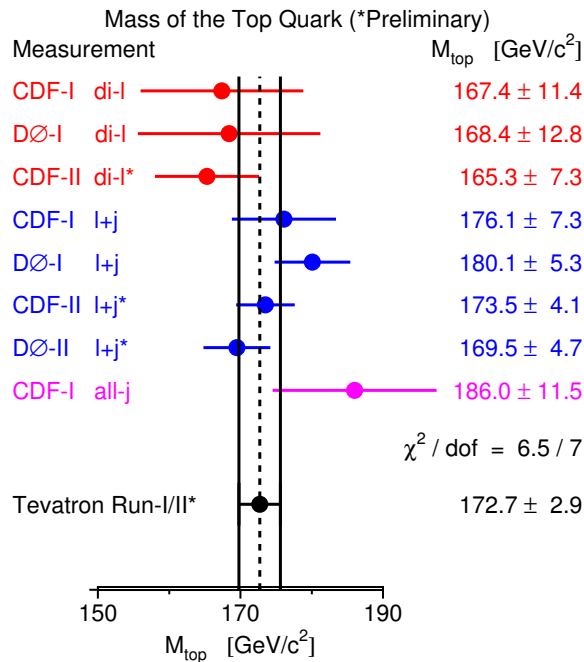


Figure 7.1: Summary of all individual measurements contributing to the new preliminary top mass combination. The DØ measurement presented in this thesis is labeled “DØ-II l+j”.

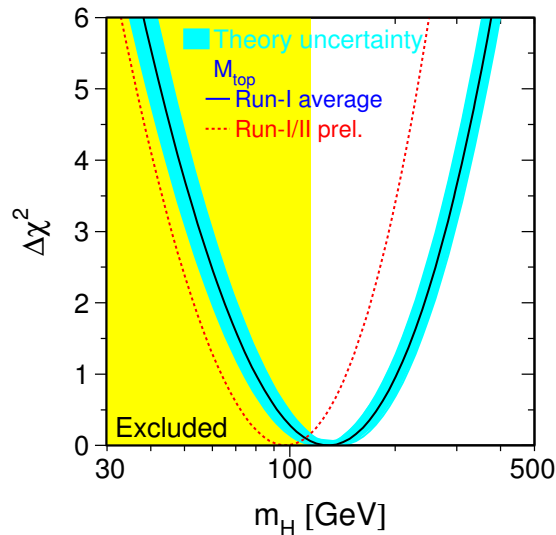


Figure 7.2: Current experimental constraints on the mass of the Higgs boson [56] (preliminary). The χ^2 of a global fit to electroweak data is shown as a function of the Higgs mass. The solid line corresponds to the result for the previous world average of the top quark mass of 178.0 ± 4.3 GeV. The dotted line shows the result for the new world average of the top quark mass of 172.7 ± 2.9 GeV.

Appendix A

MC Calibration for $e + jets$ and $\mu + jets$ events

The bias and pull calibration of the mass fitting procedure is described in detail in Section 6.4 for the combined $\ell+jets$ channel. The measurement of the top quark mass in the $e+jets$ and $\mu+jets$ channels serves as a cross check to the $\ell+jets$ measurement, and the corresponding calibration plots are presented.

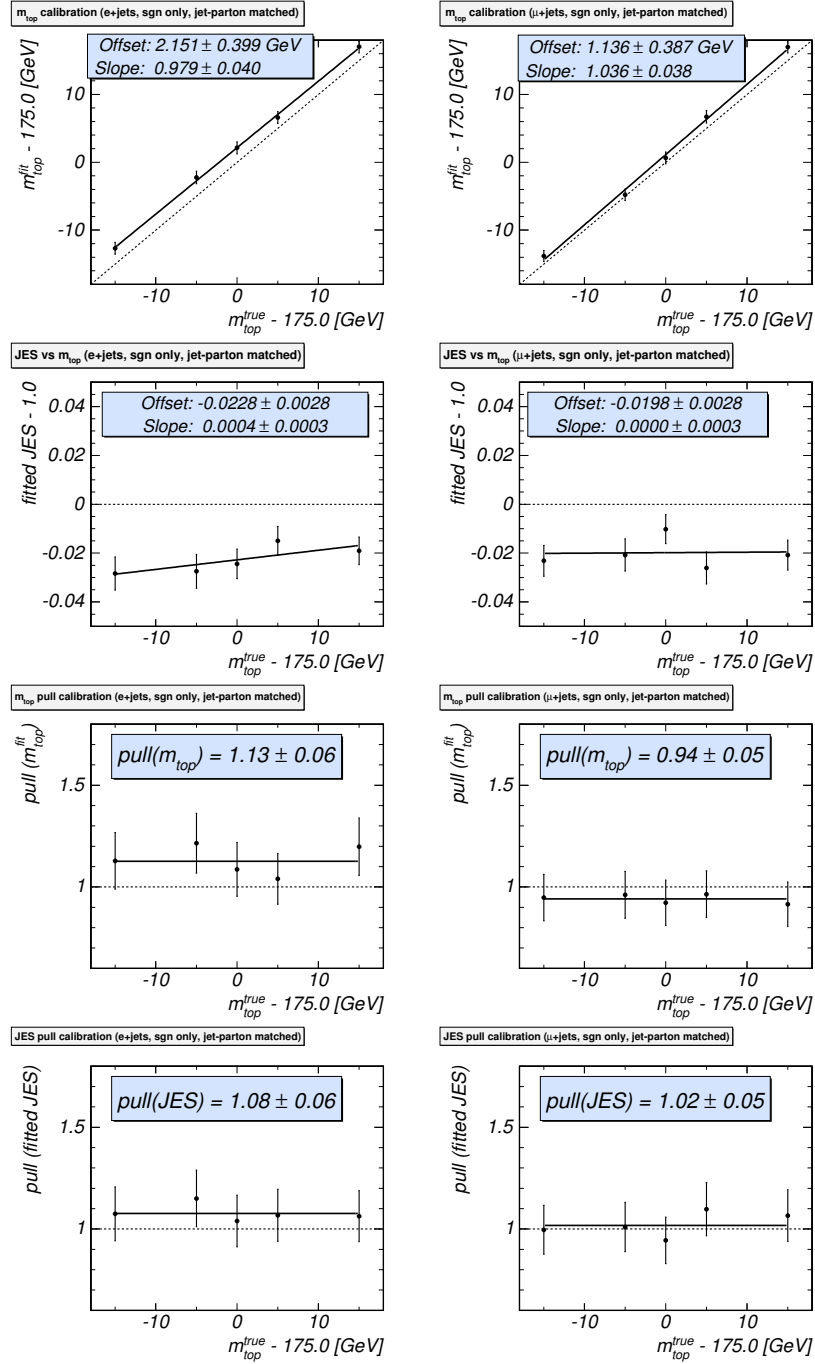


Figure A.1: Fitted m_{top} , JES , and corresponding pull calibrations for jet-parton matched $e+jets$ (left) and $\mu+jets$ (right) signal events as a function of the true top quark mass.

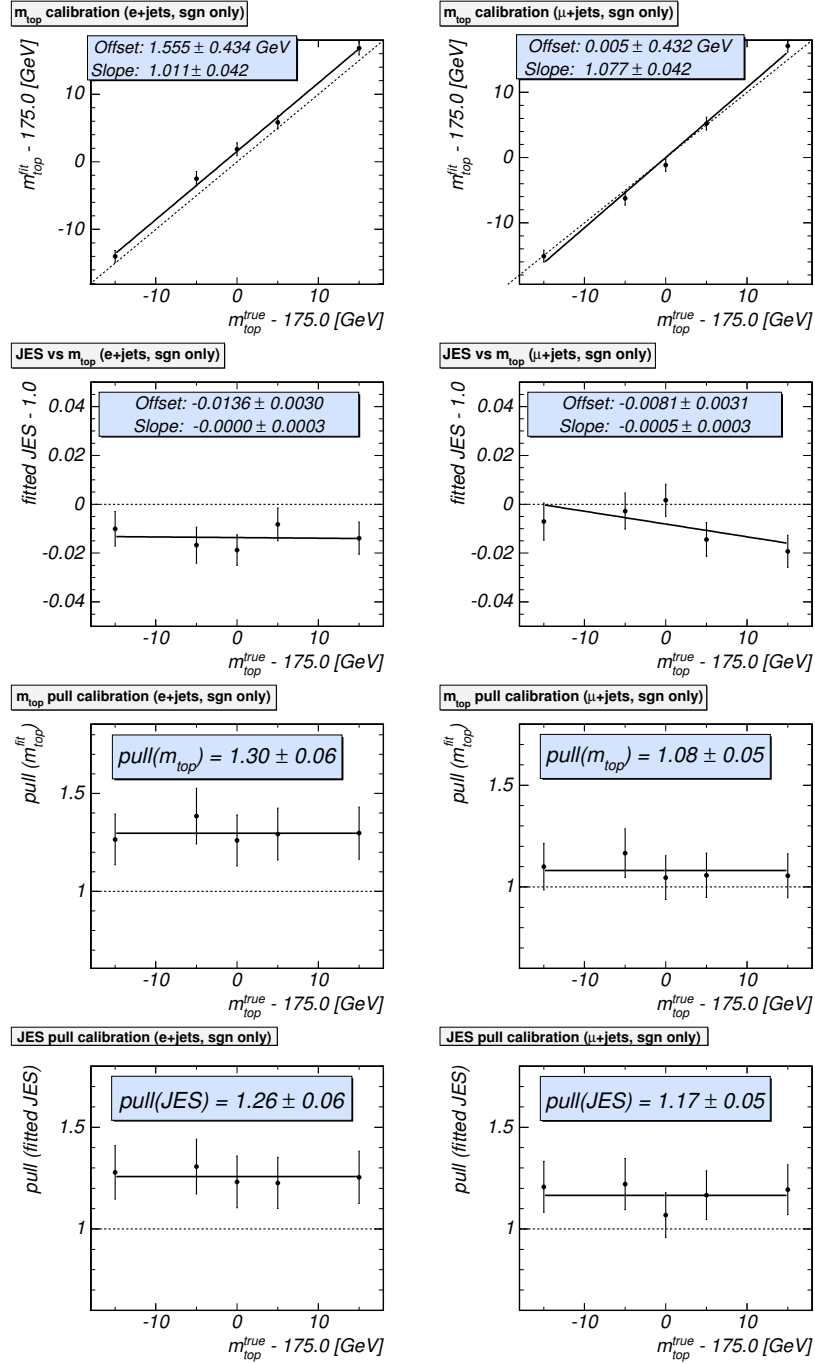


Figure A.2: Fitted m_{top} , JES , and corresponding pull calibrations for $e+\text{jets}$ (left) and $\mu+\text{jets}$ (right) signal events as a function of the true top quark mass.

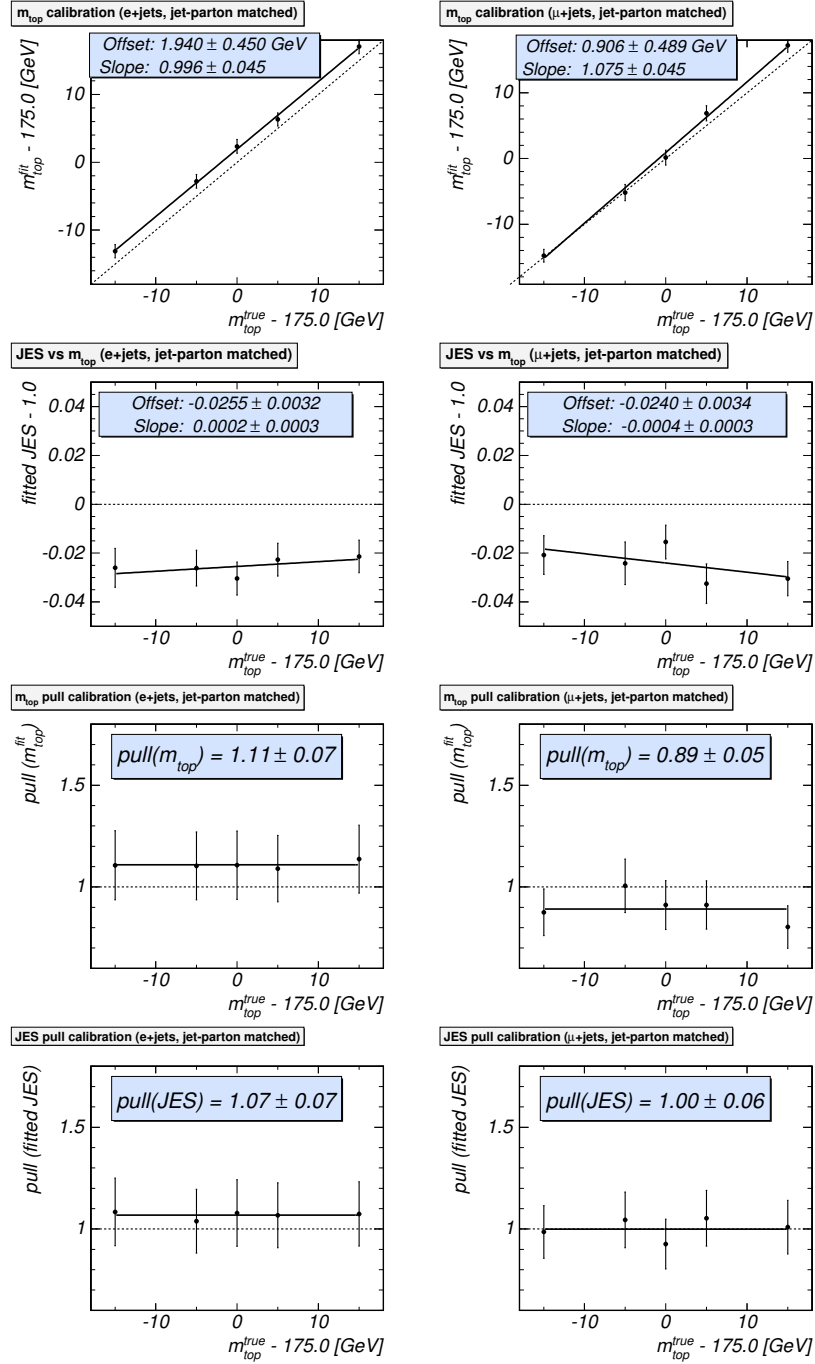


Figure A.3: Fitted m_{top} , JES , and corresponding pull calibrations for jet-parton matched $e+jets$ (left) and $\mu+jets$ (right) events as a function of the true top quark mass.

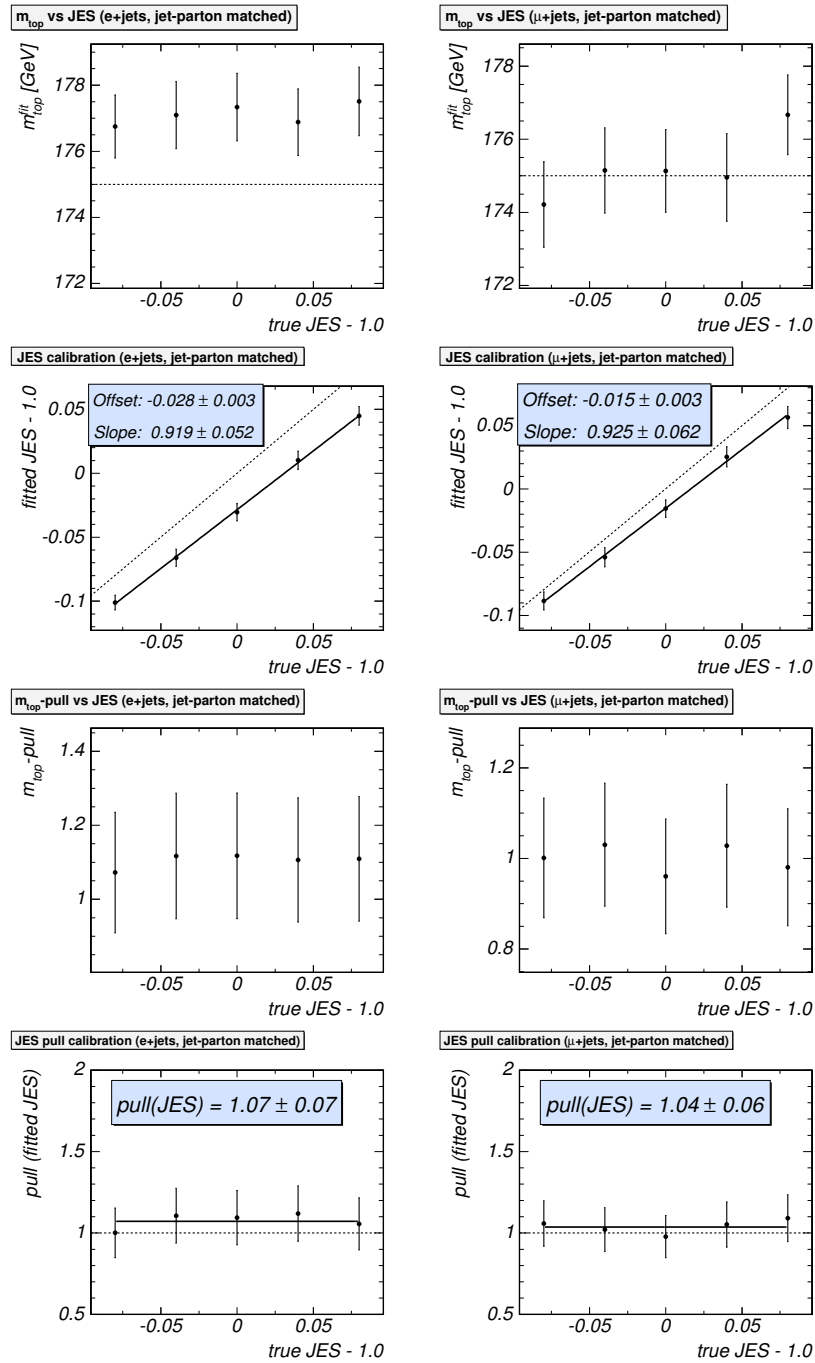


Figure A.4: Fitted m_{top} , JES , and corresponding pull calibrations for jet-parton matched e +jets (left) and μ +jets (right) events as a function of the true jet energy scale.

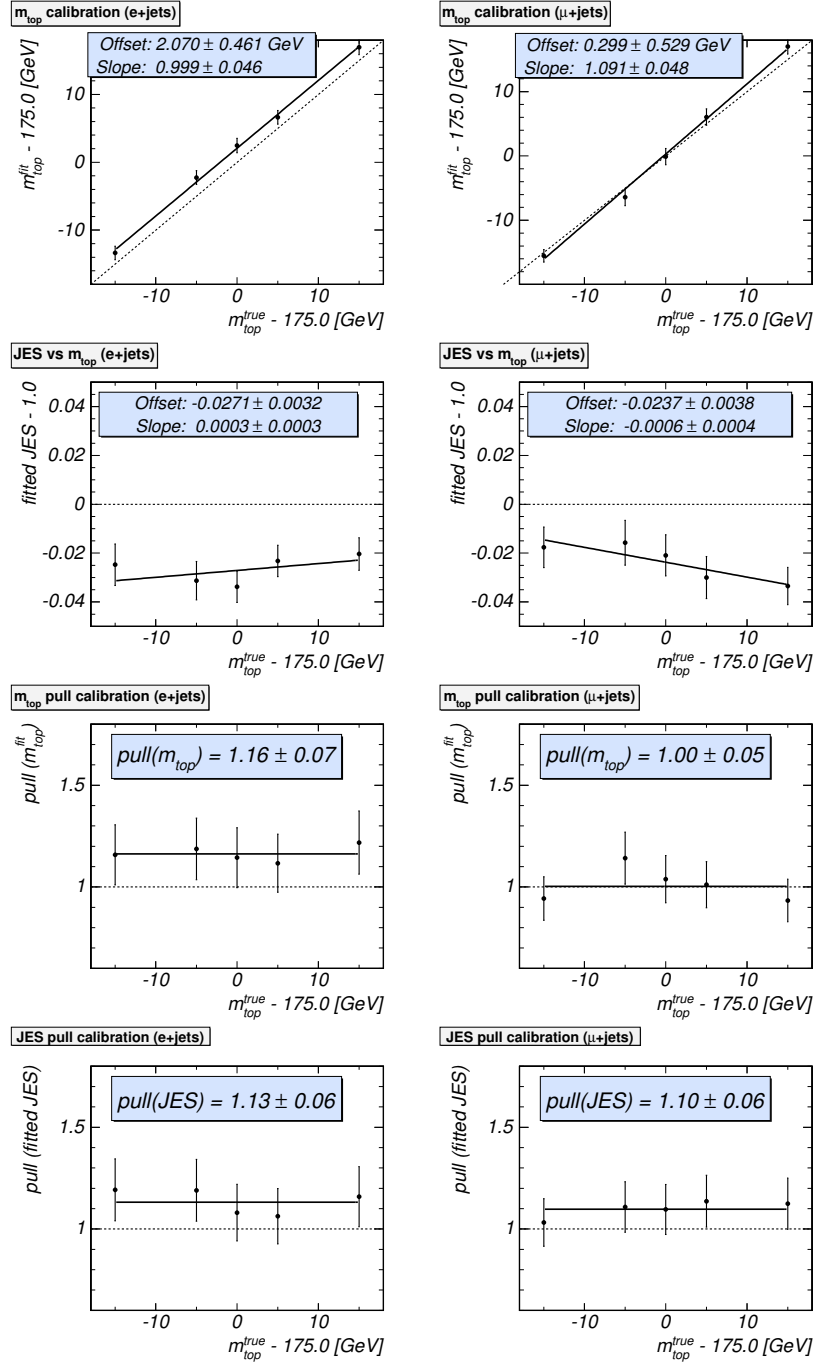


Figure A.5: Final calibration: fitted m_{top} , JES , and corresponding pull calibrations for $e+jets$ (left) and $\mu+jets$ (right) events as a function of the true top quark mass.

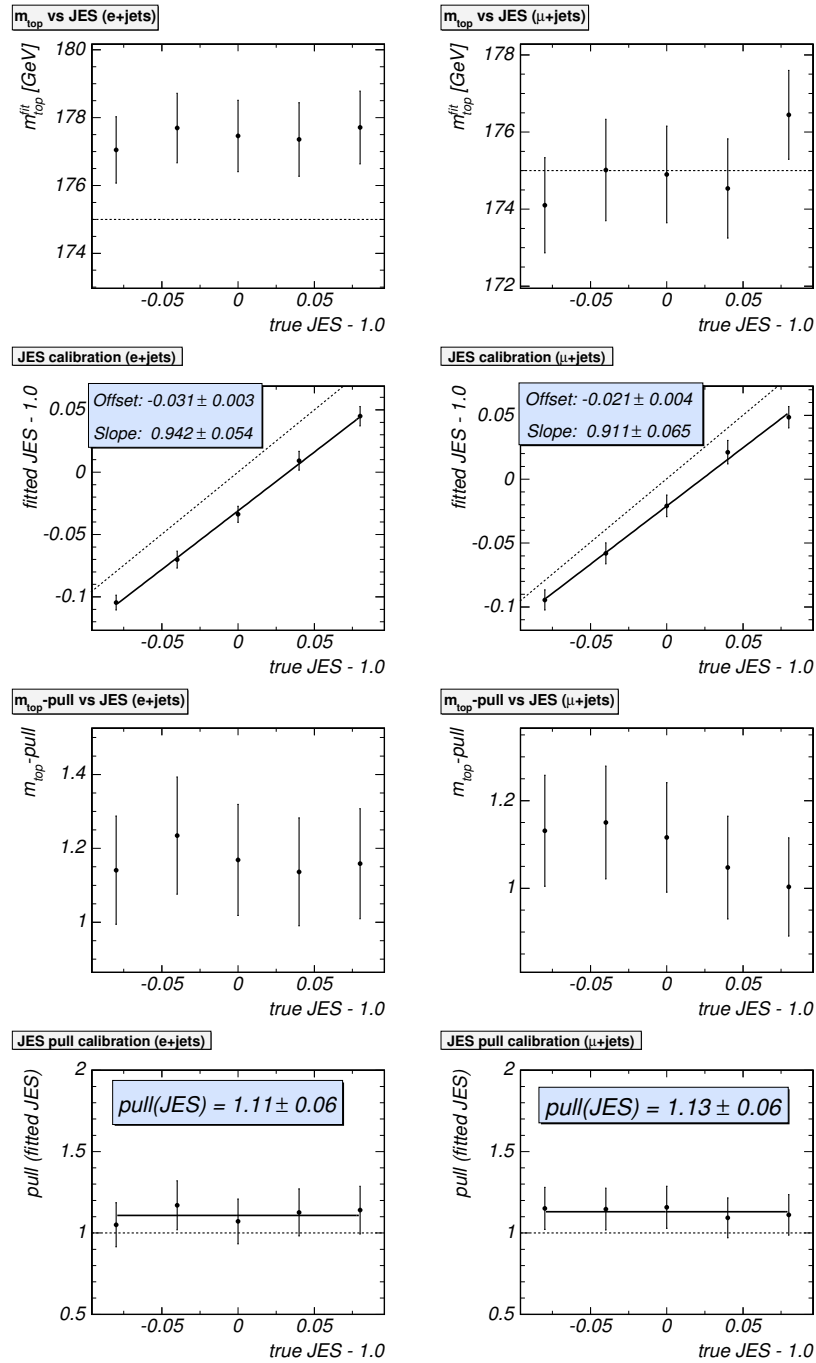


Figure A.6: Final calibration: fitted m_{top} , JES , and corresponding pull calibrations for $e+jets$ (left) and $\mu+jets$ (right) events as a function of the true jet energy scale.

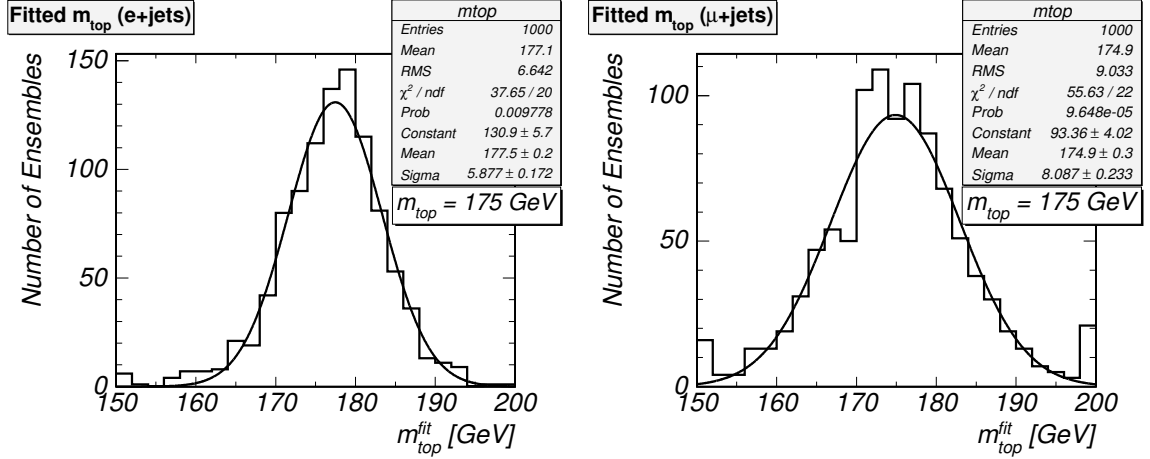


Figure A.7: Fitted m_{top} distributions for $m_{top} = 175 \text{ GeV}$ for e+jets (left) and μ +jets (right) events.

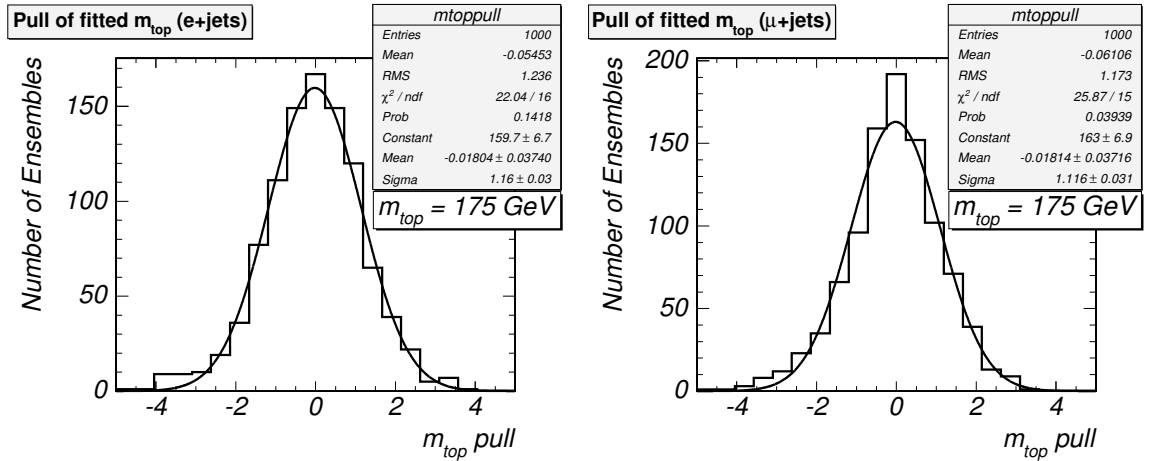


Figure A.8: Fitted m_{top} -pull distributions for $m_{top} = 175 \text{ GeV}$ for e+jets (left) and μ +jets (right) events.

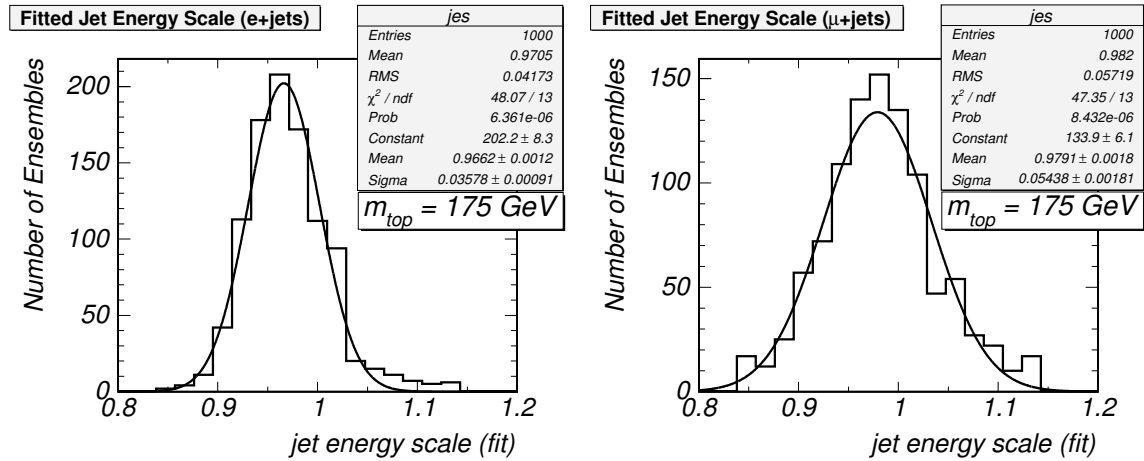


Figure A.9: Fitted JES distributions for $m_{\text{top}} = 175 \text{ GeV}$ for e+jets (left) and μ +jets (right) events.

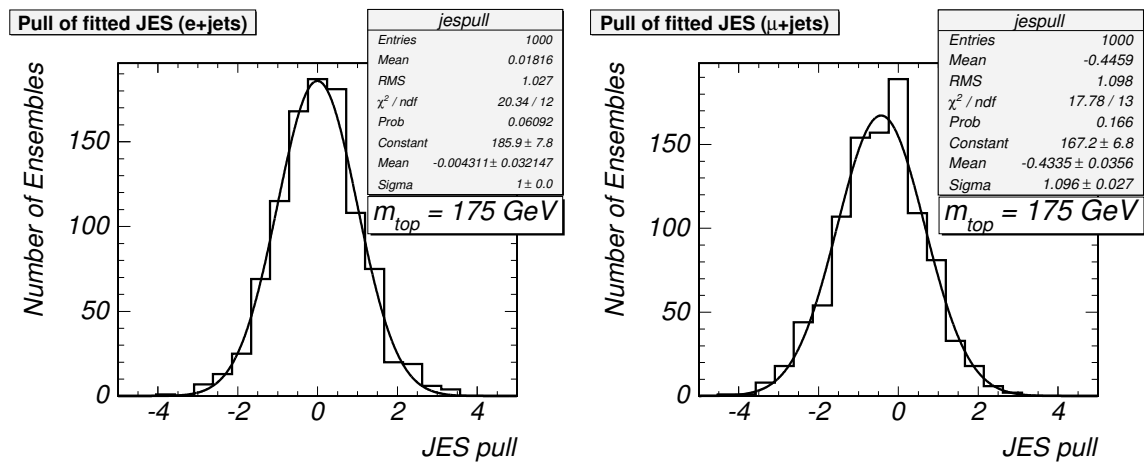


Figure A.10: Fitted JES -pull distributions for $m_{\text{top}} = 175 \text{ GeV}$ for e+jets (left) and μ +jets (right) events.

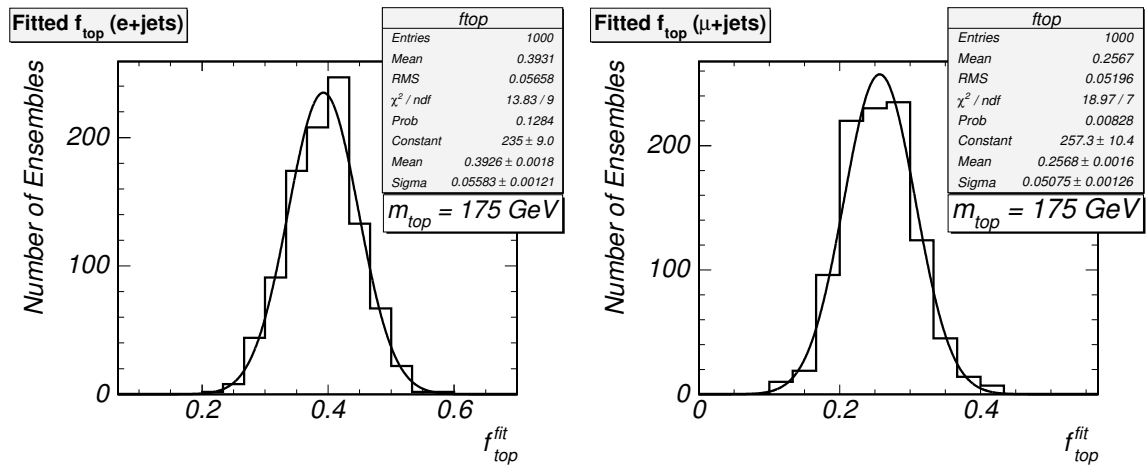


Figure A.11: Fitted signal fraction f_{top} for $m_{top} = 175 \text{ GeV}$ for e+jets (left) and μ +jets (right) events.

Appendix B

Solving the Event Kinematics

As stated in Section 5.3.1, the 4-momenta of the $t\bar{t}$ decay products have to be calculated from the values of the integration variables $|\vec{p}_d|$, $m_{d\bar{u}}^2$, $m_{b\bar{d}\bar{u}}^2$, $m_{b\ell\nu}^2$, $p_{b\nu}^z$, and q_μ/p_μ^T (in the μ +jets case), the measured jet and lepton angles, and the electron energy (in the e+jets case). The calculation is derived in this section.

In the following, p_a is the 4-momentum of particle a , and similarly m_a , E_a , and $|\vec{p}_a|$ are its mass, energy, and momentum magnitude in the laboratory frame, respectively. The symbol p_{ab} is defined as the sum of the 4-momenta of particles a and b ; corresponding notations are used for their energy and the magnitude of the sum of their momenta. The angle between particles a and b in the laboratory frame is denoted by $\alpha_{a,b}$, and M_{had} is defined as $M_{had} = \frac{1}{2} (m_{b\bar{d}\bar{u}}^2 - m_b^2 - m_{d\bar{u}}^2)$.

The momentum $|\vec{p}_{\bar{u}}|$ of the second quark from the hadronically decaying W is obtained as

$$m_{d\bar{u}}^2 = 2|\vec{p}_d||\vec{p}_{\bar{u}}|(1 - \cos \alpha_{d,\bar{u}}) \quad (\text{B.1})$$

$$\Leftrightarrow |\vec{p}_{\bar{u}}| = \frac{m_{d\bar{u}}^2}{2|\vec{p}_d|(1 - \cos \alpha_{d,\bar{u}})} \quad (\text{B.2})$$

The momentum $|\vec{p}_{\bar{b}}|$ of the b-quark from the corresponding top quark can be derived as follows (the notation in this section reflects the case where the anti-top quark decays to the hadronically decaying W boson):

$$m_{b\bar{d}\bar{u}}^2 = m_b^2 + m_{d\bar{u}}^2 + 2(E_{\bar{b}}E_{d\bar{u}} - \vec{p}_{\bar{b}} \cdot \vec{p}_{d\bar{u}}) \quad (\text{B.3})$$

$$\Leftrightarrow \frac{M_{had} + |\vec{p}_{\bar{b}}||\vec{p}_{d\bar{u}}| \cos \alpha_{\bar{b},d\bar{u}}}{E_{d\bar{u}}} = \sqrt{|\vec{p}_{\bar{b}}|^2 + m_b^2} \quad (\text{B.4})$$

After squaring, Equation (B.4) yields a quadratic equation. With $A = \frac{|\vec{p}_{d\bar{u}}|}{E_{d\bar{u}}} \cos \alpha_{\bar{b},d\bar{u}}$ one obtains:

$$|\vec{p}_{\bar{b}}| = \frac{AM_{had}}{(1 - A^2)E_{d\bar{u}}} + \sqrt{\left(\frac{AM_{had}}{(1 - A^2)E_{d\bar{u}}}\right)^2 + \frac{\frac{M_{b\bar{d}\bar{u}}^2}{E_{d\bar{u}}^2} - m_b^2}{1 - A^2}}. \quad (\text{B.5})$$

The second solution is negative and therefore not considered. Note that Equation (B.4) only has a solution if $M_{had} + |\vec{p}_{\bar{b}}||\vec{p}_{d\bar{u}}| \cos \alpha_{\bar{b},d\bar{u}} > 0$, which has to be checked with the value computed from Equation (B.5).

The momentum $|\vec{p}_b|$ of the b-quark from the top quark with the leptonically decaying W can be obtained from the invariant mass of this top quark:

$$m_{b\ell\nu}^2 = m_b^2 + 2(p_b p_\ell + p_b p_\nu + p_\ell p_\nu) \quad (\text{B.6})$$

$$= m_b^2 + 2(p_b p_\ell + p_b(p_{b\nu} - p_b) + p_\ell(p_{b\nu} - p_b)) \quad (\text{B.7})$$

$$= -m_b^2 + 2(p_b p_{b\nu} + p_\ell p_{b\nu}) \quad (\text{B.8})$$

Here, the neutrino 4-momentum has been expressed as the difference between $p_{b\nu} = p_b + p_\nu$ and p_b . This is helpful because $p_{b\nu} = p_{b\ell\nu} - p_\ell$, and $p_{b\ell\nu}$ can be inferred directly from the integration variables: $p_{b\ell\nu}^x = -p_{bd\bar{u}}^x$ and $p_{b\ell\nu}^y = -p_{bd\bar{u}}^y$, since the $t\bar{t}$ system is assumed to have zero transverse momentum; $p_{b\ell\nu}^z = p_{b\nu}^z + p_\ell^z$ where $p_{b\nu}^z$ is an integration variable itself; and $E_{b\ell\nu}$ can be obtained since $m_{b\ell\nu}^2$ is an integration variable. The 4-momentum of the lepton is assumed to be well measured (electron case) or can be directly inferred from one integration variable (muon case). One then obtains an expression for the magnitude of the momentum of the b quark from the top decay with the leptonically decaying W as follows:

$$m_{b\ell\nu}^2 + m_b^2 - 2p_\ell p_{b\nu} = 2(E_b E_{b\nu} - |\vec{p}_b| |\vec{p}_{b\nu}| \cos \alpha_{b,b\nu}) \quad (\text{B.9})$$

$$\Leftrightarrow \underbrace{\frac{m_{b\ell\nu}^2 + m_b^2 - 2p_\ell p_{b\nu}}{2E_{b\nu}}}_{=:G} = E_b - |\vec{p}_b| \underbrace{\frac{|\vec{p}_{b\nu}|}{E_{b\nu}} \cos \alpha_{b,b\nu}}_{=:H} \quad (\text{B.10})$$

$$\Rightarrow (G + |\vec{p}_b| H)^2 = |\vec{p}_b|^2 + m_b^2 \quad (\text{B.11})$$

$$\Rightarrow |\vec{p}_b| = \frac{GH}{1 - H^2} \pm \sqrt{\left(\frac{GH}{1 - H^2}\right)^2 + \frac{G^2 - m_b^2}{1 - H^2}}. \quad (\text{B.12})$$

The neutrino momentum can now be obtained from $\vec{p}_\nu = \vec{p}_{b\ell\nu} - \vec{p}_b - \vec{p}_\ell$. In the above computation, it has to be checked that a physical solution is obtained; otherwise the point in integration space does not contribute to the integral that yields P_{sgn} . This applies for example to the transition from Equation (B.10) to Equation (B.11), where it must be checked that the solution of the squared equation also solves the original one.

The energies of the colliding partons are given by

$$E_\pm = \frac{1}{2} (E_{b\ell\nu\bar{b}d\bar{u}} \pm p_{b\ell\nu\bar{b}d\bar{u}}^z). \quad (\text{B.13})$$

It has to be checked that both parton energies are smaller than the beam energy.

Appendix C

The Jacobian Determinant for the P_{sgn} Integration

In the following, the Jacobian determinant for the transition from an integral over parton momenta in spherical coordinates to an integral over the integration variables $|\vec{p}_d|$, $m_{d\bar{u}}^2$, $m_{b\bar{d}\bar{u}}^2$, $m_{b\ell\nu}^2$, and $p_{b\nu}^z$ is derived. The determinant is

$$\begin{aligned}
 \det(J) &= \det \begin{pmatrix} \frac{\partial|\vec{p}_d|}{\partial|\vec{p}_d|} & \frac{\partial m_{d\bar{u}}^2}{\partial|\vec{p}_d|} & \frac{\partial m_{b\bar{d}\bar{u}}^2}{\partial|\vec{p}_d|} & \frac{\partial m_{b\ell\nu}^2}{\partial|\vec{p}_d|} & \frac{\partial p_{b\nu}^z}{\partial|\vec{p}_d|} \\ \frac{\partial|\vec{p}_d|}{\partial|\vec{p}_{\bar{u}}|} & \frac{\partial m_{d\bar{u}}^2}{\partial|\vec{p}_{\bar{u}}|} & \frac{\partial m_{b\bar{d}\bar{u}}^2}{\partial|\vec{p}_{\bar{u}}|} & \frac{\partial m_{b\ell\nu}^2}{\partial|\vec{p}_{\bar{u}}|} & \frac{\partial p_{b\nu}^z}{\partial|\vec{p}_{\bar{u}}|} \\ \frac{\partial|\vec{p}_d|}{\partial|\vec{p}_b|} & \frac{\partial m_{d\bar{u}}^2}{\partial|\vec{p}_b|} & \frac{\partial m_{b\bar{d}\bar{u}}^2}{\partial|\vec{p}_b|} & \frac{\partial m_{b\ell\nu}^2}{\partial|\vec{p}_b|} & \frac{\partial p_{b\nu}^z}{\partial|\vec{p}_b|} \\ \frac{\partial|\vec{p}_d|}{\partial|\vec{p}_b|} & \frac{\partial m_{d\bar{u}}^2}{\partial|\vec{p}_b|} & \frac{\partial m_{b\bar{d}\bar{u}}^2}{\partial|\vec{p}_b|} & \frac{\partial m_{b\ell\nu}^2}{\partial|\vec{p}_b|} & \frac{\partial p_{b\nu}^z}{\partial|\vec{p}_b|} \\ \frac{\partial|\vec{p}_d|}{\partial p_{b\nu}^z} & \frac{\partial m_{d\bar{u}}^2}{\partial p_{b\nu}^z} & \frac{\partial m_{b\bar{d}\bar{u}}^2}{\partial p_{b\nu}^z} & \frac{\partial m_{b\ell\nu}^2}{\partial p_{b\nu}^z} & \frac{\partial p_{b\nu}^z}{\partial p_{b\nu}^z} \end{pmatrix} \\
 &= \det \begin{pmatrix} 1 & \frac{\partial m_{d\bar{u}}^2}{\partial|\vec{p}_d|} & \frac{\partial m_{b\bar{d}\bar{u}}^2}{\partial|\vec{p}_d|} & \frac{\partial m_{b\ell\nu}^2}{\partial|\vec{p}_d|} & 0 \\ 0 & \frac{\partial m_{d\bar{u}}^2}{\partial|\vec{p}_{\bar{u}}|} & \frac{\partial m_{b\bar{d}\bar{u}}^2}{\partial|\vec{p}_{\bar{u}}|} & \frac{\partial m_{b\ell\nu}^2}{\partial|\vec{p}_{\bar{u}}|} & 0 \\ 0 & 0 & \frac{\partial m_{b\bar{d}\bar{u}}^2}{\partial|\vec{p}_b|} & \frac{\partial m_{b\ell\nu}^2}{\partial|\vec{p}_b|} & 0 \\ 0 & 0 & 0 & \frac{\partial m_{b\ell\nu}^2}{\partial|\vec{p}_b|} & \frac{\partial p_{b\nu}^z}{\partial|\vec{p}_b|} \\ 0 & 0 & 0 & \frac{\partial m_{b\ell\nu}^2}{\partial p_{b\nu}^z} & \frac{\partial p_{b\nu}^z}{\partial p_{b\nu}^z} \end{pmatrix} \\
 &= \frac{\partial m_{d\bar{u}}^2}{\partial|\vec{p}_{\bar{u}}|} \frac{\partial m_{b\bar{d}\bar{u}}^2}{\partial|\vec{p}_b|} \left(\frac{\partial m_{b\ell\nu}^2}{\partial|\vec{p}_b|} \frac{\partial p_{b\nu}^z}{\partial p_{b\nu}^z} - \frac{\partial p_{b\nu}^z}{\partial|\vec{p}_b|} \frac{\partial m_{b\ell\nu}^2}{\partial p_{b\nu}^z} \right). \tag{C.1}
 \end{aligned}$$

To derive the relevant derivatives, it is important to note that the transverse momentum components of the neutrino (and thus also its energy) implicitly depend on the energies of all other final state particles through the condition that the $t\bar{t}$ transverse momentum be zero. In particular, the dependence on the momentum $|\vec{p}_b|$ of the b quark from the top with the leptonic W decay is (where u_a^x stands for the x component of the unit vector along the direction of \vec{p}_a etc.)

$$\frac{\partial p_\nu^x}{\partial |\vec{p}_b|} = -u_b^x \quad (\text{C.2})$$

$$\frac{\partial p_\nu^y}{\partial |\vec{p}_b|} = -u_b^y \quad (\text{C.3})$$

$$\frac{\partial p_\nu^z}{\partial |\vec{p}_b|} = 0 \quad (\text{C.4})$$

$$\begin{aligned} \frac{\partial E_\nu}{\partial |\vec{p}_b|} &= \frac{\partial \left(\sqrt{p_\nu^{x2} + p_\nu^{y2} + p_\nu^{z2}} \right)}{\partial |\vec{p}_b|} \\ &= \frac{1}{E_\nu} \left(p_\nu^x \frac{\partial p_\nu^x}{\partial |\vec{p}_b|} + p_\nu^y \frac{\partial p_\nu^y}{\partial |\vec{p}_b|} \right) \\ &= -(u_\nu^x u_b^x + u_\nu^y u_b^y) . \end{aligned} \quad (\text{C.5})$$

The partial derivatives relevant for the Jacobian are then

$$\begin{aligned} \frac{\partial m_{d\bar{u}}^2}{\partial |\vec{p}_u|} &= \frac{\partial (2|\vec{p}_d||\vec{p}_u| (1 - \cos \alpha_{d,\bar{u}}))}{\partial |\vec{p}_u|} \\ &= 2|\vec{p}_d| (1 - \cos \alpha_{d,\bar{u}}) \end{aligned} \quad (\text{C.6})$$

$$\begin{aligned} \frac{\partial m_{b\bar{d}}^2}{\partial |\vec{p}_b|} &= \frac{\partial (m_b^2 + 2(E_{\bar{b}}E_d - \vec{p}_{\bar{b}} \cdot \vec{p}_d + E_{\bar{b}}E_{\bar{u}} - \vec{p}_{\bar{b}} \cdot \vec{p}_{\bar{u}} + E_dE_{\bar{u}} - \vec{p}_d \cdot \vec{p}_{\bar{u}}))}{\partial |\vec{p}_b|} \\ &= 2 \left(|\vec{p}_d| \left(\frac{\partial E_{\bar{b}}}{\partial |\vec{p}_b|} - \cos \alpha_{d,\bar{b}} \right) + |\vec{p}_{\bar{u}}| \left(\frac{\partial E_{\bar{b}}}{\partial |\vec{p}_b|} - \cos \alpha_{\bar{u},\bar{b}} \right) \right) \\ &= 2|\vec{p}_d| \left(\frac{|\vec{p}_{\bar{b}}|}{E_{\bar{b}}} - \cos \alpha_{d,\bar{b}} \right) + 2|\vec{p}_{\bar{u}}| \left(\frac{|\vec{p}_{\bar{b}}|}{E_{\bar{b}}} - \cos \alpha_{\bar{u},\bar{b}} \right) \end{aligned} \quad (\text{C.7})$$

$$\begin{aligned} \frac{\partial m_{b\ell\nu}^2}{\partial |\vec{p}_b|} &= \frac{\partial (m_b^2 + 2E_\nu E_\ell + 2E_\nu E_b + 2E_\ell E_b - 2\vec{p}_\nu \cdot \vec{p}_\ell - 2\vec{p}_\nu \cdot \vec{p}_b - 2\vec{p}_\ell \cdot \vec{p}_b)}{\partial |\vec{p}_b|} \\ &= 2E_\ell \frac{\partial E_\nu}{\partial |\vec{p}_b|} + 2E_\ell \frac{|\vec{p}_b|}{E_b} + 2E_\nu \frac{|\vec{p}_b|}{E_b} + 2E_b \frac{\partial E_\nu}{\partial |\vec{p}_b|} + 2(p_\ell^x u_b^x + p_\ell^y u_b^y) \\ &\quad - 2(p_\ell^x u_b^x + p_\ell^y u_b^y + p_\ell^z u_b^z) - 2\vec{p}_\nu \cdot \vec{u}_b + 2(p_b^x u_b^x + p_b^y u_b^y) \\ &= 2(E_\ell + E_\nu) \frac{|\vec{p}_b|}{E_b} - 2(E_\ell + E_b)(u_\nu^x u_b^x + u_\nu^y u_b^y) \\ &\quad - 2p_\ell^z u_b^z - 2\vec{p}_\nu \cdot \vec{u}_b + 2(p_b^x u_b^x + p_b^y u_b^y) \end{aligned} \quad (\text{C.8})$$

$$\frac{\partial p_{b\nu}^z}{\partial |\vec{p}_b|} = u_b^z \quad (\text{C.9})$$

$$\begin{aligned} \frac{\partial m_{b\ell\nu}^2}{\partial p_\nu^z} &= \frac{\partial (m_b^2 + 2E_\nu E_\ell + 2E_\nu E_b + 2E_\ell E_b - 2\vec{p}_\nu \cdot \vec{p}_\ell - 2\vec{p}_\nu \cdot \vec{p}_b - 2\vec{p}_\ell \cdot \vec{p}_b)}{\partial p_\nu^z} \\ &= 2(p_\nu^z (E_\ell + E_b) - (p_\ell^z + p_b^z)) \end{aligned} \quad (\text{C.10})$$

$$\frac{\partial p_{b\nu}^z}{\partial p_\nu^z} = 1 . \quad (\text{C.11})$$

The transformation for the muon momentum requires special attention: While the muon transverse momentum p_μ^T is always positive, the integration is over the *signed* quantity q_μ/p_μ^T .

This is necessary because a muon with a given charge and large transverse momentum may be reconstructed with the opposite charge, i.e. a track bending in the wrong direction. However, the calculation of the event kinematics and the matrix element do not depend on the lepton charge. Therefore, the integration is carried out over positive $1/p_\mu^T$ values only, and the integrand is multiplied by the sum of transfer function factors for both correct and wrong muon charge reconstruction.

It should be noted that for the numerical integration performed here, where the integral is always computed from the lower to the upper boundary irrespective of the sign of the Jacobian determinant, the *absolute value* of the determinant has to be included as a factor in the integration. The total factor to be included in the integration is thus

$$\left| \frac{1}{\det(J)} \right| \quad (\text{C.12})$$

with $\det(J)$ given in (C.1).

No Jacobian factor is included for the transformation from Cartesian to spherical coordinates for the momenta. This is motivated in the following for the case of the muon transfer function.

In the e+jets case, the value of P_{sgn} is computed with a δ distribution as lepton transfer function:

$$\begin{aligned} P_{\text{sgn}}(\vec{x}_{\text{jets}}, \vec{x}_\ell) &= \int F(\vec{y}_{\text{quarks}}, \vec{y}_\ell) W_{\text{jets}}(\vec{x}_{\text{jets}}, \vec{y}_{\text{quarks}}) \\ &\quad \delta(p_{\ell,\text{meas}}^x - p_{\ell,\text{true}}^x) \delta(p_{\ell,\text{meas}}^y - p_{\ell,\text{true}}^y) \delta(p_{\ell,\text{meas}}^z - p_{\ell,\text{true}}^z) \\ &\quad d\vec{y}_{\text{quarks}} dp_{\ell,\text{true}}^x dp_{\ell,\text{true}}^y dp_{\ell,\text{true}}^z, \end{aligned} \quad (\text{C.13})$$

where \vec{x}_{jets} and \vec{x}_ℓ stand for the measured jet and lepton momenta, and \vec{y}_{quarks} and \vec{y}_ℓ for the assumed true values in the integration. Transforming to an integral over different coordinates, e.g.

$$\begin{aligned} P_{\text{sgn}}(\vec{x}_{\text{jets}}, \vec{x}_\ell) &= \int F(\vec{y}_{\text{quarks}}, \vec{y}_\ell) W_{\text{jets}}(\vec{x}_{\text{jets}}, \vec{y}_{\text{quarks}}) \\ &\quad \delta(|p_{\ell,\text{meas}}| - |p_{\ell,\text{true}}|) \delta(\cos \theta_{\ell,\text{meas}} - \cos \theta_{\ell,\text{true}}) \delta(\phi_{\ell,\text{meas}} - \phi_{\ell,\text{true}}) \\ &\quad d\vec{y}_{\text{quarks}} d|p_{\ell,\text{true}}| d\cos \theta_{\ell,\text{true}} d\phi_{\ell,\text{true}}, \end{aligned} \quad (\text{C.14})$$

does not change the integral because in both cases the δ distributions simply “pick” the value of the integrand at the correct location.

For the transformation from (C.13) to (C.14) a factor of $|p_{\ell,\text{true}}|^2$ does have to be included (as Jacobian for the transformation from Cartesian to spherical coordinates). However, this factor is automatically eliminated because the δ distributions have different arguments,

$$\int \delta(ax) dx = \frac{1}{a} \int \delta(x) dx \quad (\text{C.15})$$

holds, and a corresponding factor of $1/|p_{\ell,\text{true}}|^2$ is introduced during the transformation. This argument is valid for the transformation between any set of coordinates, e.g. also between $(p_\ell^x, p_\ell^y, p_\ell^z)$ and $(1/|p_\ell^T|, \cos \theta_\ell, \phi_\ell)$.

For the transition to an integration with a lepton transfer function that describes a non-vanishing detector resolution, as in the μ +jets case, it is important to note that

$$\int \delta(1/|p_{\ell, \text{meas}}^T| - 1/|p_{\ell, \text{true}}^T|) d(1/|p_{\ell, \text{true}}^T|) = \int W_{\ell}(1/|p_{\ell, \text{meas}}^T|, 1/|p_{\ell, \text{true}}^T|) d(1/|p_{\ell, \text{true}}^T|) = 1 . \quad (\text{C.16})$$

The first integral is the limiting case of the second for an ideal detector. Thus, for the P_{sgn} integration there is no factor to be included in (C.12) due to the transformation from Cartesian to spherical coordinates for the quark momenta, nor the transformation from Cartesian lepton momentum to $(1/|p_{\ell}^T|, \cos \theta_{\ell}, \phi_{\ell})$:

$$\begin{aligned} P_{\text{sgn}}(\vec{x}_{\text{jets}}, \vec{x}_{\ell}) &= \int F(\vec{y}_{\text{quarks}}, \vec{y}_{\ell}) W_{\text{jets}}(\vec{x}_{\text{jets}}, \vec{y}_{\text{quarks}}) W_{\ell}(\vec{x}_{\ell}, \vec{y}_{\ell}) \\ &\quad d\vec{y}_{\text{quarks}} dp_{\ell, \text{true}}^x dp_{\ell, \text{true}}^y dp_{\ell, \text{true}}^z \\ &= \int F(\vec{y}_{\text{quarks}}, \vec{y}_{\ell}) W_{\text{jets}}(\vec{x}_{\text{jets}}, \vec{y}_{\text{quarks}}) W_{\ell}(\vec{x}_{\ell}, \vec{y}_{\ell}) \\ &\quad d\vec{y}_{\text{quarks}} d(1/|p_{\ell, \text{true}}^T|) d \cos \theta_{\ell, \text{true}} d\phi_{\ell, \text{true}} , \end{aligned} \quad (\text{C.17})$$

where

$$W_{\ell}(\vec{x}_{\ell}, \vec{y}_{\ell}) = W'_{\ell}(1/|p_{\ell, \text{true}}^T|, 1/|p_{\ell, \text{meas}}^T|) \delta(\cos \theta_{\ell, \text{meas}} - \cos \theta_{\ell, \text{true}}) \delta(\phi_{\ell, \text{meas}} - \phi_{\ell, \text{true}}) \quad (\text{C.18})$$

and

$$\int W'_{\ell}(1/|p_{\ell, \text{true}}^T|, 1/|p_{\ell, \text{meas}}^T|) d(1/|p_{\ell, \text{true}}^T|) = 1 . \quad (\text{C.19})$$

To be very specific, one would in fact have to write

$$\int_0^{\infty} (W'_{\ell}(1/|p_{\ell, \text{true}}^T|, 1/|p_{\ell, \text{meas}}^T|) + W'_{\ell}(-1/|p_{\ell, \text{true}}^T|, 1/|p_{\ell, \text{meas}}^T|)) d(1/|p_{\ell, \text{true}}^T|) = 1 , \quad (\text{C.20})$$

therefore

$$\begin{aligned} P_{\text{sgn}}(\vec{x}_{\text{jets}}, \vec{x}_{\ell}) &= \int F(\vec{y}_{\text{quarks}}, \vec{y}_{\ell}) W_{\text{jets}}(\vec{x}_{\text{jets}}, \vec{y}_{\text{quarks}}) \\ &\quad (W'_{\ell}(1/|p_{\ell, \text{true}}^T|, 1/|p_{\ell, \text{meas}}^T|) + W'_{\ell}(-1/|p_{\ell, \text{true}}^T|, 1/|p_{\ell, \text{meas}}^T|)) \\ &\quad \delta(\cos \theta_{\ell, \text{meas}} - \cos \theta_{\ell, \text{true}}) \delta(\phi_{\ell, \text{meas}} - \phi_{\ell, \text{true}}) \\ &\quad d\vec{y}_{\text{quarks}} d(1/|p_{\ell, \text{true}}^T|) d \cos \theta_{\ell, \text{true}} d\phi_{\ell, \text{true}} , \end{aligned} \quad (\text{C.21})$$

which is the formula implemented in the P_{sgn} calculation.

Appendix D

Transfer Function Cross-Checks

A number of cross-checks are performed to verify the performance of the jet transfer functions derived in Section 5.2.1. The simplest one is to plot the δE distribution from MC, and then generate δE values according to the transfer function using the same events. If the transfer function describes the MC, these two distributions should agree. Figures D.1-D.12 show the results of this test. The filled histogram is the δE distribution from MC, and the empty histogram is the distribution generated by the transfer function. Each plot is in bins of parton energy, < 40 , 40-60, 60-80, 80-100, 100-120, and > 120 GeV.

Studies performed for the ideogram analysis [57] have shown that significant shifts in mass distributions can occur when parton-level corrections are derived from samples having different selection requirements. The transfer functions for the matrix element analysis have been derived from MC samples with loose requirements to obtain as many events as possible (the “loose” sample). A second set of transfer functions has also been calculated using the same event selection that is used for the rest of the matrix element analysis (the “tight” sample). A comparison of the two transfer functions is shown in Figures D.13 and D.14.

Cross checks were performed using the two samples. In these cross checks, W mass and top mass distributions are generated using the energies of the jets directly from reco (i.e., no transfer functions are used) to create a reference histogram. Next, the parton energies are smeared according to the transfer function and the W and top candidate masses are constructed from the smeared parton energies. A fixed offset is added to each candidate mass, and a likelihood is calculated that compares the reference histogram to the offset histogram. A graph of $-2 \ln \mathcal{L}$ versus offset is constructed, and this graph is fit with a parabola to determine the most likely offset and the uncertainty on the offset.

Three sets of $-2 \ln \mathcal{L}$ curves are constructed. The first uses the tight transfer function on the tight event sample, the second uses the tight transfer function on the loose event sample, and the third uses the loose transfer function on the tight event sample. The difference in the shifts on the W mass are slightly less than 1 GeV, with uncertainties on the offset of 0.1 GeV. The difference in the shifts of the top mass are smaller, with uncertainties of about 0.3 GeV.

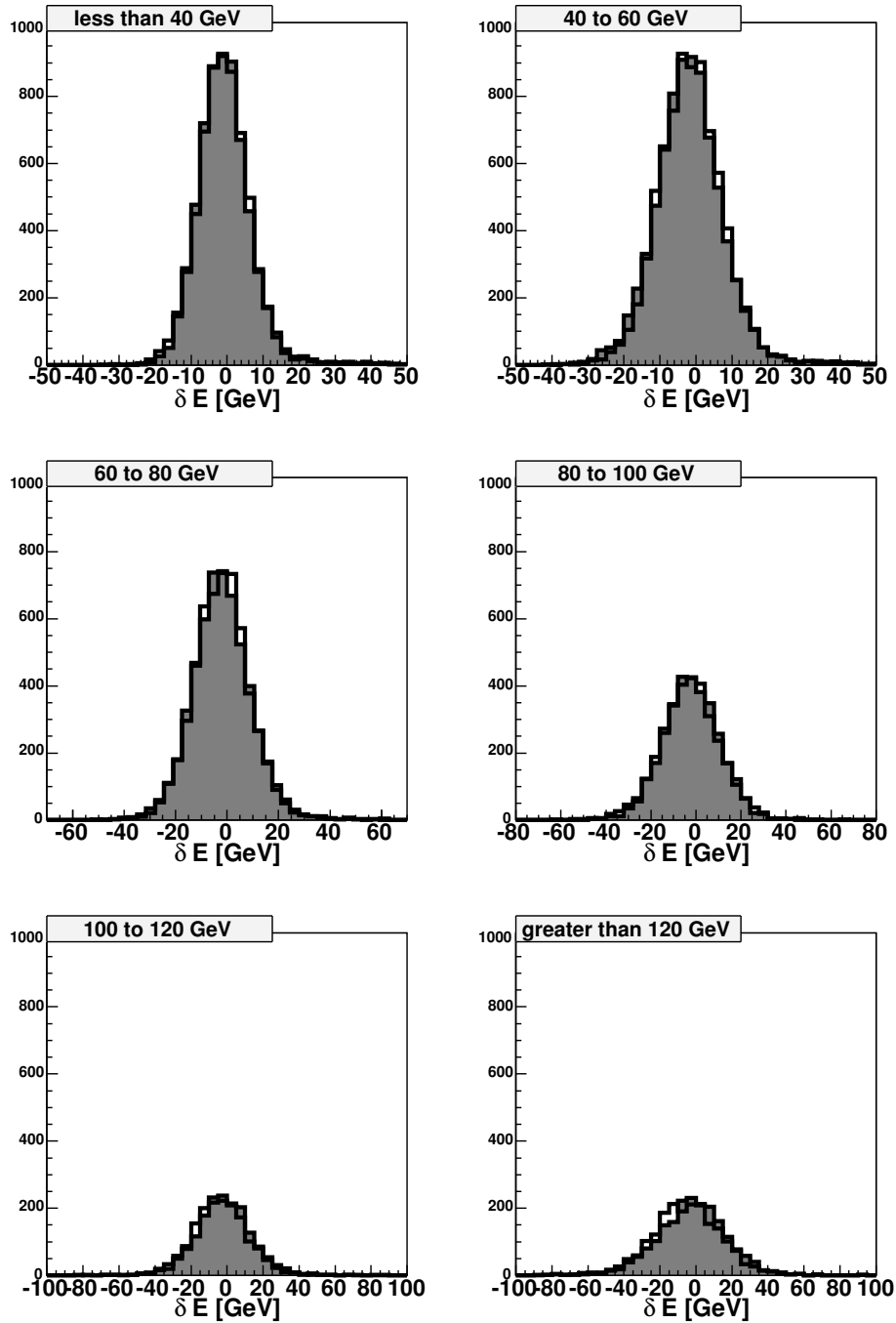


Figure D.1: Light quark $\delta E = E_{jet} - E_{parton}$ distribution for $|\eta| < 0.5$. The filled histogram is the δE distribution from MC, and the empty histogram is the distribution generated by the transfer function.

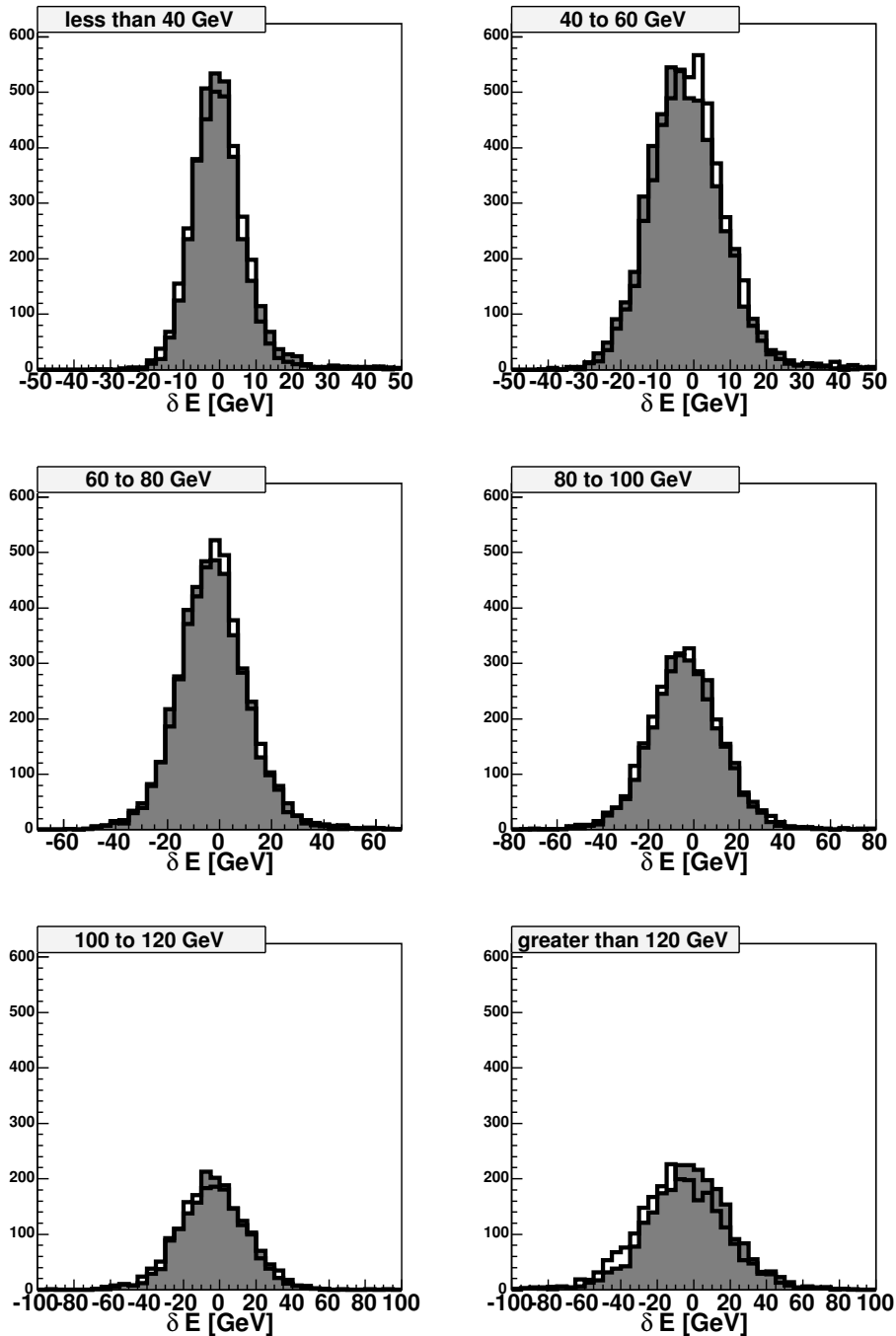


Figure D.2: Light quark $\delta E = E_{jet} - E_{parton}$ distribution for $0.5 < |\eta| < 1.0$. The filled histogram is the δE distribution from MC, and the empty histogram is the distribution generated by the transfer function.

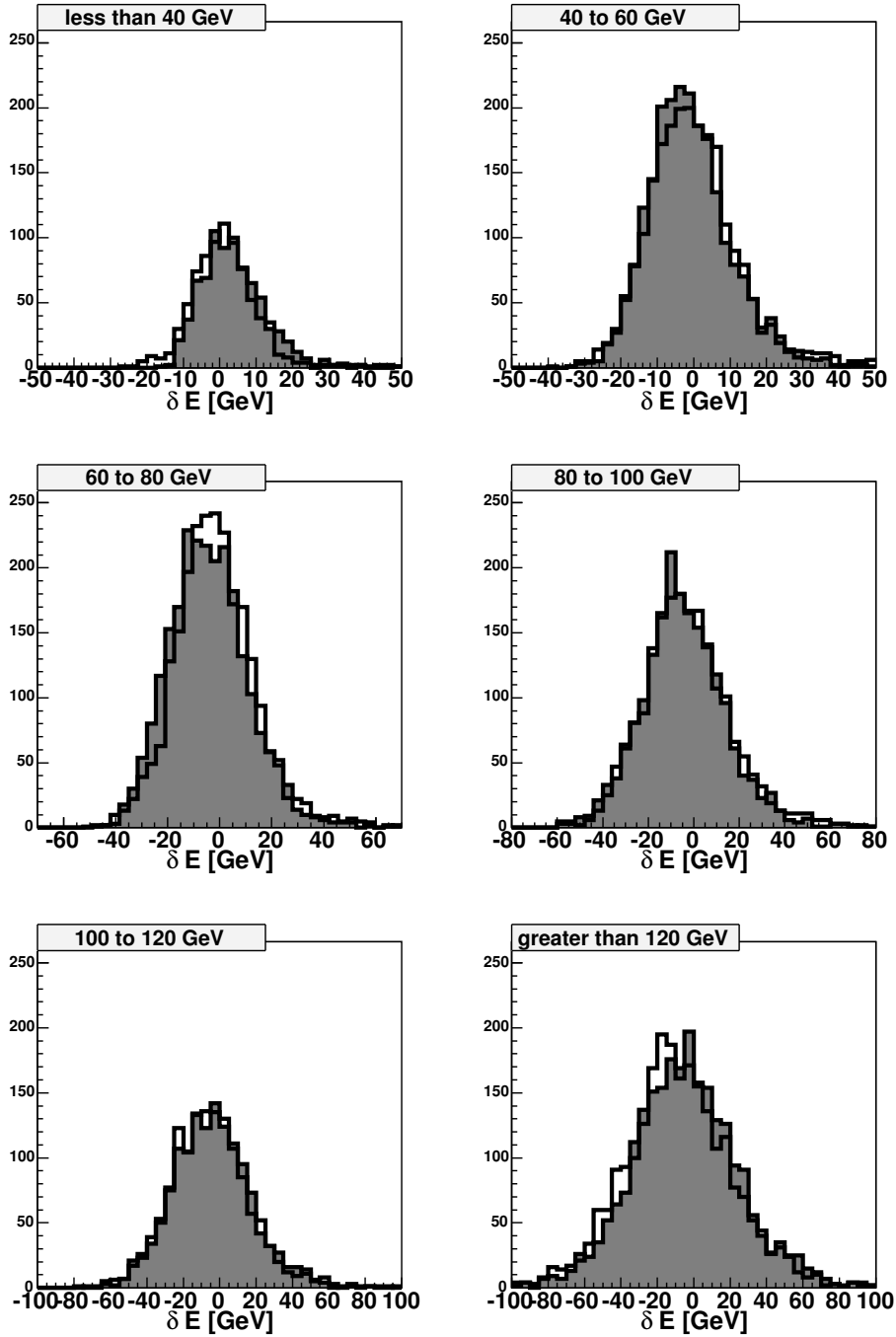


Figure D.3: Light quark $\delta E = E_{jet} - E_{parton}$ distribution for $1.0 < |\eta| < 1.5$. The filled histogram is the δE distribution from MC, and the empty histogram is the distribution generated by the transfer function.

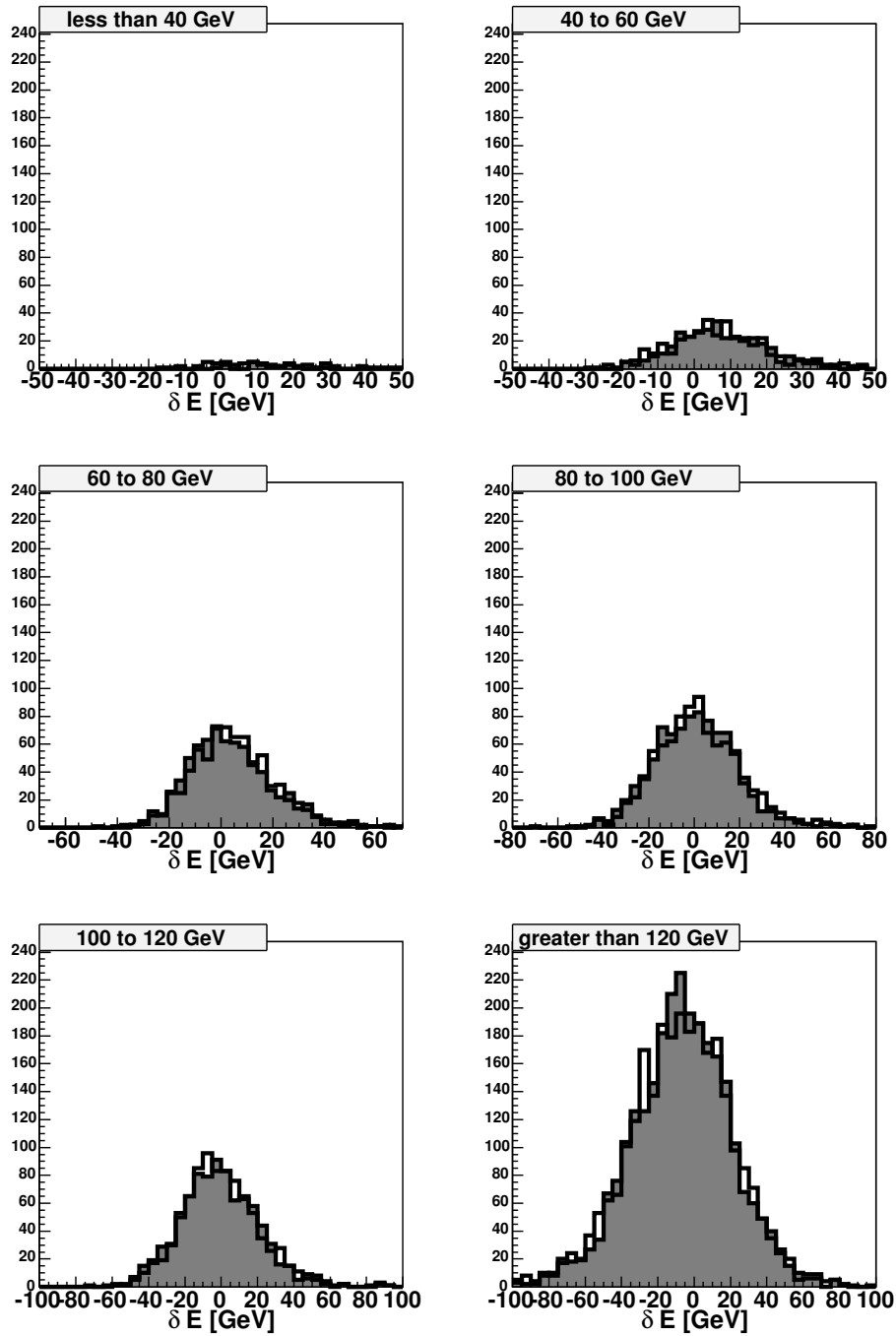


Figure D.4: Light quark $\delta E = E_{jet} - E_{parton}$ distribution for $1.5 < |\eta| < 2.5$. The filled histogram is the δE distribution from MC, and the empty histogram is the distribution generated by the transfer function.

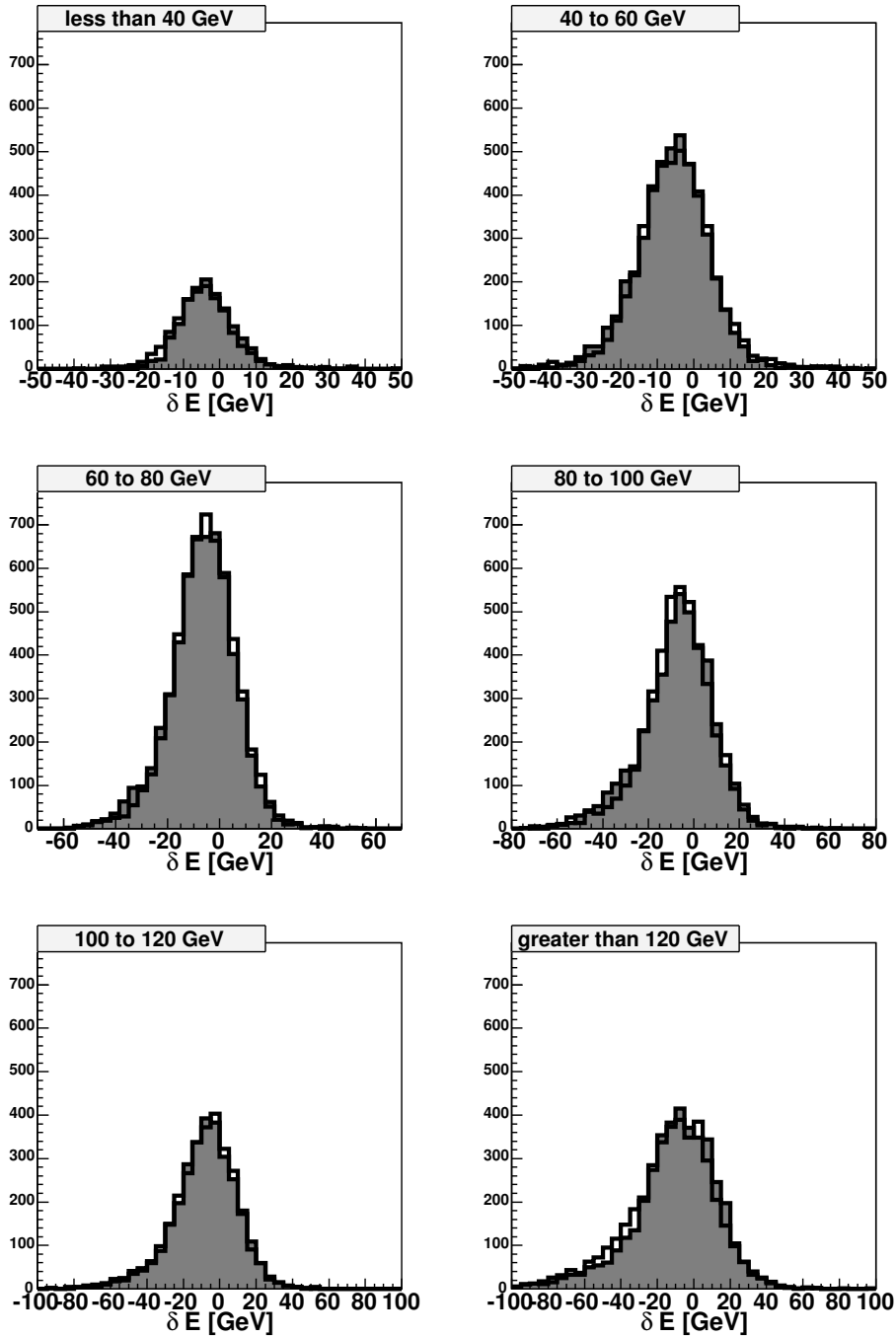


Figure D.5: b quark $\delta E = E_{jet} - E_{parton}$ distribution for $|\eta| < 0.5$. The filled histogram is the δE distribution from MC, and the empty histogram is the distribution generated by the transfer function.

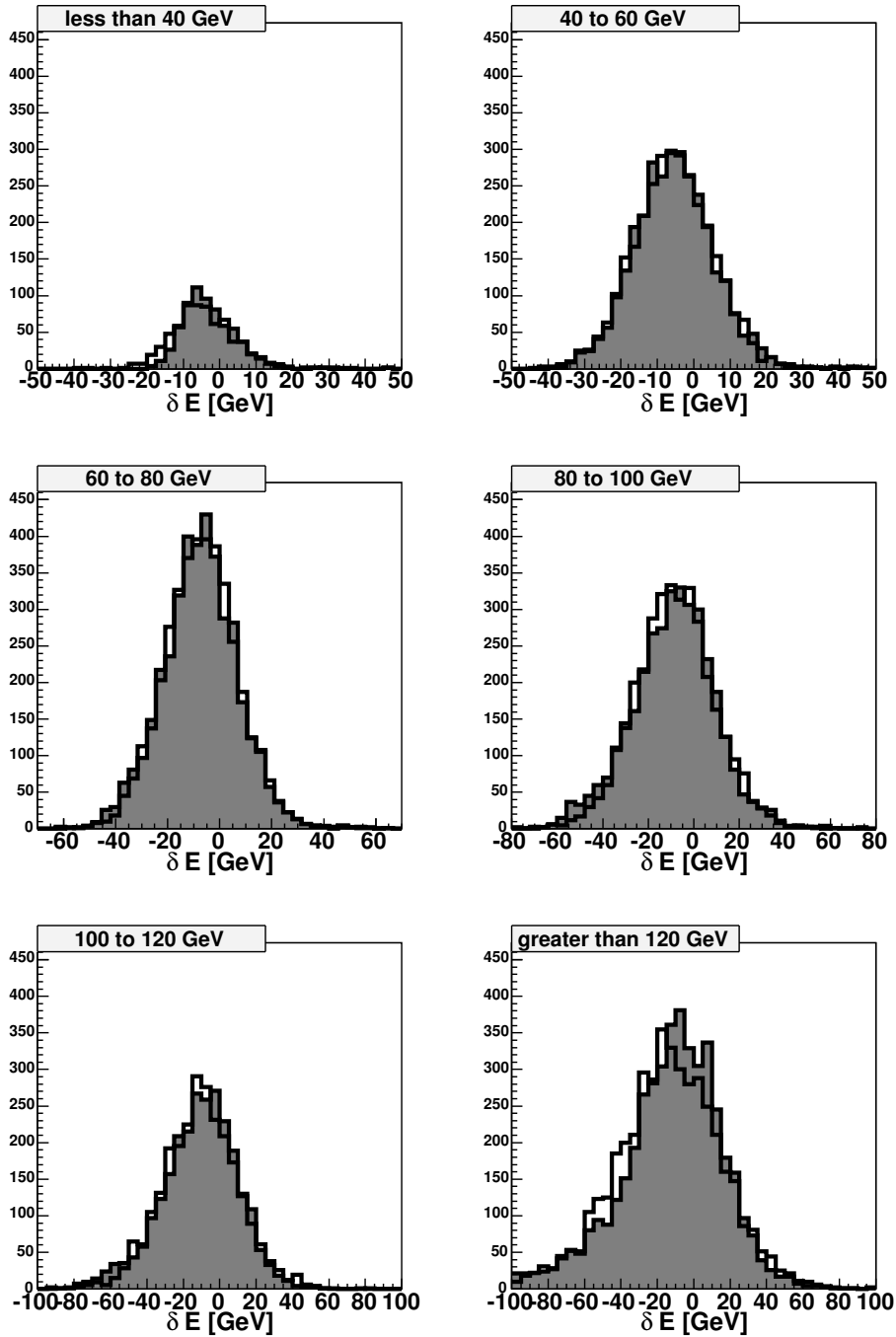


Figure D.6: b quark $\delta E = E_{jet} - E_{parton}$ distribution for $0.5 < |\eta| < 1.0$. The filled histogram is the δE distribution from MC, and the empty histogram is the distribution generated by the transfer function.

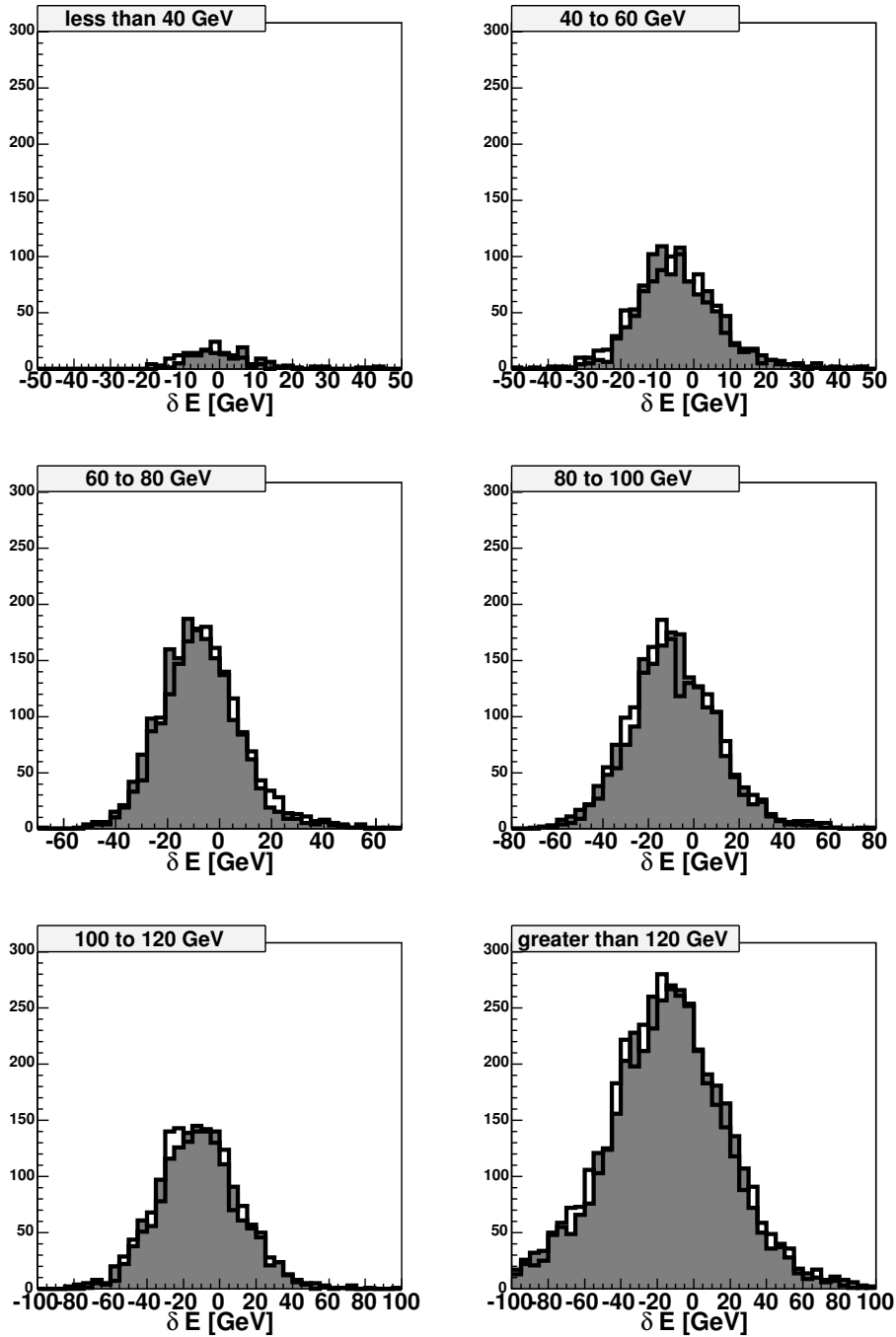


Figure D.7: b quark $\delta E = E_{jet} - E_{parton}$ distribution for $1.0 < |\eta| < 1.5$. The filled histogram is the δE distribution from MC, and the empty histogram is the distribution generated by the transfer function.

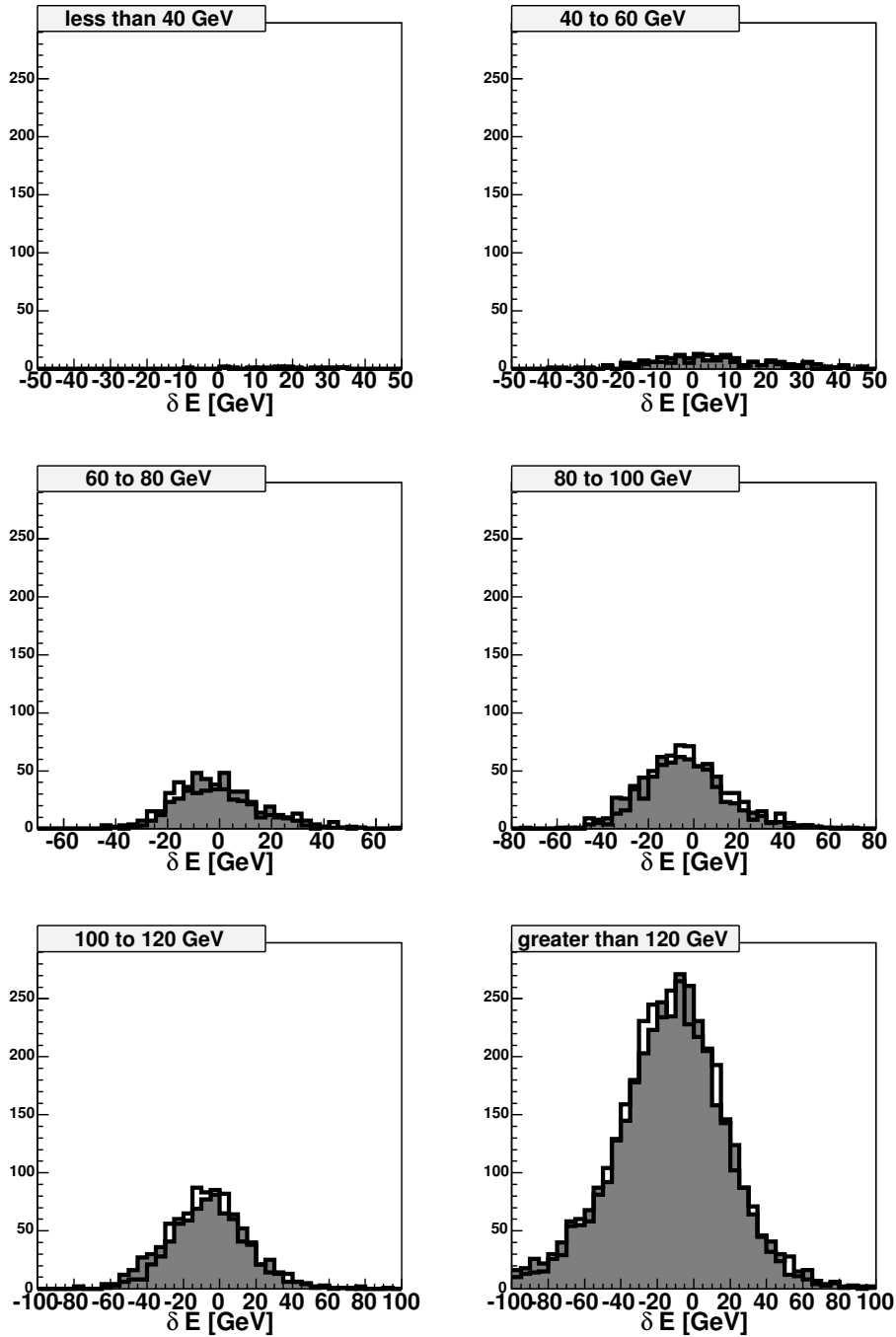


Figure D.8: b quark $\delta E = E_{jet} - E_{parton}$ distribution for $1.5 < |\eta| < 2.5$. The filled histogram is the δE distribution from MC, and the empty histogram is the distribution generated by the transfer function.

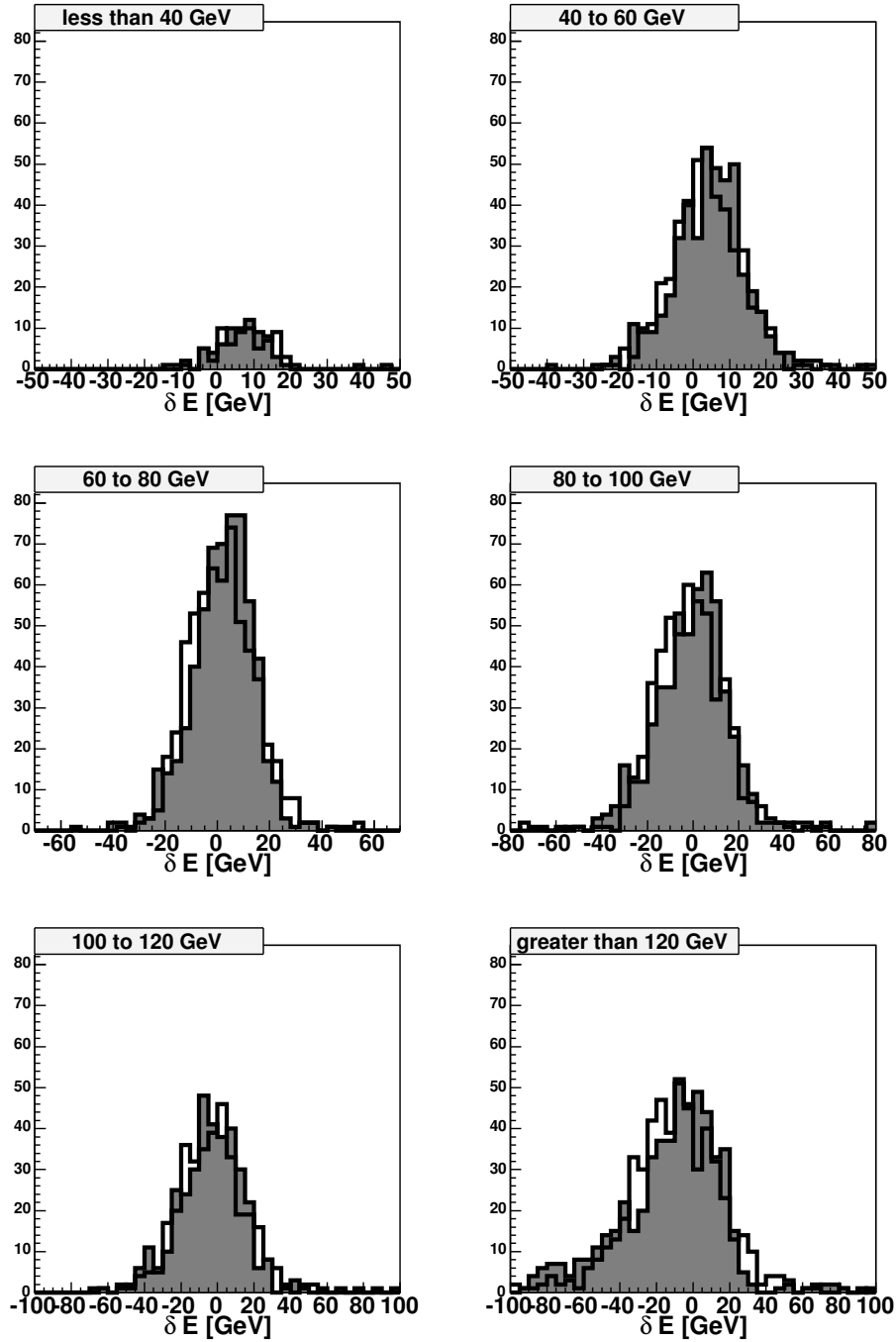


Figure D.9: μ -tagged b quark $\delta E = E_{jet} - E_{parton}$ distribution for $|\eta| < 0.5$. The filled histogram is the δE distribution from MC, and the empty histogram is the distribution generated by the transfer function.

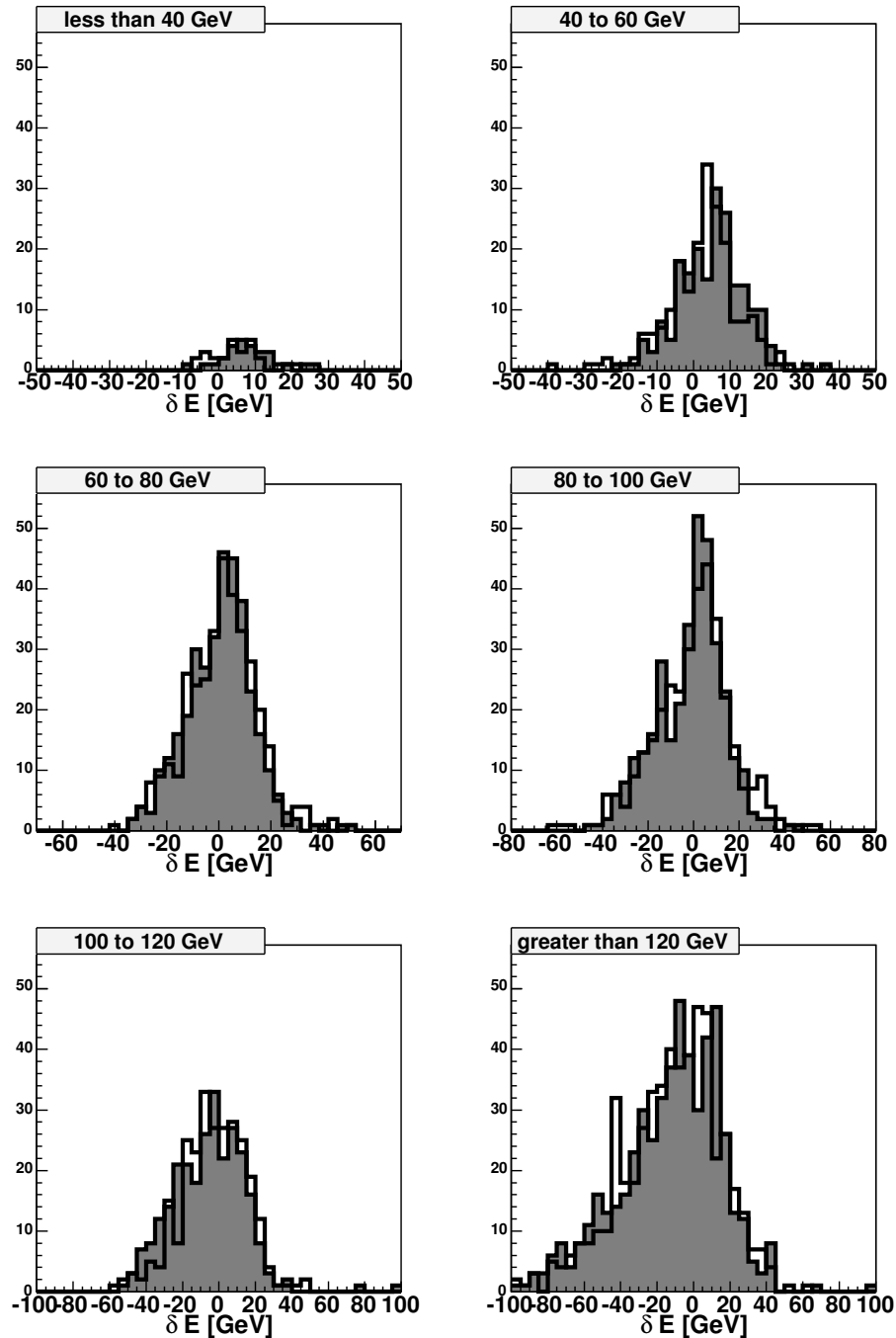


Figure D.10: μ -tagged b quark $\delta E = E_{jet} - E_{parton}$ distribution for $0.5 < |\eta| < 1.0$. The filled histogram is the δE distribution from MC, and the empty histogram is the distribution generated by the transfer function.

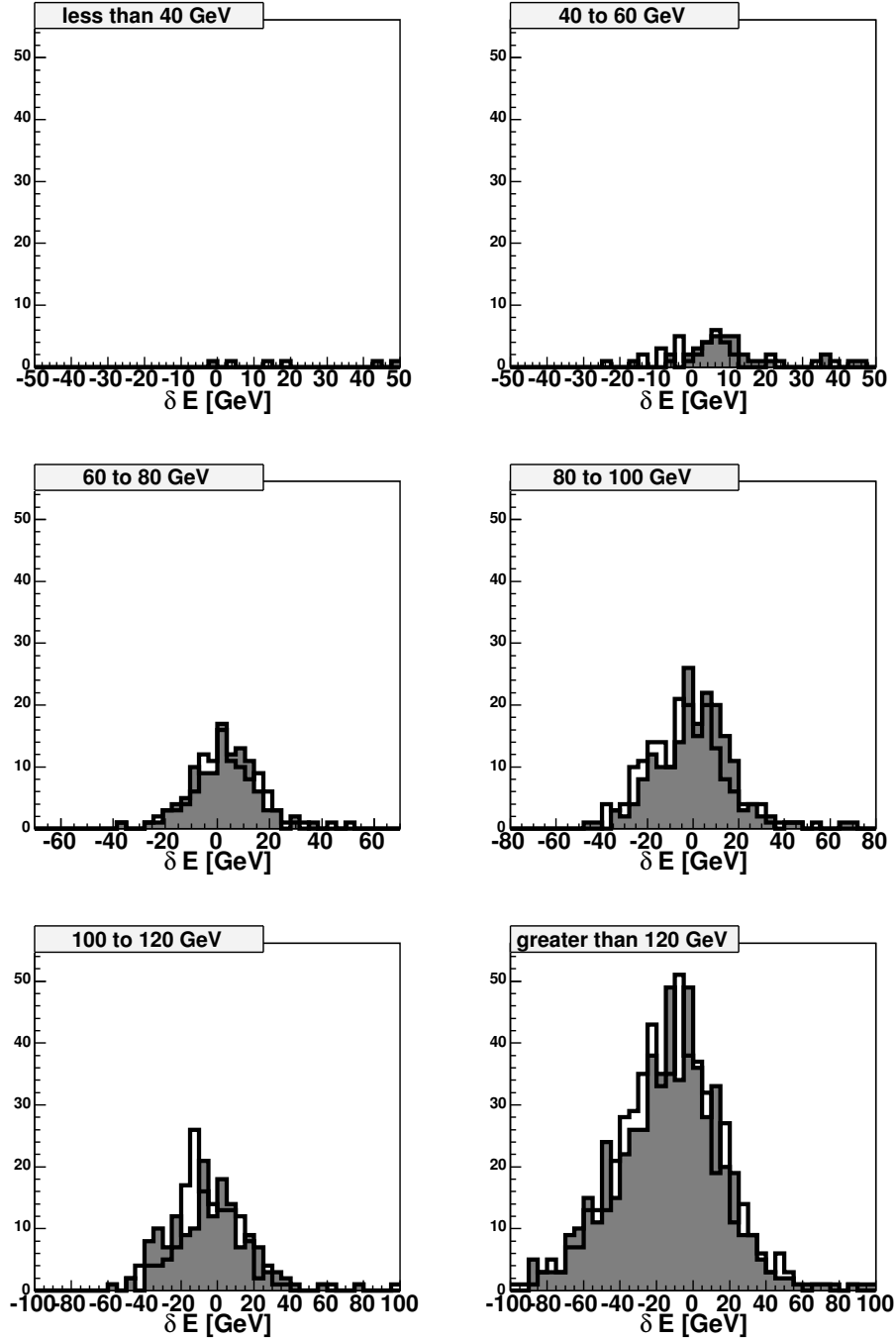


Figure D.11: μ -tagged b quark $\delta E = E_{jet} - E_{parton}$ distribution for $1.0 < |\eta| < 1.5$. The filled histogram is the δE distribution from MC, and the empty histogram is the distribution generated by the transfer function.

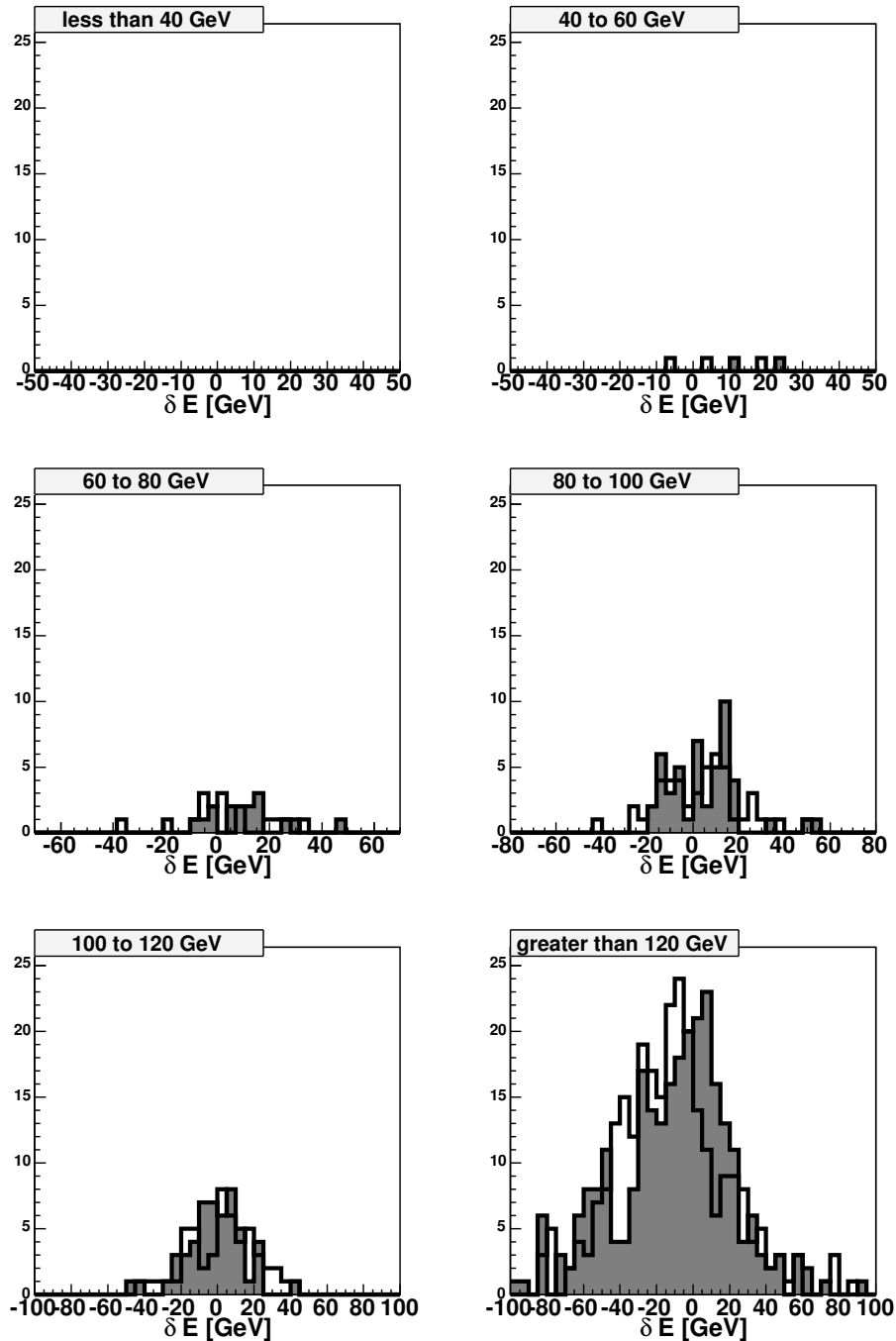


Figure D.12: μ -tagged b quark $\delta E = E_{jet} - E_{parton}$ distribution for $1.5 < |\eta| < 2.5$. The filled histogram is the δE distribution from MC, and the empty histogram is the distribution generated by the transfer function.

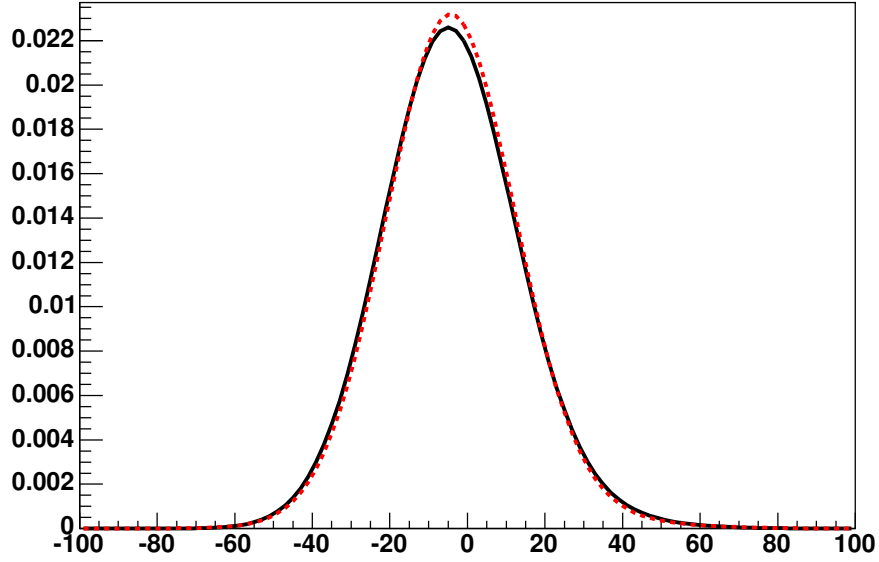


Figure D.13: Transfer functions using matrix element selection (solid black), and loser transfer function selection (dashed red), for light quarks with $0.5 < |\eta| < 1.0$ and parton energy of 100 GeV.

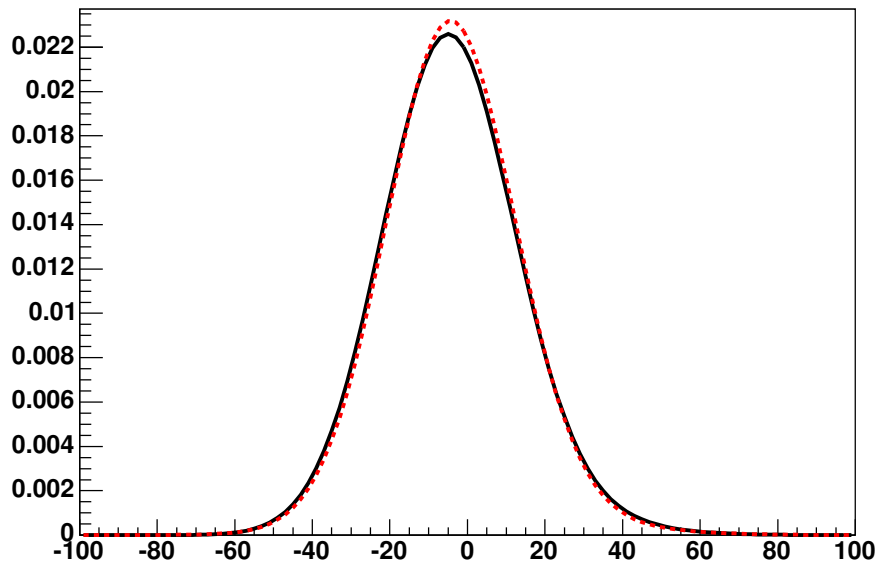


Figure D.14: Transfer functions using matrix element selection (solid black), and loser transfer function selection (dashed red), for b quarks with $0.5 < |\eta| < 1.0$ and parton energy of 100 GeV.

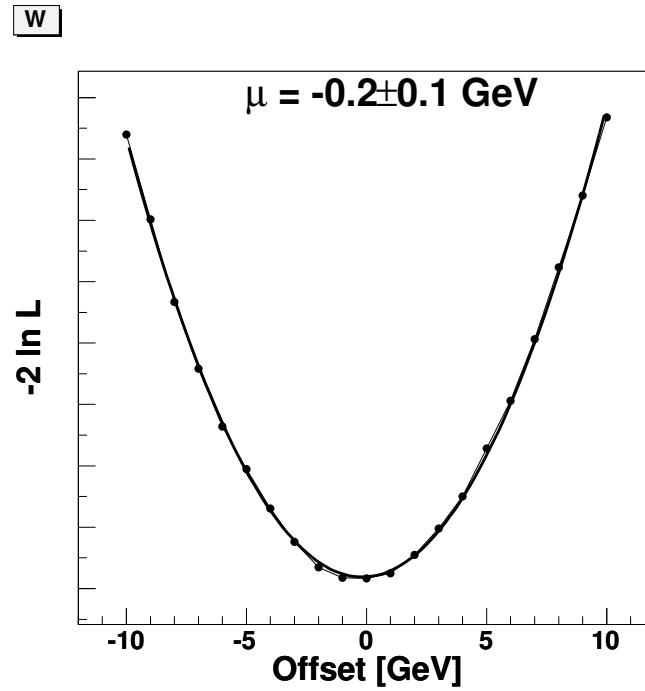


Figure D.15: $-2 \ln \mathcal{L}$ for the W mass distributions for the tight transfer function on the tight event sample.

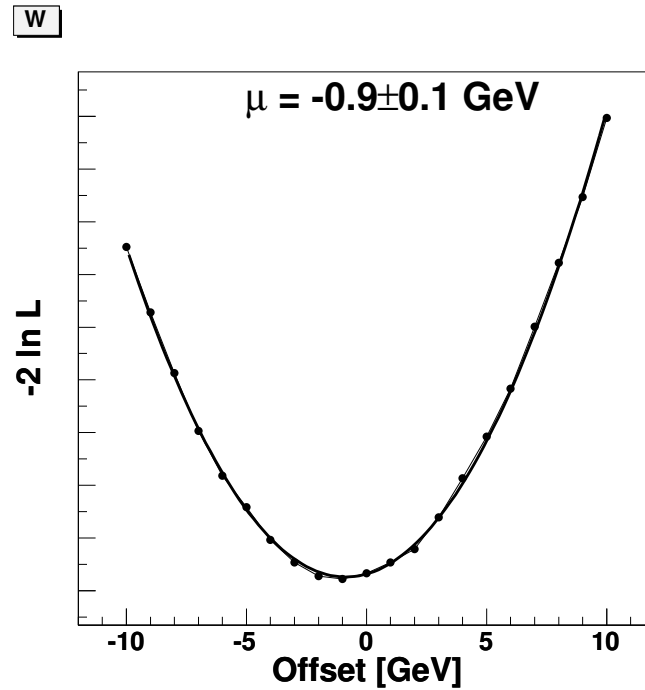


Figure D.16: $-2 \ln \mathcal{L}$ for the W mass distributions for the loose transfer function on the tight event sample.

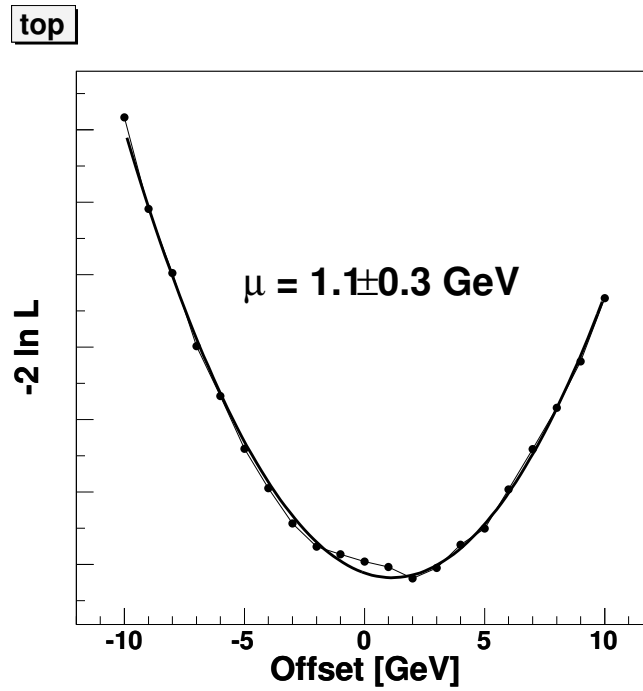


Figure D.17: $-2 \ln \mathcal{L}$ for the top mass distributions for the tight transfer function on the tight event sample.

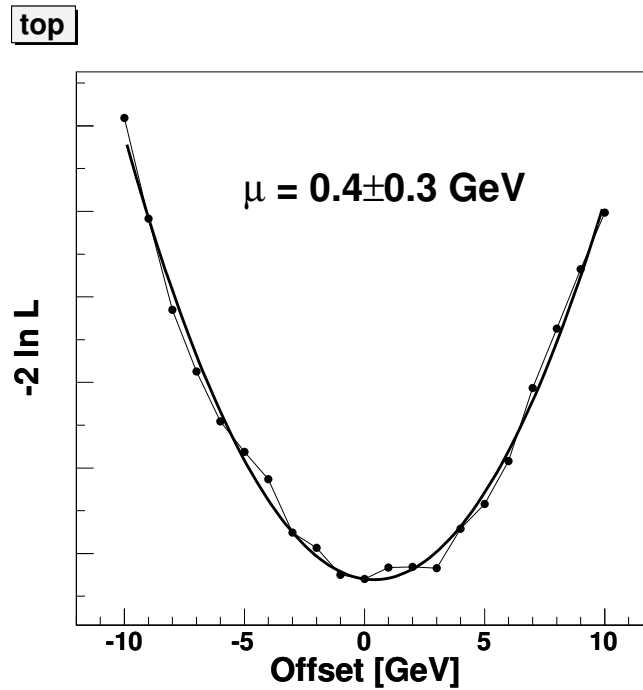


Figure D.18: $-2 \ln \mathcal{L}$ for the top mass distributions for the loose transfer function on the tight event sample.

Appendix E

Data to Monte Carlo Comparison

This section compares various kinematic distributions of the 320 pb^{-1} ℓ +jets dataset under study with the prediction from Monte Carlo events. e +jets and μ +jets events are treated separately. Since there is no Monte Carlo sample which describes the QCD (Multijet) background, a QCD sample is derived from data: the full preselection is applied but the isolation requirement of the lepton is inverted. The total number of Monte Carlo events (signal+background) is normalized to the number of data events.

The kinematic distributions of jets and the isolated lepton in our events are the key to the validity of the matrix element method calibration, which is based on the simulation. All distributions show good agreement: the data as collected with the DØ detector is well modeled by the Monte Carlo samples run through detector simulation. The topological variables are the inputs to the topological likelihood fit described in Section 6.3.2. Although the fit result does not directly enter the mass fit, the derived sample composition enters the P_{bkg} normalization and yields the related systematic uncertainty. As further control plots, the distributions of various quantities of the leptonically decaying W boson are provided.

Note that all plots include the η -dependent jet energy corrections and their propagation to \cancel{E}_T and all related topological variables.

E.1 Events with exactly 4 jets (signal sample)

In this section, the distributions are shown for the signal selection, requiring exactly 4 jets in the event. Monte Carlo samples for $t\bar{t}$ ($m_{\text{top}} = 175 \text{ GeV}$), W + jets and the QCD sample extracted from data are added together according to the expected relative fractions (see Section 6.3.2) and compared to the data.

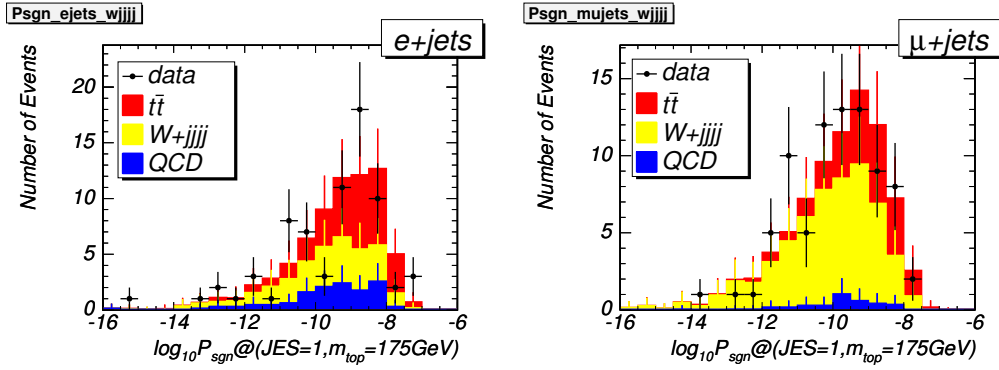


Figure E.1: Signal Probability P_{sgn} ($m_{\text{top}} = 175.0$ GeV) for $e+\text{jets}$ and $\mu+\text{jets}$ events for $n_{\text{jets}} = 4$.

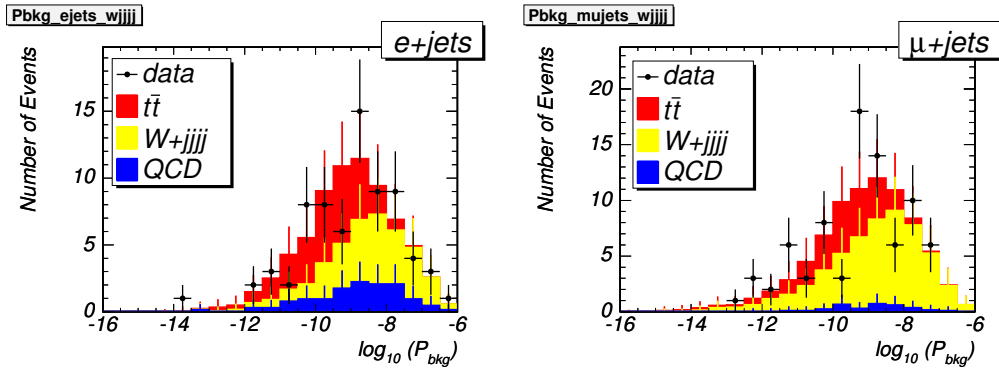


Figure E.2: Background Probability P_{bkg} for $e+\text{jets}$ and $\mu+\text{jets}$ events for $n_{\text{jets}} = 4$.

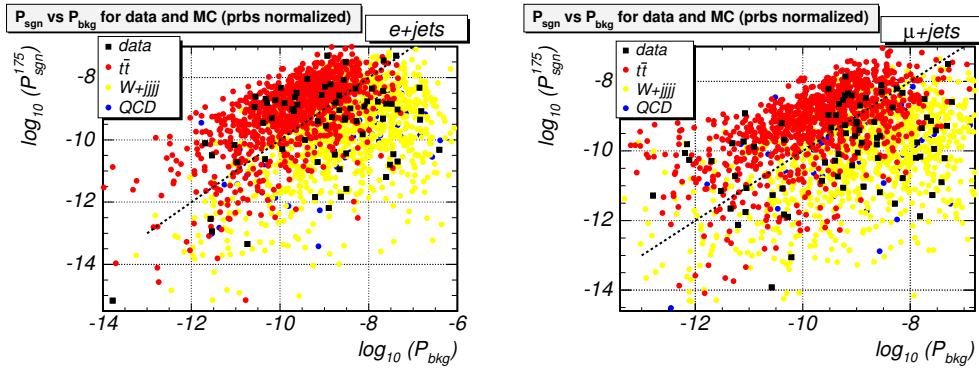


Figure E.3: Signal Probability P_{sgn} vs Background Probability P_{bkg} for $e+\text{jets}$ and $\mu+\text{jets}$ events for $n_{\text{jets}} = 4$.

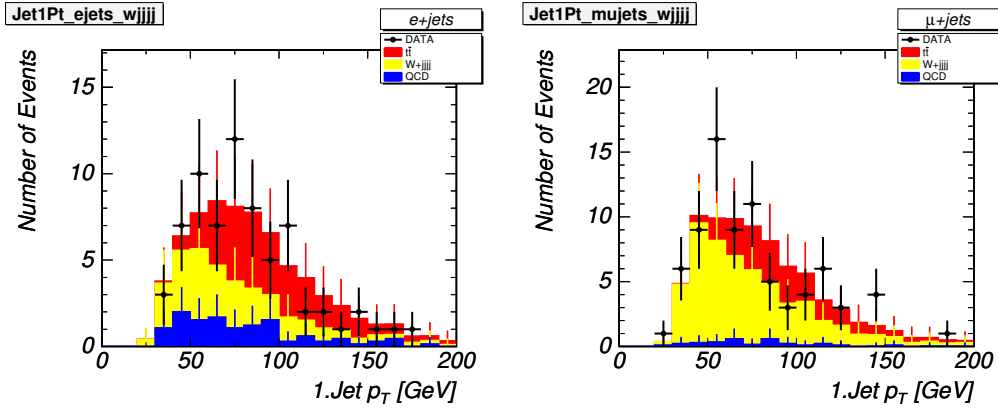


Figure E.4: Transverse momentum p_T of the leading (1.) jet for e+jets and μ +jets events for $n_{jets} = 4$.

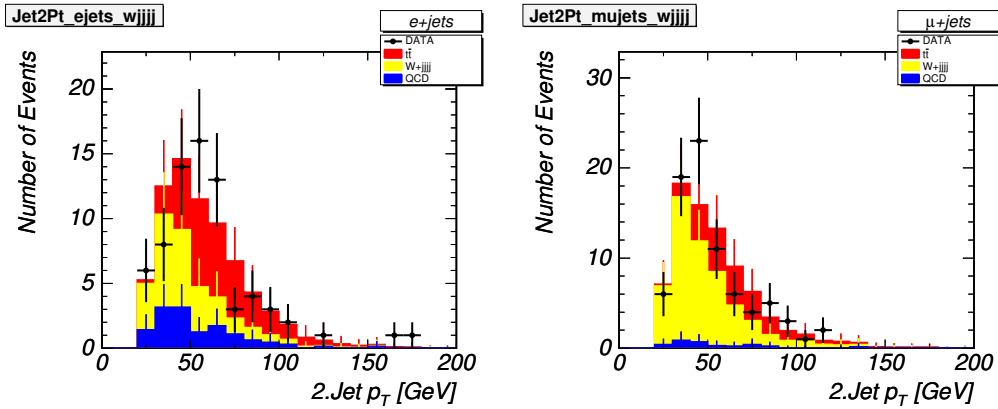


Figure E.5: Transverse momentum p_T of the 2. jet for e+jets and μ +jets events for $n_{jets} = 4$.

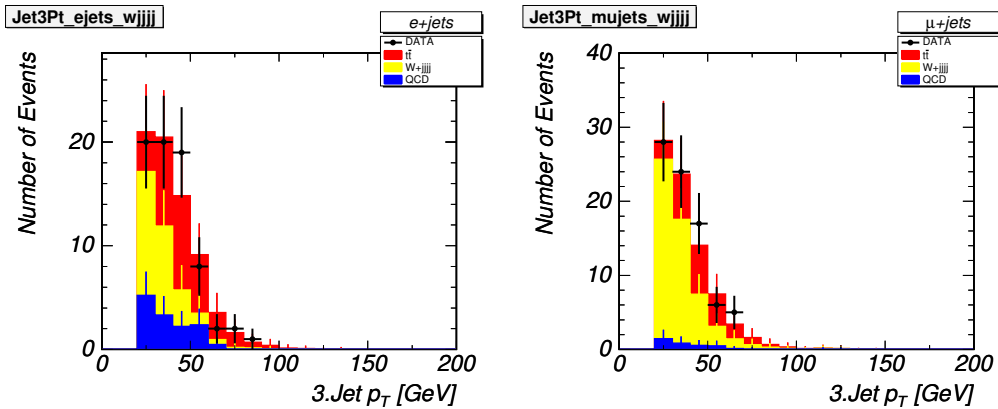


Figure E.6: Transverse momentum p_T of the 3. jet for e+jets and μ +jets events for $n_{jets} = 4$.

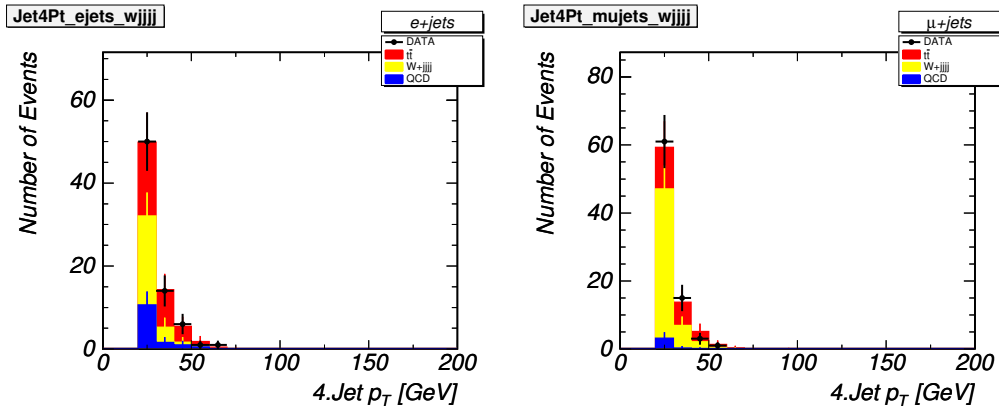


Figure E.7: Transverse momentum p_T of the 4. jet for e+jets and μ +jets events for $n_{jets} = 4$.

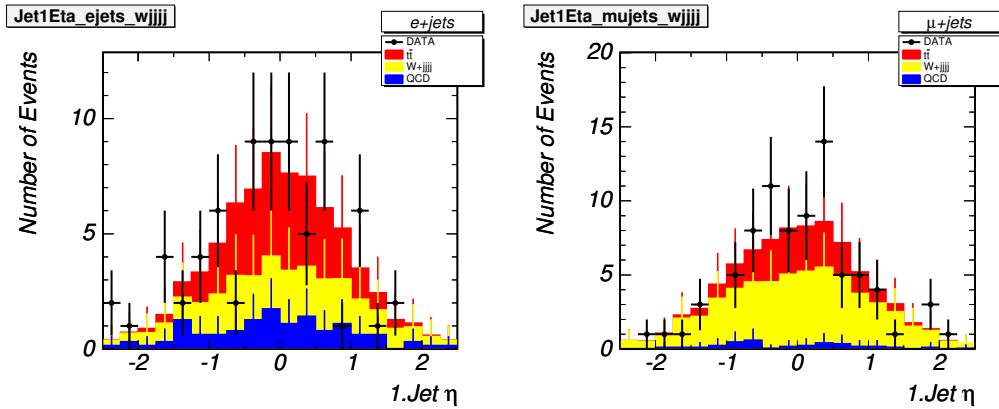


Figure E.8: Pseudorapidity η of the leading (1.) jet for e+jets and μ +jets events for $n_{jets} = 4$.

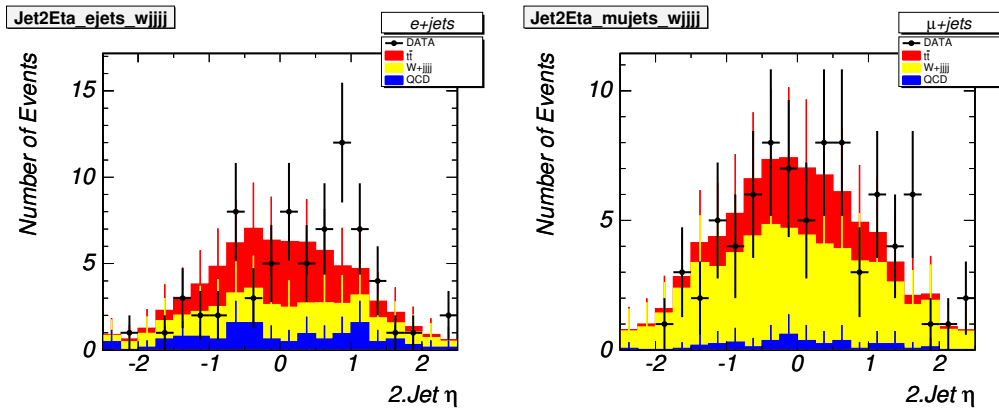


Figure E.9: Pseudorapidity η of the 2. jet for e+jets and μ +jets events for $n_{jets} = 4$.

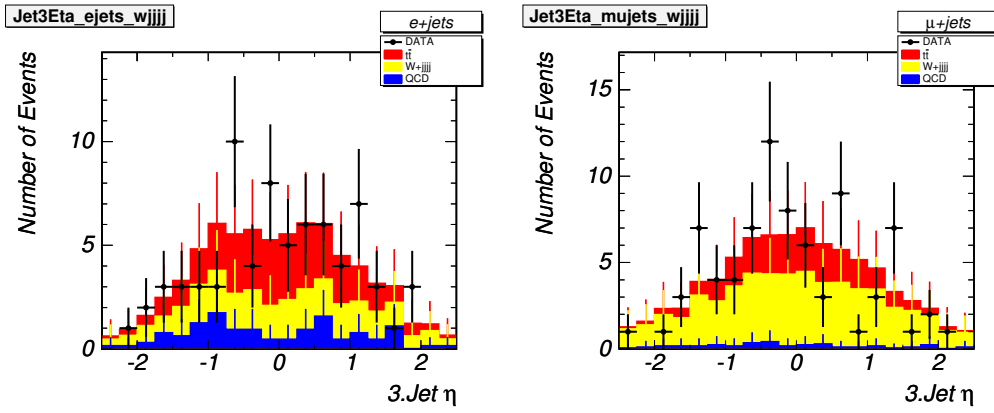


Figure E.10: Pseudorapidity η of the 3. jet for e+jets and μ +jets events for $n_{jets} = 4$.

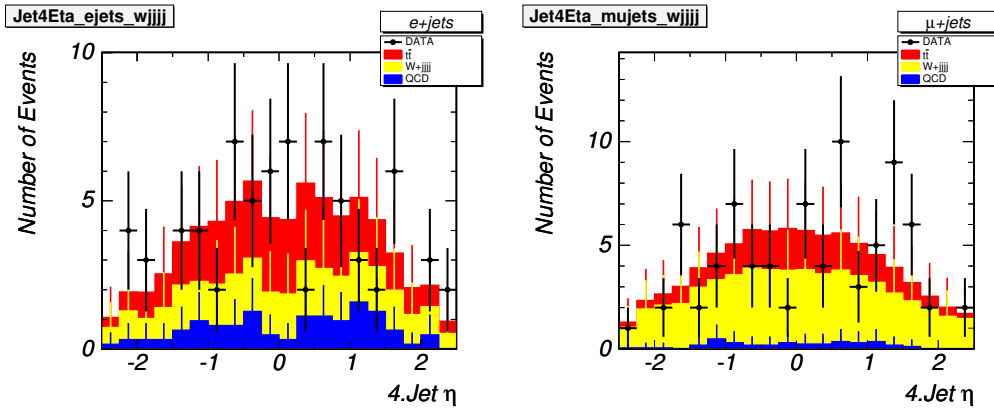


Figure E.11: Pseudorapidity η of the 4. jet for e+jets and μ +jets events for $n_{jets} = 4$.

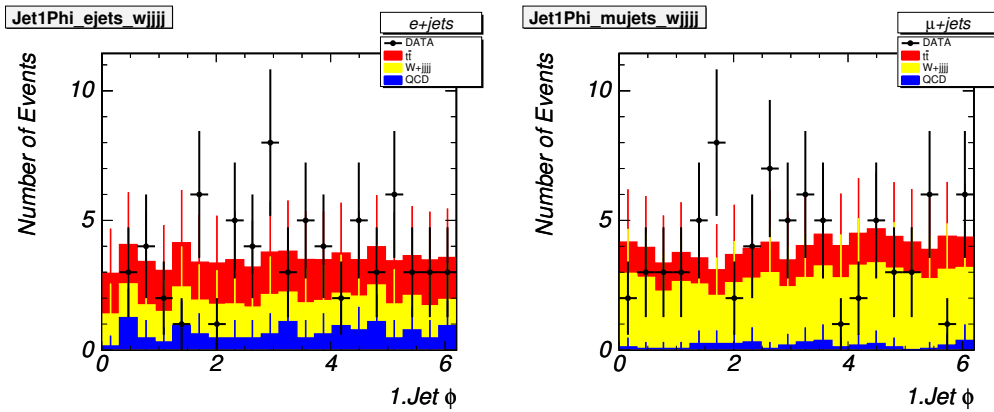


Figure E.12: ϕ angle of the leading (1.) jet for e+jets and μ +jets events for $n_{jets} = 4$.

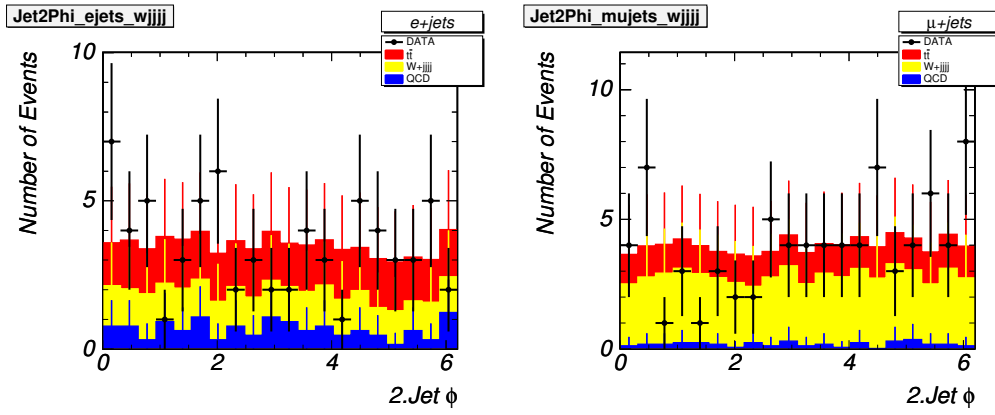


Figure E.13: ϕ angle of the 2. jet for e+jets and μ +jets events for $n_{jets} = 4$.

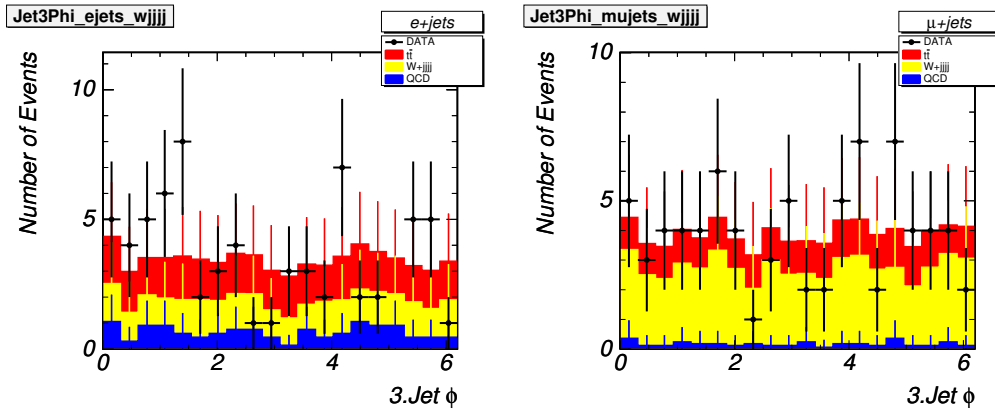


Figure E.14: ϕ angle of the 3. jet for e+jets and μ +jets events for $n_{jets} = 4$.

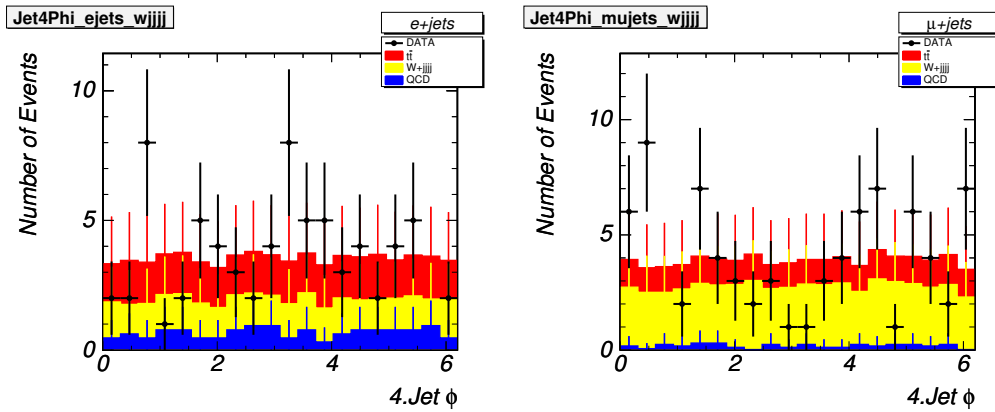


Figure E.15: ϕ angle of the 4. jet for e+jets and μ +jets events for $n_{jets} = 4$.

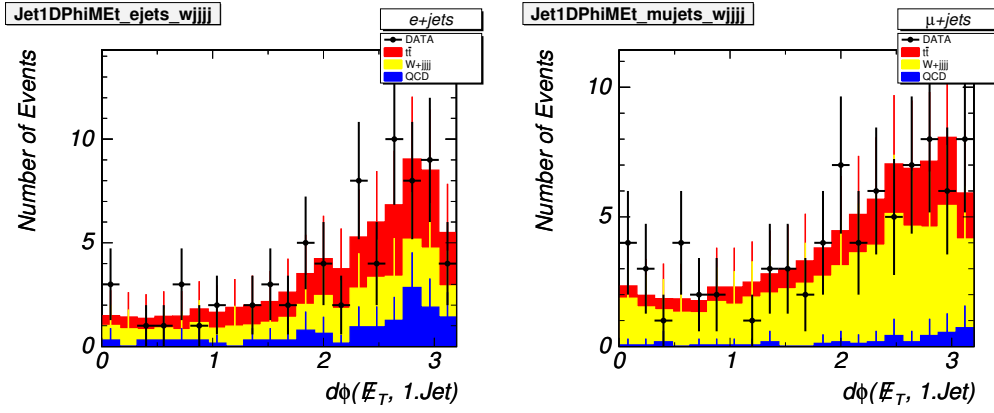


Figure E.16: ϕ angle between the leading (1.) jet and \cancel{E}_T for e+jets and μ +jets events for $n_{jets} = 4$.

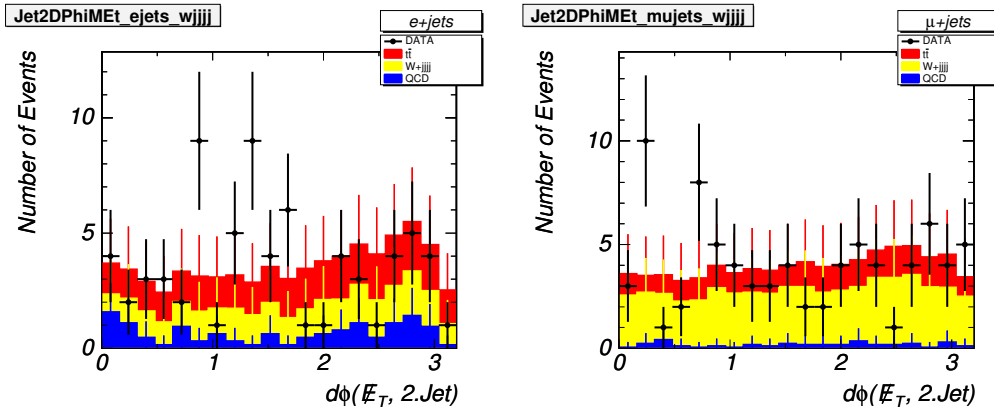


Figure E.17: ϕ angle between the 2. jet and \cancel{E}_T for e+jets and μ +jets events for $n_{jets} = 4$.

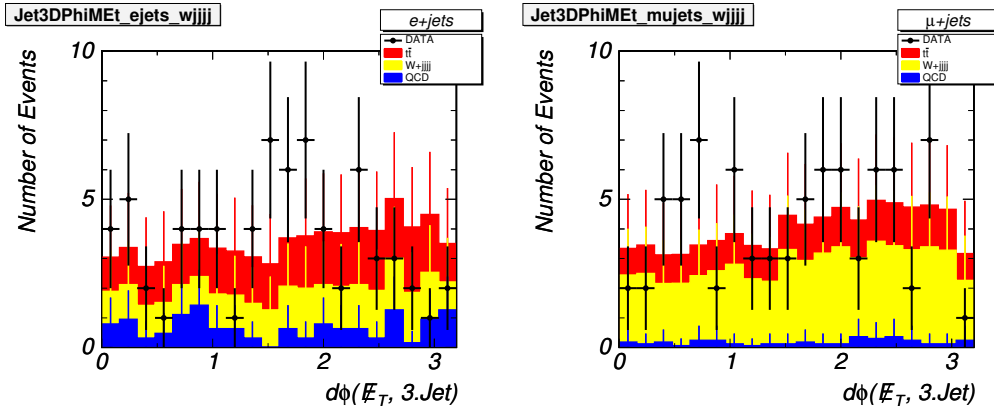


Figure E.18: ϕ angle between the 3. jet and \cancel{E}_T for e+jets and μ +jets events for $n_{jets} = 4$.

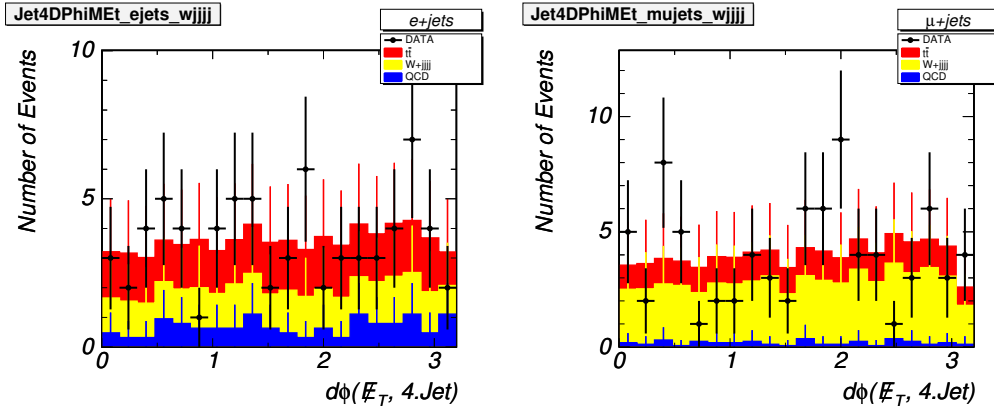


Figure E.19: ϕ angle between the 4. jet and \vec{E}_T^{miss} for e+jets and μ +jets events for $n_{\text{jets}} = 4$.

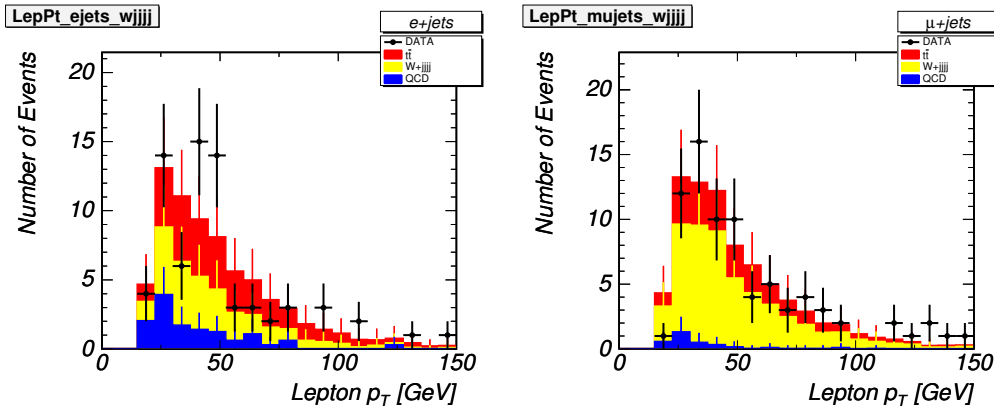


Figure E.20: Transverse momentum p_T of the lepton for e+jets and μ +jets events for $n_{\text{jets}} = 4$.

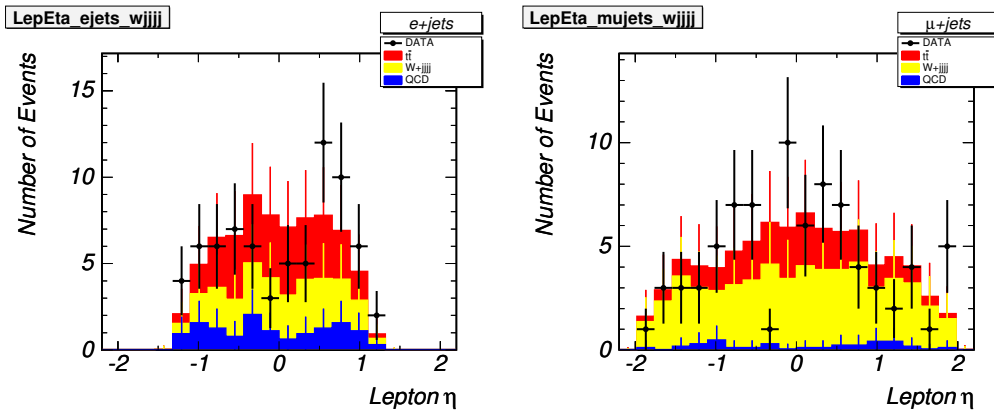


Figure E.21: Pseudorapidity η of the lepton for e+jets and μ +jets events for $n_{\text{jets}} = 4$.

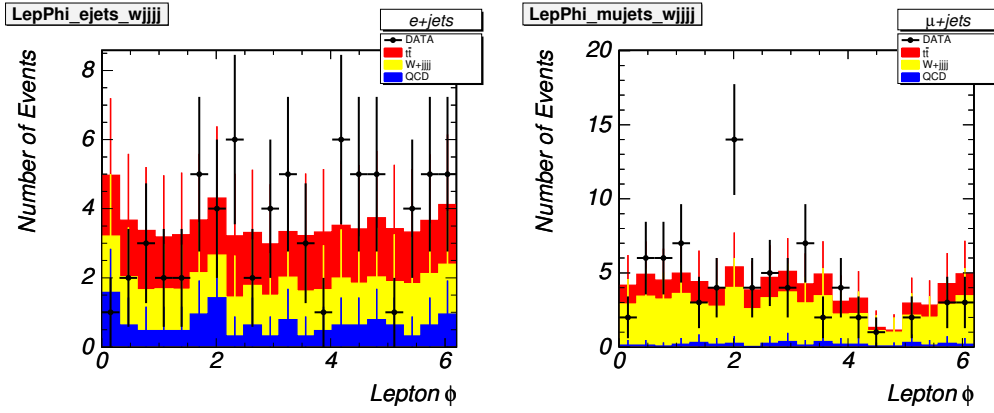


Figure E.22: ϕ angle of the lepton for e+jets and μ +jets events for $n_{jets} = 4$.

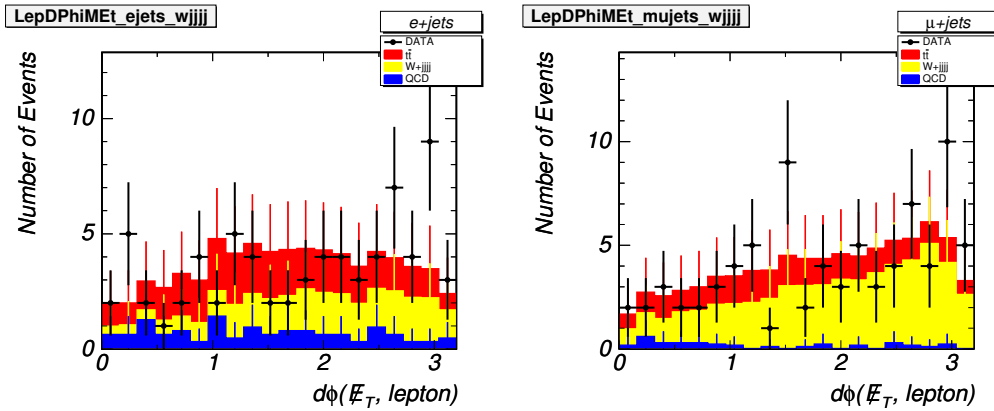


Figure E.23: ϕ angle between the lepton and \cancel{E}_T for e+jets and μ +jets events for $n_{jets} = 4$.

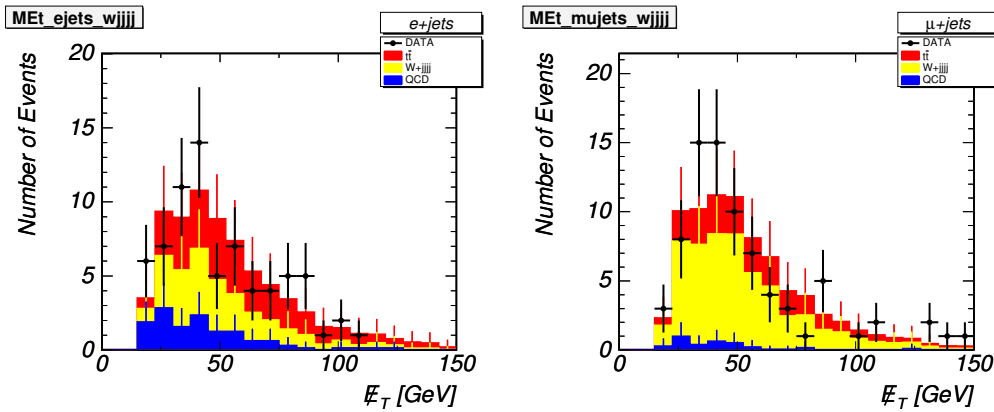


Figure E.24: Missing transverse energy \cancel{E}_T for e+jets and μ +jets events for $n_{jets} = 4$.

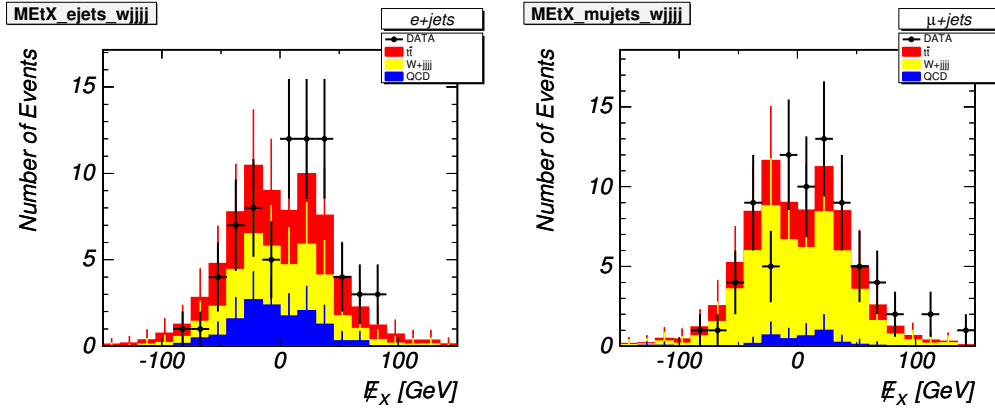


Figure E.25: x -component of E_T for $e+jets$ and $\mu+jets$ events for $n_{jets} = 4$.

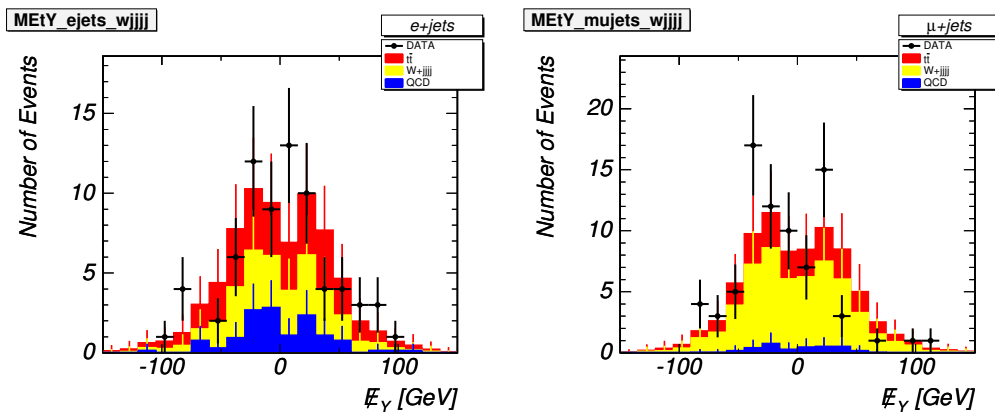


Figure E.26: y -component of E_T for $e+jets$ and $\mu+jets$ events for $n_{jets} = 4$.

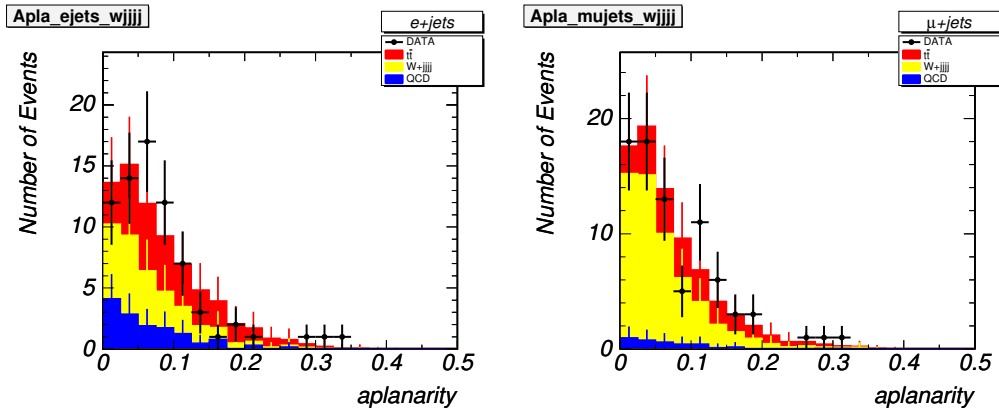


Figure E.27: Aplanarity for e+jets and μ +jets events for $n_{jets} = 4$.

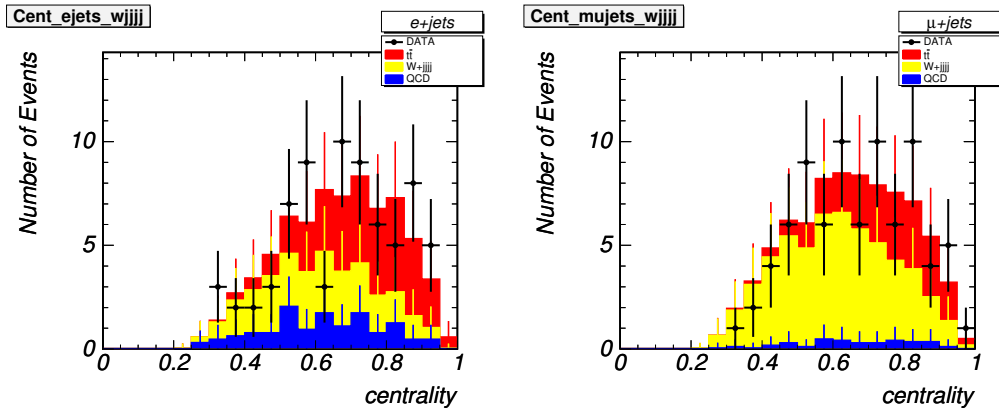


Figure E.28: Centrality for e+jets and μ +jets events for $n_{jets} = 4$.

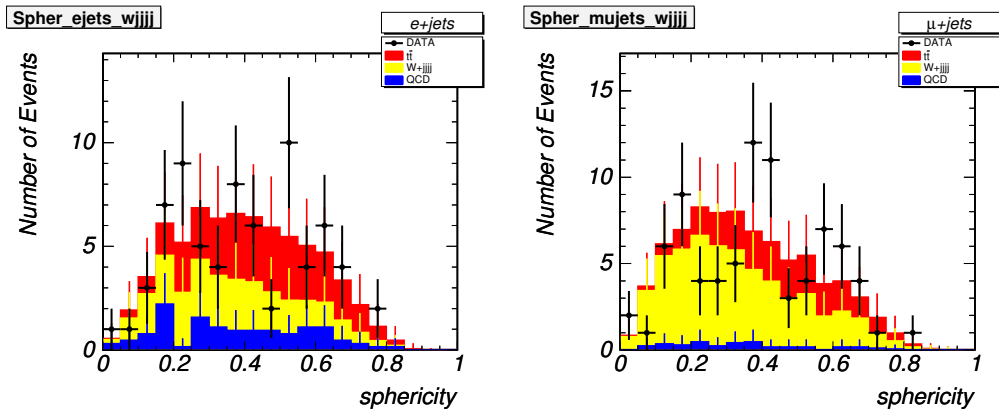


Figure E.29: Sphericity for e+jets and μ +jets events for $n_{jets} = 4$.

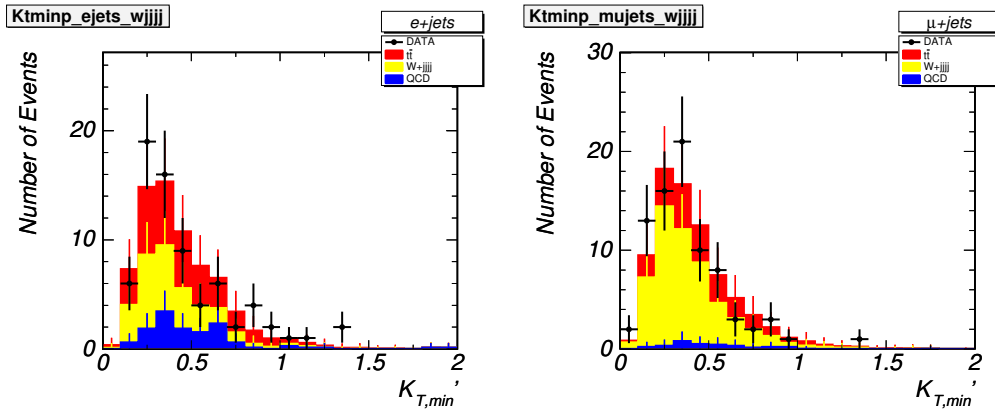


Figure E.30: $K'_{T,min}$ for e+jets and μ +jets events for $n_{jets} = 4$.

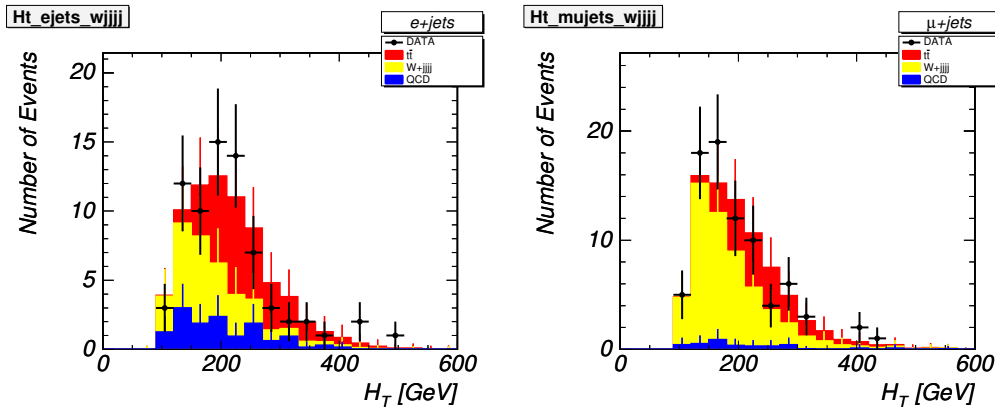


Figure E.31: H_T for e+jets and μ +jets events for $n_{jets} = 4$.

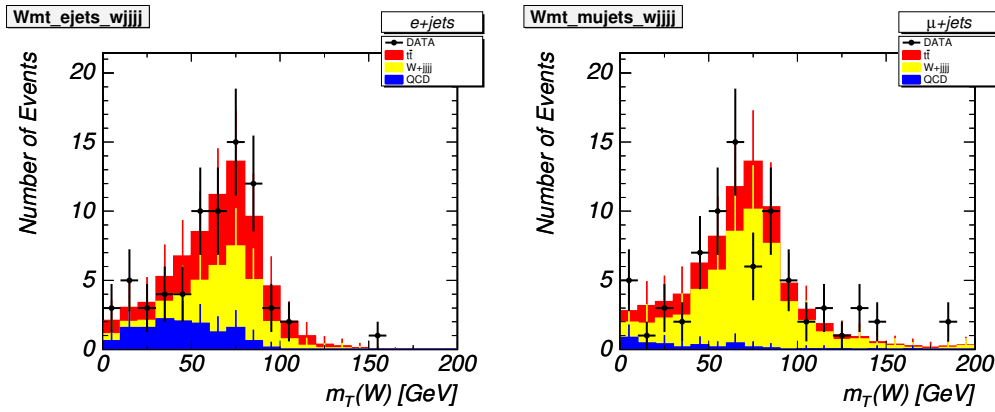


Figure E.32: Transverse mass m_T of the leptonically decaying W for e+jets and μ +jets events for $n_{jets} = 4$.

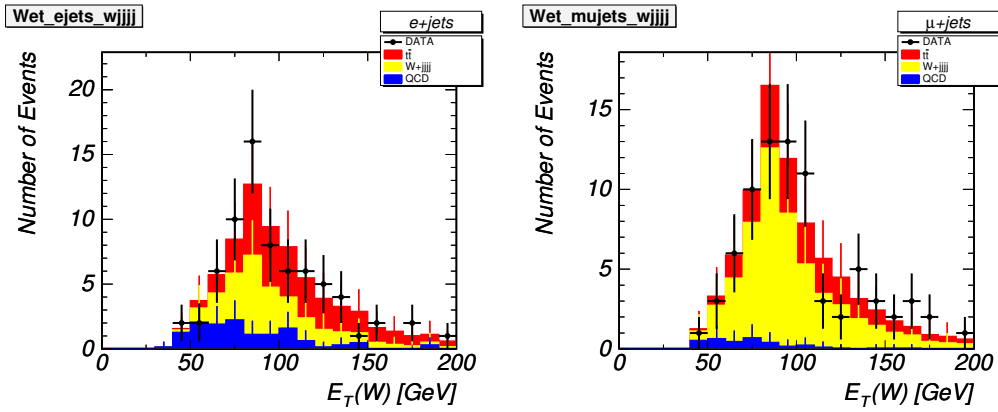


Figure E.33: Transverse energy E_T of the leptonically decaying W for $e+jets$ and $\mu+jets$ events for $n_{jets} = 4$.

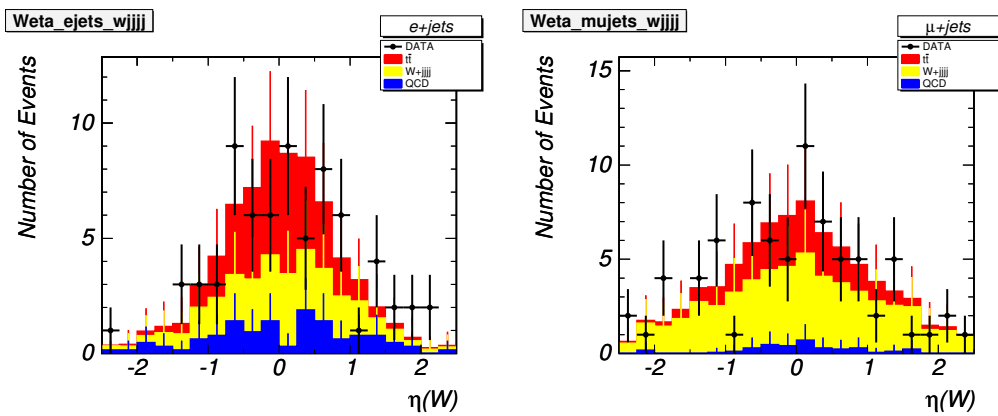


Figure E.34: Pseudorapidity η of the leptonically decaying W for $e+jets$ and $\mu+jets$ events for $n_{jets} = 4$.

E.2 Events with exactly 3 jets

In this section, the distributions are shown for events which pass all criteria of the event selection but have exactly 3 jets. These events originate dominantly from W + jets and QCD. The Multijet background is subtracted bin-by-bin from all data distributions using the Matrix Method (see Section 6.3.1) and compared to the W + jets Monte Carlo sample.

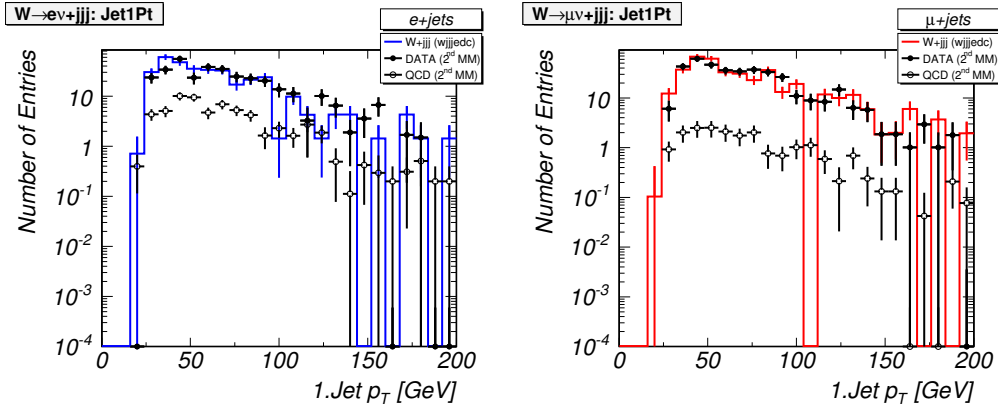


Figure E.35: Transverse momentum p_T of the leading (1.) jet for e+jets and μ +jets events for $n_{jets} = 3$.

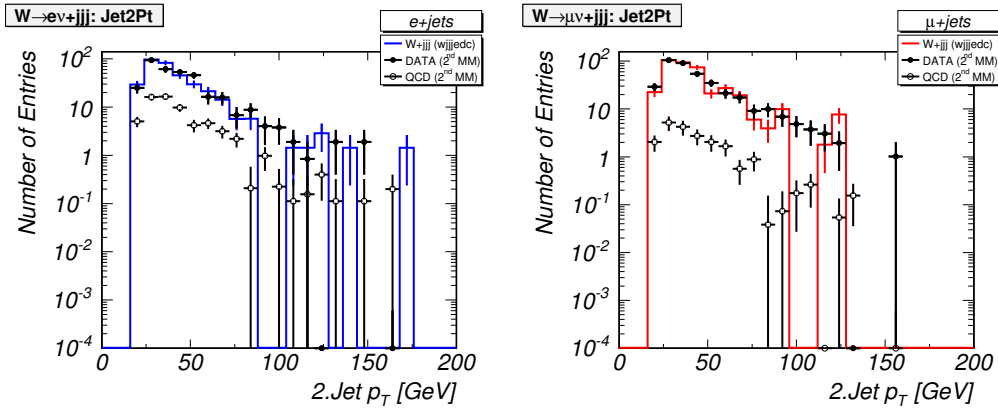


Figure E.36: Transverse momentum p_T of the 2. jet for e+jets and μ +jets events for $n_{jets} = 3$.

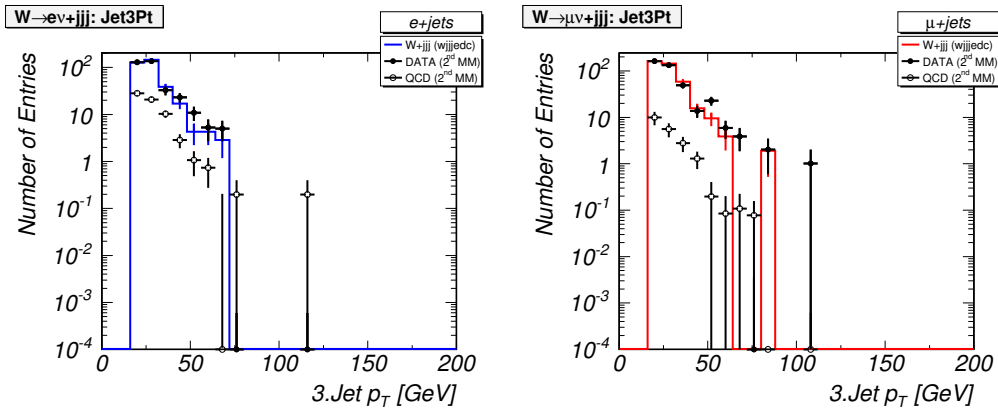


Figure E.37: Transverse momentum p_T of the 3. jet for e+jets and μ +jets events for $n_{jets} = 3$.

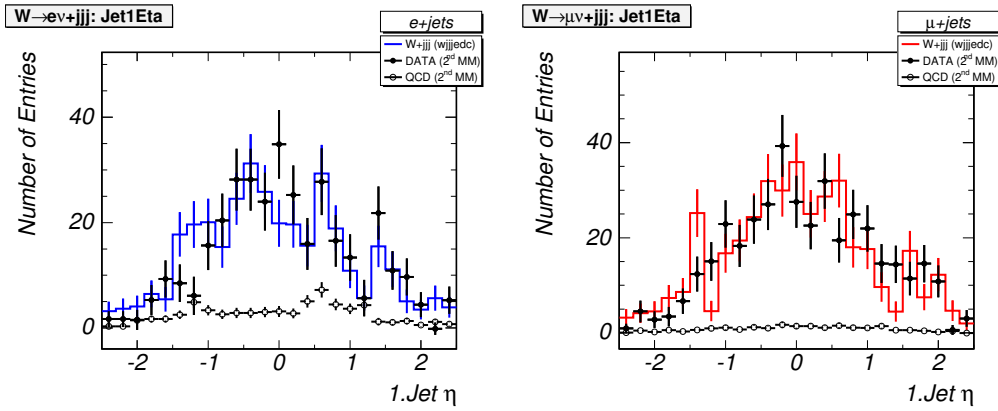


Figure E.38: Pseudorapidity η of the leading (1.) jet for e+jets and μ +jets events for $n_{jets} = 3$.

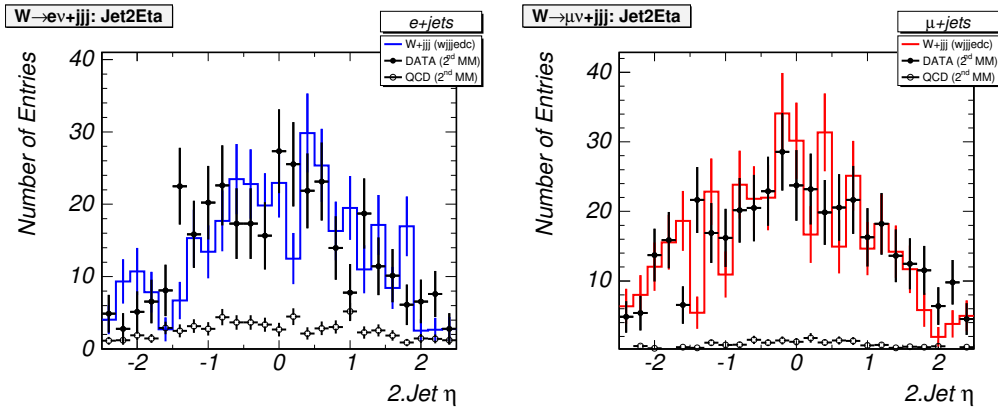


Figure E.39: Pseudorapidity η of the 2. jet for e+jets and μ +jets events for $n_{jets} = 3$.

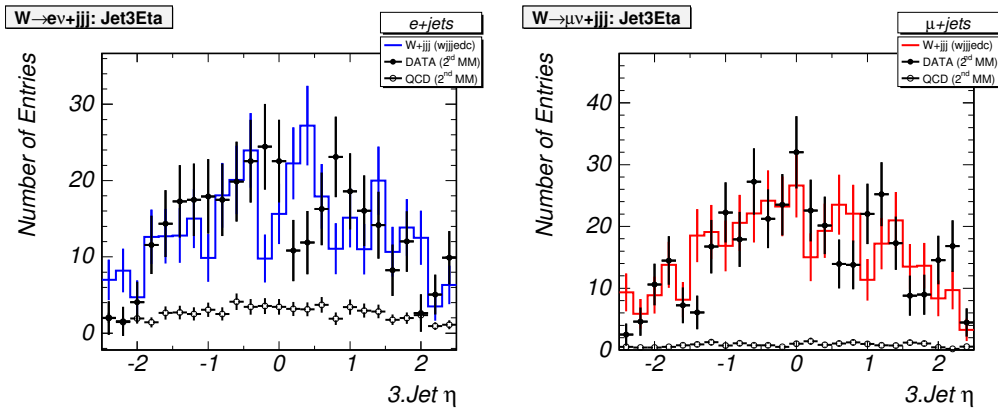
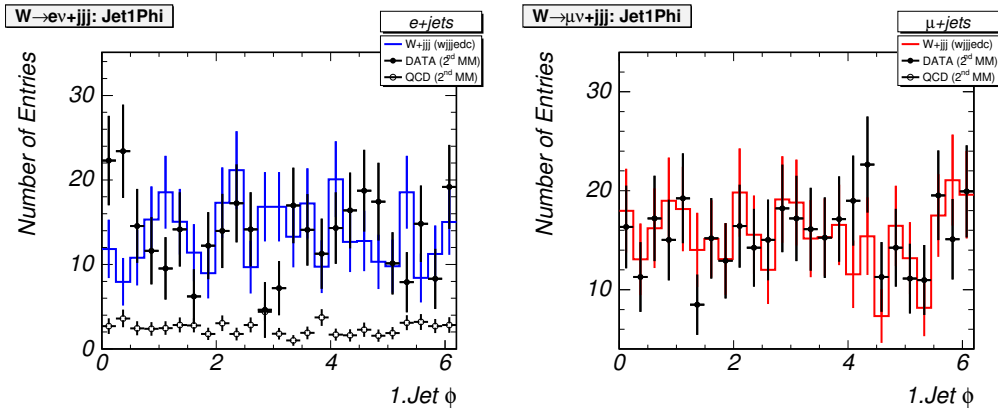
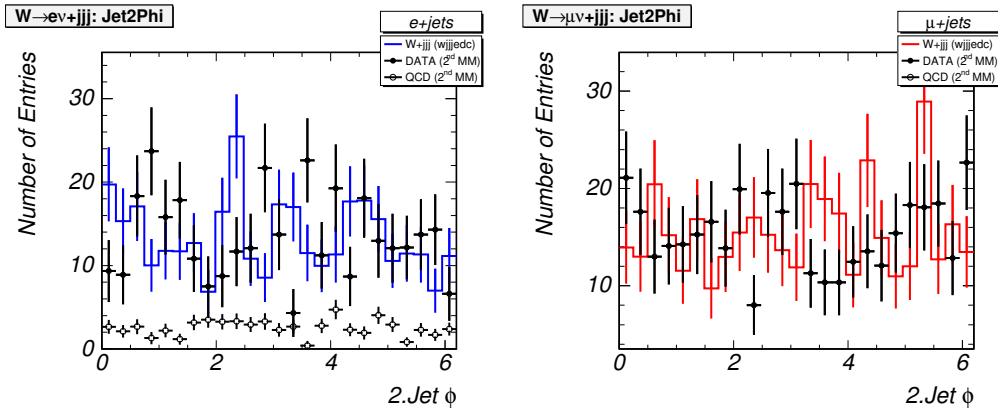
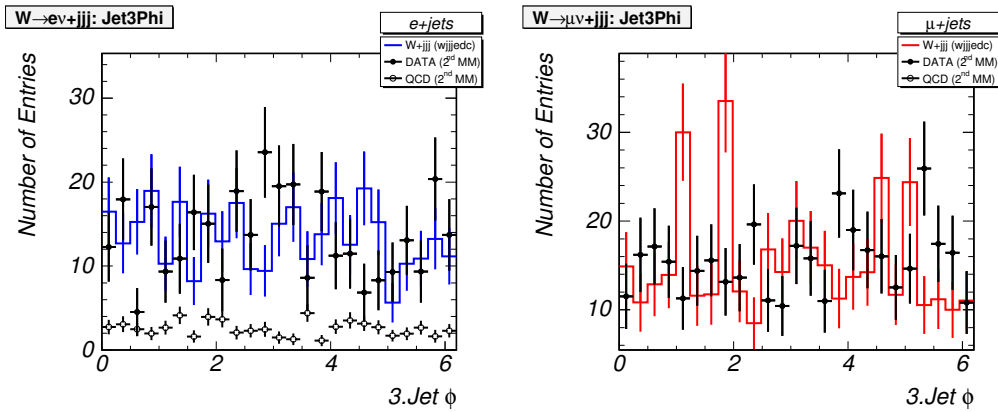


Figure E.40: Pseudorapidity η of the 3. jet for e+jets and μ +jets events for $n_{jets} = 3$.

Figure E.41: ϕ angle of the leading (1.) jet for e+jets and μ +jets events for $n_{jets} = 3$.Figure E.42: ϕ angle of the 2. jet for e+jets and μ +jets events for $n_{jets} = 3$.Figure E.43: ϕ angle of the 3. jet for e+jets and μ +jets events for $n_{jets} = 3$.

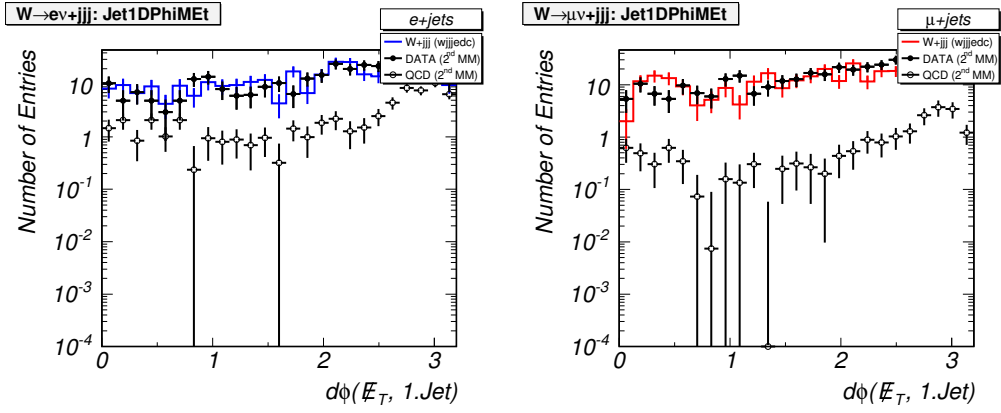


Figure E.44: ϕ angle between the leading (1.) jet and \cancel{E}_T for e+jets and μ +jets events for $n_{jets} = 3$.

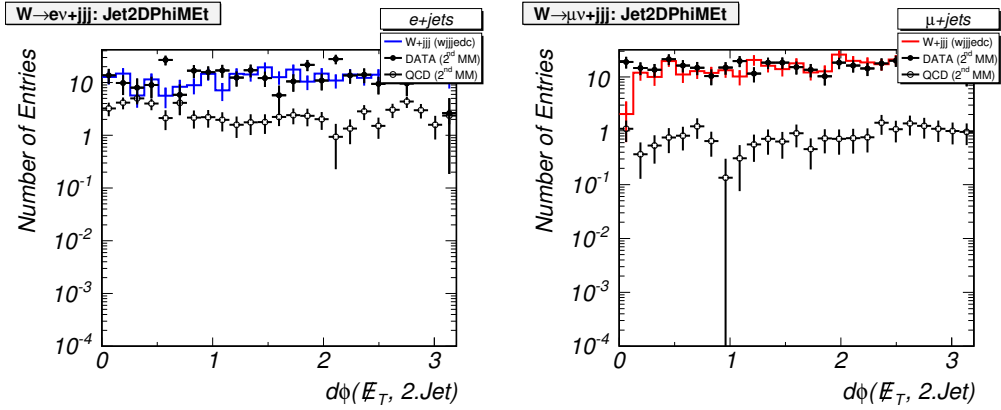


Figure E.45: ϕ angle between the 2. jet and \cancel{E}_T for e+jets and μ +jets events for $n_{jets} = 3$.

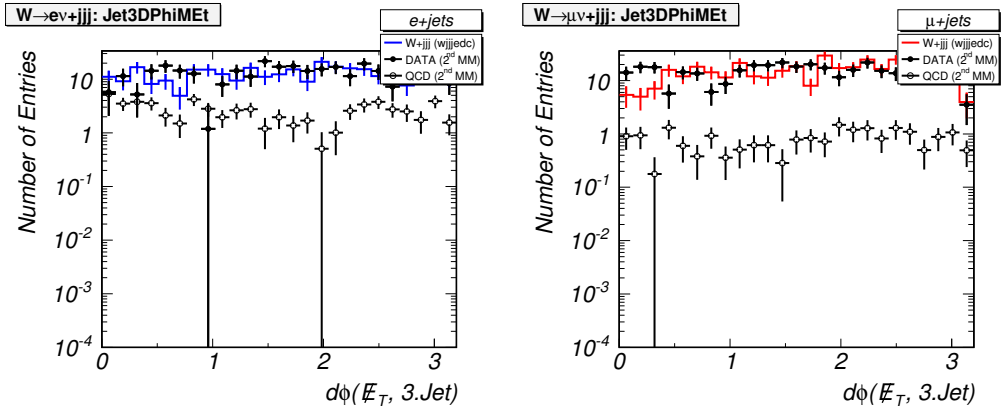
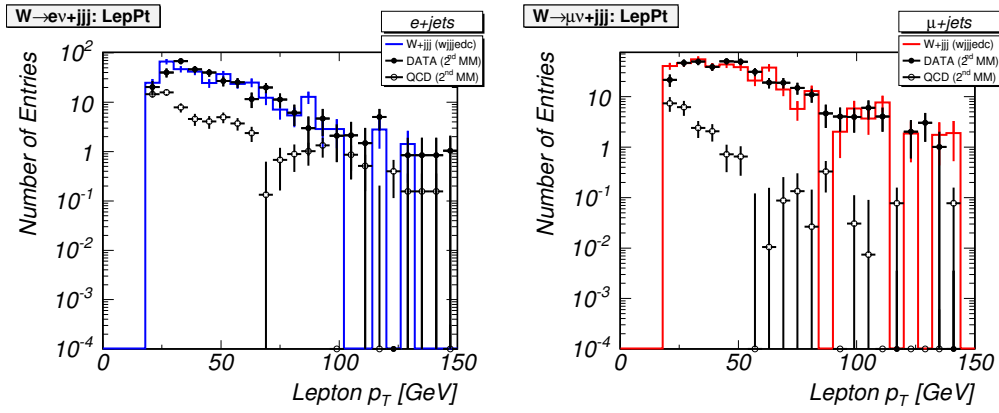
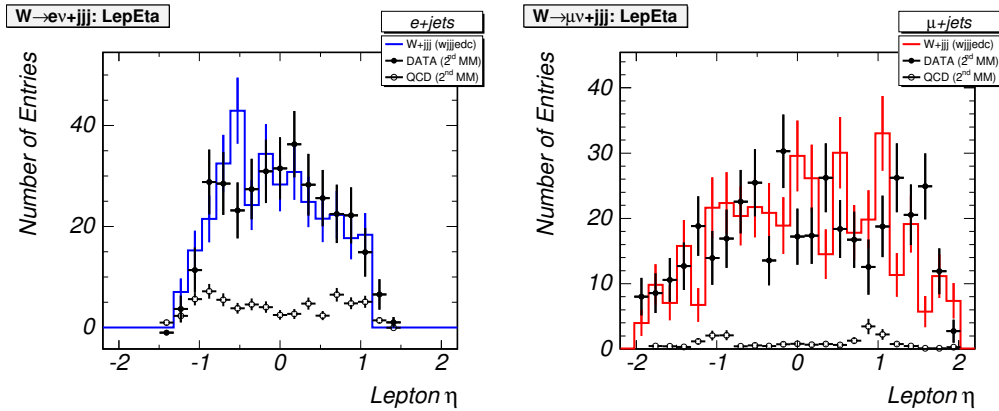
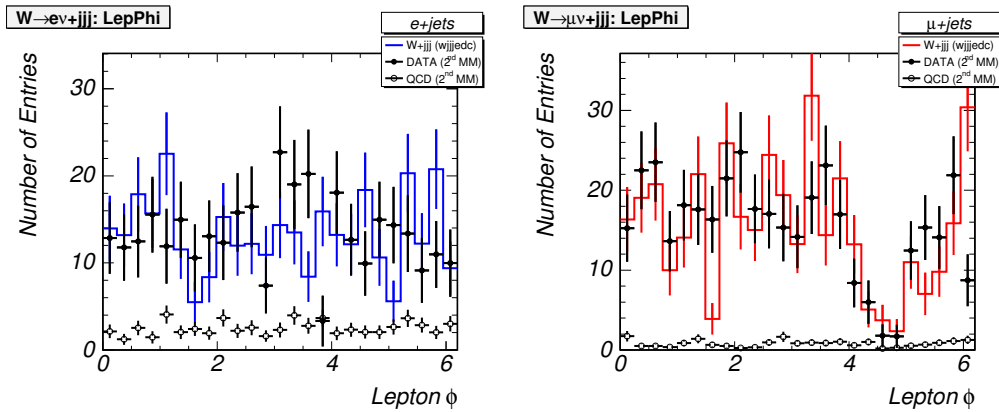


Figure E.46: ϕ angle between the 3. jet and \cancel{E}_T for e+jets and μ +jets events for $n_{jets} = 3$.

Figure E.47: Transverse momentum p_T of the lepton for e+jets and μ +jets events for $n_{jets} = 3$.Figure E.48: Pseudorapidity η of the lepton for e+jets and μ +jets events for $n_{jets} = 3$.Figure E.49: ϕ angle of the lepton for e+jets and μ +jets events for $n_{jets} = 3$.

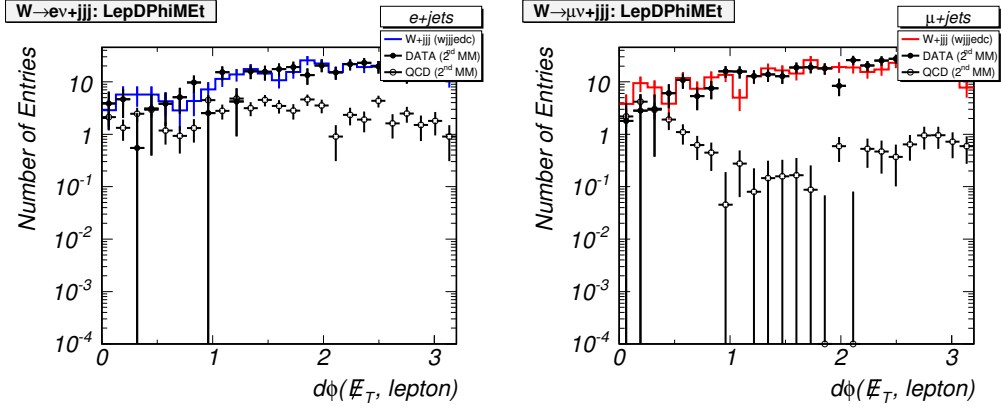


Figure E.50: ϕ angle between the lepton and \cancel{E}_T for e+jets and μ +jets events for $n_{jets} = 3$.

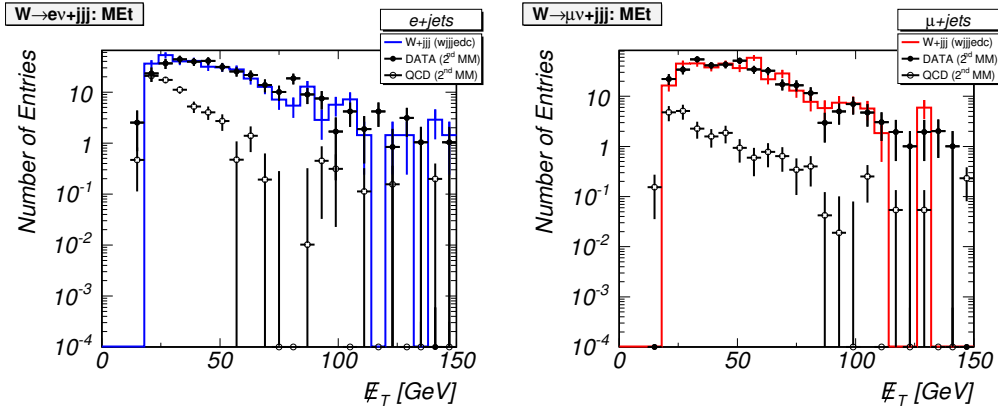


Figure E.51: Missing transverse energy \cancel{E}_T for e+jets and μ +jets events for $n_{jets} = 3$.

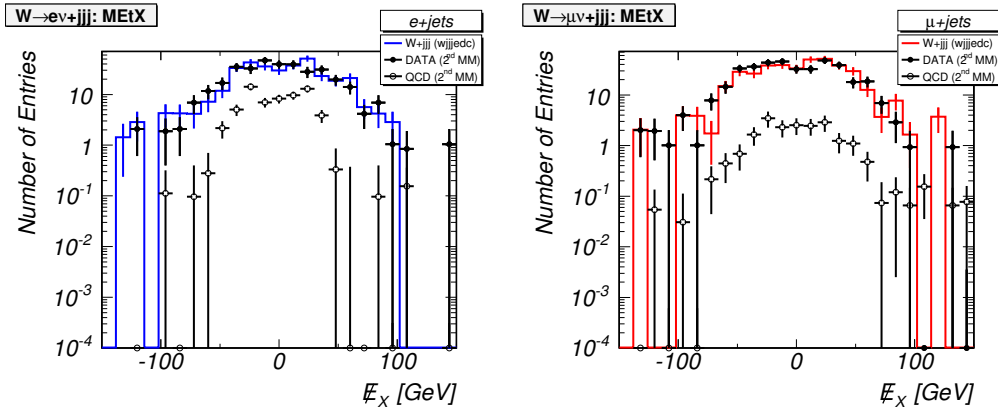


Figure E.52: x -component of \cancel{E}_T for e+jets and μ +jets events for $n_{jets} = 3$.

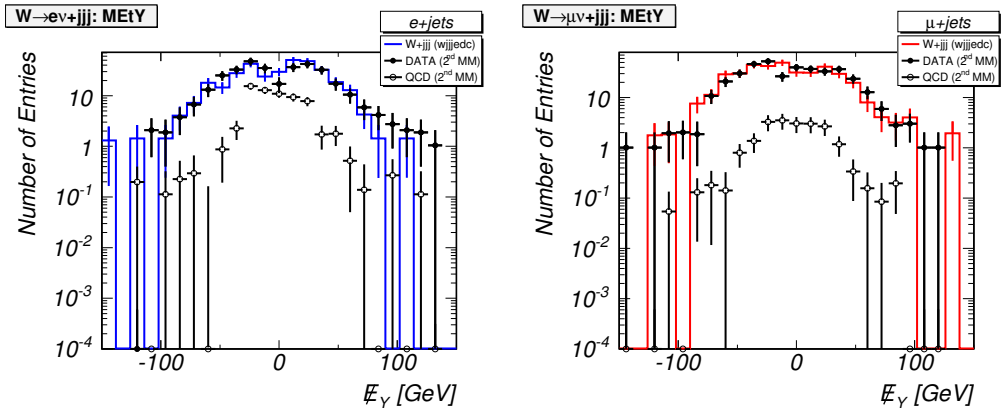


Figure E.53: y -component of E_T for e +jets and μ +jets events for $n_{jets} = 3$.

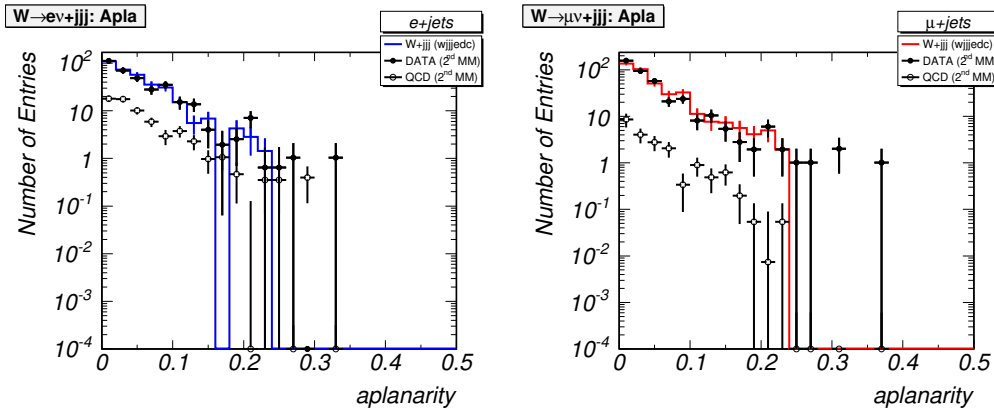


Figure E.54: Aplanarity for e +jets and μ +jets events for $n_{jets} = 3$.

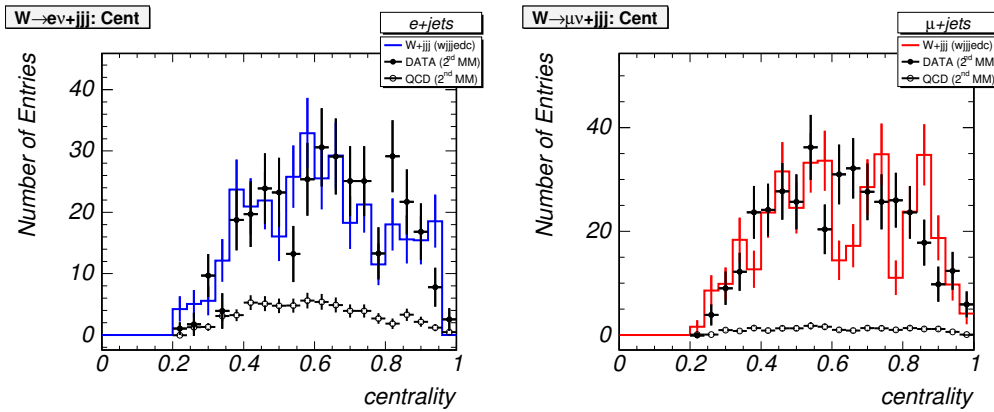
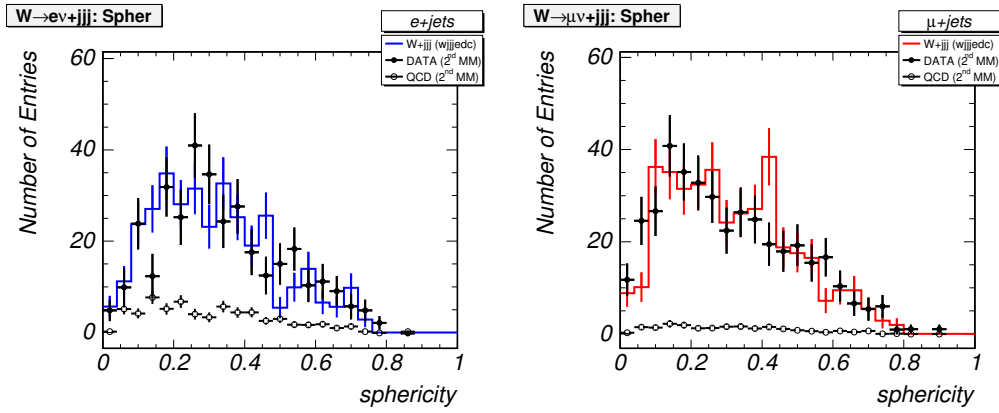
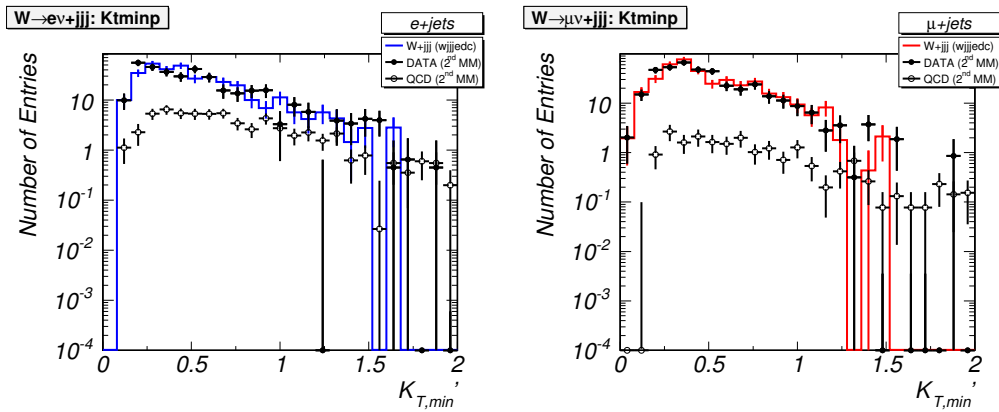
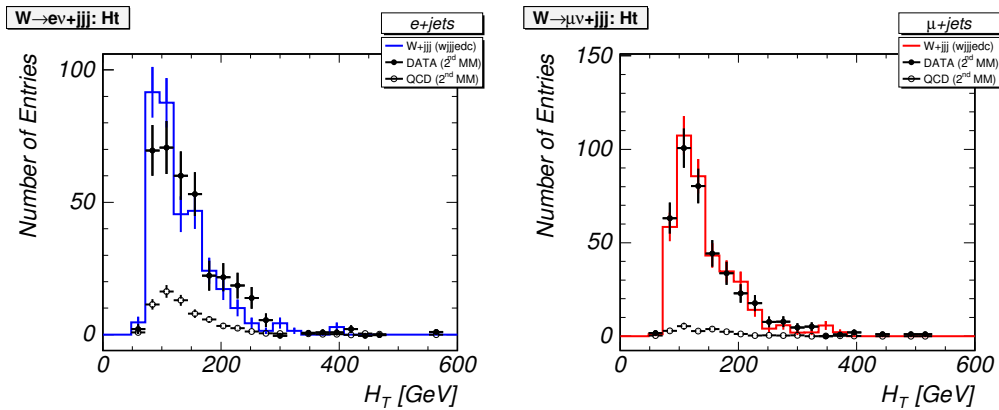


Figure E.55: Centrality for e +jets and μ +jets events for $n_{jets} = 3$.

Figure E.56: Sphericity for e+jets and μ +jets events for $n_{jets} = 3$.Figure E.57: $K'_{T,min}$ for e+jets and μ +jets events for $n_{jets} = 3$.Figure E.58: H_T for e+jets and μ +jets events for $n_{jets} = 3$.

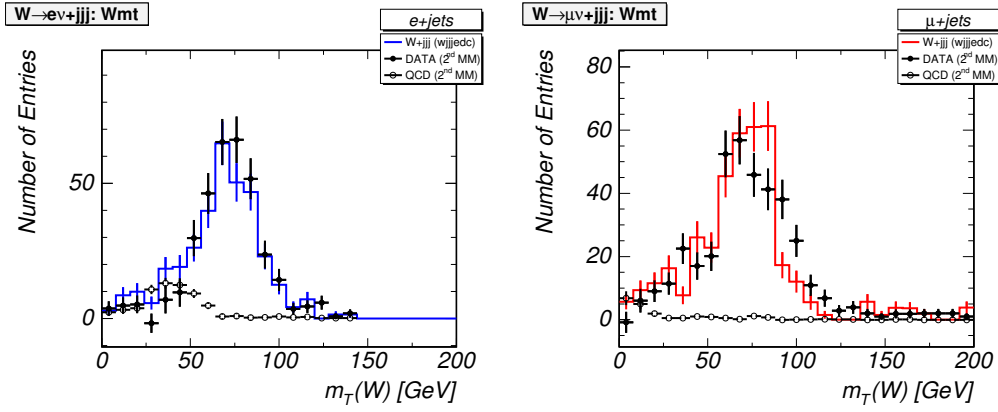


Figure E.59: Transverse mass m_T of the leptonically decaying W for e+jets and μ +jets events for $n_{jets} = 3$.

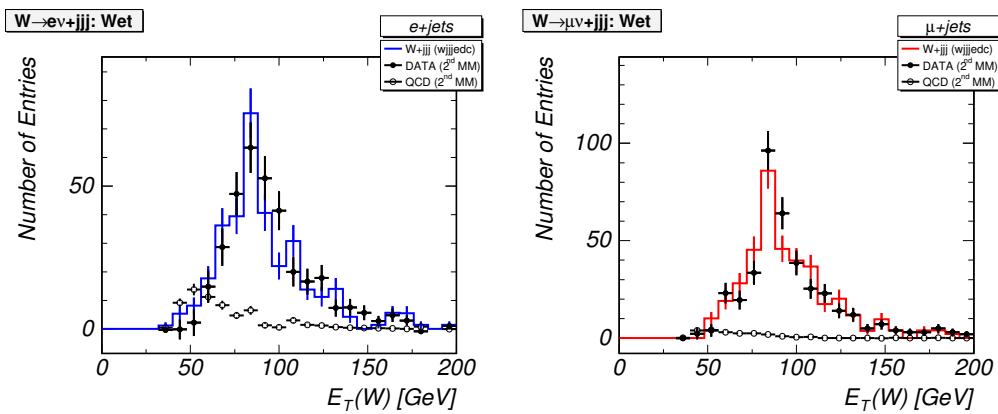


Figure E.60: Transverse energy E_T of the leptonically decaying W for e+jets and μ +jets events for $n_{jets} = 3$.

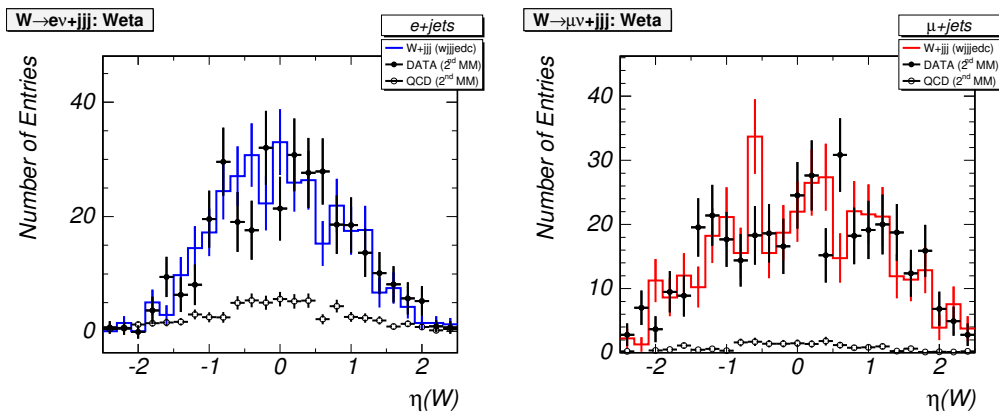


Figure E.61: Pseudorapidity η of the leptonically decaying W for $e+jets$ and $\mu+jets$ events for $n_{jets} = 3$.

E.3 Events with exactly 2 jets

In this section, the distributions are shown for events which pass all criteria of the event selection but have exactly 2 jets. These events originate dominantly from W + jets and QCD. The Multijet background is subtracted bin-by-bin from all data distributions using the Matrix Method (see Section 6.3.1) and compared to the W + jets Monte Carlo sample.

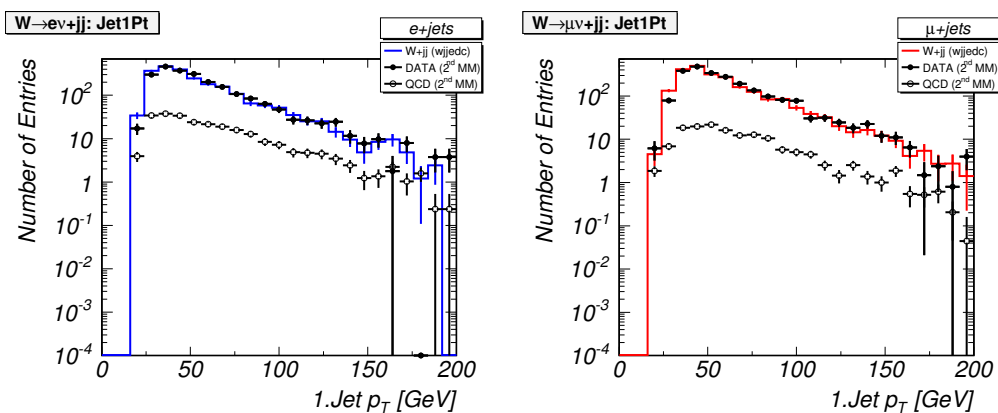


Figure E.62: Transverse momentum p_T of the leading (1.) jet for e+jets and μ +jets events for $n_{jets} = 2$.

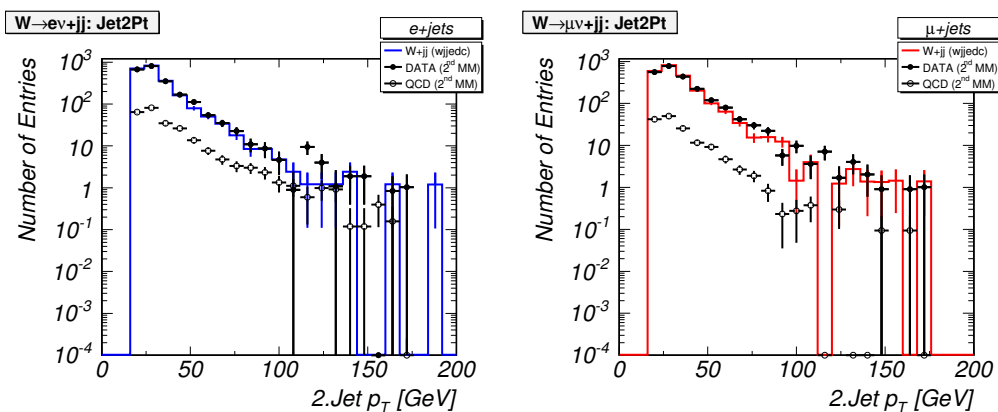


Figure E.63: Transverse momentum p_T of the 2. jet for e+jets and μ +jets events for $n_{jets} = 2$.

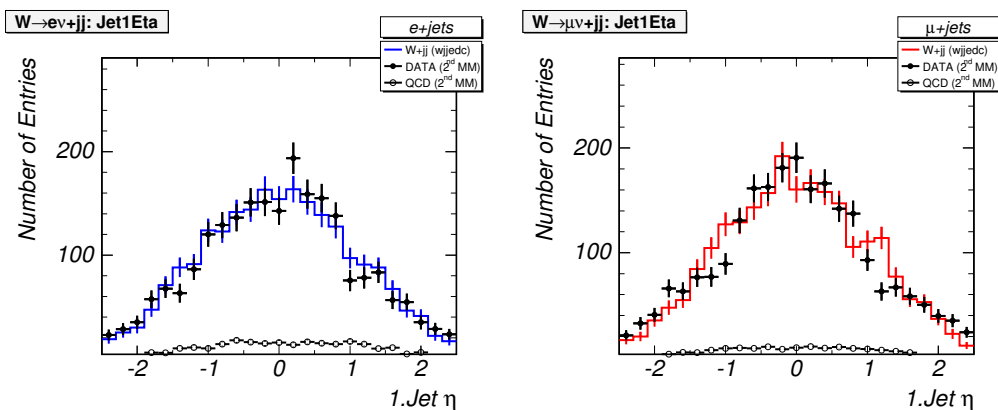


Figure E.64: Pseudorapidity η of the leading (1.) jet for e+jets and μ +jets events for $n_{jets} = 2$.

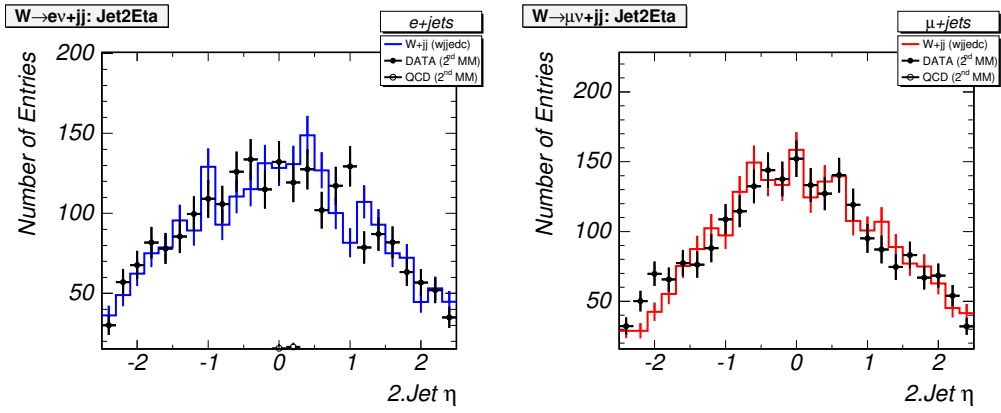


Figure E.65: Pseudorapidity η of the 2. jet for e+jets and μ +jets events for $n_{jets} = 2$.

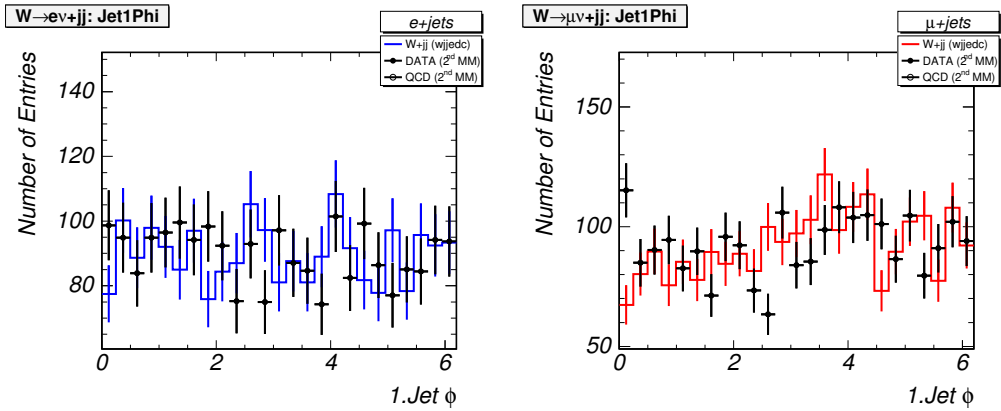


Figure E.66: ϕ angle of the leading (1.) jet for e+jets and μ +jets events for $n_{jets} = 2$.

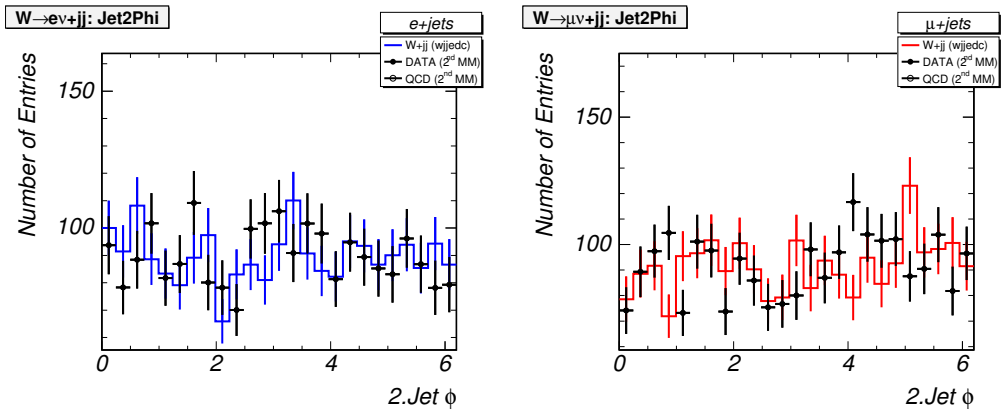


Figure E.67: ϕ angle of the 2. jet for e+jets and μ +jets events for $n_{jets} = 2$.

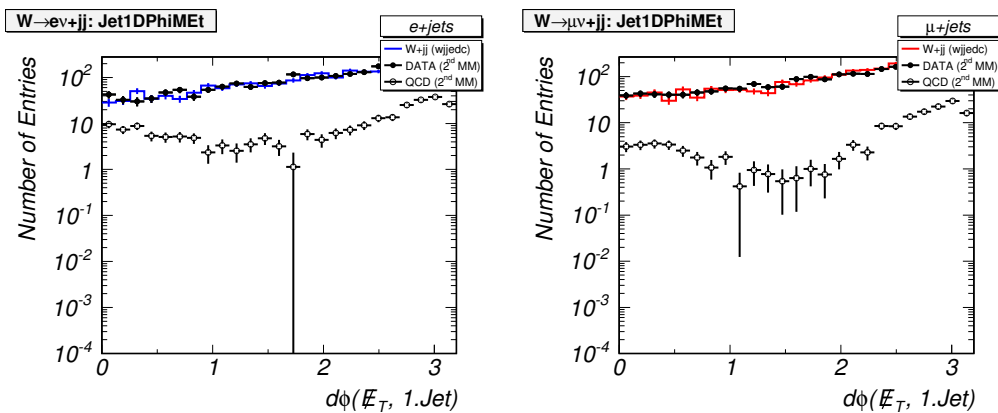


Figure E.68: ϕ angle between the leading (1.) jet and \cancel{E}_T for e+jets and μ +jets events for $n_{jets} = 2$.

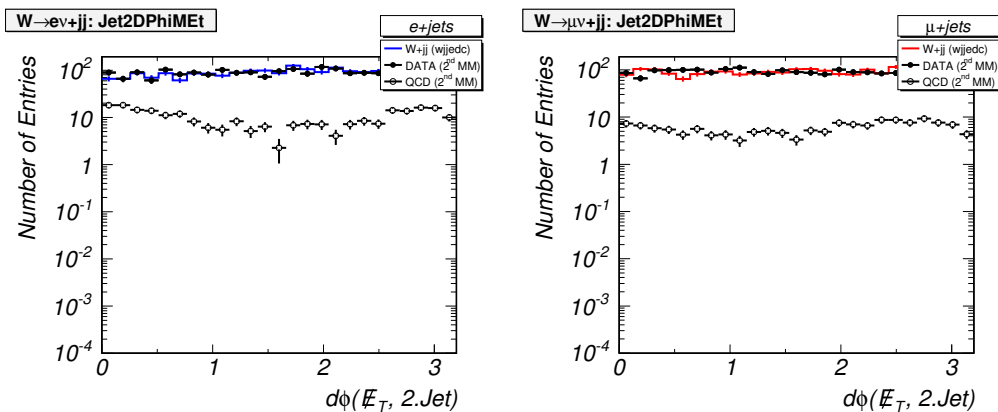


Figure E.69: ϕ angle between the 2. jet and \cancel{E}_T for e+jets and μ +jets events for $n_{jets} = 2$.

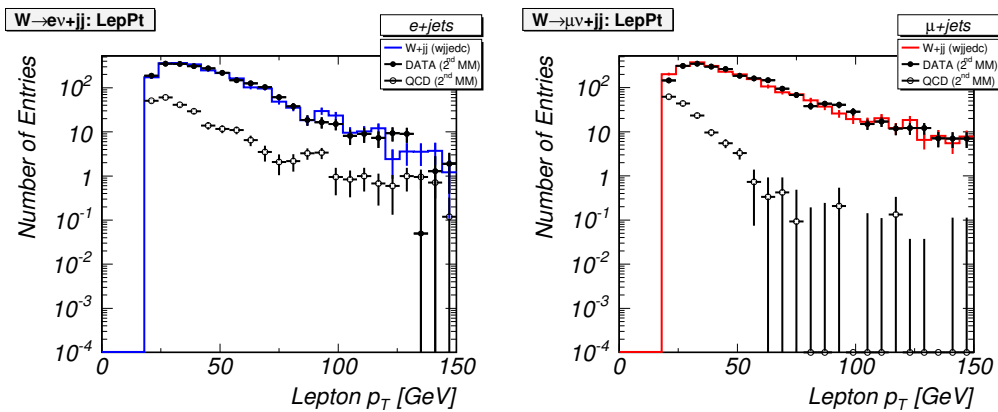


Figure E.70: Transverse momentum p_T of the lepton for e+jets and μ +jets events for $n_{jets} = 2$.

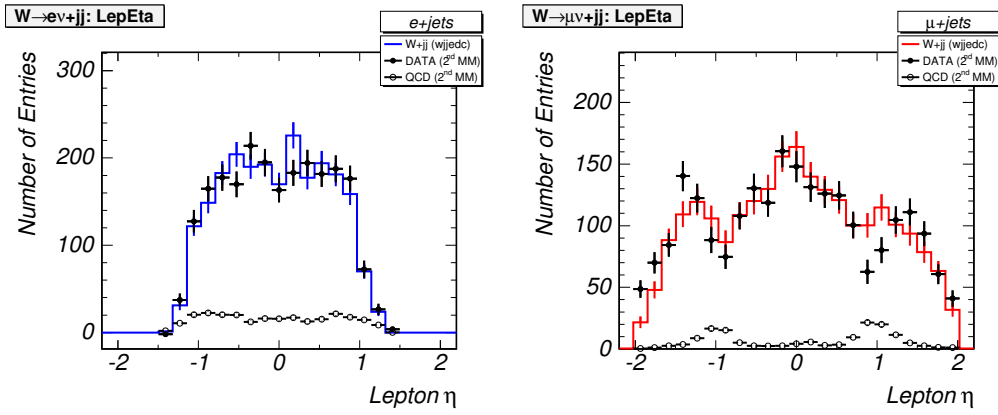


Figure E.71: Pseudorapidity η of the lepton for e+jets and μ +jets events for $n_{jets} = 2$.

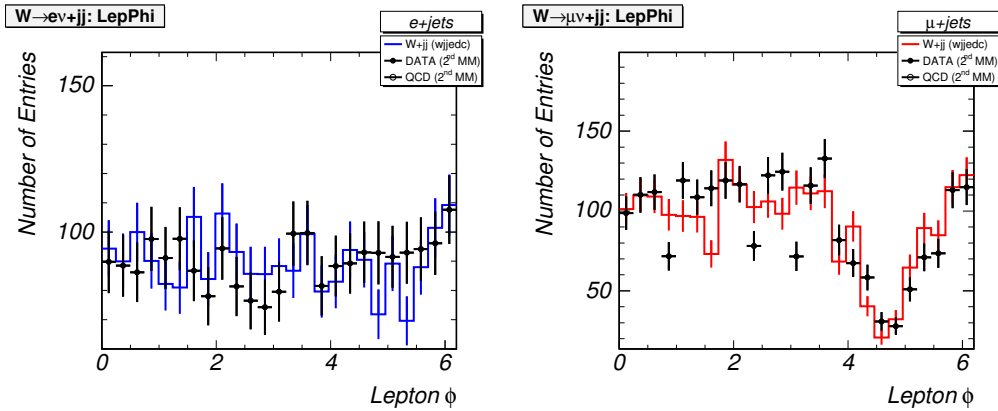


Figure E.72: ϕ angle of the lepton for e+jets and μ +jets events for $n_{jets} = 2$.

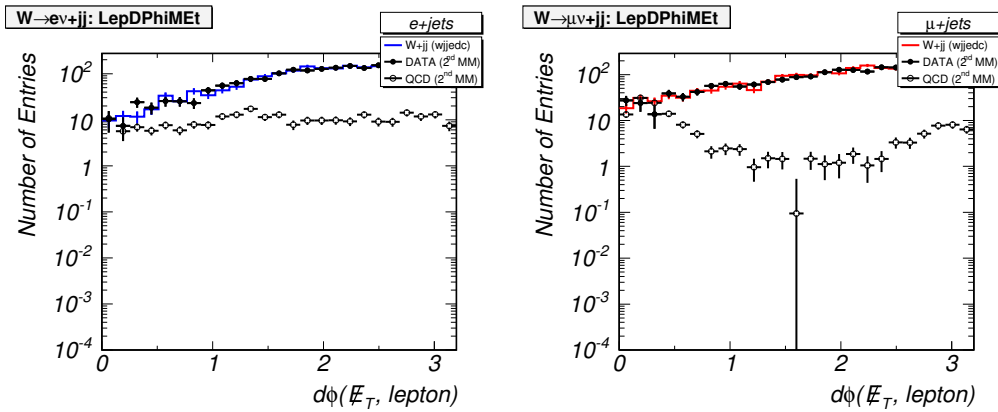


Figure E.73: ϕ angle between the lepton and \cancel{E}_T for e+jets and μ +jets events for $n_{jets} = 2$.

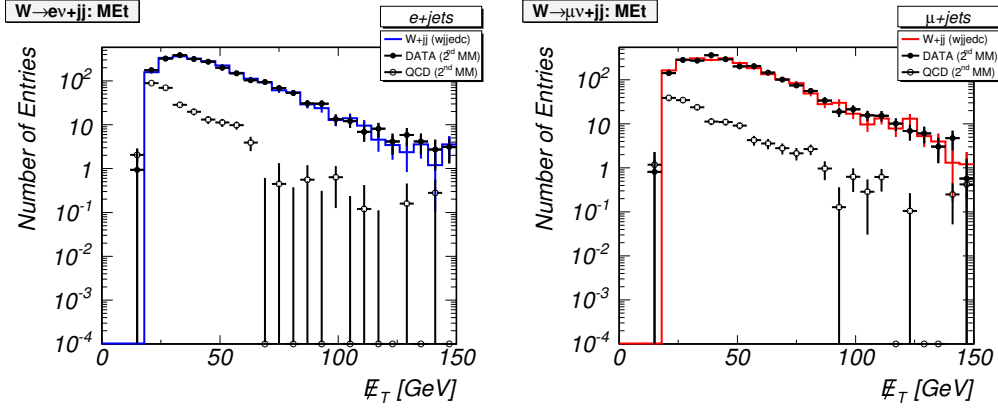


Figure E.74: Missing transverse energy E_T for e+jets and μ +jets events for $n_{jets} = 2$.

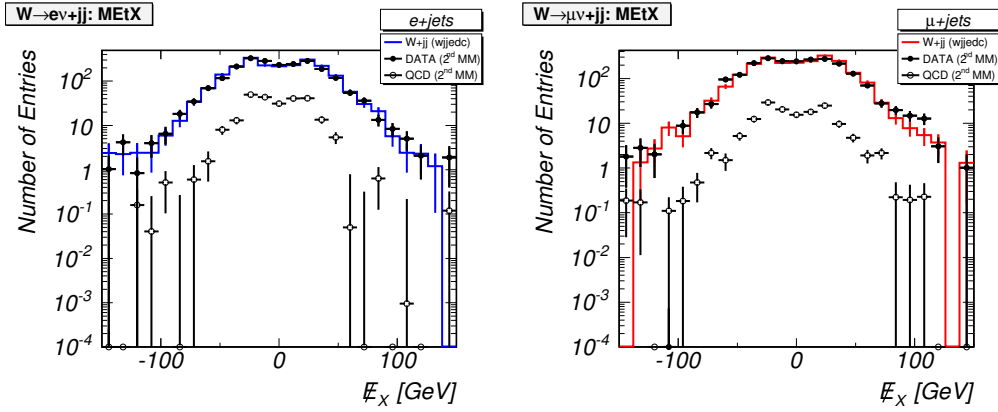


Figure E.75: x -component of E_T for e+jets and μ +jets events for $n_{jets} = 2$.

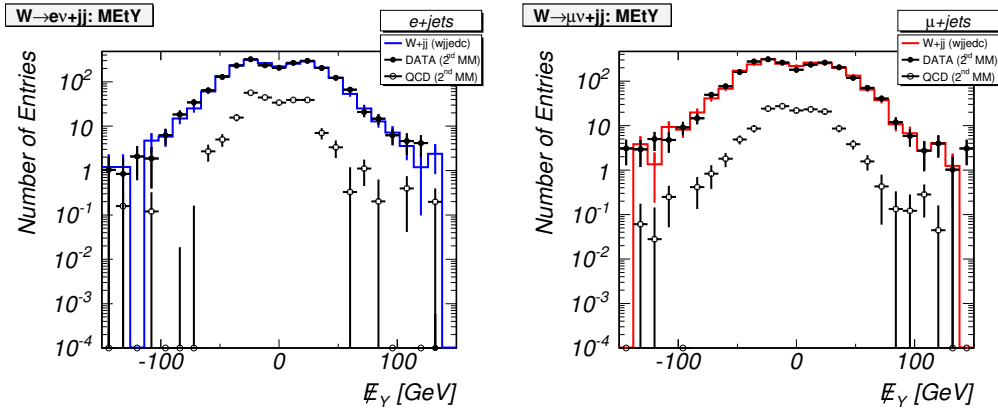


Figure E.76: y -component of E_T for e+jets and μ +jets events for $n_{jets} = 2$.

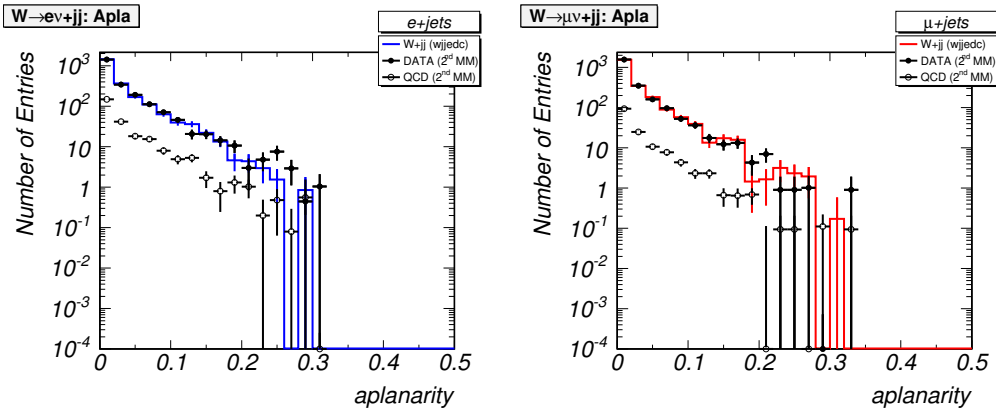


Figure E.77: Aplanarity for e+jets and μ +jets events for $n_{jets} = 2$.

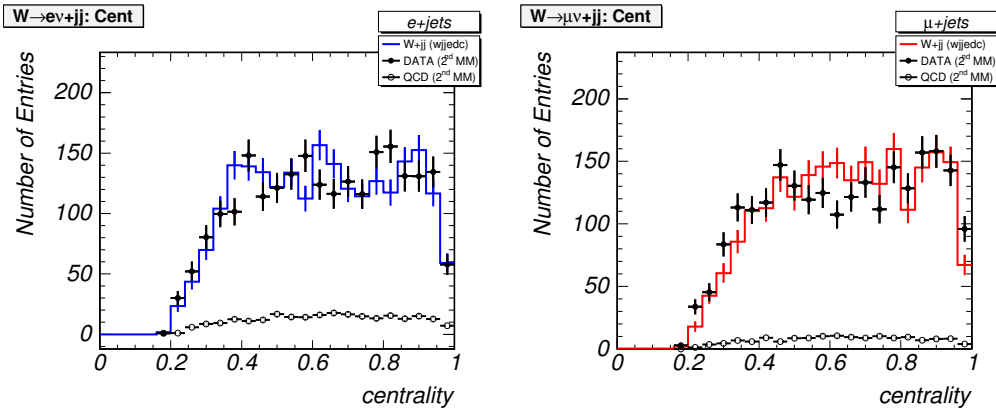


Figure E.78: Centrality for e+jets and μ +jets events for $n_{jets} = 2$.

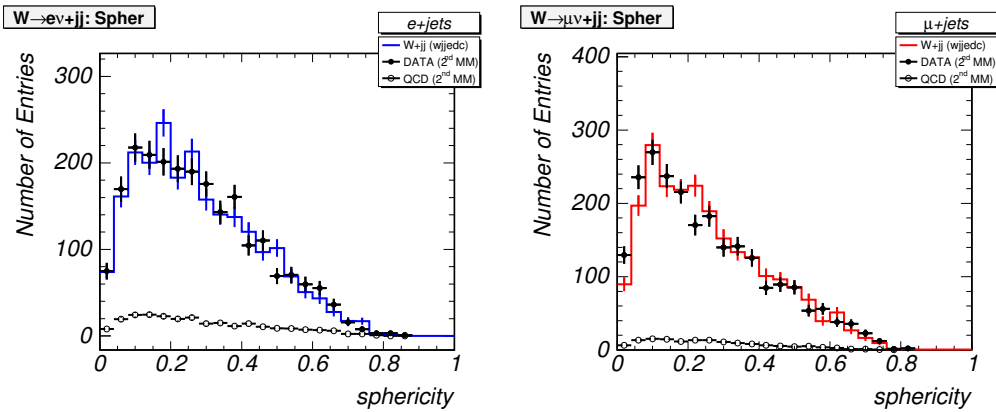
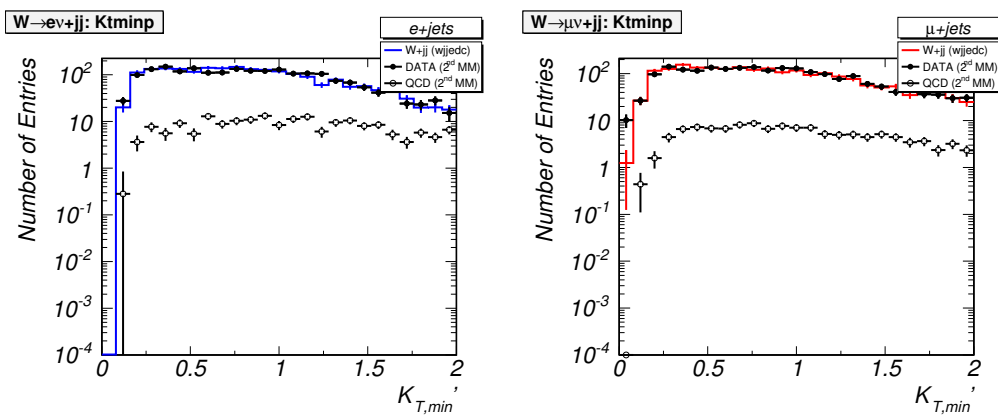
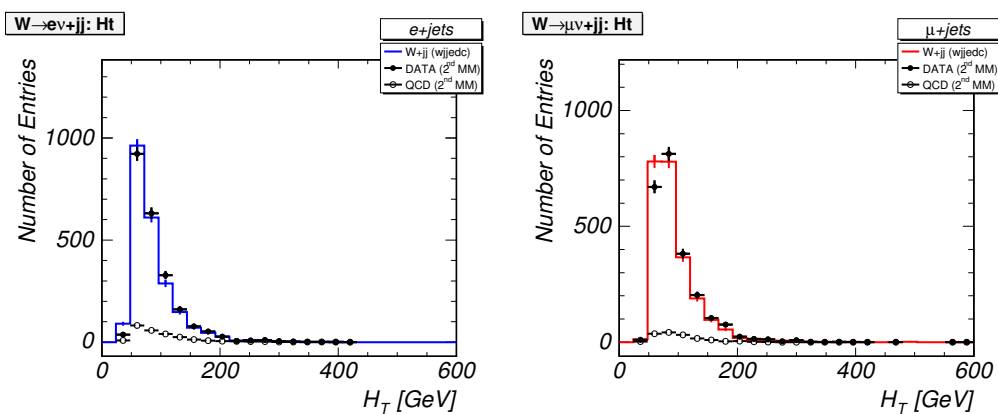
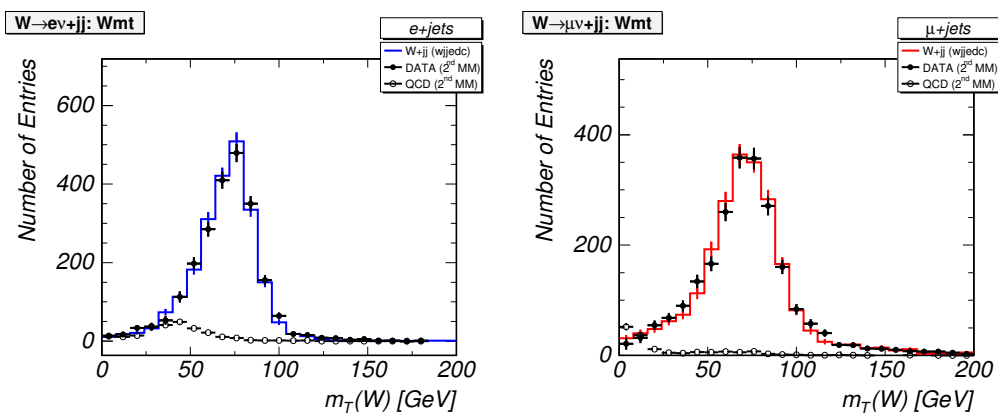


Figure E.79: Sphericity for e+jets and μ +jets events for $n_{jets} = 2$.

Figure E.80: $K'_{T,min}$ for e+jets and μ +jets events for $n_{jets} = 2$.Figure E.81: H_T for e+jets and μ +jets events for $n_{jets} = 2$.Figure E.82: Transverse mass m_T of the leptonically decaying W for e+jets and μ +jets events for $n_{jets} = 2$.

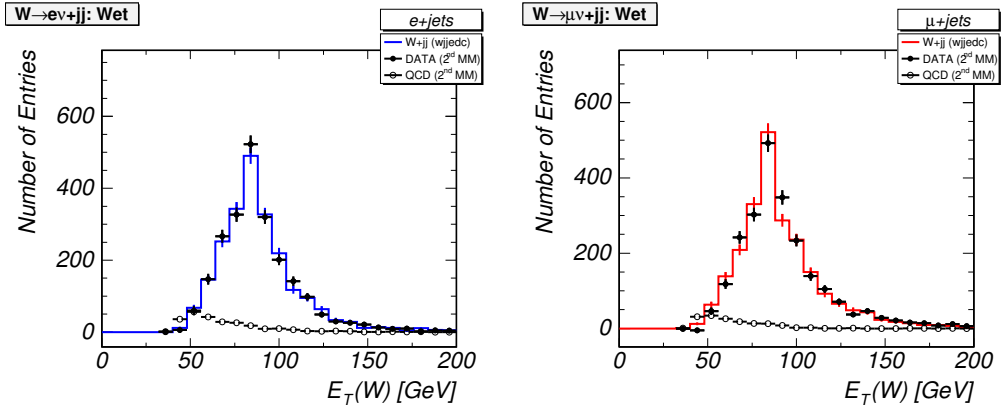


Figure E.83: Transverse energy E_T of the leptonically decaying W for e+jets and μ +jets events for $n_{jets} = 2$.

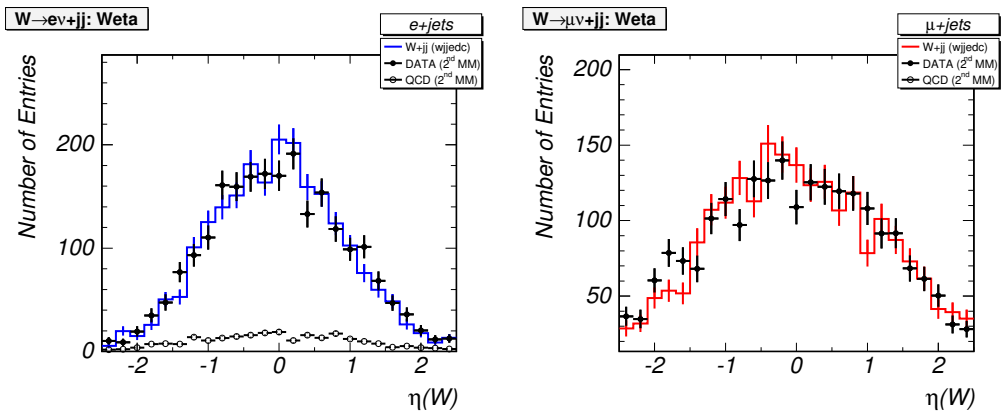


Figure E.84: Pseudorapidity η of the leptonically decaying W for e+jets and μ +jets events for $n_{jets} = 2$.

Bibliography

- [1] V. Abrazov *et al.* [The DØ collaboration], *t \bar{t} Production Cross Section in p \bar{p} Collisions at $\sqrt{s} = 1.8$ TeV*, Phys. Rev. D 67 012004, (2003).
- [2] T. Affolder *et al.*, *Measurement of the t \bar{t} Production Cross Section in p \bar{p} Collisions at $\sqrt{s} = 1.8$ TeV*, Phys. Rev. D 64, 032003 (2001).
- [3] V.M. Abazov *et al.*, *A precision measurement of the mass of the Top quark*, Nature 429:638-642 (2004).
- [4] F. Canelli, J. Estrada, T. Ferbel, G. Gutierrez, *Description of a method developed to measure the mass of the top quark at DØ*, DØ Note 3975 (2002).
- [5] J. Estrada, G. Gutierrez, *Understanding the improvement in the calculation of the top-quark mass using the full matrix element*, DØ Note 3811 (2000).
- [6] *Fermilab's Chain of Accelerators*,
<http://www-bd.fnal.gov/public/chain.html>
Fermilab Beams division, *Run II Handbook*,
<http://www-bd.fnal.gov/runII/index.html>
- [7] C.W. Schmidt, *The Fermilab 400-MeV Linac upgrade*, FERMILAB-CONF-93-111 (1993).
- [8] J. Marriner, *Stochastic Cooling Overview*, FERMILAB-CONF-03-158 (2003).
- [9] DØ Collaboration, V.M. Abazov *et al.*, *The Upgraded DØ Detector*, hep-physics/0507191, (2005).
- [10] S. Eidelman *et al.*, *The Review of Particle Physics*, Phys. Lett. B 592, 1 (2004).
- [11] J. Huston *et al.*, *New Generation of Parton Distributions with Uncertainties from Global QCD Analysis*, JHEP 0207:12 (2002).
- [12] V.M. Abazov *et al.* [DØ Collaboration], *Measurement of the t \bar{t} Production Cross Section in p \bar{p} Collisions at $\sqrt{s} = 1.96$ TeV using Kinematic Characteristics of Lepton+Jets Events*, hep-ex/0504043 (2005).
- [13] D. Acosta *et al.* [CDF Collaboration], *Measurement of the t \bar{t} Production Cross Section in p \bar{p} Collisions using the Kinematics of Lepton+Jet Events*, hep-ex/0504053 (2005).

- [14] N. Kidonakis, R. Vogt, *Next-to-next-to-leading order soft-gluon corrections in top quark hadroproduction*, Phys. Rev. D 68, 114014 (2003).
- [15] M. Cacciari *et al.*, *The $t\bar{t}$ cross section at 1.8 TeV and 1.96 TeV: a Study of the Systematics due to Parton Densities and Scale Dependence.*, JHEP 404, 68 (2004).
- [16] The LEP Collaborations, the LEP EW Group, the SLD EW and HF groups, *A Combination of Preliminary Electroweak Measurements and Constraints on the Standard Model*, hep-ex/0412015 (2004).
- [17] The CDF Collaboration, the D0 Collaboration, and the Tevatron Electroweak Working Group, *Combination of CDF and D0 Results on the Top-Quark Mass*, hep-ex/0404010 (2004).
- [18] S. Willenbrock, *Hadron Colliders, the Standard Model and Beyond*, he-ph/0212032 (2002).
- [19] R. E. Kalman, *A New Approach to Linear Filtering and Prediction Problems*, J. Bas. Eng. 82D 35 (1960).
- [20] R. E. Kalman, R. S. Brucy, *New Methods and Results in Linear Filtering and Prediction Theory*, J. Bas. Eng. 83D 95 (1961).
- [21] P. Billoir, *Track Fitting with Multiple Scattering: a New Method*, Nucl. Instrum. Meth. A 225, 352 (1984).
- [22] A. Garcia-Bellido *et al.*, *Primary Vertex Certification in p14*, DØ Note 4320 (2004).
- [23] A. Schwartzman, M. Narain, *Probabilistic Primary Vertex Selection*, DØ Note 4042 (2002).
- [24] C. Clement *et al.*, *p14 Muon-ID certification note*, DØ Note 4350 (2004).
- [25] E. Nurse, P. Telford, *Measurement of cross section times branching ratio for $Z \rightarrow \mu\mu$ in $p\bar{p}$ collisions at 1.96 TeV*, DØ Note 4231 (2003).
- [26] Top Physics Working Group, *DØ Top Analyses and Data Sample for the Winter Conference 2004*, DØ Note 4419 (2004).
- [27] S. J. Park *et al.*, *Elektron Likelihood in p14*, DØ Note 4449 (2004).
- [28] G. Blazey *et al.*, *Run II Jet Physics*, DØ Note 3750 (2000).
- [29] U. Bassler, G. Bernardi, *Towards a Coherent Treatment of Calorimetric Energies: Missing Transverse Energy, Jets, E.M. Objects and the T42 Algorithm*, DØ Note 4124 (2003).
- [30] U. Bassler, G. Bernardi, S. Trincaz-Duvoid, J.-R. Vilmant, *Technical Description of the T42 Algorithm for the Calorimeter Noise Suppression*, DØ Note 4146 (2003).
- [31] G. Bernardi, E. Busato, J.-R. Vilmant, *Improvements from the T42 Algorithm on Calorimeter Object Reconstruction*, DØ Note 4335 (2004).

- [32] J.-L. Agram *et al.*, *Jet Energy Scale at D0 RunII*, DØ Note 4720 (2005).
- [33] J.-F. Grivaz, N. Makovec, *The Relative Data - Monte Carlo Jet Energy Scale*, DØ Note 4807 (2005).
- [34] M. Angelou *et al.*, *Top Trigger Efficiency Measurements and the top_trigger package*, DØ Note 4512 (2004).
- [35] R. Schwienhorst, *Top Trigger Selection and Application of Turn-On Curves to Monte Carlo*, DØ Note 4508 (2004).
- [36] K. Ranjan *et al.*, *Calorimeter Event Quality Using Level 1 Confirmation*, DØ Note 4554 (2004).
- [37] F. Fiedler, P. Haefner, *Determination of the Muon Transfer Function for Top Mass Measurements*, DØ Note 4818 (2005).
- [38] G.P. Lepage, *A New Algorithm for Adaptive Multidimensional Integration*, Journal of Computational Physics 27:192-203, (1978).
- [39] G.P. Lepage, *VEGAS: An Adaptive Multi-dimensional Integration Program*, Cornell preprint CLNS:80-447, (1980).
- [40] M. Galassi *et al.*, *GNU Scientific Library Reference Manual (2nd Ed.)*, ISBN 0954161734, <http://www.gnu.org/software/gsl/>.
- [41] G. Mahlon, S. Parke, *Maximizing Spin Correlations on Top Quark Pair Production at the Tevatron*, Phys. Lett. 80, 2063 (1997).
- [42] F.A. Berends, H. Kuijf, B. Tausk, W.T. Giele, *On the Production of a W and Jets at Hadron Colliders*, Nucl. Phys. B 357:32-64 (1991).
- [43] M. Mulders, *Ensemble testing for the Top Mass measurement*, DØ Note 4460, (2004).
- [44] R. Barlow, *Application of the Bootstrap resampling technique to Particle Physics experiments*, <http://www.hep.man.ac.uk/preprints/manhep99-4.ps> (2000).
- [45] F. Maltoni, T. Stelzer, *MadEvent: Automatic Event Generation with MadGraph*, JHEP 302, 27 (2003).
- [46] M.L. Mangano *et al.*, *ALPGEN, a Generator for Hard Multiparton Processes in Hadronic Collisions*, JHEP 307, 1 (2003).
- [47] M.-A. Pleier *et al.*, *Measurement of the $t\bar{t}$ Production Cross-Section at $\sqrt{s} = 1.96$ TeV in the Electron+Jets Final State using a Topological Method*, DØ Note 4662 (2004).
- [48] T. Golling, *Measurement of the $t\bar{t}$ Production Cross-Section at $\sqrt{s} = 1.96$ TeV in the Muon+Jets Final State using a Topological Method*, DØ Note 4667 (2004).
- [49] P. Schieferdecker *et al.*, *The Matrix Method and its Error Calculation*, DØ Note 4564, (2004).

- [50] J. Cammin, R. Demina, *The Relative Data - Monte Carlo b-Jet Energy Scale*, DØ Note in preparation (2005).
- [51] M.G. Bowler, *e+ e- Production of Heavy Quarks in the String Model.*, Z. Phys C11, 169 (1981).
- [52] C. Peterson *et. al*, *Scaling Violations in Inclusive e+ e- Annihilation Spectra.*, Phys. Rev. D27, 105 (1983).
- [53] A. Schwartzman, C. Tully, *Effect of h/e on the Relative b-to-light Jet Energy Scale Systematics*, DØ Note 4870, (2005).
- [54] H. L. Lai *et al.* [CTEQ Collaboration], *Global QCD analysis of parton structure of the nucleon: CTEQ5 parton distributions*, Eur. Phys. J. C 12, 375 (2000).
- [55] The CDF Collaboration, the D0 Collaboration, and the Tevatron Electroweak Working Group, *Combination of CDF and D0 Results on the Top-Quark Mass*, hep-ex/0507091 (2005).
- [56] The LEP Electroweak Working Group, <http://lepewwg.web.cern.ch/LEPEWWG/>
- [57] M. Mulders, M. Weber, *Top Mass Measurement with b-tagging and Jet Energy Scale Fit in the Lepton+Jets Channel using the Ideogram Method*, DØ Note 4802 (2005).

Curriculum Vitae

Philipp Schieferdecker

Personal Information

Born February 20th 1975 in Munich, Germany.

Nationality German.

Marital Status Married.

Education

2001–2005 Ph. D., Physics, expected October 2005
Ludwig-Maximilians Universität, München, Germany
Thesis: *Measurement of the Top Quark Mass with the Matrix Element Method in the Lepton+Jets Final State at DØ Run II*

1995–2001 Diplom, Physics, 2001
Ludwig-Maximilians Universität, München, Germany
Thesis: *Feasibility Study of a Magnetic Monopole Trigger in $p\bar{p}$ -collisions*

1994–1995 Military Service, Gebirgsjägerbatallion 232, Berchtesgaden, Germany.

1985–1994 Abitur, Wilhelmsgymnasium, München, Germany.

1981–1985 Elementary School, Gebeleschule, München, Germany.

Academic Honors

09/2004–07/2005 Fellow of the DFG Training Research School (Graduiertenkolleg 1054)
"Particle Physics at the Energy Frontier of New Phenomena".

Publications "Simulating Magnetic Monopoles by Extending GEANT"
(accepted by NIM/A)

DØ author since March 2004.

"A step towards a Computing GRID for the LHC Experiments: ATLAS Data Challenge 1" (submitted to NIM/A).

"A cosmic Ray Measurement Facility for ATLAS Muon Chambers",
e-Print Archive: physics/0307147, contributed to the EPS2003 conference.

Munich, Germany, August 3rd 2005